INVESTIGATION OF VISCOELASTIC-CREEP AND MECHANICAL-HYSTERESIS BEHAVIOR OF HYDROSTATICALLY STRESSED CRYSTAL USING THE PHASE FIELD CRYSTAL METHOD

JATUPON EM-UDOM

A THESIS SUBMITTED IN PARTIAL FULFILLMENT
OF THE REQUIREMENT FOR THE DEGREE OF
DOCTOR OF ENGINEERING IN INDUSTRIAL ENGINEERING
FACULTY OF ENGINEERING
KING MONGKUT'S INSTITUTE OF TECHNOLOGY LADKRABANG
2020

KMITL-2020-EN-D-218-011

INVESTIGATION OF VISCOELASTIC-CREEP AND MECHANICAL-HYSTERESIS BEHAVIOR OF HYDROSTATICALLY STRESSED CRYSTAL USING THE PHASE FIELD CRYSTAL METHOD

JATUPON EM-UDOM

A THESIS SUBMITTED IN PARTIAL FULFILLMENT
OF THE REQUIREMENT FOR THE DEGREE OF
DOCTOR OF ENGINEERING IN INDUSTRIAL ENGINEERING
FACULTY OF ENGINEERING
KING MONGKUT'S INSTITUTE OF TECHNOLOGY LADKRABANG
2020

KMITL-2020-EN-D-218-011

การศึกษาพฤติกรรมแบบวิสโคอิลาสติกครีพและแมคคานิคอลฮิสเทอรีซิสสำหรับโครงสร้างผลึกภายใต้ความเค้นแบบไฮโดรสแตติกด้วยระเบียบวิธีเฟสฟิลด์คริสตัล

INVESTIGATION OF VISCOELASTIC-CREEP AND MECHANICAL-HYSTERESIS BEHAVIOR OF HYDROSTATICALLY STRESSED CRYSTAL USING THE PHASE FIELD CRYSTAL METHOD

จตุพล เอมอุดม

JATUPON EM-UDOM

วิทยานิพนธ์นี้เป็นส่วนหนึ่งของการศึกษาตามหลักสูตรปริญญาวิศวกรรมศาสตรดุษฎีบัณฑิต

สาขาวิชาวิศวกรรมอุตสาหการ

คณะวิศวกรรมศาสตร์

สถาบันเทคโนโลยีพระจอมเกล้าเจ้าคุณทหารลาดกระบัง

พ.ศ.2563

KMITL-2020-EN-D-218-011

หัวข้อวิทยานิพนธ์	การศึกษาพฤติกรรมแบบวิสโคอิลาสติกครีพและแมคคานิคอลฮิสเทอรีซิสสำหรับโครงสร้างผลึกภายใต้ความเค้นแบบไฮโดรสแตติกด้วยระเบียบวิธีเฟสฟิลด์คริสตัล
นักศึกษา	นาย จตุพล เอมอุดม
รหัสประจำตัว	56601382
ปริญญา	วิศวกรรมศาสตรดุษฎีบัณฑิต
สาขาวิชา	วิศวกรรมอุตสาหการ
พ.ศ.	2563
อาจารย์ที่ปรึกษาวิทยานิพนธ์	ผศ.ดร.นิรันดร์ พิสุทธอานนท์

บทคัดย่อ

วัสดุแดมปิ้งเป็นวัสดุที่ถูกนำมาใช้อย่างแพร่หลายในงานวิศวกรรม คุณสมบัติที่สำคัญของวัสดุชนิดนี้มีความสัมพันธ์กับพฤติกรรมวิสโคอิลาสติกซิตี้และแมคคานิคอลฮิสเทอรีซิส ในทศวรรษที่ผ่านมาแบบจำลองเฟสฟิลด์คริสตัลเป็นแบบจำลองได้ถูกนำมาใช้อย่างแพร่หลายในการศึกษาปรากฏการณ์ที่เกิดขึ้นในวัสดุ โดยงานวิจัยฉบับนี้ได้นำแบบจำลองดังกล่าวมาใช้ร่วมกับสมการควบคุมแรงดันพลวัตและสมการควบคุมแรงดันพลวัตแบบดัดแปลงในการศึกษาพฤติกรรมแบบวิสโคอิลาสติกครีพและแมคคานิคอลฮิสเทอรีซิส โดยข้อดีของสมการควบคุมแรงดันพลวัตก็คือสามารถช่วยให้เราทำการควบคุมการเสียรูปของวัสดุได้โดยการกำหนดแรงดันควบคุมจากภายนอกซึ่งเอื้อต่อการศึกษาเทียบเคียงกับปรากฏการณ์ในการทดลองจริงภายใต้แรงดันกระทำหลายรูปแบบ สำหรับการศึกษาทดสอบแบบจำลองในงานวิจัยนี้เราได้ทำการทดสอบกับโครงสร้างผลึกแบบลูกบาศก์บอดี้เซ็นเตอร์ ภายใต้แรงดันแบบไฮโดรสแตติก 2 แบบ คือ ภายใต้แรงดันคงที่สำหรับศึกษาพฤติกรรมของวิสโคอิลาสติกครีพ และ ภายใต้แรงดันกระทำแบบสัญญาณไซน์สำหรับศึกษาพฤติกรรมแมคคานิคอลฮิสเทอรีซิส โดยผลการทดสอบเราจะสังเกตเห็นการตอบสนองของความเครียดที่หน่วงตามเวลาจากแรงดันทั้งสองแบบซึ่งเป็นข้อยืนยันของการมีอยู่ของพฤติกรรมวิสโคอิลาสติกซิตี้ที่ถูกทำนายด้วยแบบจำลอง โดยระดับของความเป็นวิสโคอิลาสติกนั้นสามารถถูกควบคุมผ่านทางพารามิเตอร์ของสมการการควบคุมแรงดันพลวัต อย่างไรก็ตามแม้ว่าแบบจำลองเฟสฟิลด์คริสตัลที่ถูกนำมาใช้ร่วมกับสมการควบคุมแรงดันพลวัตจะสามารถอธิบายพฤติกรรมวิสโคอิลาสติกครีพได้ดี แต่การทำนายพฤติกรรมแมคคานิคอลฮิสเทอรีซิสโดยอาศัยวิธีการนี้ก็ยังมีข้อผิดพลาดอยู่โดยเฉพาะอย่างยิ่งที่ความถี่สูง ดังนั้นเราจึงได้ทำการดัดแปลงสมการควบคุมแรงดันพลวัตดังกล่าวโดยทำการเพิ่มเทอมอนุพันธ์ของแรงดันเทียบกับเวลาเข้าไป โดยเราเรียกสมการดังกล่าวนี้ว่าสมการควบคุมแรงดันพลวัตแบบดัดแปลง โดยสมการดัดแปลงที่เรานำเสนอนี้เมื่อนำมาใช้ร่วมกับแบบจำลองเฟสฟิลด์คริสตัลได้ช่วยให้เราสามารถที่จะทำนายพฤติกรรมของแมคคานิคอลฮิสเทอรีซิสรวมถึงพารามิเตอร์ที่เกี่ยวข้องมีความสอดคล้องใกล้เคียงกับวัสดุจริงที่ย่านความถี่ที่กว้างขึ้น เราหวังเป็นอย่างยิ่งว่าวิธีการเฟสฟิลด์คริสตัลที่นำมาใช้ร่วมกับสมการควบคุมแรงดันพลวัตแบบดัดแปลงนี้จะสามารถนำไปขยายผลต่อในการศึกษาในระบบที่มีความซับซ้อนขึ้น และยังคงสามารถที่จะแสดงพฤติกรรมแมคคานิคอลฮิสเทอริซิสได้อย่างแม่นยำอันจะนำไปสู่การทำนายพารามิเตอร์ที่มีความน่าเชื่อถือมากยิ่งขึ้นในการออกแบบวัสดุแดมปิ้ง

Thesis	Investigation of Viscoelastic-Creep and Mechanical-Hysteresis Behavior of Hydrostatically Stressed Crystal Using the Phase Field Crystal Method
Student	Mr. Jatupon Em-Udom
Student ID.	56601382
Degree	Doctor of Engineering
Program	Industrial Engineering
Year	2020
Thesis Advisor	Asst.Prof.Dr. Nirand Pisutha-Arnond

ABSTRACT

Damping materials have been used in numerous engineering applications. The important property that plays a key role in these materials is a damping capacity which is related to viscoelasticity and mechanical hysteresis behavior. During the last decade, the phase-field crystal method has emerged as a robust tool in predicting materials phenomena. In this work, we investigate viscoelastic-creep and mechanical-hysteresis behaviors predicted by the PFC method that is incorporated with pressure-controlled dynamics equation, referred to as PFC-PCD method, and our recently proposed modified pressure-controlled dynamics equation, referred to as PFC-MPCD method. The advantage of the PCD equation enables the control of deformation using external pressure which allows studies of experimentally-observed phenomena under different types of applied pressure. In particular, we simulate a hydrostatically-stressed of the body-centered-cubic crystal subjected to two types of pressure profiles: constant pressure for the viscoelastic-creep, and sinusoidal pressure for the mechanical-hysteresis. According to the results, we observe that the PFC-PCD method can exhibit delayed strain responses from both types of pressure which is indicative of viscoelasticity, and the degree of viscoelasticity can be controlled by the parameter in the PCD equation. Nonetheless, although the PFC-PCD is successful in predicting viscoelastic-creep, the mechanical-hysteresis produced by this method is inaccurate, in particular, at the high-pressure oscillation frequency. Therefore, we modify the existing PCD equation by introducing the pressure time derivative term, denoted as the MPCD equation. This MPCD equation enables us to produce mechanical-hysteresis consistent with the solid material behavior at broader frequency range. We expect that this new PFC-MPCD method can be extended to a more complex system and still be capable to produce the accurate mechanical hysteresis behavior and its related parameters which results in predicting more reliable parameters in damping material design.

กิตติกรรมประกาศ

วิทยานิพนธ์เล่มนี้นี้ได้รับการสนับสนุนเงินทุนจากโครงการพัฒนาศักยภาพบุคลากรเพื่อการวิจัยและพัฒนาสำหรับภาคอุตสาหกรรม (NSTDA-University-Industry Research Collaboration, NUI-RC) ภายใต้หมายเลขสัญญา NUI-RC-M33-22-59-001D รวมถึงการสนับสนุนในด้านสถานที่ เอกสาร ตำรา และ เครื่องคอมพิวเตอร์ที่ใช้สำหรับการทำการคำนวณขั้นสูงเพื่อประกอบในงานวิจัยจาก ภาควิชาวิศวกรรมอุตสาหการ คณะ วิศวกรรมศาสตร์ สถาบันเทคโนโลยีพระจอมเกล้าเจ้าคุณทหารลาดกระบัง และ สำนักงานกองทุนสนับสนุนการวิจัย (TRF) ภายใต้หมายเลขสัญญา TRF5880008 ทางกระผมขอแสดงความขอบคุณทุกภาคส่วน ทุกองค์กรมา ณ ที่นี้ด้วย และนอกจากนี้กระผมเองยังต้องขอแสดงความขอบคุณอาจารย์ที่ปรึกษาวิทยานิพนธ์ อาจารย์ ผศ.ดร. นิรันดร์ พิสุทธอานนท์ ที่ท่านคอยให้การสนับสนุนและช่วยเหลือในทุกๆเรื่อง อาทิเช่น การให้คำแนะนำปรึกษาปัญหาทางด้านเทคนิคและด้านวิชาการเชิงลึก อีกทั้งยังช่วยแนะนำ แก้ไขพัฒนาโค้ดโปรแกรมในการจำลองเหตุการณ์เสมือนจริง รวมถึงการจัดหาแหล่งเงินทุนสนับสนุนการวิจัยและค่าใช้จ่ายในการประชุมวิชาการทั้งในและนอกประเทศ และ การจัดหาเอกสาร ตำรา บทความทางวิชาการ และอุปกรณ์คอมพิวเตอร์ความเร็วสูง เพื่อสนับสนุนงานวิจัย พร้อมกับตรวจสอบแก้ไขปรับปรุงบทความวิจัยอย่างหามรุ่งหามค่ำ รวมถึงคอยช่วยสนับสนุนให้กำลังใจและช่วยแก้ไขวิกฤติในทุกด้านจนทุกอย่างผ่านพ้นลุล่วงไปได้ด้วยดี จนงานวิจัยชิ้นนี้ได้รับการตอบรับให้ตีพิมพ์ลงในวารสารทางวิชาการชั้นนำในระดับนานาชาติได้ นอกจากนี้ทางกระผมเองยังต้องขอแสดงความขอบคุณ อาจารย์ รศ.วิชาญ เตชิดธีระ ภาควิชา ฟิสิกส์ คณะ วิทยาศาสตร์ สถาบันเทคโนโลยีพระจอมเกล้าเจ้าคุณทหารลาดกระบัง สำหรับการให้คำแนะนำด้านเทคนิค และ ดร.ศาศวัต มหบุญพาชัย สังกัด ศูนย์เทคโนโลยีและวัสดุแห่งชาติ สำนักงานพัฒนาวิทยาศาสตร์และเทคโนโลยีแห่งชาติ (สวทช.) สำหรับคำปรึกษาและการสนับสนุนเงินทุนวิจัยจากโครงการ NSTDA-University-Industry Research Collaboration (NUI-RC) อีกทั้ง คุณ วิทยา แก้วพวง บริษัท เวสเทิร์น ดิจิตอล ประเทศไทย จำกัด สำหรับการให้การสนับสนุนจากทางภาคอุตสาหกรรม ท้ายที่สุดนี้กระผมต้องขอกราบขอบพระคุณ คุณพ่อ พสุธร เอมอุดม คุณแม่ นิรมล เอมอุดม ที่ให้การสนับสนุนในทุกเรื่องและให้กำลังใจตลอดเรื่อยมา จนลูกคนนี้ได้มีทุกวันนี้ สำหรับคุณงามความดีอันใดที่เกิดจากวิทยานิพนธ์ฉบับนี้ ข้าพเจ้าขอมอบให้กับบิดามารดา ซึ่งเป็นที่รักและเคารพยิ่ง ตลอดจนครูอาจารย์และผู้มีพระคุณที่เป็นที่เคารพทุกท่านที่ยังมิได้กล่าวถึง ณ ที่นี้ที่ได้ประสิทธิ์ประสาทวิชาความรู้และถ่ายทอดประสบการณ์ที่ดีให้แก่ข้าพเจ้า

จตุพล   เอมอุดม

TABLE OF CONTENTS

LIST OF TABLES

LIST OF FIGURES

CHAPTER 1

Introduction

1.1 Background

Damping materials have been used in many engineering applications and, in particular, in energy absorption such as noise reduction, vibration isolation and impact absorber. It is of vital importance as one can damp vibrations in mechanical systems so as to prolong the service life of components, also reduce acoustic noise. There are several classes of damping material ranging from structural steel to polymers and rubber.

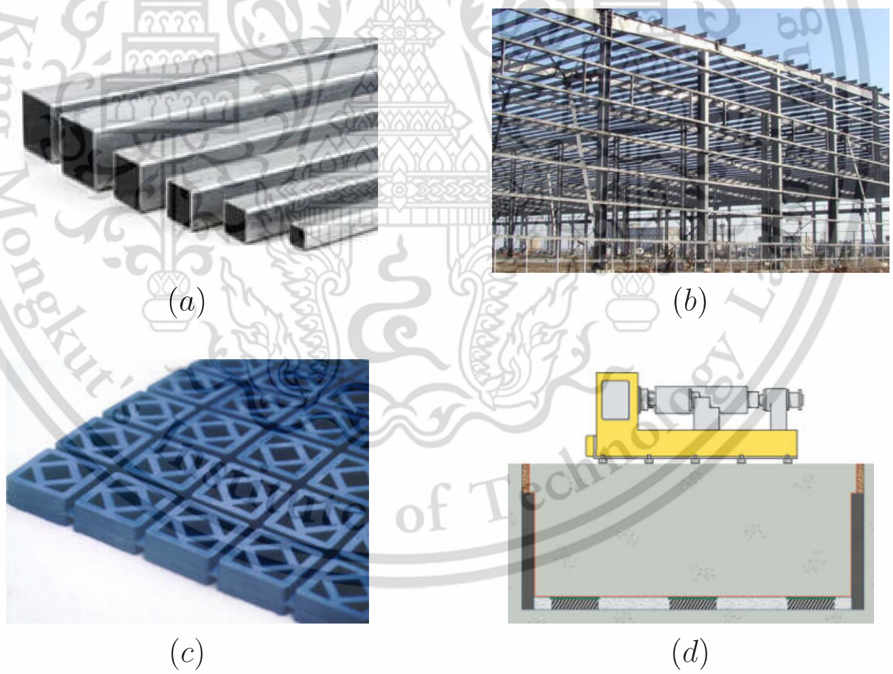

Figure 1.1: Damping materials and their applications (a) Structural steel [2] (b) Vibration damping in infrastructure design [3] (c) Rubber [4] (d) Noise reduction in rotating machinery [5].

Damping of structures can be achieved via layers of high-damping materials, typically polymers, by external lumped dampers that may contain a viscous device, or using materials with intrinsically high damping [6]. Structural metals such as steel, brass and aluminum alloys exhibit very low damping of 10^{-3} or less such as steel (10^{-4}), brass ($9x10^{-5}$) and aluminum alloys ($< 10^{-5}$). Material damping of structural metals is very low; therefore, structural damping obtained via specifically designed structures can be used in the cases where high damping is required to compensate for the drawback of low intrinsic damping. A maximal combination of stiffness and damping is desirable for the damping layer and structural damping applications in which it is intended that vibration in machinery and vehicles be reduced.

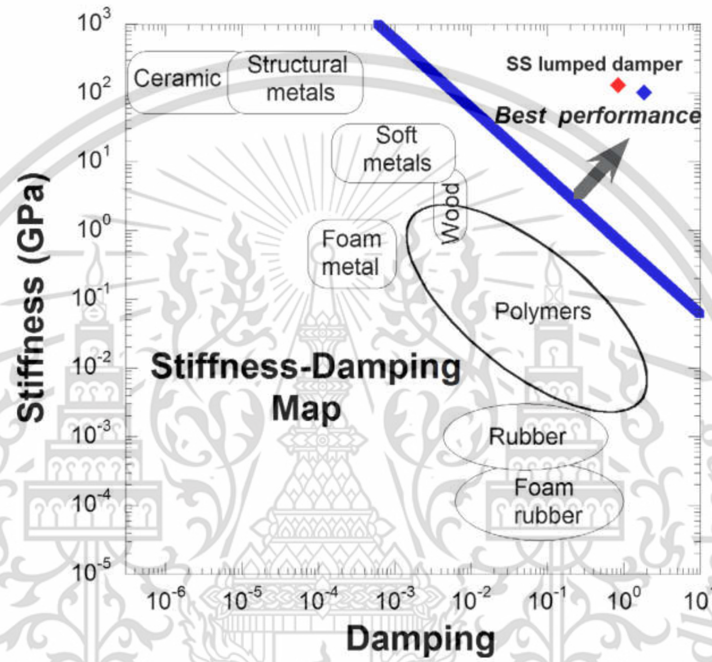

Figure 1.2: Stiffness-damping map for several classes of materials in the linear regime at ambient temperature. The diagonal line, thick blue line, represents a constant figure of merit $|G^*|\tan(\delta) = 0.6$. Commercial damping layers typically have a lower figure of merit. The solid diamond symbols represent the properties of the stainless steel damper modules in the nonlinear regime. It should be noted that the measure of damping in linear systems is $\tan(\delta)$ where δ is the phase shift between stress and strain response [6].

Figure 1.2 illustrates the stiffness-damping map for several classes of material at ambient temperature. The diagonal in the figure depicts $|G^*|\tan(\delta) = 0.6.$ occupy the region to the left of that line. Most materials occupy the region to the left of that line for example structural materials occupy regions to the left or far to the left in the diagram, high stiffness with low damping capacity. On the other hand, most rubbery and polymeric materials occupy the lower right, low stiffness with high damping capacity. To select the appropriate damping material in intended application depends on the character of that application for example noise associated with material damping is of interest in the context of experiments designed to detect gravitational waves. The wires supporting interferometer mirrors generate noise proportional to their damping, so low damping materials are preferable. Whereas, materials and structures with high damping are intended for applications in which high damping is desired, for example to reduce vibration amplitude or to reduce the time scale for vibration to die out after an impulse.

Damping capacity indicates the ability of material in dissipating energy during the deformation which can be measured through mechanical-hysteresis curve of viscoelasticity. Viscoelasticity is the behavior with both viscous and elastic characteristics; thus materials with viscoelastic behavior can return to its original configuration when unloaded but does so in a time dependent manner [7]. The viscous property also leads to the fact that materials response depends on the rate at which it is deformed. Viscoelastic behavior is characterized by three phenomena; viscoelastic-creep, stress relaxation and mechanical-hysteresis behavior. Figure 1.3 (a) shows viscoelastic creep response

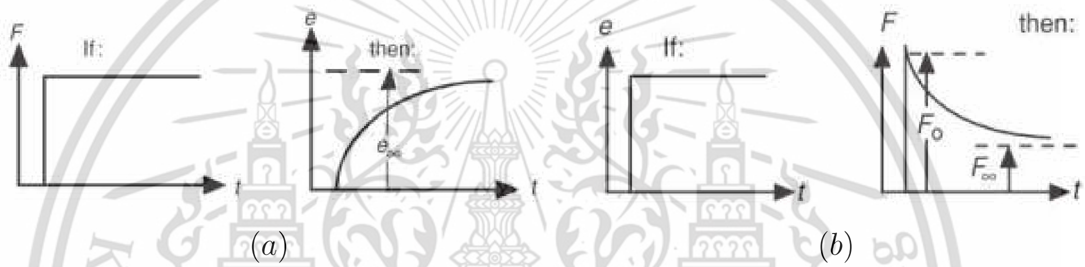

Figure 1.3: (a) Viscoelastic-creep under constant applied load (b) Stress relaxation under applied constant strain [7].

under applied constant load. The system behavior demonstrates transient strain response in the early stage and reaches its steady-state value, e_∞, as t approaches to infinity. While, figure 1.3 (b) illustrates stress relaxation under applied constant strain. The stress response tends to relax as increasing t and reaches its steady-state value, F_∞, as t approaches to infinity. Figure 1.4 shows mechanical-hystersis curve established by sinusoidal stress oscillation and its corresponding strain response where $\sigma(t) = \sigma_0 \sin(\omega t)$ is sinusoidal stress oscillation, $e(t) = e_0 \sin(\omega t - \delta)$ represents strain response corresponding to sinusoidal stress oscillation and the δ parameter is phase lag between sinusoidal stress oscillation, $\sigma(t)$, and strain response, $e(t)$. As we mention earlier that the δ parameter closely related to damping capacity of material. Now it's time to demonstrate how the relationship can be constructed. We will establish energy loss relation first. Let ΔU denote the energy loss per cycle per volume below [7]

$$\Delta U = \oint \sigma de \tag{1.1}$$

Note that $de = e_0 \cos(\omega t - \delta) d(\omega t)$. Substitute this relation into Eq. (1.1), we obtain [7]

$$\Delta U = \oint \sigma_0 e_0 \sin(\omega t) \cos(\omega t - \delta) d(\omega t) \tag{1.2}$$

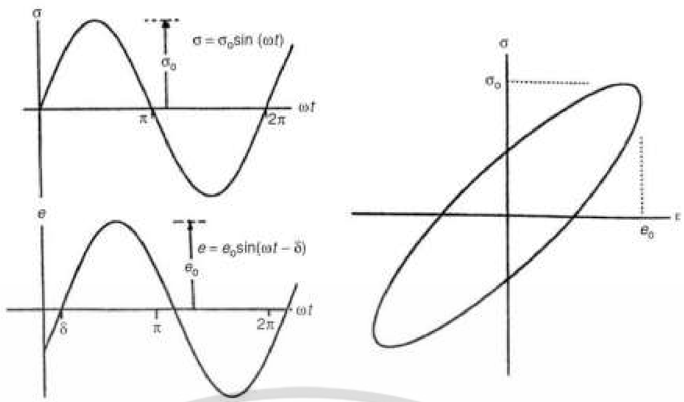

Figure 1.4: Mechanical-hysteresis behavior under sinusoidal stress oscillation established by sinusoidal stress oscillation, $\sigma(t)$, and strain response, $e(t)$ [7].

If we integrate equation Eq. (1.2) from 0 to 2π, we have [7]

$$\frac{\Delta U}{U} = 2\pi \sin(\delta) \tag{1.3}$$

If the δ is small, equation (1.3) yields [7]

$$\frac{\Delta U}{U} \approx 2\pi\delta \tag{1.4}$$

where $U = \sigma_0 e_0/2$. To derive damping capacity of material, we start regarding the

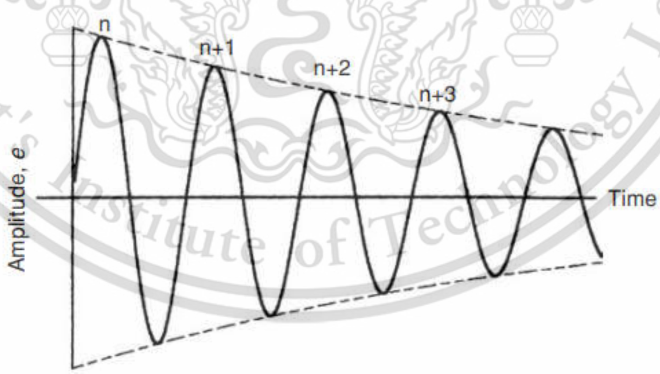

Figure 1.5: Natural decay of strain oscillation,e, induced by sinusoidal stress oscillation, σ. The damping capacity can be obtained regarding this plot [7].

definition of natural decay, Fig. 1.5, established by logarithmic decrement below [7]

$$\Lambda = \ln\left(\frac{e_{n+1}}{e_n}\right) \tag{1.5}$$

where Λ is damping capacity of material. Denote that $U_n = \sigma_n e_n/2 = Ee_n^2/2$ and $U_{n+1} = \sigma_{n+1}e_{n+1}/2 = Ee_{n+1}^2/2$. Then, we obtain [7]

$$\frac{e_{n+1}}{e_n} = \left(1 + \frac{\Delta U}{U}\right)^{\frac{1}{2}}, \qquad U_{n+1} = U_n + \Delta U \tag{1.6}$$

Note that $U \equiv U_n$. Substitute Eq. (1.6) into Eq. (1.5), it yields [7]

$$\Lambda = \frac{1}{2}\ln\left(1 + \frac{\Delta U}{U}\right) \tag{1.7}$$

Using the Taylor's expansion on the logarithmic term on the right hand side of the equation. Then, we obtain damping capacity relation below [7]

$$\Lambda \approx \pi\delta \tag{1.8}$$

Note that if Taylor's expansion is assumed, the logarithmic term $\ln(1 + \Delta U/U) = (\Delta U/U - (\Delta U/U)^2/2 + ...)$. Then, we obtain $\ln(1 + \Delta U/U) \approx \Delta U/U$ if small $\Delta U/U$ value is speculated. The mechanical-hysteresis curve can provide not only the information of loss tangent factor parameter, $\tan(\delta)$, but also the other two important dynamic parameters e.g. storage modulus parameter, G_{storage}, and loss modulus parameter, G_{loss}, regarding Fig. 1.6. According to Fig. 1.6, the loss tangent factor, $\tan(\delta)$,

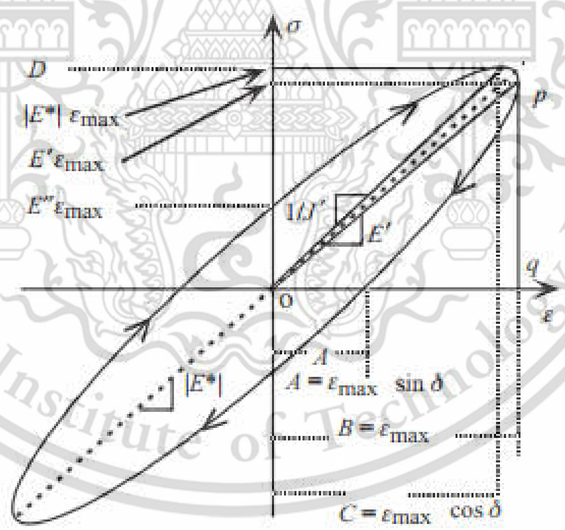

Figure 1.6: Stress, σ, and strain, ε, for a linearly viscoelastic material under oscillatory loading. Illustration of slopes and intercepts. Storage modulus, G_{storage}, represents the energy storage during the system deformation whereas loss modulus, G_{loss}, represents the dissipated energy during the system deformation. Note that $G^* = G_{\text{storage}} + jG_{\text{loss}}$ represents complex modulus and $\tan(\delta)$ is defined by $G_{\text{loss}}/G_{\text{storage}}$ [8].

can be calculated from the ratio of A/C where A is the strain value at zero stress condition and C is the strain value at maximum stress condition. While, the storage modulus G_{storage} and G_{loss} can be calculated from the ratio of E/B and F/B, respectively, where E is the the stress value at maximum strain condition, F is the stress at zero strain condition and B is the maximum strain value. Moreover, the mechanical-hysteresis curve is frequency dependent behavior. If the frequency is high enough, there is no relaxation and therefore no damping, and the modulus, $G_{\text{storage}} = \sigma/\varepsilon_{\text{max}}$, is high. On the other hand, at low frequencies, there is complete relaxation with the result that there is no damping, but the modulus will be lower. Whereas, at intermediate frequencies, there is partial relaxation, with high damping and a frequency dependent modulus. The hysteresis curves for high, low, and intermediate frequencies

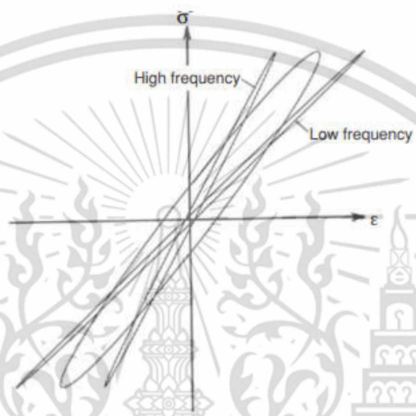

Figure 1.7: The influence of oscillation frequency on mechanical-hysteresis behavior. The damping capacity of material is low at low and high frequency value whereas the damping capacity of material is high at intermediate frequency value [7].

are illustrated in Fig. 1.7, and Fig. 1.8 illustrates the corresponding interdependence of loss tangent factor and both complex moduli. Figure 1.8 demonstrates the results in a log–log coordinate system used frequently to present experimental data [9]. The important parts of the frequency curves are discussed as follows. At zero frequency, G_{loss} parameter and tan(δ) are zero. G_{storage} is equal to the static modulus G_0 and the initial slopes of the log G_{storage}–log ω functions are zero. All loss parameters start to increase with increasing frequency and the slope of G_{storage}–log ω function, also, the value of G_{storage} start to increase too. Figure 1.9 shows the influence of applied load frequency on storage modulus and loss tangent factor in poly-methyl methacrylate, PMMA, material [8]. The illustration demonstrates that the loss tangent factor, tan(δ), passes at least one peak location and storage modulus, G_{storage}, starts with finite value at very low frequency value and begins rising at increasing then becomes stable at very high frequency range. Figure 1.10 shows the influence of temperature on storage modulus, loss modulus and loss tangent factor in poly-methyl methacrylate, PMMA, material. PMMA exhibits a large peak, called an α peak, in the loss tangent at 135°C and a smaller one, called a β peak, at 20°C [8]. Figure 1.11 and Figure 1.12 demonstrate the influence of frequency, f, and temperature, T, on dynamic viscoelastic properties, respectively. Frequency dependent damping of ZA27 alloy and pure cast

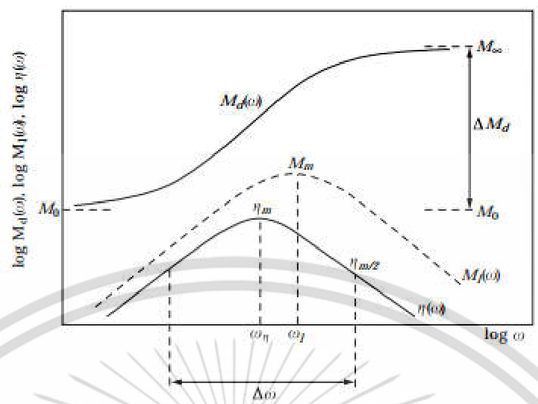

Figure 1.8: The typical characters of frequency dependence of any storage modulus, loss modulus and loss tangent factor of real solid materials plotted in log–log system for the case of one loss maximum [9].

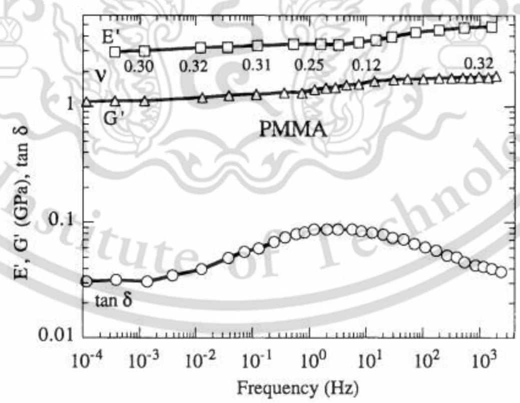

Figure 1.9: Complex moduli parameters in poly-methyl methacrylate, PMMA. The influence of applied load frequency, f, on storage modulus, G_{storage}, in both shear and tensile mode and loss tangent factor, $\tan(\delta)$ [8].

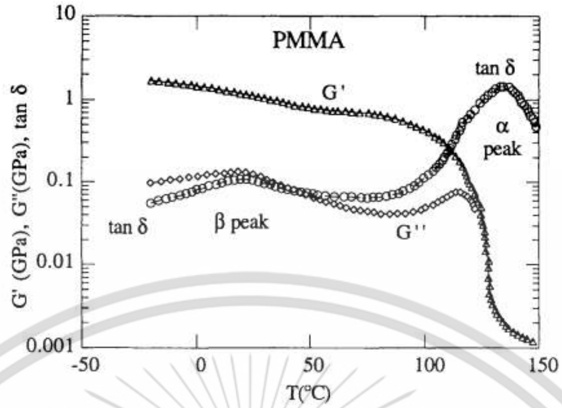

Figure 1.10: Complex moduli parameters in poly-methyl methacrylate, PMMA. The influence of temperature T on storage modulus, G_{storage}, loss modulus G_{loss} and loss tangent factor, tan(δ) [8].

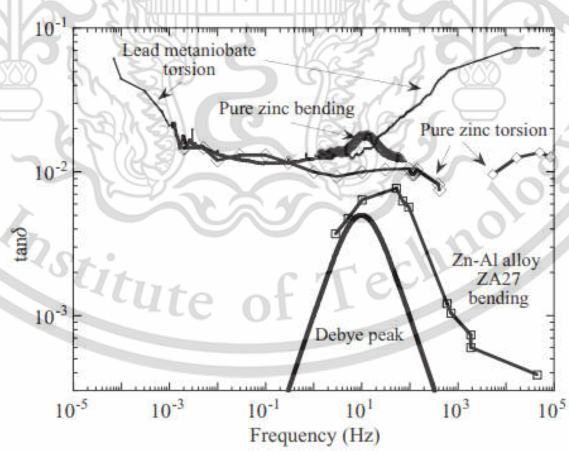

Figure 1.11: Complex moduli parameters in metallic material. The influence of frequency f on loss tangent factor, tan(δ). The tan(δ) of zinc and zinc alloy at 20°C, as a function of frequency [8].

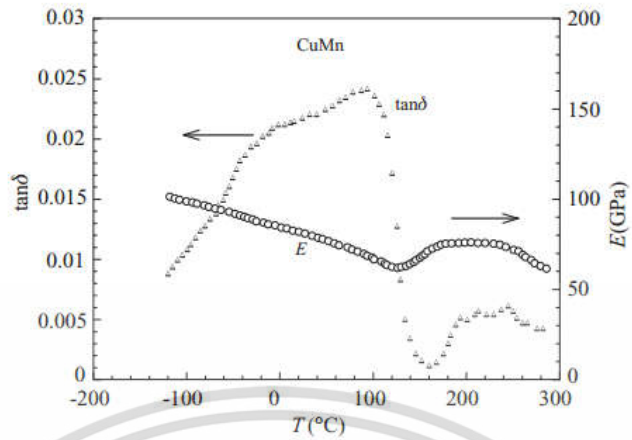

Figure 1.12: Complex moduli parameters in in metallic material. The influence of temperature T on storage modulus and loss tangent factor, $\tan(\delta)$. A class of manganese-copper alloys is of interest in applications which require high damping capacity [8].

zinc is compared in Fig. 1.11 and the damping capacity of Mn-Cu is high for a structural metal application as illustrated in Fig. 1.12 [8].

In order to select the damping material for specific application, these viscoelastic parameters and their suitable working conditions should be known accurately. There are two approaches to predict these viscoelastic parameters and their suitable working condition e.g. experimental approach and computational approach. For experimental

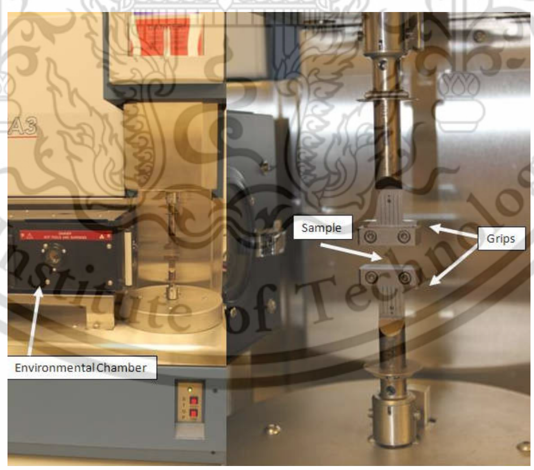

Figure 1.13: A typical Dynamic mechanical analysis (DMA) tester with grips to hold sample and environmental chamber to provide different temperature conditions. A sample is mounted on the grips and the environmental chamber can slide over to enclose the sample [10].

approach as shown in Fig. 1.13, this technique is called dynamic mechanical analysis

(DMA), also known as dynamic mechanical spectroscopy. It is a technique used to study and characterize materials. It is most useful for studying the viscoelastic behavior of polymers. A sinusoidal stress is applied and the strain in the material is measured, allowing one to determine the complex modulus. The temperature of the sample or the frequency of the stress are often varied, leading to variations in the complex modulus; this approach can be used to locate the glass transition temperature of the material, as well as to identify transitions corresponding to other molecular motions.

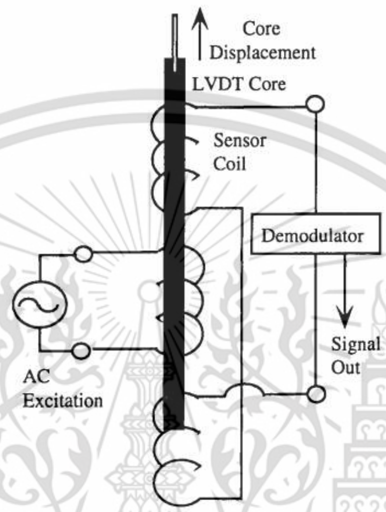

Figure 1.14: Schematic diagram of an LVDT in displacement and strain measurement [11].

In displacement and strain measurement [11], Linear variable differential transformers (LVDTs), as shown in Fig. 1.14, consist of several coils of wire surrounding a core of iron or other magnetic material. The core is usually attached to the specimen grip or a connected part of the apparatus. One coil, the primary, is supplied with a sinusoidal electrical signal at several kilohertz. Electrical signals induced in the secondary coils depend on the position of the core. These signals are demodulated, rectified, and filtered to obtain an electrical signal proportional to core displacement. Similar transducers used to detect rotary motion are called rotary variable differential transformers (RVDTs). The upper bound for frequency of the displacement signal may be as high as 1 kHz, depending on the physical size of the LVDT. Studies at low frequencies or long times are limited by drift in the electronics. Foil strain gages [11], as shown in Fig. 1.15, consist of an electrically conductive film, commonly a metal, upon a flexible substrate. Strain in the gage results in a change in electrical resistance. Strain gages are cemented to the specimen and connected to electronics which convert the resistance change to a voltage proportional to strain. Strain gages are too stiff to be used on soft polymers, rubber, or flexible foam; errors due to gage stiffness can even be problematic for glassy polymers. The strain gage itself imposes no upper limit on frequency other than that of the size of the gage in relation to the wavelength of stress waves in the material to which it is cemented. For gages of typical size, this upper limit can be on the order of 1 MHz. However, the electronic amplification system used with strain gages may impose further frequency limits. Strain gages respond to strain from thermal effects as well as strain resulting from stress. For accurate measurements of strain over long periods of time, considerable care must be exercised in the control of temperature and in matching the thermal expansion of the strain gage with that of the material to which it is cemented. Moreover, the cement used to attach the strain gage must be evaluated for possible creep which could introduce further errors. Cyanoacrylate cement intended for strain gage use exhibits lower creep than "super-glue" Cyanoacrylate cement for general purposes. For tests on rubbery materials or soft biological tissues, foil strain gages are not suitable. One can use a thin rubber tube filled with mercury as a strain gage for tests involving large deformation or compliant materials. Capacitive transducers [11], as shown in Fig. 1.16, are based on the fact

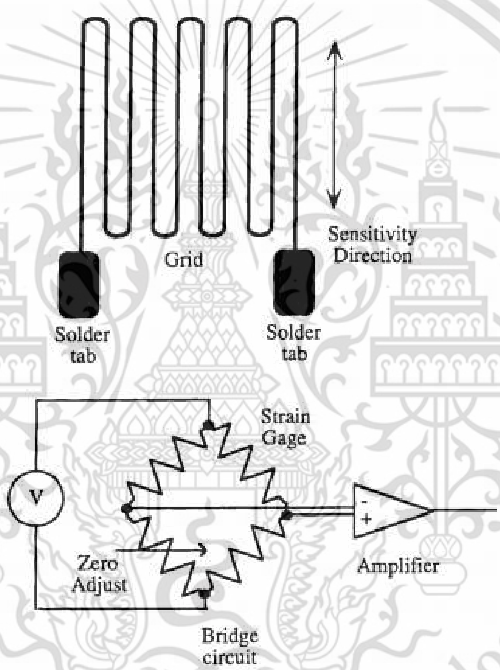

Figure 1.15: Strain gage, (top) Shape of foil strain gage grid, (bottom) Bridge circuit for strain gages [11].

that the capacitance C of a capacitor depends on the spacing between the plates. For a parallel plate capacitor of plate area A and spacing d, $C = \varepsilon_0 A/d$, with ε_0 as the permittivity of free space. This variation of capacitance with plate position can be used to convert linear or angular displacement into an electrical signal. In a typical application, the capacitive transducer is excited by a high frequency sinusoidal electrical signal and is connected to electronics which determine the capacitance, usually by determining the current which passes through the transducer. The signal is then rectified and filtered; the frequency response is therefore limited. Extensometers [11], as shown in Fig. 1.17, are devices clipped or otherwise attached to a specimen in tension to determine the relative displacement between the two attachment points.

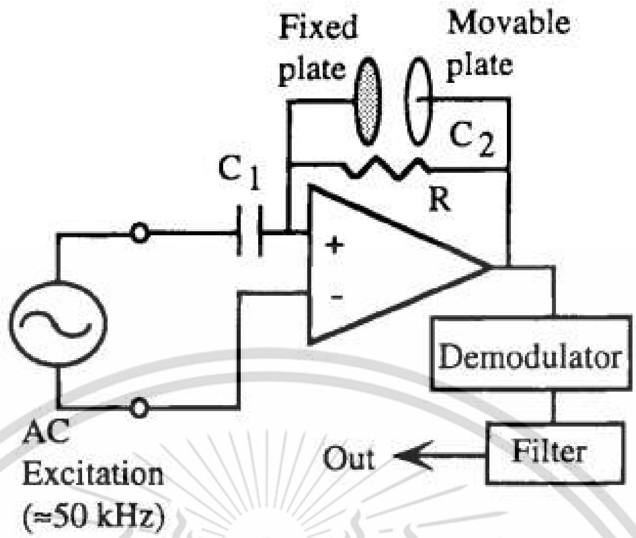

Figure 1.16: Capacitive displacement transducer and electronics [11].

They may be based on strain gages or LVDTs. Since they are attached off the specimen axis, response at high frequency is not to be expected; an upper bound from 30 to 100 Hz is as much as can be expected. Moreover, extensometers impose spring loads of 14 to 100 g (0.14 to 0.98 N) and so are suitable only for relatively stiff specimens. Optical methods can be extremely sensitive and offer the advantage that little or no mass needs to be attached to the specimen. To measure axial motion [11], one mirror of a Michelson interferometer, as shown in Fig. 1.18, can be attached to the specimen. One fringe corresponds to half a wavelength of light. The light can be converted to an electrical signal via a light-sensitive diode. Fractional fringes can be readily measured and corresponding displacement can be inferred via a digital counter or computer. The wavelength of light from the commonly used helium neon laser is 632.8 nm. Axial motion can also be measured using fiber optic sensors in which white light from one bundle of fibers is directed to the specimen. Reflected light from the specimen is then detected and the resulting signal is amplified electronically. This reflected light depends sensitively on displacement. Deformation of compliant materials such as rubber or soft biological tissue may be monitored with the aid of fiduciary marks on the specimen. For example, ink spots may be applied with a microscopic pipette, and observed via a calibrated microscope or a video system. As for angular displacements, they are readily measured either by interferometric or "optical lever" methods. An interferometer incorporating one or more right-angle prisms as reflective elements offers great sensitivity to angular displacement. In the optical lever a beam of light is reflected from a mirror attached to the specimen. For creep tests a light beam may be reflected to a distant target and its displacement measured with a caliper. For dynamic tests it is expedient to convert the light to an electrical signal. One way of doing this involves projecting the image of a grating on another grating.

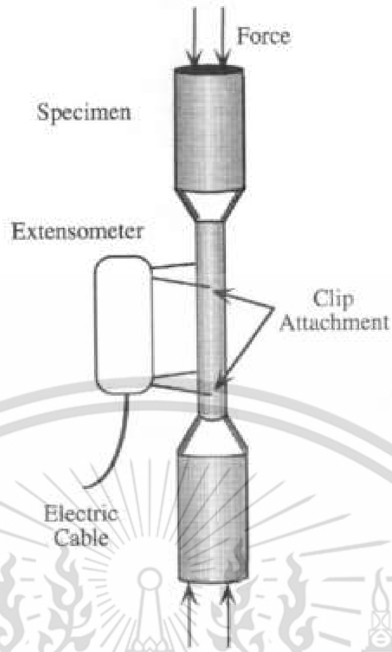

Figure 1.17: Extensometer attached to a specimen. The electric signal out is proportional to the displacement between the clip points [11].

The resulting light intensity signal is then converted to an electric signal by a photodiode. Light beam displacement can also be converted to an electrical signal by a split photodiode connected to a subtractor preamplifier. Semiconductor sensors sensitive to the position of an incident light beam are commercially available, but they have limited frequency response.

In force measurement [11], force and torque transducers, known as load cells and torque cells, respectively, involve measuring the displacement or strain of a deformable substrate, typically steel. Representative arrangements of strain gages for load cells and torque cells are shown in Fig. 1.19. Alternative forms of load cell include the proving ring which is compressed along a diameter, and configurations involving bending of plates. Torque cells are based on solid or hollow shafts, or cruciform arrangements fitted with strain gages. As with other transducers, load cells have characteristics of linearity, linear range, sensitivity, and frequency or time response. They typically contain a bar or plate of metal, usually steel, upon which strain gages are cemented. The detected strain signal on the bar is proportional to the force upon it, provided the metal and the strain gages are loaded below their proportional limit, one factor which limits the linear range. Overload capability is limited by yield in the metal parts of the transducer. Since steel itself is not perfectly elastic but exhibits a small viscoelastic response, testing machines which use load cells of this type are not suitable for the study of materials with extremely low loss. Torque cells are similar to load cells in their use of strain gages; the metal portion and the strain gage orientation are configured differently so that the detected strain signal is a response principally

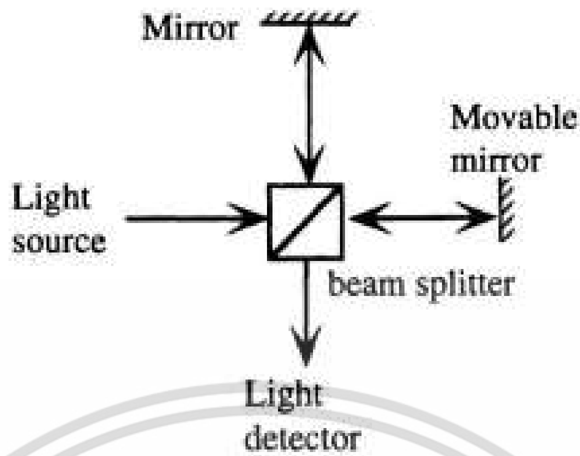

Figure 1.18: Michelson interferometer configuration for determining linear displacement. Moving mirror is attached to a specimen surface (not shown) [11].

to torque and not to any superposed axial load. The compliance of the load cell is important, in particular, the load cell should be much stiffer than any specimen tested. It is also important that the load cell be sensitive only to the kind of load to be measured and not to other loads. In biaxial tests, both tension and torsion may be applied. The torque channel should be sensitive only to torque, not to axial load. This characteristic is referred to as absence of cross talk. Load cells based on piezoelectric crystals are also available; they offer superior stiffness for dynamic studies. However, there is no response at zero frequency, and there are phase errors at low frequency, though the frequency range can extend below 0.001 Hz.

In environment control [11], viscoelastic properties depend on temperature; therefore, some form of temperature control is usually used in viscoelastic measurements. If the method of time-temperature superposition is to be used, then capability for conducting tests at several constant temperatures is required. Alternatively, the experimenter may measure dynamic properties at constant frequency, and may perform a temperature scan. As for the precision of temperature control, polymers are very sensitive to temperature, particularly in the transition region. It is therefore desirable to control temperature to within 0.1 °C over the length of the specimen and for the duration of the experiment. To achieve such control, a stream of air can be passed through a temperature control device, and directed to the specimen through a system of baffles. In tension-compression tests, a length change can arise from creep or from thermal expansion. Excellent temperature control is required in such studies to obtain good creep or relaxation results. Since thermal expansion of an isotropic material has no shear or torsional component, torsion tests are less demanding of accurate temperature control than are tension-compression tests. Many polymers, as well as materials, such as wood, of biological origin, are sensitive to hydration as well as to temperature. Humidity control is important for such materials; in the study of tissue such as bone, the specimen should be kept fully hydrated under physiological saline

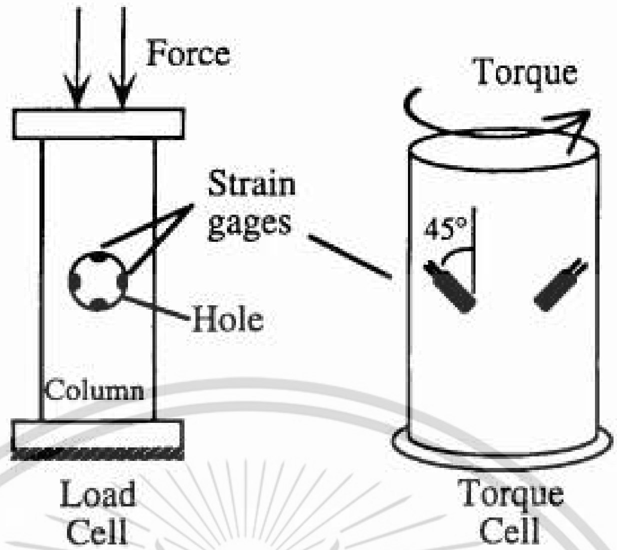

Figure 1.19: Torsional and axial test setting depending on which type of viscoelastic parameter, torsion mode or axial mode, is required [11].

solution. The creep behavior of concrete is also dependent on hydration. Metals which exhibit magnetic behavior are sensitive to external magnetic fields. If electromagnetic methods are used to apply force or torque to the specimen, care must be taken that magnetic fields in the vicinity of the specimen are controlled.

In the past few decades, the employment of numerical methods in materials science is promoted by the increasing capability of computer systems in terms of speed and information storage, and by the growing demands for quantitative predictions in industry and research. The scientific branch that has matured within this interdisciplinary field, bringing together approaches from materials science, physics, computer science, mathematics, chemistry, and mechanical engineering, is often referred to as computational materials science. The computational material science has become an alternative choice to predict various material properties and phenomena and can help speeding up the design process and reducing the cost of the real experimental study.

Computer simulation nowadays complements most if not all fields of materials science and engineering [12]. For instance, simulations in materials physics aim at predicting microstructural phenomena at the atomic scale using ab-initio molecular dynamics and Monte Carlo methods. Simulations in materials science pertaining to mechanical engineering typically focus on large-scale construction problems using finite element approaches where the microstructure is reduced to the incorporation of averaging constitutive laws.

In contrast to these examples, the original domain of materials science is the investigation of lattice defect ensembles at the mesoscale [12]. The use of simulations in this particular field represents a great challenge, in that it must bridge enormous space and time scales and provide concepts to adequately describe complex many-body interaction phenomena. For this purpose a number of new concepts have been developed which enable one to handle the interaction of many individual lattice defects in a more or less discrete fashion. The latter aspect is of special interest, since most microstructural evolution phenomena are highly nonlinear and entail self-organization on a microstructural scale

In contrast to atomic-scale molecular dynamics and Monte Carlo simulations, most mesoscale approaches are formulated as continuum models, but often with a discrete consideration of lattice defects [12]. The methods include deterministic and probabilistic cellular automata which may account for both short-range (local) and long-range (global) interactions, Ginzburg–Landau-, Cahn–Hilliard-, and Allen–Cahn-type phase field methods, dislocation dynamics, polycrystal and nonlinear crystal plasticity finite element models, topological network and vertex models, boundary dynamics, and multistate kinetic Potts methods. However, classical techniques such as molecular dynamics, Metropolis Monte Carlo, and conventional finite element simulations are also used extensively.

Scale [m]	Simulation method	Typical applications
$10^{-10} - 10^{-6}$	Metropolis Monte Carlo	thermodynamics, diffusion, ordering
$10^{-10} - 10^{-6}$	cluster variation method	thermodynamics
$10^{-10} - 10^{-6}$	Ising model	magnetism
$10^{-10} - 10^{-6}$	Bragg-Williams-Gorsky model	thermodynamics
$10^{-10} - 10^{-6}$	molecular field approximation	thermodynamics
$10^{-10} - 10^{-6}$	molecular dynamics (embedded atom, shell, empirical pair, bond order, effective medium, and second moment potentials)	structure and dynamics of lattice defects
$10^{-12} - 10^{-8}$	ab-initio molecular dynamics (tight-binding potentials, local density functional theory)	materials constants, structure and dynamics of simple lattice defects

Figure 1.20: Space scales and methods in materials simulation, nano–micro level [12].

Advanced microstructure simulations should meet three major requirements. First, they should enable one to use, or even derive, advanced path-independent microstructure property relations with quantitative validity. Second, they should provide insight into the underlying thermodynamic and path-dependent physical principles that govern the complex nature of microstructure evolution at the various space and time scales. Third, they should allow one, at least in certain cases, to replace and complement experimentation by simulation.

In engineering terms microstructure simulations should thus provide a convenient means of predicting and understanding material properties and microstructure evolution for technical applications under conditions that have not yet been studied or that are not amenable to experiments. To fulfill these requirements and at the same time to optimize the predictive power of models, the various numerical methods are increasingly complemented by the concept of integrated modeling and simulation. This term characterizes the coupling of computer codes with the aim of bridging the scale

Scale [m]	Simulation method	Typical applications
$10^{-10} - 10^{0}$	cellular automata	recrystallization, grain growth, and phase transformation phenomena, fluid dynamics, crystallograhpic texture, crystal plasticity
$10^{-7} - 10^{-2}$	spring models	fracture mechanics
$10^{-7} - 10^{-2}$	vertex models, network models, grain boundary dynamics	subgrain coarsening, recrystallization, secondary recrystallization, nucleation, recovery, grain growth, fatigue
$10^{-7} - 10^{-2}$	geometrical, topological, and component models	recrystallization, grain growth, secondary recrystallization, crystallographic textures, solidification, crystal topology
$10^{-9} - 10^{-4}$	dislocation dynamics	crystal plasticity, recovery, microtexture, dislocation patterning, thermal activation
$10^{-9} - 10^{-5}$	kinetic Ginzburg–Landau-type phase field models	diffusion, interface motion, precipitation formation and coarsening, polycrystal and polyphase grain coarsening phenomena, isostructural and non-isostructural phase transformation, type II superconductivity
$10^{-9} - 10^{-5}$	multistate kinetic Potts models	recrystallization, grain growth, phase transformation, crystallographic textures

Figure 1.21: Space scales and methods in materials simulation, micro–meso level [12].

Scale [m]	Simulation method	Typical applications
$10^{-5} - 10^{0}$	large-scale finite element, finite difference, linear iteration, and boundary element methods	averaged solution of differential equations at the macroscopic scale (mechanics, electromagnetic fields, hydrodynamics, temperature fields)
$10^{-6} - 10^{0}$	crystal plasticity finite element models, finite elements with advanced constitutive laws considering microstructure	microstructure mechanics of complex alloys, fracture mechanics, textures, crystal slip, solidification
$10^{-6} - 10^{0}$	Taylor–Bishop–Hill, relaxed constraints, Sachs, Voigt, and Reuss models, Hashin–Shtrikman model, Eshelby and Kröner-type self-consistent models	polyphase and polycrystal elasticity and plasticity, microstructure homogenization, crystallographic textures, Taylor factors, crystal slip
$10^{-8} - 10^{0}$	cluster models	polycrystal elasticity
$10^{-10} - 10^{0}$	percolation models	nucleation, fracture mechanics, phase transformation, current transport, plasticity, superconductivity

Figure 1.22: Space scales and methods in materials simulation, meso-macro level [12].

discrepancies between different simulation levels. This can be achieved by either simultaneous integration or sequential integration. The first notion means that various interacting simulation codes, which may use different numerical techniques, are employed simultaneously in one computer experiment. The second term describes the alternative method of an adequate parameter-transfer between simulations that are used sequentially.

Since microstructure evolution is path-dependent [12], concepts of integrated modeling and simulation should include as many of the microstructurally relevant processing steps and parameters as possible. However, such a procedure requires the incorporation of various space and time scales which can differ by some orders of magnitude. One reasonable approach for combining various scales consists in the incorporation of constitutive laws that have been derived from non-averaged, i.e. space- and time-discretized, simulations on the appropriate smaller scale. In such a concept, the results obtained from simulations on a certain scale are averaged and condensed before being considered at the next scale. This means that the phenomenological character of the model equations used in each step increases with increasing scale.

However, there is also a more direct way of bridging scale discrepancies [12]. Some of the simulation techniques mentioned above were originally confined to particular space and time scales. This applies especially to methods which reveal intrinsic physical scaling parameters, e.g. molecular dynamics and some Monte Carlo methods. In contrast, most mesoscale models are continuum approaches, i.e. they are not intrinsically calibrated and have thus a larger potential for spanning time and length scales. In this context especially the various crystal plasticity finite element, cellular automaton, dislocation dynamics, boundary dynamics, and multistate Potts models are of importance.

For instance, the finite element technique is designed to provide approximate solutions to coupled sets of partial differential equations subject to appropriate boundary and initial-value conditions [12]. Its application in computational materials science was originally confined to solving elastic and simple plastic problems at the macroscopic level using averaging constitutive laws and the conditions for equilibrium and compatibility. However, through the introduction of improved constitutive laws, i.e. elements of crystal plasticity, finite element methods are nowadays increasingly capable of considering material heterogeneity also at the mesoscopic level. This trend in finite element simulations points from the macroscopic to the mesoscopic scale. For the Potts model, which has its roots in the stochastic Metropolis Monte Carlo method, the reverse applies. By mapping generalized spin numbers to discrete domains which comprise cells with identical spin, it enables one to extend the use of the Monte Carlo algorithm to the description of interfaces. This approach points from the microscopic to the mesoscopic scale. In summary, although there are numerous computational techniques used nowadays, to select a proper computational technique for specific task depends on the length and time scales of each application, as shown in Fig. 1.23.

In nanoscopic-microscopic scale [12], the prediction of microstructures at the atomic scale requires the solution of a Schrodinger wave equation for about 1023 nuclei and their electronic shells1. Such a differential equation must be equipped with a Hamiltonian describing all particle interactions occurring. For a single particle in a potential

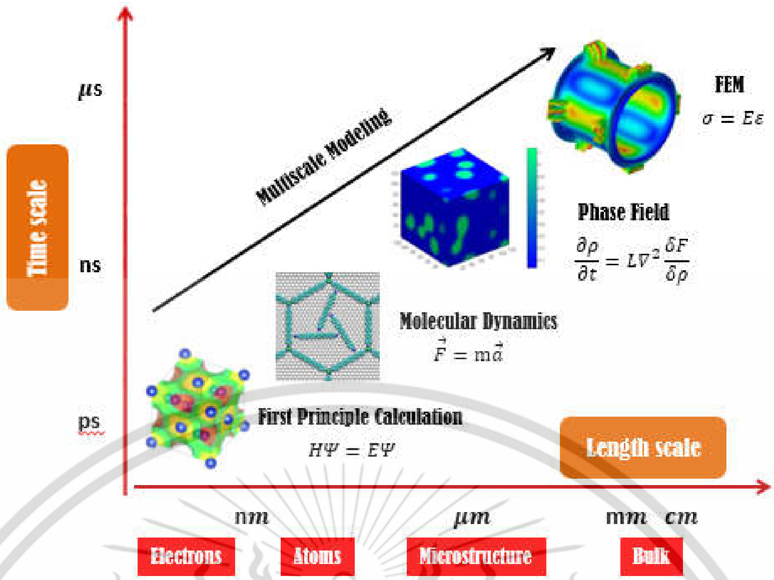

Figure 1.23: Computational technique chart. The choice of each computational technique depends on the length and time scales of each application. Adapted from [12].

$U(\mathsf{r})$ with mass m and coordinates r whose wave function is $\Psi(\mathsf{r}, t)$ the time-dependent Schrodinger equation assumes the form below [12]

$$-\frac{\hbar^2}{2m}\nabla^2\Psi(\mathsf{r},t) + U(\mathsf{r})\Psi(\mathsf{r},t) = i\hbar\frac{\partial\Psi(\mathsf{r},t)}{\partial t} \tag{1.9}$$

where $\hbar = h/(2\pi)$ and h is Planck's constant. $\Psi(\mathsf{r}, t)$ has the interpretation that $|\Psi(\mathsf{r}, t)|^2 dr_x dr_y dr_z$ is the probability that the particle may be observed in the volume element $dr_x dr_y dr_z$ at any particular time. For a bound particle in an eigenstate of energy E_k. Equation (1.9) may be separated into a time-dependent and a time-independent part below [12]

$$\Psi(\mathsf{r},t) = \psi_k(\mathsf{r})exp\left(-i\frac{E_k t}{\hbar}\right) \tag{1.10}$$

The time-independent Schrodinger equation is [12], by substitution,

$$-\frac{\hbar^2}{2m}\nabla^2\psi(\mathsf{r})_k + U(\mathsf{r})\psi(\mathsf{r})_k = E_k\psi(\mathsf{r})_k \tag{1.11}$$

In analogy to the classical energy equation, this time-independent expression can be regarded as an operator equation, with $i\hbar\nabla$ replacing the classical momentum p in the expression $p^2/(2m)$ for the kinetic energy [12]

$$\mathcal{H}\psi(\mathsf{r})_k = E_k\psi(\mathsf{r})_k \tag{1.12}$$

where $\mathcal{H}$ is the Hamilton operator. The analogy to the classical description may be used to generalize equation (4.3) to cases with N particles, including their mutual interactions as follow [12]

$$-\frac{\hbar^2}{2}\left(\sum_i \frac{1}{m_i}\nabla_i^2\right)\Psi(\mathsf{r}_1,\mathsf{r}_2,...,\mathsf{r}_N)_k + U(\mathsf{r}_1,\mathsf{r}_2,...,\mathsf{r}_N)\Psi(\mathsf{r}_1,\mathsf{r}_2,...,\mathsf{r}_N)_k = E_k\Psi(\mathsf{r}_1,\mathsf{r}_2,...,\mathsf{r}_N)_k \tag{1.13}$$

For instance, a material consisting of i electrons of mass me with a negative unit charge $q_e = -e$ and the spatial coordinates r_{e_i}, and j nuclei of mass m_n with a positive charge $q_n = z_n e$ and the spatial coordinates r_{n_j}, can be described by the eigenvalue wave equation [12]

$$\begin{aligned} &-\frac{\hbar^2}{2m_e}\left(\sum_i \nabla_i^2\right)\psi(\mathsf{r}_{e_1},\mathsf{r}_{e_2},...,\mathsf{r}_{e_n},\mathsf{r}_{n_1},\mathsf{r}_{n_2},...,\mathsf{r}_{n_j})_k \\ &-\frac{\hbar^2}{2}\sum_j \frac{1}{m_{n_j}}\nabla_j^2\psi(\mathsf{r}_{e_1},\mathsf{r}_{e_2},...,\mathsf{r}_{e_n},\mathsf{r}_{n_1},\mathsf{r}_{n_2},...,\mathsf{r}_{n_j})_k \\ &+\left(\sum_{i1,i2}\frac{e^2}{|\mathsf{r}_{e_{i1}}-\mathsf{r}_{e_{i2}}|}+\sum_{i,j}\frac{z_j e^2}{|\mathsf{r}_{e_i}-\mathsf{r}_{n_j}|}+\sum_{j1,j2}\frac{z_{j1}z_{j2}e^2}{|\mathsf{r}_{n_{j1}}-\mathsf{r}_{n_{j2}}|}\right)\psi(\mathsf{r}_{e_1},\mathsf{r}_{e_2},...,\mathsf{r}_{e_n},\mathsf{r}_{n_1},\mathsf{r}_{n_2},...,\mathsf{r}_{n_j})_k \\ &= E_k\psi(\mathsf{r}_{e_1},\mathsf{r}_{e_2},...,\mathsf{r}_{e_n},\mathsf{r}_{n_1},\mathsf{r}_{n_2},...,\mathsf{r}_{n_j})_k \end{aligned} \tag{1.14}$$

The terms that appear in this Hamilton operator suggest a distinction between those material properties that are determined by the lattice dynamics $(\mathsf{r}_{n_j}, \hbar^2/(2m_{n_j}))$, e.g., propagation of acoustic waves, thermal expansion, the non-electronic part of the specific heat, thermal conductivity of semiconductors and ceramics, and structural defects, and those that are determined by the electronic system $(\mathsf{r}_{e_i}, \hbar^2/(2m_{e_i}))$, e.g. electrical conductivity, thermal conductivity of metals, and superconductivity. At first view such a concept seems somewhat inaccurate, because it is the wave functions of the electrons and thus the electronic charge density that determine the position of the atomic nuclei. However, decoupling the motions of the light electrons from those of the heavy nuclei can be justified by the fact that the relaxation time of the electrons is typically three orders of magnitude below that of the atomic nuclei. This amounts to a situation where the electronic system practically remains in its ground-state irrespective of the positions of the nuclei. This concept is referred to as the adiabatic or Born–Oppenheimer approximation. Its employment in the present case allows one to approximate the exact wave function ψ in Eq. (1.14) as a product of two separate wave functions, where one portion describes the dynamics of the electrons φ and a second portion describes the dynamics of the nuclei ϕ, $\psi(\mathsf{r}_{e_1},\mathsf{r}_{e_2},...,\mathsf{r}_{e_i},\mathsf{r}_{n_1},\mathsf{r}_{n_2},...,\mathsf{r}_{n_j}) = \varphi(\mathsf{r}_{e_1},\mathsf{r}_{e_2},...,\mathsf{r}_{e_i})\phi(\mathsf{r}_{n_1},\mathsf{r}_{n_2},...,\mathsf{r}_{n_j})$. This approach amounts to separating the dynamics of the heavy constituents, nuclei, from that of the light ones, electrons. The corresponding Schrodinger equation is [12]

$$\left(-\frac{\hbar^2}{2m_e}\sum_i \nabla_i^2 + \sum_{i1,i2}\frac{e^2}{|\mathbf{r}_{ei1}-\mathbf{r}_{ei2}|} + \sum_{i,j}\frac{z_j e^2}{|\mathbf{r}_{e_i}-\mathbf{r}_{n_j}|}\right)\varphi(\mathbf{r}_{e_1},\mathbf{r}_{e_2},...,\mathbf{r}_{e_i})_{k_e} = E^e_{k_e}\varphi(\mathbf{r}_{e_1},\mathbf{r}_{e_2},...,\mathbf{r}_{e_i})_{k_e} \tag{1.15}$$

for the electronic system with the eigenvalues E_{k_e} and [12]

$$\left(-\frac{\hbar^2}{2}\sum_j \frac{1}{m_n}\nabla_j^2 + \sum_{j1,j2}\frac{z_{j1}z_{j2}e^2}{|\mathbf{r}_{ej1}-\mathbf{r}_{nj2}|} + \sum_{i,j}\frac{z_j e^2}{|\mathbf{r}_{e_i}-\mathbf{r}_{n_j}|}\right)\phi(\mathbf{r}_{n_1},\mathbf{r}_{n_2},...,\mathbf{r}_{n_j})_{k_n} = E^n_{k_n}\phi(\mathbf{r}_{n_1},\mathbf{r}_{n_2},...,\mathbf{r}_{n_j})_{k_n} \tag{1.16}$$

for the nuclei with the eigenvalues E_{k_n}. Approximate solutions of Eq. (1.15) using Hartee–Fock or local electron density functional theory form the basis of electronic ground state calculations with fixed coordinates for the nuclei. Since the exact ground state wave function will have a lower energy than any other admissible wave function, it is straightforward to express these theories in a variational form. Equation (1.16) is the starting point for the prediction of atomic configurations with instantaneously equilibrated electrons. The solution methods can be principally grouped into probabilistic and deterministic approaches. While the first class is usually referred to as Monte Carlo methods, the second one is referred to as molecular dynamics. In computational materials science, Monte Carlo methods are most widely used to determine stochastically equilibrium states for known distribution functions or to solve directly integral formulations of the equation of motion.

Statistical Monte Carlo integrations represent classical methods for the prediction of equilibrium configurations, i.e. of path-independent properties of canonical ensembles. However, they also gain momentum as approximation methods for the simulation of path-dependent behavior such as is often investigated in the field of microstructure dynamics. It must be clearly underlined that Monte Carlo methods are not principally confined to equilibrium predictions but can be used to solve any differential equation which can be turned into an integral form. The original idea of the various Monte Carlo approaches is to provide a probabilistic means for numerical integration. In general, they are thus not intrinsically scaled to the atomistic regime but can be used at any scale, provided they are applied to an appropriate probabilistic model.

Molecular dynamics methods are based on turning Eq. (1.16) into a classical form by replacing the quantum mechanical expression for the kinetic energy by the classical momentum term [12]

$$\frac{1}{2}\sum_j \frac{p^2}{m_j} + U = \sum_j m_j v_j^2 = E \tag{1.17}$$

and solving it for a nucleus in the potential U using Newton's law of motion below [12]

$$m\frac{\partial v}{\partial t} = -\nabla U \tag{1.18}$$

While, Monte Carlo techniques prevail in simulations of equilibrium properties, Molecular dynamics approaches are mainly used to solve discretely the equation of motion. They are hence of particular importance in the prediction of the dynamics of lattice defects.

In microscopic-mesoscopic scale [12], the quantitative investigation and prediction of microstructure evolution, and the derivation of corresponding microstructure-property relations at the micro- and mesoscale, constitute possibly the broadest and most characteristic discipline of computational materials science. Structure evolution at the microscopic–mesoscopic level is typically a thermodynamically non-equilibrium process, and thus mainly governed by kinetics. In other words, thermodynamics prescribes the principal direction of microstructure evolution while kinetics selects one out of many possible microstructural paths. This non-equilibrium character of structure evolution leads to a large variety of lattice defect structures and interactions.

Optimizing microstructure evolution at the mesoscopic scale is of fundamental importance, since it is particularly these non-equilibrium ingredients that can lead to beneficial materials properties. A thorough understanding of microstructural mechanisms thus enables one to tailor materials with certain property profiles for specific applications.

Investigating microstructural phenomena at realistic time and space scales, for predicting macroscopic properties, requires the consideration of relatively large portions of material, as shown in Fig. 1.24 [12]. However, due to the huge number of atoms involved ($\approx 10^{23}$ in a cubic centimeter), mesoscale simulations of microstructures can be performed neither by exactly solving the Schrodinger equation nor by using phenomenological atomistic approaches, such as molecular dynamics in conjunction with empirical potentials. This means that appropriate mesoscale simulations must be formulated which are capable of spanning a wider range of scales allowing predictions far beyond the atomic scale.

In most cases, this requires the introduction of continuum models in which averaging constitutive relations and phenomenological rate equations replace the exact or approximate solution of the equations of motion of all atoms. However, due to the large variety of mesoscale mechanisms and possible constitutive laws, there exists no unique method of formulating mesoscale models.

Essentially all engineering materials contain certain types of microstructures, and our success of designing new materials is largely dependent on our ability to control them [12]. Microstructure is a general term which refers to a spatial distribution of structural features which can be phases of different compositions and/or crystal structures, or grains of different orientations, or domains of different structural variants, or domains of different electrical or magnetic polarizations, as well as structural defects such as dislocations. The length scales of structural features in a microstructure are typically in the range of nanometers to a few microns, and in some cases they can be hundreds of microns. It is the size, shape, and spatial arrangement of the local structural features in a microstructure that determine the physical properties of a material such as mechanical, electrical, magnetic and optical properties.

Microstructures evolve during materials processing or in service at high temperatures. Microstructure evolution may be caused by phase transformations to reduce

Scale [m]	Characteristic phenomenon or defect
10^{-10}–10^{-7}	point defects, atomic clusters, short-range order, structural units in glasses and interfaces, dislocation cores, crack tips, nuclei
10^{-9}–10^{-5}	spinodal decomposition, coatings, thin films, surface corrosion
10^{-9}–10^{-4}	diblock-, triblock-, and starblock-copolymers, massive and athermal transformations, interface facets, dislocation sources, pile-ups
10^{-9}–10^{-3}	particles, precipitations, dendrites, eutectics, eutectoids
10^{-8}–10^{-5}	microcracks, cracks, powder, magnetic domains, internal stresses
10^{-8}–10^{-4}	stacking faults, microbands, microtwins, dislocation channels
10^{-8}–10^{-3}	spherolites in polymers, structure domains/crystal clusters (crystalline, amorphous) in metals, ceramics, glass, and polymers
10^{-8}–10^{-2}	clusters of conformative defects in polymers
10^{-8}–10^{-1}	dislocations, dislocation walls, disclinations, magnetic walls, subgrains, high-angle grain boundaries, interfaces
10^{-7}–10^{-1}	grains, shear bands, second phases in composites
10^{-7}–10^{0}	diffusion, convection, heat transport, current transport
10^{-7}–10^{0}	microstructural percolation paths (fracture, recrystallization, interface wetting, diffusion, corrosion, current, Bloch walls)
10^{-6}–10^{1}	surfaces, sample necking, fracture surfaces

Figure 1.24: Typical scales in microstructures [12].

the bulk free energy or by particle or domain coarsening to eliminate the total interfacial energy. It may also take place to respond to external fields such as an applied stress or electrical or magnetic field. Ideally, one would like to capture the optimum microstructure during processing for desirable properties and slow down or even stop its evolution during applications. In order to realize and achieve such optimum microstructures and control their evolution, one must be able to predict the temporal microstructure evolution under given processing conditions such as temperature, cooling rates, pressure, and composition. There has been an enormous effort in developing various types of microstructure models in the recent past. One of the computational models that have received tremendous attention during the last decade is the phase-field method for modeling microstructure evolution processes and a number of reviews on the method have appeared. The phase-field method describes a microstructure as a whole using one or more field variables which are continuous functions of space. It is based on a diffuse-interface description for the thermodynamics of inhomogeneous systems. The field variables, and thus the microstructure evolution, evolve with time according to a set of well established kinetic equations. One of the most attractive features for the phase-field method is the fact that one does not have to explicitly track the usually complicated interfaces during a microstructure evolution, as one has to do in a conventional modeling in order to specify the boundary conditions at the interfaces.

The name Phase-field model was first introduced in modeling solidification of a pure melt [13]. The idea was to avoid the explicit tracking of a solid-liquid interface during solidification by replacing the sharp solid-liquid interface using an artificial, continuous, non-conserved phase field, i.e. a diffuse interface. Instead of defining a moving boundary condition at the solid-liquid interface, the interface movement is described by the temporal evolution of the zero or a certain level-set of the phase field. Such a diffuse-interface description of an interface was first proposed more than a century ago by Van der Walls for fluid interfaces using a density field. The magnetic domain theory by Landau and Lifshitz has essentially the same structure. The best known diffuse-interface theory to us today is due to Cahn and Hilliard who studied the interphase boundaries described by a composition field which subsequently lead to the development of the well known Cahn's theory of Spinodal decomposition concerning the evolution kinetics of a conserved composition field. The diffuse-interface description of an antiphase domain wall motion was first proposed by Allen and Cahn, i.e. the Allen-Cahn equation for a non-conserved long-range order parameter. It is the Allen-Cahn equation which governs the evolution of the non-conserved phase field in solidification modeling. The Cahn-Hilliard nonlinear diffusion equation and the Allen-Cahn, sometimes also called the time-dependent Ginzburg-Landau, equation provide the basic governing equations for phase-field models. With random thermal noises, both types of equations become stochastic, and their applications to studying critical dynamics as well as to modeling the morphological pattern formation during ordering and phase separation of quenched systems have been extensively explored long before the term phase field was coined.

Although phase-field models may be presented in different forms for different applications, they are all based on a common set of fundamentals with regard to the representation of a microstructure, the thermodynamic description, and the kinetic evolution equations for microstructures [13]. In a phase-field model, a microstructure is described using one or more physical and/or artificial field variables. These variables are uniform inside a phase or domain away from the interfaces. The same phase or the same types of domains have the same uniform values for the field variables. Different values of the field variables, for example, 0 and 1, distinguish different phases or domains. Across the interfaces between different phases or domains, the field variables vary continuously from one uniform value corresponding to one type of phase or domain to another uniform value corresponding to another phase or domain. Therefore, the interfaces in a phase-field model are diffuse and possess a certain thickness. The variation of a field variable across an interface is schematically shown in Fig. 1.25.

Field variables can be either conserved or non-conserved, depending on if they satisfy the local conservation law, $\partial\phi/\partial t = -\nabla \cdot J$ where ϕ is a field variable and J is the corresponding flux [13]. For example, composition and temperature fields are both conserved while long-range order parameter fields describing ordered domain structures are non-conserved. It is easy to understand that the artificial phase-field in solidification modeling of a single-component liquid is non-conserved since its value can go from 0 to 1 for the whole system.

Artificial fields are introduced for the sole purpose of avoiding tracking the interfaces. Essentially all phase-field models of solidification employ an artificial field, called the phase field [13]. The interfacial width described by artificial fields has no directional relationship to the physical width of a real interface. The thermodynamic

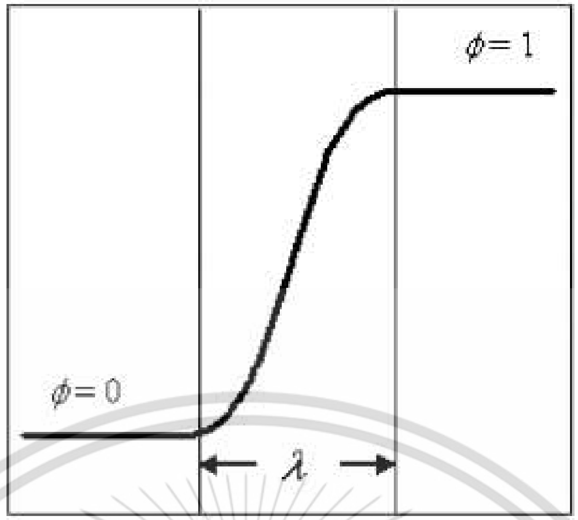

Figure 1.25: A schematic diagram showing the distribution of a field variable across an interface. Both $\phi = 0$ and $\phi = 1$ parameters represent two phases separated by a diffuse interface with a thickness roughly λ [13].

and kinetic coefficients in the phase-field equations are chosen to match the corresponding parameters in the conventional sharp-interface equations through sharp or thin-interface analyzes. Physical fields refer to well-defined order parameter fields which can be experimentally measured. The interfacial width described by a physical field is also expected to reflect the actual interfacial width. In phenomenological theories of phase transformations, order parameter fields are used to characterize the nature and the critical temperatures of the phase transformations which produce the microstructure. A well known example is the long-range order parameter for order-disorder transformations. The corresponding order parameter field can be employed to describe the antiphase domain structure resulted from ordering. Another example is a composition field which describes the morphological evolution during phase separation either through nucleation and growth or spinodal decomposition or during precipitate coarsening. In the phase-field approach, the thermodynamics of an inhomogeneous microstructure is described by the diffuse-interface theory of Cahn and Hilliard. According to the Cahn-Hilliard theory, for a system described by a composition field, the local free energy, $f(c)$, for an inhomogeneous system depends not only on the local composition, c, but also on the neighboring compositions, i.e. composition gradients, ∇c. Truncating at the second order in the free energy expansion in terms of composition gradients with respect to a uniform composition, the total chemical free energy of a system with volume, V, is given by [13]

$$F = \int \left[f(c) + \frac{\alpha}{2}(\nabla c)^2 \right] d^3r \tag{1.19}$$

where α is the composition gradient energy coefficient. The gradient energy term is zero inside a phase or domain where the composition if uniform, but is nonzero across interfaces where the composition field varies. Equation (1.19) represents the total chemical free energy of a microstructure including the bulk chemical free energy as well as the excess free energy associated with all the interfaces in the microstructure.

For a more general inhomogeneous system described by a field variable by a set of conserved field c_i and a set of non-conserved field η_i, the total free energy can be written as [13]

$$F = \int \left[f(c_1, c_2, ..., c_n, \eta_1, \eta_2, ..., \eta_p) + \sum_{i=1}^{n} \alpha_i (\nabla c_i)^2 + \sum_{i=1}^{3} \sum_{j=1}^{3} \sum_{k=1}^{p} \beta_{ij} \nabla_i \eta_k \nabla_j \eta_k \right] d^3r + F_G \tag{1.20}$$

where α_i, β_{ij} are gradient energy coefficient and $F_G \equiv \int\int G(r-r')d^3rd^3r'$ represents pair-wise, non-local, long-range interactions such as elastic, electrostatic and magnetic interactions between volume element d^3r and volume element d^3r'. For example, long-range elastic interactions arise in coherent systems where the lattice planes and directions across the interfaces are continuous, and the lattice parameters of the phases depend on the field variable. For simplicity, many-body interactions, for example, many-body elastic interactions that appear in systems with a strong elastic modulus inhomogeneity are ignored in the discussions below.

For the local free energy, the main difference among different phase-field models lies in the construction of f as a function of field variables. A simple and familiar system is a two-phase binary system described a physical composition field. If one is interested in a real system with a known free energy function as a function of temperature, it can be directly used. On the other hand, if one is only interested in modeling the morphological evolution in a model system, a simple double-well potential may be used. For example [13],

$$f = -\frac{A}{2}c^2 + \frac{B}{4}c^4 \tag{1.21}$$

where A and B are constants. At equilibrium, equation (1.21) describes two phases with compositions $+\sqrt{A/B}$ and $-\sqrt{A/B}$, respectively. For the case of isothermal solidification of a binary liquid, an artificial field, ϕ, is introduced, in addition to the physical field, composition c. The artificial field, also called the phase field, is used to distinguish solid and liquid phases and to automatically take into account the boundary conditions at the interfaces. The local free energy as a function of composition c and ϕ can be expressed as [13]

$$f(c,\phi) = h(\phi)f^S(c) + [1-h(\phi)]f^L(c) + wg(\phi) \tag{1.22}$$

where $f^S(c)$ and $f^L(c)$ are the free energy densities of solid and liquid as a function of composition at a given temperature, respectively. $g(\phi)$ is a double-well potential which is only a function of the artificial field. A possible functional form for g is [13]

$$g(\phi) = 16w\phi^2(\phi-1)^2 \tag{1.23}$$

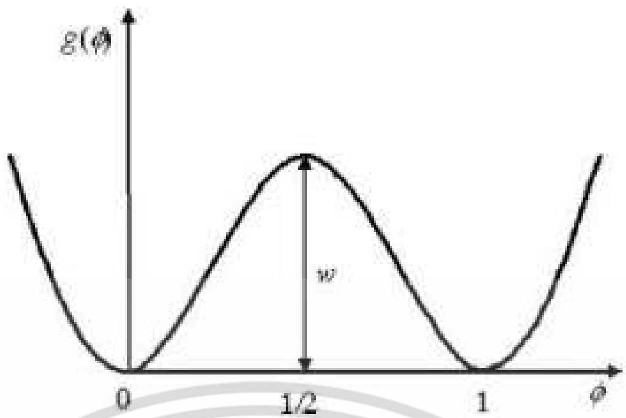

Figure 1.26: Illustration of a double-well potential with potential depth of w [13].

which has minima at $\phi = 0$ and $\phi = 1$. w in Eq. (1.23) represents the depth of the two wells at $\phi = 0$ and $\phi = 1$ with respect to the local maximum at $\phi = 1/2$, as shown in Fig. 1.26. The function, $h(\phi)$ in Eq. (1.20), is required to have the following properties [13]

$$h(0) = 0, \quad h(1) = 1, \quad \left.\frac{dh}{d\phi}\right|_{\phi=0} = \left.\frac{dh}{d\phi}\right|_{\phi=1} = 0 \tag{1.24}$$

There properties ensure that the equilibrium values, 0 and 1, for the phase field in the double-well potential are not affected by the chemical free energies f^S and f^L. An example which satisfies the conditions given in Eq. (1.24) is [13]

$$h(\phi) = \phi^3(6\phi^2 - 15\phi + 10) \tag{1.25}$$

Therefore, in this model, $\phi = 0$ represents the liquid phase since $h(0) = 0$ and $f(c, 0) = f^L(c)$. Similarly, $\phi = 1$ describes the solid phase with $h(1) = 1$ and $f(c, 0) = f^S(c)$. Across the interface, the local free energy has contributions from both the liquid and solid chemical free energies as well as the double-well potential.

For gradient energy and interfacial energy, As mentioned above, in the diffuse-interface description, the free energy of an inhomogeneous system, such as a microstructure, also depends on the gradients of the field variables. α in Eq. (1.19) is the gradient energy coefficient which characterizes the energy penalty due to the field inhomogeneity at the interfaces, i.e. the interfacial energy contribution to the total free energy. Examples of interfaces include solid-liquid interphase boundaries during solidification, grain boundaries, matrix-precipitate interfaces during precipitation reactions and precipitate coarsening, and domain boundaries in ordered phases, ferroelectric crystals and ferromagnetic systems. For a given free energy model and a given set of gradient energy coefficients, the specific interfacial energy, interfacial energy per unit area, can be calculated for an equilibrium interface. It is important to realize that the integral of the gradient energy term only counts part of the interfacial energy. The total interfacial energy for a flat interface should be calculated from [13]

$$\gamma = \frac{\Delta F}{S} = \int \left[f(c) - f_0(c) + \frac{\alpha}{2}(\nabla c)^2 \right] d^3 r \tag{1.26}$$

where S is the interfacial area and $f_0(c)$ is the bulk equilibrium free energy density as a function of composition represented by the common tangent line for a binary system. For an interface at equilibrium, the total gradient energy is half of the the total interfacial energy. Analytical expressions for the interfacial energy in terms of free energy parameters and the gradient energy coefficients are only available for very simple cases that an analytical solution for the equilibrium profile of field variable across the interface can be derived. For example, for a simple double-well potential with a single phase-field variable, the equilibrium profile is described by a hyperbolic tangent function.

For more general cases, the interfacial energy has to be computed numerically. However, in general, the interfacial energy (σ), interfacial width (λ), the double-well depth of a free energy model (Δf), and the gradient coefficient (α) obey the following set of relationships [13],

$$\sigma \propto \sqrt{\alpha \Delta f}, \qquad \lambda \propto \sqrt{\alpha \Delta f}, \qquad \sigma \propto \lambda \Delta f \tag{1.27}$$

It is also easy to understand that why a wider interface may be employed if one can artificially eliminate the chemical free energy contribution, Δf , and only use the depth of the double-well potential to yield the same interfacial energy. In crystalline solids, interfacial energies are generally anisotropic. The interfacial energy anisotropy is usually a function of temperature with the degree of anisotropy larger at low temperatures. The type and degree of interfacial energy anisotropy affect the particle shapes or interface orientations during microstructure evolution.

For Non-local interactions, the second integral in Eq. (1.20) represents the nonlocal contributions to the total free energy from long-range interactions such as elastic interactions, electric dipole-dipole interactions, and electrostatic interactions. These long-range interactions are usually obtained by solving the corresponding mechanical and electrostatic equilibrium equations for a given microstructure. For example, for the long-range elastic interactions, the following mechanical equilibrium equation has to be solved under given mechanical boundary conditions [13],

$$\frac{\partial \sigma_{ij}}{\partial r_j} = 0, \qquad \sigma_{ij}(r) = \lambda_{ijkl}(r) \left[\varepsilon_{kl}(r) - \varepsilon^0_{kl}(c, \phi, P_i, ...) \right] \tag{1.28}$$

where σ_{ij} is the local elastic stress, r_j is the jth component of the position vector, **r**, $\lambda_{ijkl}(r)$ is the elastic stiffness tensor which varies with space, $\varepsilon_{jk}(r)$ is the total strain state at a given position in a microstructure, and ε^0_{kl} is the local stress-free strain or transformation strain or eigenstrain which is also a function of position through its dependence on field variables. Similarly, for a system with long-range electrostatic interactions, the local electric displacement satisfies the following electrostatic equilibrium equation with appropriate boundary conditions [13],

$$\frac{\partial D_i}{\partial r_i} = 4\pi \rho_f, \qquad \frac{\partial E_i}{\partial r_i} = 4\pi \rho_t \tag{1.29}$$

where D_i and E_i are the ith components of the electric displacement field and the electric field, respectively, ρ_f is the local free charge density and ρ_t is the local total charge density which includes the effective charge associated with electric polarizations.

In all PF model, the temporal and spatial evolution of field variables follows the same set of kinetic equations. All conserved fields, c_i, evolve with time according to the Cahn-Hilliard equation (1.30) whereas the non-conserved fields, η_p, are governed by Allen-Cahn equation (1.31) [13].

$$\frac{\partial c_i(\vec{r},t)}{\partial t} = \nabla M_{ij} \nabla \frac{\delta F}{\delta c_j(\vec{r},t)} \tag{1.30}$$

$$\frac{\partial \eta_p(\vec{r},t)}{\partial t} = -Lpq \frac{\delta F}{\delta \eta_q(\vec{r},t)} \tag{1.31}$$

where M_{ij} and L_{pq} are atomic or interface mobility. F is the total free energy of a system which is a functional of all the relevant conserved and non-conserved fields given by Eq. (1.20).

By numerically solving the systems of Cahn-Hilliard diffusion equations and the Allen-Cahn relaxation equations subject to appropriate initial and boundary conditions, the evolution profiles of the field variables, and thus the microstructure evolution can be obtained [13]. Most of the phase-field simulations employ the second-order finite-difference discretization in space using uniform grids and the forward Euler method for time stepping to solve the phase-field equations for simplicity. It is well known that in such an explicit scheme, the time step has to be small to keep the numerical solutions stable. Dramatic savings in computation time and improvement in numerical accuracy can be achieved by using more advanced numerical approaches such as the semi-implicit Fourier Spectral method and adaptive-grid finite-element method.

The microstructure of most of engineering materials consists of multiple grains with different crystallographic orientations [13]. The understanding of the factors influencing the evolution of a grain structure is of great scientific and technological importance, because physical properties, such as corrosion resistance, thermal and electrical conductivity; and mechanical properties, such strength, ductility, and toughness, depend on the mean grain size and the grain size distribution. The local energy at the grain boundaries, or interfaces, is higher than the corresponding bulk energies of the grains forming the grain boundaries. This extra energy associated with the grain boundaries provides a thermodynamic driving force to move the grain boundary in a manner as to minimize the total free energy. Such motion of grain boundaries in polycrystalline materials results in grain growth which is a process of growth of some grains and shrinking of some others. Thus, grain growth decreases the total number of grains and increases the average grain size.

For the case of study in Fig. 1.27, the phase-field model is the adaptation of the grain growth model given by Eq. (1.32). In the model, each grain is described by one order parameter η_i which takes the value of one for a designated grain and the value of zero in other grains. The evolution of the order parameters described by the non-conserved Allen–Cahn equation in the form of [14]

$$\frac{\partial \eta_i}{\partial t} = -L_i \frac{\delta F}{\delta \eta_i} \tag{1.32}$$

where Li is the mobility coefficient and F is the free energy functional which is taken as [14],

$$F = \int_V \left[f(\eta_1, \eta_2, ..., \eta_N) + \sum_i^N \frac{\kappa_i}{2} |\nabla \eta_i|^2 \right] dv \tag{1.33}$$

in which κ_i are the gradient energy coefficients and f is the local free energy density. The specific form of local free energy which is independent of orientation is given by [14]

$$f(\eta_1, \eta_2, ..., \eta_N) = \sum_i^N \left(-\frac{A}{2}\eta_i^2 + \frac{B}{4}\eta_i^4 \right) + \sum_i^N \sum_{i \neq j}^N \eta_i^2 \eta_j^2 \tag{1.34}$$

in which A and B are positive constants. For $A = B = 1$, for two order parameters η_1 and η_2 the shape of this local free functional is given in Fig. 1.28. As can be seen, it goes through a minimum at equal depth for η values of zero and one. There have been

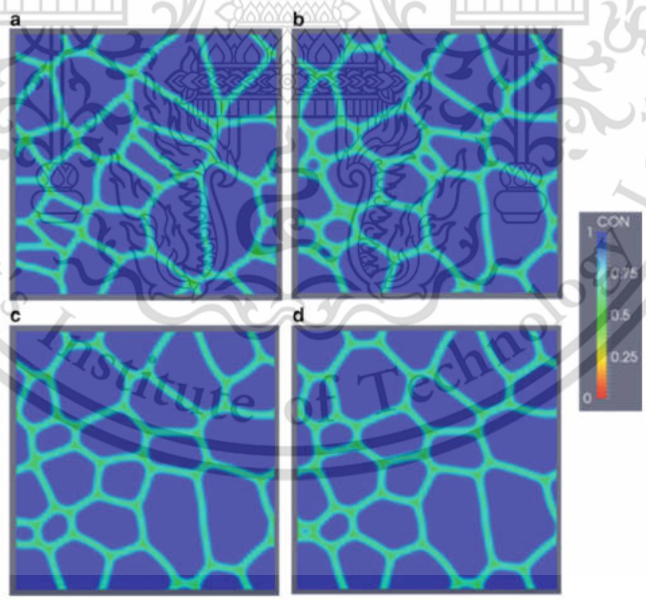

Figure 1.27: Time evolution of polycrystalline microstructure due to grain growth non-for conserved Allen–Cahn equations in phase-field modeling. The non-dimensional times are (a) 0.5, (b) 12.5, (c) 18.75, and (d) 25.0 [14].

many significant advances in phase-field modeling in materials science over the last

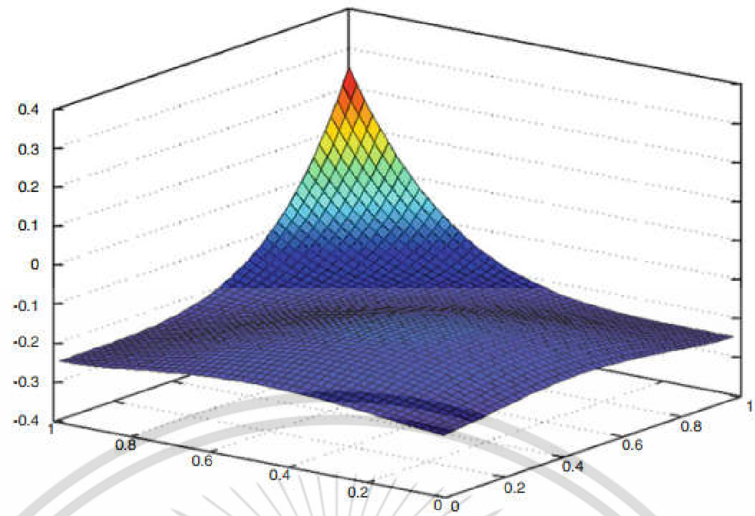

Figure 1.28: For $A = B = 1$ and for two order parameters η_1 (x-axis) and η_2 (y-axis) the shape of the local free functional (z-axis), Eq. (1.34). As can be seen, it goes through a minimum at equal depth for η values of zero and one [14].

decade. Arguably the most important has been the development of asymptotic analysis techniques that connect the phase-field equations with sharp interface models of solidification in the computationally tractable, thin interface, limits. These methods have been instrumental in making the phase-field method a viable tool for quantitative modeling of microstructural evolution, especially when coupled with adaptive mesh refinement algorithms opening up a new window to truly multiscale computation of microstructure evolution.

A limitation of traditional phase-field models is that they are formulated in terms of fields that are spatially uniform in equilibrium. This precludes most physical phenomena that arise from the periodic symmetries inherent in crystalline phases, including elastic and plastic deformation, anisotropy, and multiple grain orientations [24]. One way around this problem has been to couple the traditional fields with one or more auxiliary fields that describe, for example, the density of dislocation, the continuum stress and strain fields and the crystal grain orientation. These approaches have proven quite useful in various applications such as polycrystalline solidification. Nevertheless, it has proven quite challenging to incorporate elastoplasticity, diffusive phase transformation kinetics, and anisotropic surface energy effects into a single, thermodynamically consistent model.

Recently, a new extension to conventional phase-field (PF) model has emerged known as phase-field crystal (PF) model. This method can describe the evolution of the atomic density of a system according to dissipative dynamics driven by free energy minimization [24]. In PFC approach the free energy functional of a solid phase is minimized when the density field is periodic function. Because of its periodic function in nature, it naturally gives rise to elastic effects, multiple crystal orientations, nucleation and the motion of dislocations which contribute the advantage over conventional PF model in terms of self-consistency [24].

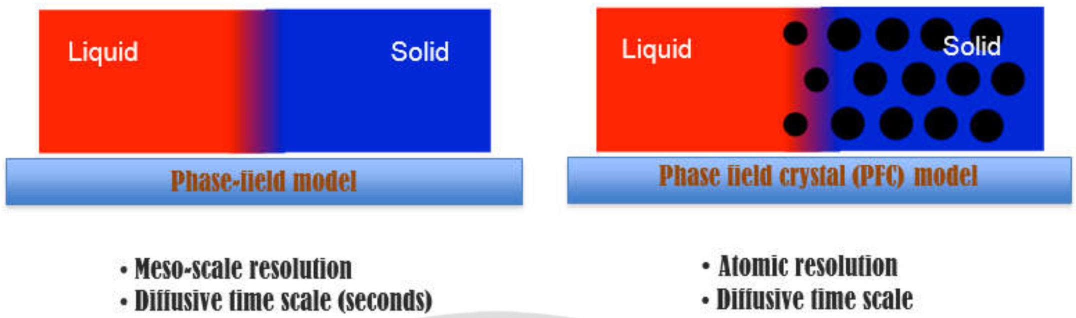

Figure 1.29: Features of conventional PF vs. PFC. The density field in PF model is spatially uniform in equilibrium whereas the density field of solid phase in PFC model is periodic function in equilibrium.

The quintessential advantage of the PFC method is that it integrates atomic vibrations on time scales many orders of magnitude longer than those associated with the Debye frequency, approximated $1/\omega_D\ 10–13s$ [24]. This allows elastic and plastic effects emerging at the atomic scale to be self-consistently incorporated on the diffusive time scales that govern phase transformation kinetics. The study of such phenomena using molecular dynamics (MD) simulations is prohibitively expensive since MD is constrained to evolve at the scale of femtoseconds, precluding the study of physics of nanostructured materials, where the relevant length scales are atomic and time scales are mesoscopic.

The simplest known free energy functional that meets this condition is the form given by Swift and Hohenberg to study the convective instabilities. This free energy functional is expressed as [14]

$$F(\phi(r)) = \int \left\{ \frac{\phi(r)}{2} \left[\alpha + \lambda \left(q_0^2 + \nabla^2 \right)^2 \right] \phi(r) - \frac{h}{3}\phi(r)^3 + \frac{g}{4}\phi(r)^4 \right\} dr \tag{1.35}$$

where α, λ, h, g_0 and g are phenomenological parameters to fit the properties of the material of interest. It is convenient to rewrite the Eq. (1.35) in dimensionless form, by introducing a new set of variables as [14]

$$x = q_0 r, \qquad \psi = \sqrt{g}\lambda q_0^4 \left(\phi - \frac{h}{3g} \right), \qquad \varepsilon = \frac{1}{\lambda q_0^4} \left(\frac{h}{3g} - \alpha \right) \tag{1.36}$$

in which all terms that are either constant or linearly dependent to the dimensionless order parameter field ψ can be ignored and the value of h is usually taken as zero. Then, a dimensionless free energy $\tilde{F}$ as $g\lambda^{-2}g_0^{-5}$ times the original free energy, without the constant and linear parts, takes the form [14]

$$\tilde{F}(\psi(x)) = \int \left\{ \varepsilon \frac{\psi(x)^2}{2} + \frac{1}{4}\psi(x)^4 + \frac{\psi(x)}{2} \left(1 + \nabla^2 \right)^2 \psi(x) \right\} dx \tag{1.37}$$

Here, ε is a constant proportional to the deviation of the temperature from the melting temperature; therefore, it takes a negative value. The first two terms in the integrand constitute a double-well potential and guarantees the presence of solid and liquid phases. The last term, containing gradient term, accounts for the deviation from the equilibrium profile owing to increase in elastic strain energy and/or the presence of other energy risers such as the lattice defects. Even in its simplest form, the PFC model of Eq. (1.37) is a powerful modeling technique. By considering the atomic configurations, the phase diagram given in Fig. 1.30 is derived from Eq. (1.37).

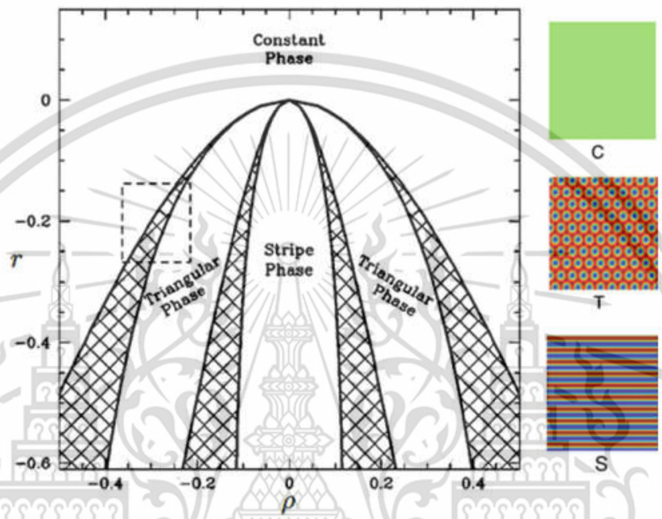

Figure 1.30: Phase diagram derived from Eq. (1.37). The hatched regions indicate the regions of coexistence phase [14].

Figure 1.30 indicates the equilibrium phases [14]. These include constant (liquid) phase, stripe phase, triangular structure in two-dimension and body-centered cubic, BCC, structure in three dimension and the coexistence regions in which liquid and solid phases are in equilibrium together.

According to numerous advantages, PFC approach is widely used to study many important material phenomena including grain growth, dendritic and eutectic solidification and epitaxial growth. It provides a continuum-scale representation of the atomic density field that evolves on diffusive time scales. This will enable more detailed studies of multiple crystal structures and a more systematic examination of alloy systems. It has a great potential to model problems in physical metallurgy, including interaction of multiple dislocations, interactions of dislocations with solute field and a variety of other applications. Figure 1.31 demonstrate the simulation result of triangular phase and stripe phase evolution at various time steps [14].

A few years ago, A new PFC type theory was presented, which accounted for the full spectrum of solid-liquid-vapor phase transitions within the framework of a single density order parameter [15]. Its equilibrium properties showed the most quantitative features to date in PFC modeling of pure substances, and full consistency with thermodynamics in pressure-volume-temperature space was demonstrated. Non-equilibrium

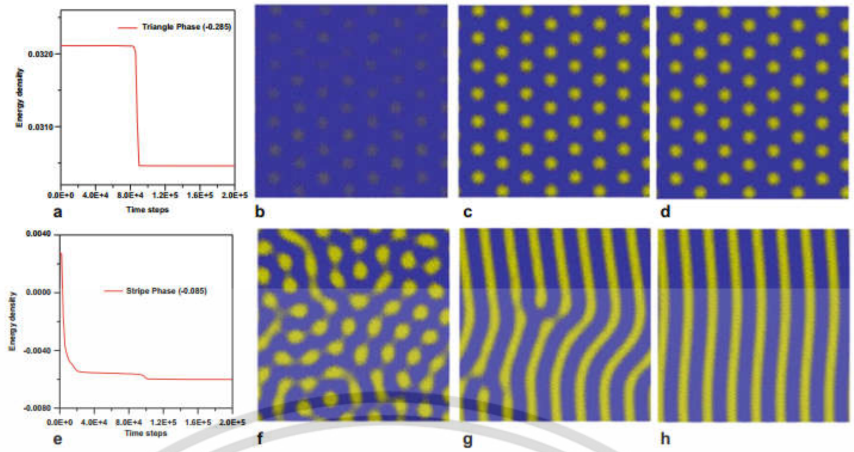

Figure 1.31: The top row for triangular phase at temperature -0.25 and with average density $\psi_0 = -0.285$. (a) Variation in free energy density. The simulation steps are: (b) 86×10^3, (c) 90×10^3, and (d) 200×10^3. The bottom row for stripe phase at temperature -0.25 with average density $\psi_0 = -0.085$. (e) Variation in free energy in density. The simulation steps are: (f) 6×10^3, (g) 60×10^3, and (h) 200×10^3 [14].

simulations show that 2 and 3-phase growth of solid, vapor and liquid can be achieved, while our formalism also allows for a full range of pressure-induced transformations. This model opens up a new window for the study of pressure driven interactions of condensed phases with vapor, an experimentally relevant paradigm previously missing from phase field crystal theories.

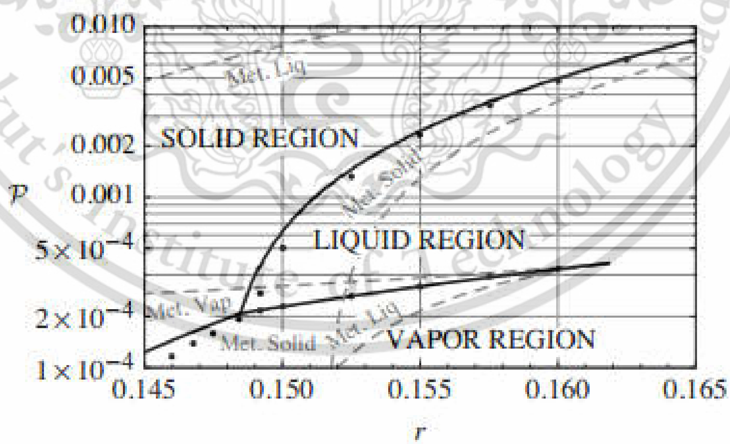

Figure 1.32: Pressure-temperature phase diagrams of model. Solid thick lines correspond to 1-mode calculations. Dashed lines show metastability regions. Black dots show average coexistence pressure from isothermal simulations [15].

To establish phase transition diagram, a method to control either the volume or the pressure of the system was also implemented, called pressure-controlled dynamic

(PCD) equation. This new pressure control scheme enables us to exhibit deformation by specifying external pressure which is suitable for investigating the experimentally relevant to simulate materials behavior under a pressure-controlled condition. This differs from the original formulation of the PFC method that describes non-equilibrium behavior of a system through the minimization of the free energy under controlled temperature, mass, and volume. Despite the advantage of this PCD equation, the use of this method to investigate the deformation in solid materials under externally applied pressure had not been thoroughly explored. Therefore, we saw an opportunity to implement this PCD equation to study such a problem.

We conducted a preliminary study by adopting the PFC model which incorporated the PCD equation, referred to as the PFC-PCD method, to investigate the deformation in one-dimensional crystal structure under the step pressure [25, 26]. According to the results, the time-delayed in strain response with a reduction rate was observed which was indicative of viscoelastic-creep behavior in solid materials. However, this preliminary study was solely limited to the one-dimensional case as well as if we want to predict the damping capacity property, the mechanical-hysteresis behavior needs to be established. Therefore, to obtain more realistic results, we conduct our research regarding the objectives and scopes provided in the next few sections below.

1.2 Objectives of the Research

1. To extend the PFC-PCD method in predicting viscoelastic-creep and mechanical-hysteresis behavior including its complex moduli parameters in the body-centered-cubic (BCC) crystal under externally hydrostatically-applied pressure.
2. To demonstrate the limitation of PFC-PCD method in predicting mechanical-hysteresis behavior and complex moduli parameters at high pressure oscillation frequency range.
3. To introduce a modified pressure-controlled dynamic (MPCD) equation by heuristic approach to improve the prediction accuracy of mechanical-hysteresis behavior and complex moduli parameters, in particular, at high pressure oscillation frequency where the existing PFC-PCD method can not be achieved.

1.3 Scopes of the Research

1. Implement the PFC-PCD method in predicting viscoelastic-creep behavior under hydrostatically step pressure in a BCC crystal.
2. Investigate how the PFC-PCD parameters influence viscoelastic-creep behavior under hydrostatically step pressure in a BCC crystal.
3. Implement the PFC-PCD method in predicting mechanical-hysteresis behavior and complex moduli parameters under hydrostatically sinusoidal pressure oscillation in a BCC crystal and demonstrate that this method is not consistent with the standard linear solid (SLS) model, which is normally used to model viscoelasticity in solid materials, in producing mechanical-hystersis behavior and complex moduli parameters, in particular, at the high pressure oscillation frequency range.
4. Propose a new MPCD equation by introducing the pressure time derivative term in

the original PCD equation. With the aid of Taylor's expansion under small deformation postulation, we then show that the simplified MPCD equation is consistent with the SLS model functional form.

5. Implement the PFC-MPCD method in predicting mechanical-hysteresis behavior and complex moduli parameters under hydrostatically sinusoidal pressure oscillation in a BCC crystal and then demonstrate that the PFC-MPCD method is able to produce those results consistent with SLS model and generally agreed with numerous experimental observations where PFC-PCD method can not be accomplished.

1.4 Advantages of the Research

1. To recognize not only the capability of the existing PFC-PCD method in predicting viscoelastic-creep behavior but also the limitation of this method in producing mechanical-hysteresis behavior and complex moduli parameters in BCC crystal under externally hydrostatically-applied pressure.

2. To obtain a more promising tool, PFC-MPCD method, when the prediction of mechanical-hysteresis and complex moduli parameters at the broader frequency range is necessary. This should be one of the most important step to extend the capability of the PFC method in producing more reliable parameters in damping material design.

CHAPTER 2

Theoretical Background and Literature Review

2.1 Mean Field Theory of Phase Transformations

The origins of the phase field methodology [16] have been considerably influenced by mean field theory of first and second-order phase transformations. The common first-order transformations include solidification of liquids and condensation of vapor. They are defined by a release of latent heat and discontinuous first derivative of the free energy. In contrast, second-order transformations occur at well-defined temperature, density, or concentration. There is no release of latent heat and the transformation begins spontaneously due to thermal fluctuations.

An important concept used again and again in the description of phase transformations is that of the order parameter. This is a quantity that parameterizes the change of symmetry from the parent (disordered) phase to the daughter (ordered) phase appearing after the transformation. In a first-order transformation, the order parameter of the ordered state emerges discontinuously from that of the disordered phase, below the transformation temperature. In the second-order transformation, the disordered state gives way continuously to two ordered phases with nonzero order parameter.

Mean field theory of phase transformations ignores spatial fluctuations, which always exist due to local molecular motion. The order parameter, treated as an average thermodynamic property of a phase, is used to write the free energy of a system. This approach works reasonably well in first-order transformations, where fluctuations influence only regions near nanoscale phase boundaries, even near the transition temperature. In contrast, second-order transformation fluctuations influence ordering over increasing length scales, particularly near a critical point. For such problems, spatial fluctuations play a dominant role and mean field Landau free energy functional must be augmented with terms describing spatial fluctuations.

The order parameter ϕ of a phase can be interpreted as a nonzero average of a local order parameter field $\Phi(\mathbf{r})$, which exhibits spatial variation. The bulk order parameter of the form discussed in the above examples can thus be thought of as the spatial average of the local order parameter, that is, $\phi = < \Phi(\mathbf{r}) >$, averaged over the phase. The order of a phase transformation can be linked to the possible values the average order parameter w can take. For example, a continuous change from

$\phi = 0$ above a certain critical temperature (T_c) to multiple values of $\phi \neq 0$ below a T_c denotes a second-order transformation.

2.1.1 The Landau Free Energy Functional

To illustrate Landau mean field theory [16, 27], we begin by regrouping the confrontational sum in the partition function into realizations of the order parameter that yield a specific spatial average $< \Phi(\mathbf{r}) > \equiv \phi$. Doing so, a generalized partition function is defined by

$$Q(T) = \int_{-\infty}^{\infty} \Omega(\phi) d\phi e^{-\{E(\phi)-BV\phi\}} \tag{2.1}$$

where $\Omega(\phi)$ is the density of states of the system corresponding to ϕ. The order parameter is now assumed to be defined via a volume average, where V is the volume of the system. The variable B plays the role of an ordering field in terms of which the order parameter can be defined from the partition function. The probability density of a system having an order parameter ϕ is

$$P(\phi) = \frac{1}{Q(T)} e^{-\{\hat{F}(\phi)-BV\phi\}} \tag{2.2}$$

where $\hat{F} = E(\phi) - TS(\phi)$ is called the Landau free energy. Here, $S(\phi) = k_B T \ln(\Omega(\phi))$ and $E(\phi)$ is entropy and the internal energy of the system. For a conserved order parameter, when B corresponds to a chemical potential, the Landau free energy corresponds to the Gibbs free energy. When the order parameter is coupled to an external field via B, the Gibbs free energy is given by $\hat{F}(\phi) - BV\phi$. As discussed previously, the Gibbs free energy density (or the grand potential density ω) of the system is connected to the generalized partition function by

$$f = -\frac{k_B T}{V} \ln Q(T) \tag{2.3}$$

Equation (2.2) and (2.3) can be used to compute order parameter ϕ according to

$$\phi \equiv < \phi > = \int_{-\infty}^{\infty} \phi P(\phi) d\phi \tag{2.4}$$

The premise of Landau theory is to evaluate the partition function in Eq. (2.2) around the extremum of the Boltzmann factor. This leads to the well-known extremum conditions.

$$\begin{aligned} \left.\frac{\partial \left(\hat{F}(\phi) - BV\phi\right)}{\partial \phi}\right|_{\bar{\phi}} &= 0 \\ \left.\frac{\partial^2 \left(\hat{F}(\phi) - BV\phi\right)}{\partial \phi^2}\right|_{\bar{\phi}} &> 0 \end{aligned} \tag{2.5}$$

the solutions of which define the mean order parameter $\bar{\phi}$, and in terms of which the generalized equilibrium grand potential is defined as

$$\hat{\omega} \approx \frac{\hat{F}(\bar{\phi})}{V} - B\phi \equiv \hat{f}(\bar{\phi}) - B\bar{\phi} \tag{2.6}$$

where $\hat{f}(\bar{\phi})$ is the Landau free energy density. It should also be emphasized that the Landau mean field theory entirely neglects temporal and spatial fluctuations and evaluates thermodynamic quantities at the most probable homogeneous state of the order parameter, $\bar{\phi}$. The next steps in mean field theory involve the construction of the Landau field free energy density $\hat{f}(\phi) \equiv \hat{F}(\phi)/V$. Recalling that the mean value of ϕ vanishes in the disordered state ($i.e., \phi = \bar{\phi} = 0$), and considering second-order phase transitions in the vicinity of the critical point or first-order transformations where the order parameter in the ordered phase suffers only a small jump from $\phi = \bar{\phi} = 0$, $\hat{f}(\phi)$ is assumed to be expressible in a series expansion of the form

$$\hat{f}(\phi) = \hat{f}(T, \phi = 0) + \sum_{n=2}^{M} \frac{a_n(T)}{n}\phi^n \tag{2.7}$$

The coefficients of Eq. (2.7) are dependent on temperature and other thermodynamic variables. In what follows, the free energy in Eq. (2.7) will be tailored to several practical and pedagogical phase transformation phenomena. For convenience, the hat notation will be dropped from the Landau free energy density $\hat{f}$.

2.1.2 Free Energy Density with Symmetric Phase Diagram

For the simple binary model with a symmetric, phase diagram the free energy is symmetric in the two states on either side of the spinodal concentration [16]. It is instructive to use Eq. (2.7) to construct a Landau free energy expansion. This is leading to

$$\hat{f}(\phi) = a(T) + \frac{a_2(T)}{2}\phi^2 + \frac{a_4(T)}{4}\phi^4 + O(h^6) \tag{2.8}$$

The first of the extremization conditions in Eq. (2.5) implies minimizing Eq. (2.8) with respect to the order parameter ($B = 0$ for the symmetric alloy or ferromagnet). This gives

$$\frac{\partial f}{\partial \phi} = 0 \Rightarrow \phi = \left(0, \pm\sqrt{\frac{-a_2}{a_4}}\right) \tag{2.9}$$

For the first root, $\phi = 0$, to be the only root above the critical temperature, both $a_2(T) > 0$ and $a_4(T) > 0$ ($T > Tc$). For the nonzero roots of Eq. (2.9), which emerge below the critical temperature, it is necessary that $a_2(T) < 0$ while $a_4(T) > 0$ at ($T < T_c$). Assuming that a2 continuously changes sign across the critical temperature, it is reasonable to expand it to first order in a Taylor series about $T = T_c$ according to

$a_2(T) \approx a_2^0(T-T_c)$. Meanwhile $a_4(T)$ must be of the form $a_4(T) \approx a_4^0+b_4^0(T-T_c)+...$, where a_2^0, a_4^0, and b_4^0 are positive constants. Thus, close to and below T_c, mean field theory predicts two minimum (i.e., stable) order parameter states given by

$$\phi \approx \pm\sqrt{\frac{a_2^0}{a_4^0}(T-T_c)} \tag{2.10}$$

Note that as $T \to Tc$, Equation (2.10) continuously approaches $\phi = 0$. Figure 2.1(a)

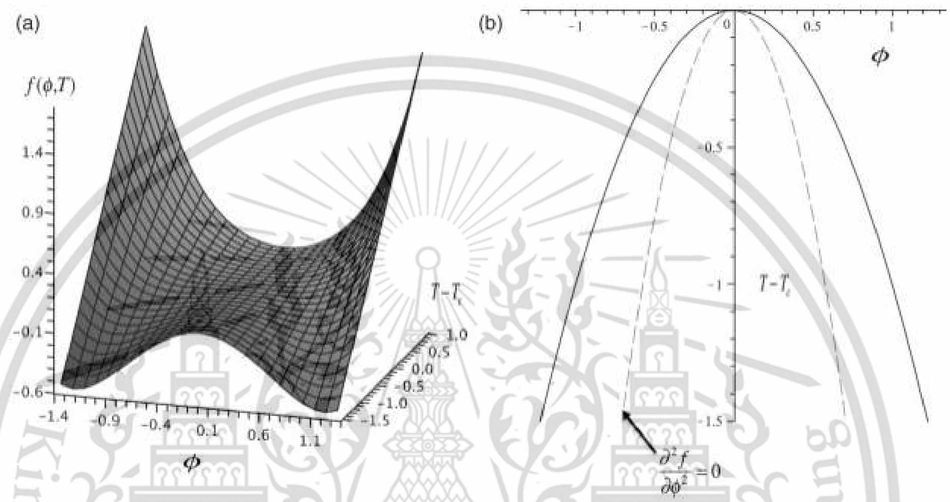

Figure 2.1: (a) Landau free energy of a simple binary mixture.Two stable phases arise continuously from one for $T < T_c$. (b) Corresponding two-phase coexistence phase diagram for $T < T_c$ [16].

shows the energy landscape of Equation (2.8), revealing the existence of one stable state above $T_c(\phi = 0)$ and two below T_c. The figure shows that the disordered, $\phi = 0$, phase gives way to two minima, that is, stable, states below $T = T_c$. Whereas, figure 2.1(b) shows the corresponding phase diagram of coexisting minima of $f(w\phi)$ in (T, ϕ) space. The dashed line indicates the so-called spinodal line defined by the locus of points where $\partial^2 f/\partial\phi^2 = 0$.

2.1.3 Free Energy Density with Nonsymmetric Phase Diagram

It is possible to represent asymmetry in a phase diagram containing a critical point by adding odd powers to the free energy expansion [16]. An example of this is a gas–liquid transition of a pure material. It is convenient to define, in this case, the order parameter to be the density difference from the critical density, that is, $\phi = \rho - \rho_c$. It turns out that the asymmetry can be addressed by retaining at least one third-order term in the Landau free energy density expansion of Eq. (2.7).

$$f(\phi,T) = a_0(T) + \frac{a_2(T)}{2}\phi^2 + \frac{a_3(T)}{3}\phi^3 + \frac{a_4(T)}{4}\phi^4 + O(\phi^6) \tag{2.11}$$

The choice of parameters can be back-engineered to obtain an appropriate phase diagram. It is assumed that $a_4(T) > 0$ for all temperatures in the neighborhood of the transition, which is still second order for the gas–liquid transition in the vicinity of the critical point. The grand potential to be minimized in this system is therefore

$$\omega(\phi, T, \mu) = f(\phi) - \Delta\mu(T)\phi \tag{2.12}$$

where $B = \partial f/\partial\phi = \mu - \mu_c \equiv \Delta\mu(T)$. The properties of a2; a3; and a4 can be better discussed by applying the extremum conditions in Eq. (2.5) to Eq. (2.12) very close to the critical point, where it is assumed that $\Delta\mu \approx 0$ to lowest order in $T - T_c$. It is the same as applying the extremum conditions to $f(\phi)$ (Eq. (2.11)), which gives

$$\begin{aligned} \phi\left(a_2 + a_3\phi + a_4\phi^2\right) = 0 \\ a_2 + 2a_3\phi + 3a_4\phi^2 > 0 \end{aligned} \tag{2.13}$$

The disordered phase is stable for $T > T_c$ for $a_2(T) > 0$. Conversely, for a continuous transition (a second-order transformation), it is required that the three roots (i.e., states) of the cubic polynomial go to one as $T \to T_c$ from below. This can be achieved by demanding that both $a_2(T) \to 0$ and $a_3(T) \to 0$ as $T \to T_c$, and that they both become negative for $T < T_c$. Once again, it is sufficient for $a_4(T)$ to be positive and nearly constant in the neighborhood of $T = T_c$. The lowest order temperature expansions of these constants satisfying these conditions are given by

$$\begin{aligned} a_2 &= a_2^0(T - T_c) \\ a_3 &= a_3^0(T - T_c) \\ a_4 &= a_4(T_c) \end{aligned} \tag{2.14}$$

In general, below the transition temperature, it is required to have two stable states whose grand potential is equal for both the liquid and gas phases. The density of these two sates, however, will in general not be symmetrically positioned about ρ_c. The trial form of the grand potential satisfying these assumptions is

$$\omega(\phi, T, \mu) = \omega_0(T) + \frac{D(T)}{4}\left(\phi - \phi_L\right)^2\left(\phi - \phi_g\right)^2 \tag{2.15}$$

Comparing Eq. (2.15) with Eq. (2.12), where the free energy is expanded according to Eq. (2.11), gives

$$\begin{aligned} D(T) &= a_4(T) \\ \frac{1}{2}\left(\phi_L(T) + \phi_g(T)\right) &= -\frac{a_3(T)}{3a_4(T)} \\ \left(\phi_L(T) - \phi_g(T)\right)^2 &= -\frac{4a_2(T)}{a_4(T)} + \frac{4a_3^2(T)}{3a_4^2(T)} \end{aligned} \tag{2.16}$$

from which the liquid–gas order parameters are determined to be, to lowest order in $T - T_c$,

$$\phi_L = -\frac{a_3^0(T - T_c)}{3a_4(T_c)} + \sqrt{\frac{-a_2^0(T - T_c)}{a_4(T_c)}}$$
$$\phi_g = -\frac{a_3^0(T - T_c)}{3a_4(T_c)} - \sqrt{\frac{-a_2^0(T - T_c)}{a_4(T_c)}} \tag{2.17}$$

Once again, one minimum density is approached continuously as $T \to T_c$ from below. It is also seen that the chemical potential is given by

$$\Delta\mu(T) = \frac{a_4(T)}{2}\left(\phi_L(T) + \phi_g(T)\right)\phi_L(T)\phi_g(T) \sim \mathcal{O}(T - T_c)^2 \tag{2.18}$$

2.1.4 Free Energy Density without Critical Point

First-order transitions typically occur between phases of different geometric symmetry [16]. As a result, the phase diagram of a first-order transition does terminate at a critical point; that is, the two coexisting phases merge into one. The simplest way to break this symmetry is by adding cubic term of negative sign to the Landau free energy density expansion of Eq. (2.7),

$$f(\phi, T) = a_0(T) + a_2(T - T_u)\frac{\phi^2}{2} - a_3\frac{\phi^3}{3} + u\frac{\phi^4}{4} \tag{2.19}$$

where a_2, a_3, and u are positive constants and T_u is a reference temperature different from a critical point. This free energy exhibits one global minimum at high temperature, two equal minima at transition temperature $T = T_m \equiv T_u + 2a_2^2/9a_3u$, and one global minimum and a metastable minimum below T_m. The free energy landscape $f(\phi, T)$ for this case is shown in Fig. 2.2, Above the transition temperature, the free energy of the high-symmetry phase ($\phi = 0$) is a global minimum – although it is evident that a second metastable low symmetry phase, $\phi_L > 0$, emerges even above T_m. Exactly at the transition temperature,

$$f(\phi_h, T_m) = f(\phi_L, T_m) \tag{2.20}$$

Note that the minimum corresponding to ϕ_L (for $T < T_m$) does not emerge continuously from ϕ_h as in a second-order transition. Instead, it emerges as a global minimum at $T = T_m$ discontinuously, that is, at discrete distance from ϕ_h.

2.1.5 The Ginsburg-Landau Free Energy Functional

Thus far, mean field free energies have been discussed, which describe only the bulk properties of the phases of a material [16]. Only bulk thermodynamics can be considered with this type of free energy, which implies, among other things, that phases are infinite in extent and are uniform. No consideration has been given to finiteness

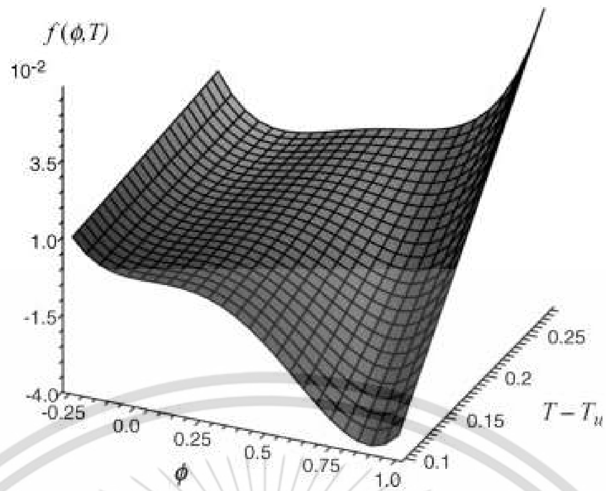

Figure 2.2: Landau free energy for a first-order transformation. The double-well curve with a cubic term in w. One global minimum arises when the coefficient of the square term in $f_{\text{bulk}}(\phi, T)$ is positive. Below the melting temperature, this phase becomes metastable and a new globally stable state of ϕ emerges [16].

of phase and, more importantly, multiple phase and the interfaces separating them. To show how to incorporate interfaces between phases, it is instructive to mention about the simple binary model. It is reasonable to expect that the interaction energy between elements is spatially dependent and varies between any two elements i and j.

$$U = \frac{1}{2}\sum_{i=1}^{N}\sum_{j\neq i}\varepsilon_{ij}(\mathsf{x}_i - \mathsf{x}_j)\phi_i\,(1-\phi_j) \tag{2.21}$$

where the constant term in Equation 2.1 has been neglected. The interaction energy depends on the separation between elements ($\varepsilon_{ij} = \varepsilon_{ji}$) and the j summation is over the nearest neighbors of the ith element for simplicity. To proceed, use is made next of the algebraic identity

$$\phi_i\,(1-\phi_j) = \frac{(|\phi_i - \phi_j|^2 - |\phi_i^2 + \phi_j^2| + 2\phi_i)}{2} \tag{2.22}$$

Equation (2.22) is substituted into Eq. (2.21), which is then simplified by making the assumption that for any i, ε_{ij} is negligible for any $j > \nu$ (which in this case spans the four nearest neighbors). These assumptions make it possible to rewrite Eq. (2.21) as

$$U = \frac{1}{4}\sum_{i=1}^{N}\sum_{j\neq i}\varepsilon_{ij}\,(\phi_i-\phi_j)^2 - \frac{1}{2}\sum_{i}^{N}(1-\phi_i)\,\phi_i\left(\sum_{j\neq i}\varepsilon_{ij}\right) \tag{2.23}$$

Further, assume that the interaction energy per particle $\varepsilon_{ij} \to \varepsilon_i/\nu$, where ε_i is the isotropic mean energy over the ν nearest neighbors of element i. In the limit where any two adjacent elements i and j represent two locations that are physically separated by an infinitesimal distance, the sum

$$\frac{1}{2}\sum_{j\neq i}(\phi_i-\phi_j)^2 = \frac{a^2}{2}\left[\left(\frac{(\phi_i-\phi_R)^2}{a^2}+\frac{(\phi_i-\phi_T)^2}{a^2}\right)+\left(\frac{(\phi_i-\phi_L)^2}{a^2}+\frac{(\phi_i-\phi_B)^2}{a^2}\right)\right] \approx a^2|\nabla\phi(\mathbf{x}_i)|^2 \tag{2.24}$$

in 2D, where ϕ_R, ϕ_T, ϕ_L, and ϕ_B represent ϕ_j evaluated at the right, top, left, and bottom neighbors of the ith element, respectively. The large round brackets in the first line of Eq. (2.24) represent the magnitudes of one-sided gradients at the point i. The vector $\mathbf{x}_i$ in second line of Eq. (2.24) represents the position centered at the element labeled by i. To make the transition to the continuum limit complete, the i summation in Eq. (2.23) is replaced by its continuum analogue, an integral. In dimensions this is accomplished by writing

$$\sum_i \to \int_V \frac{d^d\mathbf{x}}{a^d} \tag{2.25}$$

where the division by a^d is intended to encapsulate the volume that was previously contained within one element, which is the distance between two discrete points – the lattice constant. With the definitions in Eq. (2.24) and (2.25), the total internal energy in Eq. (2.23) can be written, in the 3D continuum limit, as

$$E = \int_V \left(\frac{1}{2}|W_0\nabla\phi|^2 + \frac{1}{2a^3}\varepsilon(\mathbf{x})\phi(\mathbf{x})\left(1-\phi(\mathbf{x})\right)\right) d^3\mathbf{x} \tag{2.26}$$

where the coefficient $W_0 \equiv \sqrt{\varepsilon(\mathbf{x})/(\nu a)}$ has been defined. This parameter will be seen below to be intimately connected to surface energy since it multiples a gradient in the order parameter ϕ, which varies significantly only at interfaces where there is a change of order. In a similar way, the total entropic part of the free energy can be written as

$$S = -k_B\int_V \left(\phi(\mathbf{x})\ln\phi(\mathbf{x}) + (1-\phi(\mathbf{x})\ln(1-\phi(\mathbf{x}))\right)\frac{d^3\mathbf{x}}{a^3} \tag{2.27}$$

where the integrand in Eq. (2.27) can now be seen as a local entropy density ,i.e. $\phi \to \phi(\mathbf{x})$, making the total entropy an integral of the entropy density over the volume V of the system. Combining Eq. (2.26) and (2.27) thus yields the total free energy of the binary alloy,

$$F[\phi,T] = \int_V \left\{\frac{1}{2}|W_0\nabla\phi|^2 + f\left(\phi(\mathbf{x}),T(\mathbf{x})\right)\right\} d^3\mathbf{x} \tag{2.28}$$

where the bulk free energy density is given by

$$f\left(\phi(\mathbf{x}),T(\mathbf{x})\right) = \frac{\varepsilon(\mathbf{x})}{2a^3}\phi(\mathbf{x})\left(1-\phi(\mathbf{x})\right) + \frac{k_BT}{a^3}\left(\varepsilon(\mathbf{x})\ln(\varepsilon(\mathbf{x})) + (1-\phi(\mathbf{x}))\ln\left(1-\phi(\mathbf{x})\right)\right) \tag{2.29}$$

Equation (2.28) is the simplest representation of a free energy that combines the bulk thermodynamics of a simple binary alloy with a minimal description of interfacial energy. Equation (2.28) is often referred to as the Ginzburg–Landau [28] or Cahn-Hilliard free energy [29]. The free energy of the form in Eq. (2.28) serves as a starting point for many phenomena that are modeled using the phase field methodology. In general, $f(\phi, T)$ can be a complex function such as Eq. (2.29) or it can be approximated by a polynomial series that is interpreted as a Taylor series expansion of $f(\phi, T)$ about disordered phase. This formalism allows a mesoscopic description that accounts for bulk thermodynamics and interfaces.

2.2 Nonequilibrium Dynamics

The previous section examined the significance of spatial variations in an order parameter [16]. In the context of materials microstructure, these variations demarcate regions of bulk phase from phase boundaries or interfaces. Another important aspect that must be examined is the time dependence of order parameter changes. Along with the dynamics of other fields (e.g., temperature), the dynamics of order parameters are a critical ingredient in the development of a phenomenology for modeling the microstructure evolution in phase transformations. It is typical in nonequilibrium dynamics to use a locally defined equilibrium free energy or entropy to determine the local driving forces of a phase transformation. These generalized forces or their fluxes are used to drive the subsequent kinetics of various quantities.

Kinetic equations for order parameter fields are called conserved if they take the form of a flux-conserving equation. This implies that an integral of the field over all space is a constant. While, the time evolution of fields whose global average need not be conserved is typically governed by a nonconserved equation. These include magnetization and sublattice ordering. The basic evolution equations governing conserved and nonconserved order parameters will be outlined in the next section. In all cases, the free energy being referred to is in the context of the Ginzburg–Landau free energy functional in Eq. (2.28), where $f(\phi, T)$ depends on the particular phase transformation under consideration.

2.2.1 Driving Forces and Fluxes

Consider a system that is in thermal equilibrium [16]. Its change in entropy is given by

$$dS = \frac{1}{T}dU + \frac{p}{T}dV - \sum_i \frac{\mu_i}{T}dN_i \tag{2.30}$$

where T is the temperature, V its volume, and N_i the number of particles of species i. As this system undergoes a phase transformation, the second law of thermodynamics demands that $dS > 0$ in a closed system. In the case of a constant volume, the driving forces or the so-called affinities driving the corresponding changes in internal energy

(U) and particle number (N_i) are

$$\frac{dS}{dU} = \frac{1}{T}$$
$$\frac{dS}{dN_i} = -\frac{\mu_i}{T} \tag{2.31}$$

If Eq. (2.30) is applied locally to a volume element, then the second law further implies that changes, or gradients, in S from one location in the system element to another must be mediated (i.e., accompanied) by a corresponding flow in the local internal energy and local number of particles. The flux of these two quantities is generally assumed to be given by the linear combination of gradients of the driving forces in Eq. (2.31), that is,

$$\mathsf{J}_0 = M_{00}\nabla\left(\frac{1}{T}\right) - \sum_{j=1}^{N} M_{0j}\nabla\left(\frac{\mu_j}{T}\right)$$
$$\mathsf{J}_i = M_{i0}\nabla\left(\frac{1}{T}\right) - \sum_{j=1}^{N} M_{ij}\nabla\left(\frac{\mu_j}{T}\right) \tag{2.32}$$

where J_0 is associated with a flux of internal energy and J_i is associated with the flux of particle number of species i. The coefficients of the tensor M_{ij} $(i, j = 0, ...N)$ were derived by Onsager, who also showed that the Onsager coefficient matrix is symmetric. This is referred to as the Onsager reciprocity theorem.

2.2.2 Dynamics of Nonconserved Order Parameters: Model A

Some phase transformations involve quantities (order parameters) that do not evolve constrained to a conservation law [16]. Well-known examples include magnetic domain growth, order/disordered transitions, or isothermal solidification of a pure material in the absence of a density jump. Order parameters that evolve without global conservation are called nonconserved order parameters. Motivated by Equation 4.1, a new driving force for the rate of change of nonconserved order parameter is defined as $\delta F/\delta\phi$. Since there is no conservation imposed on $< \phi >$, the simplest dissipative dynamic evolution for a nonconserved order parameter is given by Langevin-type dynamics,

$$\frac{\partial\phi}{\partial t} = -M\frac{\partial F[\phi, T]}{\partial\phi} \equiv M\left(W_0\nabla^2\phi - \frac{\partial f(\phi, T)}{\partial\phi}\right) \tag{2.33}$$

where M is related to the timescale for atomic rearrangement from the disordered phase to the ordered one. The right-hand side of Eq. (2.33) is a driving force that is tailored to drive the system down gradients in the free energy landscape of $F[\phi]$. This equation is referred to as model A in Hohenberg and Halperin classification of phase field models [30]. It is a paradigm used to describe the evolution of an order parameter that does not satisfy a global conservation law. Using, once again, $f(\phi, T)$

from Eq. (2.8), the dynamics of a system of Ising spins in the absence of an external field can be described by

$$\frac{\partial \phi}{\partial t} = M\left(W_0 \nabla^2 \phi - a_2 \phi - a_4 \phi^3\right) \tag{2.34}$$

which is arrived at by substituting Eq. (2.8) into Eq. (2.33). For a system of Ising spins in an external field, Eq. (2.19) can be used, where the constant a_3 can describe a coupling to the external field. Figure 2.3 shows a sequence of time slices in the evolution of magnetic domains numerically simulated using model A dynamics.

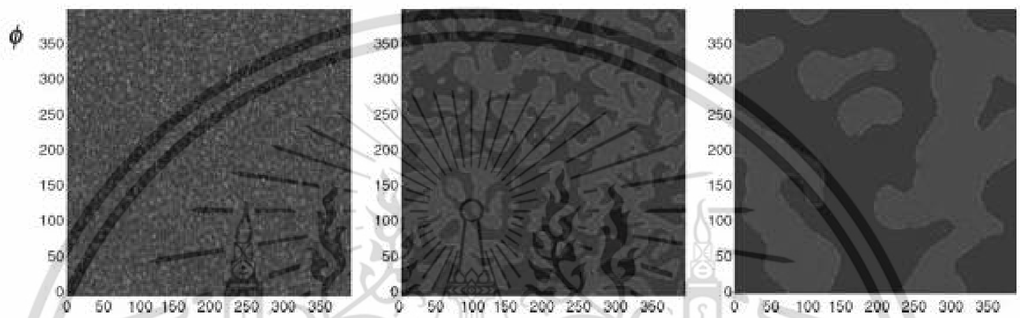

Figure 2.3: Left to right and top to bottom: Time sequence of magnetic domain formation and coarsening under model A dynamics. The gray scale is the z-direction of magnetization, with dark gray representing downward magnetization and light gray upward magnetization [16].

2.2.3 Dynamics of Conserved Order Parameters: Model B

Consider next the dynamics of a general order parameter that represents a quantity that is conserved [16]. For the specific example of the simple binary alloy, see phase diagram in Fig. 2.1(b), the definition of the order parameter represents an impurity concentration. A high-temperature disordered phase with average concentration $\phi = \phi_0$ will undergo phase separation once temperature is lowered below T_c. Since ϕ represents a concentration difference, it must satisfy the mass conservation equation

$$\frac{\partial \phi}{\partial t} = -\nabla \cdot \mathbf{J} \tag{2.35}$$

The flux in Eq. (2.35) is derived from Eq. (2.32) (assumed for simplicity that the non-diagonal Onsager coefficients are zero) as

$$\mathbf{J} = -M \nabla \cdot \mu \tag{2.36}$$

where

$$M \equiv \frac{M_{11}}{T} \approx \frac{M_{11}}{T_c} \tag{2.37}$$

is the mobility of solute. Combining Eq. (2.35)-(2.36) gives the following equation of motion for the order parameter of a phase separating alloy mixture

$$\frac{\partial \phi}{\partial t} = \nabla \cdot \left(M \nabla \frac{\delta F}{\delta \phi} \right) \tag{2.38}$$

Note that $\mu = \delta F / \delta \phi$. Equation (2.38) is the celebrated Cahn–Hilliard equation, or model B, as it is often called in the condensed matter physics literature, after the paper by Hohenberg and Halperin [30], who studied and classified the various order parameter models and the associated physical phenomena that can be used to describe them. As a specific example of the Cahn–Hilliard equation for spinodal decomposition, $f(\phi, T)$ from Eq. (2.8) is substituted into Eq. (2.38). Applying the rules of variational derivatives gives

$$\frac{\partial \phi}{\partial t} = M \nabla^2 \left(-W_0 \nabla^2 \phi + a_2 \phi + a_4 \phi^3 \right) \tag{2.39}$$

where it has been assumed for simplicity that the mobility M is a constant. Figure 2.4 shows a simulation of the dynamics of Eq. (2.39) with $a_2 = -1$ and $a_4 = 1$ and $M = 1$. The concentration field ϕ was initially set to have random initial fluctuations about

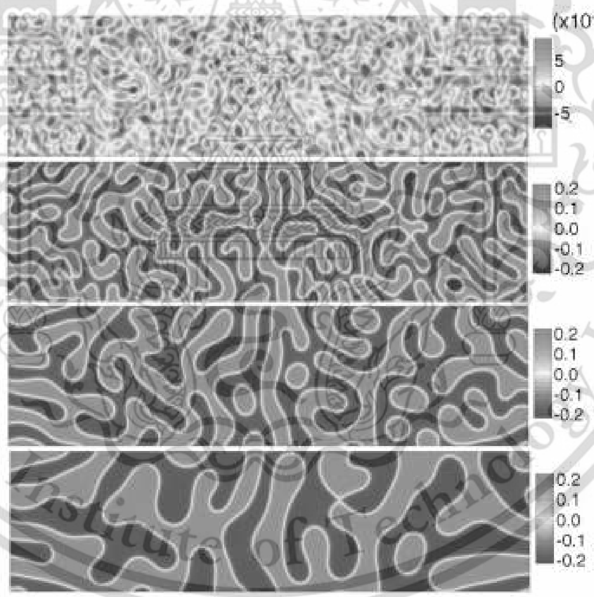

Figure 2.4: Top to bottom: Time sequence showing phase separation during spinodal decomposition. Fluctuations on small length scales grow into larger domains, the size of which diverges with time according to a power law. Shading represents different solute concentrations in the two phases, with light gray being the solute-rich phase and dark gray the solute-poor phase [16].

$\phi = 0$ and periodic boundary conditions were used in the simulation. It is seen that since $a_2 < 0$ (which is the case for $T < T_c$, phase separation occurs. The average alloy concentration satisfies $< \phi >= \phi_0 \approx 0$, the initial average of the order parameter.

2.3 PFC Method

The PFC method is characterized by its free energy functional and the dynamic equation. The simplest free energy functional was introduced by Elder and coworkers [19, 31]:

$$\mathcal{F} = \int w(\rho)\ d\mathbf{r}, \qquad w(\rho) \equiv \frac{\rho}{2}\left[a_t + \lambda(q_0^2 + \nabla^2)^2\right]\rho + g_t\frac{\rho^4}{4}, \tag{2.40}$$

where $w(\rho)$ is the free energy density, a_t, g_t, λ and q_0 are fitting parameters, ρ is the atomic number-density field. This PFC free energy functional can be minimized by a constant ρ profile, representing a liquid phase, and a periodic ρ profile, representing a crystalline solid phase. The density periodic field ϕ can be expressed in terms of Fourier expansion of the form

$$\phi(\mathbf{r}, \bar{\rho}) = \bar{\rho} + \sum_j A_j e^{i\mathbf{G}_j\cdot\mathbf{r}} + \text{c.c.}, \tag{2.41}$$

where $\mathbf{G}_j$ is a reciprocal lattice vector (RLV), A_j is an amplitude of the density wave corresponding to $\mathbf{G}_j$, $\bar{\rho}$ is an average atomic-number density, and c.c. denotes a complex conjugate. The minimization of $\mathcal{F}$ essentially results in the truncation of the summation in Eq. (2.41) to terms with small values of $|\mathbf{G}_j|$ as the terms of with higher values of $|\mathbf{G}_j|$ have vanishingly small A_j. Consequently, this particular PFC model (Eq. (2.40)) favors crystal structures that can be constructed from single set of RLVs such as stripe, hexagonal, and BCC structures in one, two and three dimensions, respectively. To this end, one can construct the so-called "one-mode" approximation of the BCC crystal by limiting the terms in Eq. (2.41) to those corresponding to $\langle 110\rangle$ RLVs or $|\mathbf{G}_j| = 2\pi\sqrt{2}/L_a$, where L_a is the lattice parameter. By assuming that A_j of the terms with the same $|\mathbf{G}_j|$ are equivalent, one obtain

$$\rho_{\text{one}} = \bar{\rho} + 4A_s\left[\cos(q_a r_1)\cos(q_a r_2) + \cos(q_a r_1)\cos(q_a r_3) + \cos(q_a r_2)\cos(q_a r_3)\right], \tag{2.42}$$

where $q_a = 2\pi/L_a$ and A_s is the density-wave amplitude.

The second ingredient of the PFC method, which is the evolution equations, governs the time evolution of the state of the system. In this work, we employ two evolution equations. The first is the Cahn-Hilliard type equation that evolves $\rho(\vec{r}, t)$ through dissipative dynamics and with mass conservation [19]:

$$\frac{\partial\rho}{\partial t} = \nabla^2\mu \equiv \nabla^2\left(\frac{\delta F}{\delta\rho}\right), \tag{2.43}$$

where $\mu = \delta F/\delta\rho$ is the chemical potential.

2.4 Interpretation of PFC Model in CDFT Aspect

In classical theory of density functional theory (CDFT) of simple liquid, the free energy functional can be expressed as [32, 33, 34, 35, 36]

$$F[\rho(\vec{r})] = F_{\text{id}}[\rho(\vec{r})] + F_{\text{ext}}[\rho(\vec{r})] + F_{\text{exc}}[\rho(\vec{r})] \tag{2.44}$$

where $F[\rho(\vec{r})]$ is total free energy functional. $F_{\text{id}}[\rho(\vec{r})]$ is free energy functional of ideal gas (non-interacting term). $F_{\text{ext}}[\rho(\vec{r})]$ is free energy functional regarding interacting potential among liquid particles (interacting term). $F_{\text{exc}}[\rho(\vec{r})]$ is excess free energy functional regarding potential from external field and $\rho(\vec{r})$ is the density field variable of liquid. In case of pure material and neglecting $F_{\text{exc}}[\rho(\vec{r})]$, the equation (2.44) yields [17]

$$\frac{F[\rho(\vec{r})]}{k_{\text{B}}T} = \int d\vec{r}\left[\rho\ln\left(\frac{\rho}{\bar{\rho}}\right) - \delta\rho\right] - \frac{1}{2}\int d\vec{r}d\vec{r}\delta\rho C^{(2)}(\vec{r},\vec{r})\delta\rho' \tag{2.45}$$

where ρ_{l} represents density of liquid state. $C^{(2)}(\vec{r},\vec{r})$ represents two-point correlation function and note that $F[\rho(\vec{r})]/k_{\text{B}}T$ is in dimensionless form. In order to obtain more intuitive formulation of equation (2.45), we consider its expansion form around its average density value, $\bar{\rho}$. Let us denote that

$$n = \frac{\rho - \bar{\rho}}{\bar{\rho}} \tag{2.46}$$

where n represents deviation of ρ around $\bar{\rho}$ in dimensionless form. Substitute equation (2.46) into equation (2.45) and use the fact that $\int d\vec{r}\delta\rho C^{(2)}(\vec{r},\vec{r})\delta\rho' = \bar{\rho}^2 nC^{(2)}n$, we obtain

$$\frac{F[\rho(\vec{r})]}{\bar{\rho}k_{\text{B}}T} = \int d\vec{r}\left[(1+n)\ln(1+n) - n\right] - \int d\vec{r}\left[n\frac{\bar{\rho}C^{(2)}}{2}n\right] \tag{2.47}$$

Consider the first term of equation (2.47) and use the Taylor's expansion of $\ln(1+n) = n - n^2/2 + n^3/3 - n^4/4 + ...$. Then, the first term inside the integral of equation (2.47) becomes

$$\begin{aligned}(1+n)\ln(1+n) - n &= n - \frac{n^2}{2} + \frac{n^3}{3} - \frac{n^4}{4} + n^2 - \frac{n^3}{2} + \frac{n^4}{3} - n - ...\\ &= \frac{n^2}{2} - \frac{n^3}{6} + \frac{n^4}{12} - ...\end{aligned} \tag{2.48}$$

Substitute this formulation into equation (2.47). We literally obtain

$$\frac{\Delta F}{\bar{\rho}k_{\text{B}}T} = \int d\vec{r}\left(n\frac{1-\bar{\rho}C^{(2)}}{2}n - \frac{n^3}{6} + \frac{n^4}{12} - ...\right) \tag{2.49}$$

where $\Delta F \equiv F - F_0$ and F_0 is free energy functional at constant density $\rho = \bar{\rho}$. The two-point correlation function $C^{(2)}$ can be expressed in Taylor's expansion form in fourier space as

$$\hat{C}^{(2)}(k) = \hat{C}_0 + \hat{C}_2k^2 + \hat{C}_4k^4 + ... \tag{2.50}$$

where $\hat{C}^{(2)}(k)$ represents two-point correlation function in fourier space. k represents fourier wave vector and $\hat{C}_{2i}$, $i = 0, 1, 2, ...$, represent the variables which parametrize material properties. In real space, the two-point correlation function is

$$C^{(2)} = \left(\hat{C}_0 - \hat{C}_2\nabla^2 + \hat{C}_4\nabla^4 - ...\right) \tag{2.51}$$

If we only consider to the fourth-order of $C^{(2)}$ function [37]. Then, we obtain

$$C^{(2)}_{4P} = \hat{C}_0 - \hat{C}_2\nabla^2 + \hat{C}_4\nabla^4 \tag{2.52}$$

where $C^{(2)}_{4P}$ represents of the fourth-order fit of two-point direct correlation function (DCF) [37]. It should be noted that $\hat{C}_0$, $\hat{C}_2$ and $\hat{C}_4$ are related with three basic properties of material, the liquid phase isothermal compressibility, $C_l \propto (1 - \bar{\rho}\hat{C}_0)$, the bulk modulus of the crystal, $B_s \propto \bar{\rho}\hat{C}_2^2/|\hat{C}_4|$, and lattice constant, $a_i \propto (\hat{C}_2/|\hat{C}_4|)^{1/2}$, [17]. The height of the first peak, $\hat{C}_m$ in Fig. 2.5, is related to the bulk modulus of

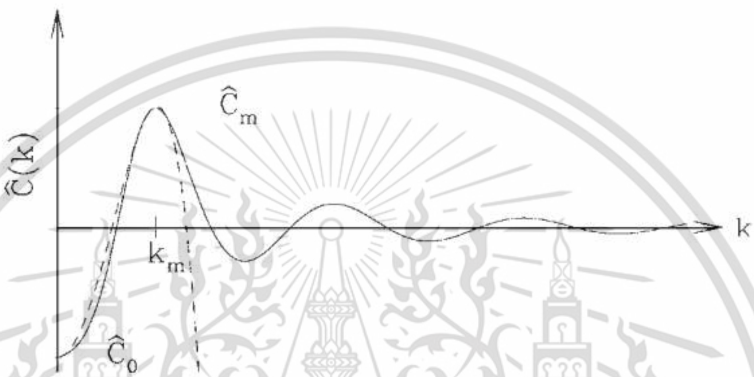

Figure 2.5: Typical liquid state of two-point direct correlation function (solid-line) and the approximation curve used by most paper (dash-line), First peak approximated by the fourth-order fitting schematic [17].

the crystalline phase and the position of the first peak determines the lattice constant. However, this simplification is only defined by three quantities which may not be adequate to fully parametrize any given material. This three parameter estimation is suitable for prediction of triangular symmetry in two dimensions and BCC symmetry in three dimensions. Other crystal symmetries can be obtained by using more complicated two-point correlation function [38]. Substitute the relation in equation (2.52) into equation (2.49). This yields

$$\frac{\Delta F_{4P}}{\bar{\rho}k_{\mathrm{B}}T} = \int d\vec{r}\left(n\frac{1-\tilde{C}_0+\tilde{C}_2\nabla^2-\tilde{C}_4\nabla^4}{2}n - \frac{n^3}{6} + \frac{n^4}{12} - ...\right) \tag{2.53}$$

where $\tilde{C}_i = \bar{\rho}\hat{C}_i$. Truncate higher order term after n^4 and introduce a_t and b_t as a respectively fitting parameter of n^3 and n^4 term. Then, equation (2.53) literally becomes

$$F_{\mathrm{PFC}} = \int d\vec{r}\left(n\frac{1-\tilde{C}_0+\tilde{C}_2\nabla^2-\tilde{C}_4\nabla^4}{2}n - \frac{a_t}{6}n^3 + \frac{b_t}{12}n^4\right) \tag{2.54}$$

where $F_{\mathrm{PFC}} \equiv \Delta F_{4P}/\bar{\rho}k_{\mathrm{B}}T$ represents PFC free energy functional approximated by CDFT model at the fourth-order of the two-point DCF.

2.5 Thermodynamic of Hydrostatically-Stressed Crystal Solids

The thermodynamic description of solids proposed by Larché and Cahn [39] which considers the solids as networks of lattices occupied by atomic species and vacancies. For a hydrostatically-stressed, multiple-component solid, the number of lattices sites (N_L) can be written as

$$N_L = \sum_{i=1}^{k} N_{A_i} + N_v, \tag{2.55}$$

where N_{A_i} and N_v are the numbers of lattices occupied by the atomic species and vacancies, respectively. The internal energy, E, is then postulated to have the following functional dependence, $E \equiv E(S, V, N_{A_1}, ..., N_{A_k}, N_v)$, where S is the entropy and V is the volume. By combining the first and the second law of thermodynamics, we can then write the differential of internal energy as [40]

$$dE = TdS - PdV + \sum_{i=1}^{k} \mu_{A_i} dN_{A_i} + \mu_v dN_v, \tag{2.56}$$

where T represents temperature. P represents pressure. μ_{A_i} represents chemical potential for each component species and μ_v represents the chemical potential of vacancy. Each term is defined by

$$\begin{aligned} T &= \left.\frac{\partial E}{\partial S}\right|_{V,\forall N_{A_i},N_v}, & P &= -\left.\frac{\partial E}{\partial V}\right|_{S,\forall N_{A_i},N_v} \\ \mu_{A_i} &= \left.\frac{\partial E}{\partial N_{A_i}}\right|_{S,V,\forall N_{A_{j\neq i}},N_v}, & \mu_v &= \left.\frac{\partial E}{\partial N_v}\right|_{S,V,\forall N_{A_i}} \end{aligned} \tag{2.57}$$

Other energy functions follow from the internal energy in the usual way used for homogeneous systems. The Helmholtz free energy of the crystal, F, is

$$F = E - TS \tag{2.58}$$

Taking total derivative of equation (2.58) and using (2.56), we obtain

$$dF = -SdT - PdV + \sum_{i=1}^{k} \mu_{A_i} dN_{A_i} + \mu_v dN_v, \tag{2.59}$$

where each intensive variable term is defined as

$$\begin{aligned} S &= -\left.\frac{\partial F}{\partial T}\right|_{V,\forall N_{A_i},N_v}, & P &= -\left.\frac{\partial F}{\partial V}\right|_{T,\forall N_{A_i},N_v} \\ \mu_{A_i} &= \left.\frac{\partial F}{\partial N_{A_i}}\right|_{T,V,\forall N_{A_{j\neq i}},N_v}, & \mu_v &= \left.\frac{\partial F}{\partial N_v}\right|_{T,V,\forall N_{A_i}} \end{aligned} \tag{2.60}$$

It should be noted that $F \equiv F(T, V, N_{A_1}, ..., N_{A_k}, N_v)$. However, the thermodynamic fields associated with most evolving systems are function of position and time, and energy regarding such a system must be calculated by integrating energy density over the volume of the system. The energy density can be expressed on both per-unit-volume basis or per-atom basis. In elastically deformed crystals, stress and deformation tensor are usually referred either to the current state (Eulerian description) or to some convenient reference state (Lagrangian description). Therefore, thermodynamics fields must also be expressible as densities referred to either the current state or to some convenient reference state.

First, the energy density in reference state is established by dividing equation (2.56) with V', reference volume. We obtain

$$de_{V'} = Tds_{V'} - PdJ + \sum_{i=1}^{k} \mu_{A_i} d\rho'_{A_i} + \mu_v d\rho'_v, \tag{2.61}$$

where $e_{V'} \equiv E/V'$ is energy density referred to reference state. $s_{V'} \equiv S/V'$ is entropy density in reference state. $J \equiv V/V'$ is the measure of deformation. $\rho'_{A_i} \equiv N_{A_i}/V'$ is atomic species (A_i) density in reference state. $\rho'_v \equiv N_v/V'$ is vacancy density in reference state. Regarding lattice site conservation equation (2.55), this can lead to site constraint relation in reference configuration as

$$\rho'_L = \sum_{i=1}^{k} \rho'_{A_i} + \rho'_v, \tag{2.62}$$

where $\rho'_L \equiv N_L/V'$ is lattice site density in reference state. If we take derivative of equation (2.62), the $d\rho'_L$ term would vanish. Then, equation (2.62) yields

$$d\rho'_v = -\sum_{i=1}^{k} d\rho'_{A_i}, \tag{2.63}$$

Substitute equation (2.63) into equation (2.61), we obtain

$$de_{V'} = Tds_{V'} - PdJ + \sum_{i=1}^{k} \mu_{A_iv} d\rho'_{A_i}, \tag{2.64}$$

where $e_{V'} \equiv e_{V'}(s_{V'}, J, \rho'_{A_1}, ..., \rho'_{A_k})$ and $\mu_{A_iv} = \mu_{A_i} - \mu_v$ is diffusion potential. To develop energy density in current state, we use the fact that all physical quantities in reference state and current state are related by $x' \equiv xJ$ where x' represents physical property in reference state and x represents physical property in current state. Therefore, equation (2.64) becomes

$$d\left(e_V J\right) = Td\left(s_V J\right) - PdJ + \sum_{i=1}^{k} \mu_{A_iv} d\left(\rho_{A_i} J\right), \tag{2.65}$$

which can be rearranged

$$e_V dJ + J de_V = T s_V dJ + T J ds_V - P dJ + \sum_{i=1}^{k} \left[\mu_{A_i v} \rho_{A_i} dJ + \mu_{A_i v} J d\rho_{A_i} \right], \qquad (2.66)$$

The equation (2.66) can be reduced to

$$de_V = T ds_V + \frac{\left[-P - f_V + \sum_{i=1}^{k} \mu_{A_i v} \rho_{A_i} \right]}{J} dJ + \sum_{i=1}^{k} \mu_{A_i v} d\rho_{A_i} \qquad (2.67)$$

where $e_V \equiv e_V(s_V, J, \rho_{A_1}, ..., \rho_{A_k})$ and $f_V = e_V - T s_V$ is Helmholtz free energy density in current state. This energy density in current state will play a crucial role in developing pressure-controlled dynamic equation in later chapter.

2.6 Classical Irreversible Thermodynamics Theory

In classical theory of irreversible thermodynamics (CIT), the local equilibrium postulation is assumed for each microscopic cell even though the entire system is out off equilibrium state. Then Gibb's fundamental relation obtained by combining the first and the second law of thermodynamics [1],

$$dE = T dS - dW + \sum_{i=1}^{k} \mu_{A_i} dN_{A_i} \qquad (2.68)$$

can be used to calculate changes in the local equilibrium states as a result of evolution of the spatial distribution of thermodynamic potentials. Dividing dE by V', reference cell volume of the system, to obtain thermodynamic relation in a new form

$$de_{V'} = T ds_{V'} - dw_{V'} + \sum_{i=1}^{k} \mu_{A_i} d\rho'_{A_i}. \qquad (2.69)$$

Note that each physical density quantity $x_{V'}$ represents that quantity density in reference state. Now that all extensive quantities are now on a per unit volume basis, equation (2.69) can be generalized as

$$T ds_{V'} = de_{V'} - \sum_{i=1}^{k} \psi_i d\xi_i \qquad (2.70)$$

where ψ_i represents a i^{th} generalized intensive quantity and ξ_i represents its conjugate extensive quantity density. Alternatively, the last term in equation (2.70) can be expanded as

$$\sum_{i=1}^{k} \psi_i d\xi_i = -P dv + \tilde{\sigma}_{kl} d\tilde{\varepsilon}_{kl} + \gamma dA + \sum_{i=1}^{k} \mu_{A_i} d\rho_{A_i} + \vec{E} \cdot d\vec{p} + \vec{H} \cdot d\vec{b} \qquad (2.71)$$

where P is pressure. $v \equiv V/V'$ is cell volume relative to reference volume. $\tilde{\sigma}_{kl}$ is the deviatoric stress tensor and $\tilde{\varepsilon}_{kl}$ is deviatoric strain tensor. γ is interfacial energy density and A is the interfacial area. μ_{A_i} is chemical potential of A_i component and $\rho_{A_i}$is atomic density of A_i component. $\vec{E}$ is electrical field and $\vec{p}$ is the total polarization density. $\vec{H}$ is the magnetic field and $\vec{b}$ is the total magnetic moment density. According to equation (2.70), the ψ_i can be scalar, vector or even tensor quantities. However, all of their product must be scalar.

Type of physical systems	Intensive variable (ψ_i)	Conjugate variable (ξ_i)
Mechanical system (HP)	$-P$	J
Mechanical system (NHP)	$\tilde{\sigma}_{kl}$	$\tilde{\varepsilon}_{kl}$
Surface tension	γ	A
Chemical system	μ_{A_i}	ρ_{A_i}
Electrical system	$\vec{E}$	$\vec{p}$
Magnetic system	$\vec{H}$	$\vec{b}$

Table 2.1: List of generalized intensive quantities and their conjugate quantities for various physical systems. Note that (HP) is hydrostatic pressure and (NHP) is non-hydrostatic pressure, deviatoric stress tensor [1].

In equilibrium thermodynamics, entropy maximization for a system with fixed internal energy determines equilibrium. However, entropy increases play an important role in irreversible thermodynamics. If each of reference cells were an isolated system, the right hand side of equation (2.70) could only increase in a kinetic process. Nonetheless, because energy, heat and mass can flow between cells during kinetic processes, they cannot be treated as isolated systems, and application of the second law must be generalized to the system of interacting cells.

In hypothetical system for modeling kinetics, the microscopic cells must be open systems. It is useful to consider entropy as a fluxlike quantity capable of flowing from one part of a system to another, just like energy, mass and charge. Entropy flux, $\vec{J}_S$, is related to the heat flux, $\vec{J}_Q$. Normally, energy, mass and charge are conserved quantity, however, entropy is not. It can be created or even destroyed locally. The local rate of entropy-density creation is denoted by $\dot{s}_{gen}$. Therefore, the total rate of entropy creation in a volume V is

$$\dot{S}_{gen} = \int_V \dot{s}_{gen} dV. \tag{2.72}$$

For more general system, the total entropy increase will depend on how much entropy is produced within it and upon how much entropy flows through its boundaries. According to equation (2.70), time derivation density in a cell is

$$\frac{\partial s}{\partial t} = \frac{1}{T}\frac{\partial e}{\partial t} - \frac{1}{T}\sum_{i=1}^{k} \psi_i \frac{\partial \xi_i}{\partial t}. \tag{2.73}$$

If we assume that all ξ_i are conserved physical quantities, $\partial\xi_i/\partial t = -\nabla\cdot\vec{J}_i$. The equation (2.73) literally becomes

$$\frac{\partial s}{\partial t} = -\frac{1}{T}\nabla\cdot\vec{J}_E + \frac{1}{T}\sum_{i=1}^{k}\psi_i\nabla\cdot\vec{J}_i. \tag{2.74}$$

Using mathematical identity (property of the divergence)

$$A\nabla\cdot\vec{B} = -\vec{B}\cdot\nabla A + \nabla\cdot(A\vec{B}). \tag{2.75}$$

Therefore, equation (2.74) can be written as

$$\frac{\partial s}{\partial t} = -\nabla\cdot\left(\frac{\vec{J}_E - \sum_i^k\psi_i\vec{J}_i}{T}\right) + \left(\vec{J}_E\cdot\nabla\frac{1}{T} - \sum_{i=1}^{k}\vec{J}_i\cdot\nabla\frac{\psi_i}{T}\right). \tag{2.76}$$

Comparing equation (2.76) with the equation (2.77) term by term as below

$$\frac{\partial s}{\partial t} = -\nabla\cdot\vec{J}_S + \dot{s}_{gen}. \tag{2.77}$$

According to equation (2.77), we obtain

$$\vec{J}_S = \frac{\vec{J}_E - \sum_i^k\psi_i\vec{J}_i}{T} \tag{2.78}$$

and

$$\dot{s}_{gen} = \vec{J}_E\cdot\nabla\frac{1}{T} - \sum_{i=1}^{k}\vec{J}_i\cdot\nabla\frac{\psi_i}{T}. \tag{2.79}$$

It should be noted that

$$\nabla\frac{1}{T} = -\frac{1}{T^2}\nabla T, \qquad \nabla\frac{\psi_i}{T} = -\frac{\psi_i}{T^2}\nabla T + \frac{1}{T}\nabla\psi_i \tag{2.80}$$

Substitute equation (2.80) into equation (2.79), this yields

$$\dot{s}_{gen} = -\left(\frac{\vec{J}_E - \sum_{i=1}^k\psi_i\vec{J}_i}{T^2}\right)\cdot\nabla T - \sum_{i=1}^{k}\frac{\vec{J}_i}{T}\cdot\nabla\psi_i. \tag{2.81}$$

Multiplying equation (2.81) by T both sides, it yields

$$T\dot{s}_{gen} = -\frac{\vec{J}_Q}{T}\cdot\nabla T - \sum_{i=1}^{k}\vec{J}_i\cdot\nabla\psi_i. \tag{2.82}$$

Note that $\vec{J}_Q = \vec{J}_E - \sum_{i=1}^k\psi_i\vec{J}_i$. Every term on the right-hand side of equation (2.82) is the scalar product of the fluxes and their coupled gradients, conjugate forces.

Type of physical systems	Flux	Force	Empirical force-flux law	
Heat	$\vec{J}_Q$	$-\frac{1}{T}\nabla T$	Fourier's law	$\vec{J}_Q = -K\nabla T$
Chemical	$\vec{J}_i$	$-\nabla \mu_i$	Fick's law	$\vec{J}_i = -M_i c_i \nabla \mu_i$
Electrical	$\vec{J}_q$	$\nabla \phi$	Ohm's law	$\vec{J}_q = -K\nabla \phi$

Table 2.2: List of thermodynamic fluxes and conjugate driving forces for some physical systems with their empirical relation [1].

In fact, each flux could be a function of other forces in addition to its conjugate force that is

$$J_{Q_i} = J_{Q_i}(F_{Q_1}, F_{Q_2}, ..., F_{Q_i}, F_{Q_{i+1}}, ..., F_{Q_N}) \tag{2.83}$$

where J_{Q_i} is thermodynamic flux and F_{Q_i} is conjugate force of Q_i factor. Furthermore, each thermodynamic flux can be written in a Taylor's expansion near its equilibrium point $J_{Q_{i0}}$.

$$J_{Q_i} = J_{Q_{i0}} + \sum_{\alpha=1}^{N} \frac{\partial J_{Q_i}}{\partial F_{Q_\alpha}} F_{Q_\alpha} + \frac{1}{2} \sum_{\alpha,\beta=1}^{N} \frac{\partial^2 J_{Q_i}}{\partial F_{Q_\alpha} \partial F_{Q_\beta}} F_{Q_\alpha} F_{Q_\beta} + \tilde{R}(F_{Q_1}, ..., F_{Q_N}) \tag{2.84}$$

where $J_{Q_{i0}} \equiv J_{Q_{i0}}(F_{Q_{10}}, F_{Q_{20}}, ..., F_{Q_{N0}})$ is thermodynamic flux at equilibrium state. $F_{Q_{i0}}$ is thermodynamic force at equilibrium state. $\tilde{R}(F_{Q_1}, F_{Q_2}, ..., F_{Q_N})$ is higher order term of expansion. It should be noted that at equilibrium state, each $J_{Q_{i0}}$ vanishes since every $F_{Q_{i0}}$ becomes zero. Furthermore, we postulate that the system is very close to its equilibrium state, therefore, each driving force is slightly deviated from its equilibrium state, $\forall F_{Q_i} << 1$. Then, the equation (2.84) can be written in linear approximation formulation as

$$J_{Q_i} = \frac{\partial J_{Q_i}}{\partial F_{Q_1}} F_{Q_1} + \frac{\partial J_{Q_i}}{\partial F_{Q_2}} F_{Q_2} + ... + \frac{\partial J_{Q_i}}{\partial F_{Q_N}} F_{Q_N} \tag{2.85}$$

or in abbreviated form,

$$J_\alpha = \sum_\beta L_{\alpha\beta} F_\beta \tag{2.86}$$

where $L_{\alpha\beta} \equiv \partial J_\alpha / \partial F_\beta$ is phenomenological coefficient. Then, we can utilize each of J_α to develop intended dynamic relation based on physical laws further. Regarding equation (2.82), it should be noted that the relation can be given in more arbitrary form as

$$T\dot{s}_{gen} = \sum_\alpha J_\alpha F_\alpha \tag{2.87}$$

Finally, the entropy creation can be expressed in a quadratic function of driving forces alone as

$$T\dot{s}_{gen} = \sum_{\alpha\beta} L_{\alpha\beta} F_\alpha F_\beta \tag{2.88}$$

Note that $T\dot{s}_{gen} \geq 0$.

2.7 Viscoelastic mechanical model

Viscoelasticity is concerned with materials which exhibit strain rate effects in response to applied stresses. These effects are manifested by the phenomena of creep under constant stress and stress relaxation under constant strain. These time-dependent phenomena may have a considerable effect on the stress distribution developed in a member, such as a thick tube made of viscoelastic material subjected to prescribed loads or prescribed surface displacements [41].

In classic elasticity, there is no time delay between application of a force and the deformation that it causes. For many materials, however, there is additional time-dependent deformation that is recoverable. This is called viscoelastic or anelastic deformation. When a load is applied to a material, there is an instantaneous elastic response, but the deformation also increases with time. Anelastic strains in metals and ceramics are usually so small that they are ignored. In many polymers, however, viscoelastic strains can be very significant [7].

Anelasticity is responsible for damping of vibrations. A high damping capacity is desirable where vibrations might interfere with the precision of instruments or machinery and for controlling unwanted noise. A low damping capacity is desirable in materials used for frequency standards, in bells, and in many musical instruments. Viscoelastic strains are often undesirable. They cause the sagging of wooden beams, denting of vinyl flooring by heavy furniture,and loss of dimensional stability in gauging equipment. The energy associated with damping is released as heat, which often causes an unwanted temperature increase. Study of damping peaks and how they are affected by processing has been useful in identifying mechanisms.

In the following discussion of mechanical models, stress σ, force per unit area, and strain e, deformation per unit length, instead of force and deformation of the model will be used to compare the stress-strain-time relation of viscoelastic materials with the viscoelastic models considered.

2.7.1 Idealized Linear Spring and Dashpot

Elastic behavior can be modeled mathematically with structures constructed from idealized spring elements. This element exhibits instantaneous elasticity and instantaneous recovery as shown in Fig. 2.6.

A spring models a perfectly linear elastic solid. The behavior is described by

$$\begin{aligned} \sigma &= Ke \\ e &= \frac{\sigma}{K} \end{aligned} \tag{2.89}$$

where e is strain, σ is applied stress and K is spring constant which can be interpreted as Young's modulus. On the other hand, a dashpot models a perfectly viscous material is shown in Fig. 2.7

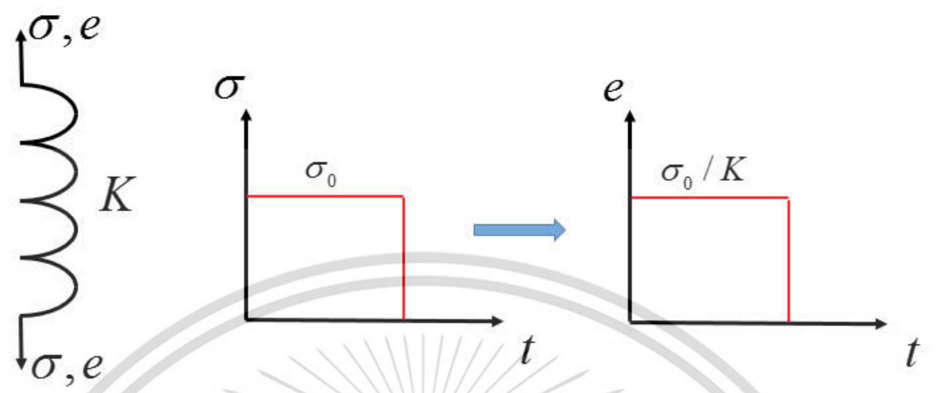

Figure 2.6: Behavior of a linear spring element which is able to exhibit instantaneous elasticity and instantaneous recovery where σ_0 is applied stress value.

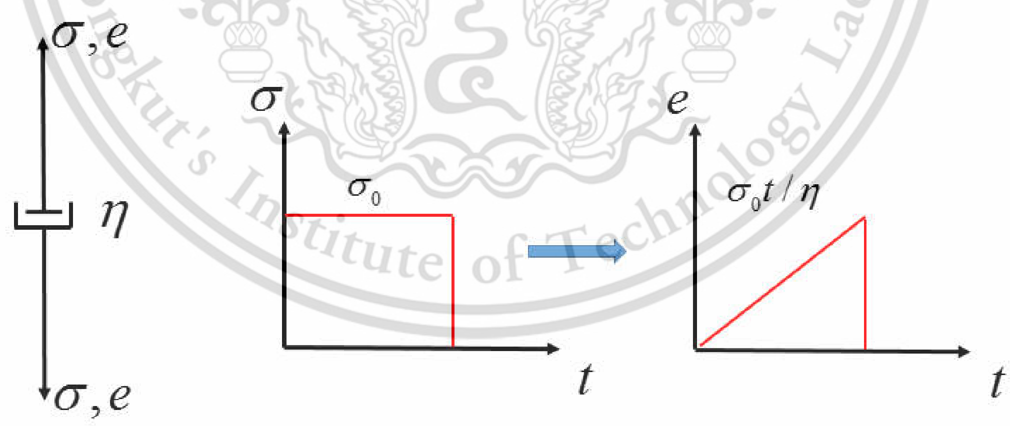

Figure 2.7: Behavior of a linear viscous element which is able to exhibit linearly time-dependent deformation where σ_0 is applied stress value.

The behavior of perfectly linear viscous model is described by

$$\sigma = \eta \dot{e}$$
$$e = \frac{\sigma_0}{\eta} t \qquad (2.90)$$

where η is the coefficient of viscosity. Equation (2.90) states that the strain rate k is proportional to the stress or, in other words, the dashpot will be deformed continuously at a constant rate when it is subjected to a step of constant stress. On the other hand, when a step of constant strain is imposed on the dashpot the stress will have an infinite value at the instant when the constant strain is imposed and the stress will then rapidly diminish with time to zero at $t = 0+$.

2.7.2 Maxwell model

The Maxwell model is a two element model consisting of a linear spring element and a linear viscous dashpot element connected in series as shown in Fig. 2.8. The stress-

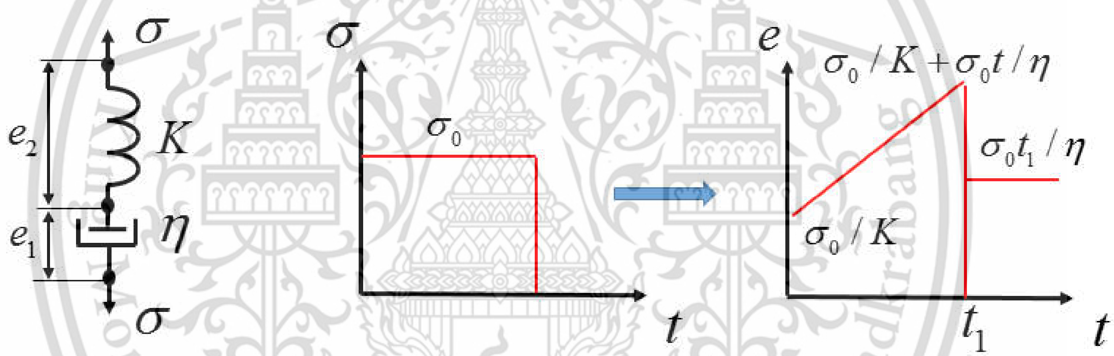

Figure 2.8: Behavior of a maxwell model which is able to exhibit linearly time-dependent deformation where σ_0 is applied stress value. If the stress is removed from the Maxwell model at time, the spring returns to zero at the instant the stress is removed, while the strain which does not disappear and forms a permanent deformation.

strain relations of spring and dashpot follow from Eq. (2.89) and (2.90), respectively.

$$\sigma = K e_2$$
$$\sigma = \eta \dot{e}_1 \qquad (2.91)$$

Since both elements are connected in series, the total strain is

$$e = e_1 + e_2 \qquad (2.92)$$

or the strain rate is

$$\dot{e} = \dot{e}_1 + \dot{e}_2 \qquad (2.93)$$

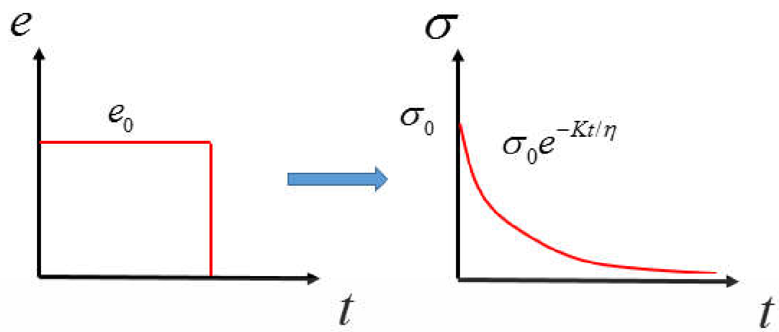

Figure 2.9: The stress relaxation phenomenon for a Maxwell model under constant strain. If the stress is removed from the Maxwell model, the elastic strain in the spring returns to zero once the instant the stress is removed.

Equations (2.91) and (2.93) contain four unknowns σ, e, e_1, e_2. Among these e_1 and e_2 are internal variables and σ and e are the external variables. Therefore, the stress-strain relation of the model can be obtained by eliminating e_1 and e_2 from these equations. Inserting Eq. (2.91) into Eq. (2.93), e_1 and e_2 can be eliminated and the following stress-strain rate relation for the Maxwell model is obtained

$$\dot{e} = \frac{\dot{\sigma}}{K} + \frac{\sigma}{\eta} \tag{2.94}$$

The strain-time relations under various stress conditions and stress-time relations under given strain input can be obtained by solving differential Eq. (2.94). The following strain-time relation can be obtained after applying integration together with the initial condition $\sigma = \sigma_0$ at $t = t_0$.

$$e = \frac{\sigma_0}{K} + \frac{\sigma_0}{\eta} t \tag{2.95}$$

If the stress is removed from the Maxwell model at time t_l, the elastic strain σ_0/K in the spring returns to zero at the instant the stress is removed, while $(\sigma_0/\eta)t_1$ represents a permanent strain which does not disappear. If the Maxwell model is subjected to a constant strain e_O at time $t = 0$, for which the initial value of stress is σ_0, the stress response can be obtained by integrating Eq. (2.94) for these initial conditions with the following result

$$\sigma(t) = \sigma_0 e^{-Kt/\eta} \tag{2.96}$$

Equation (2.96) describes the stress relaxation phenomenon for a Maxwell model under constant strain. The stress relaxation is shown in Fig. 2.9.

2.7.3 Kelvin-Voigt model

The Kelvin model is shown in Fig. 2.10 where a spring element and dashpot element are connected in parallel. The spring and dashpot have the following stress-strain

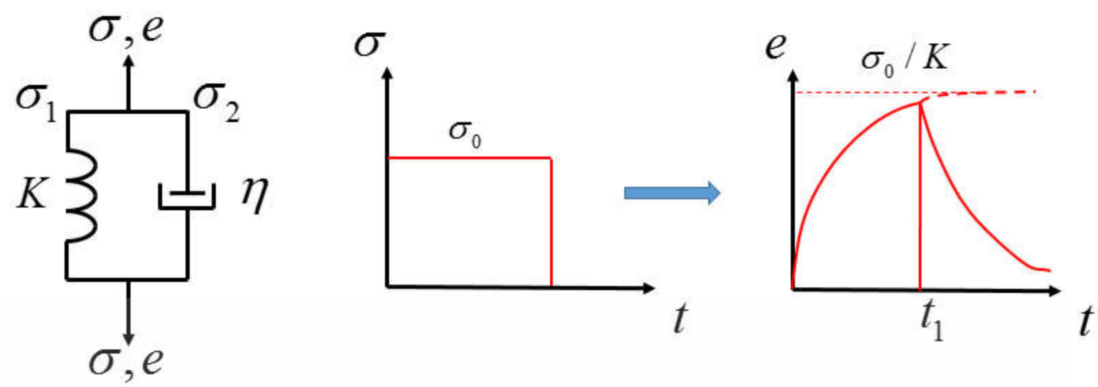

Figure 2.10: Creep and recovery behavior of Kelvin-Voigt model.

relations according to Eq. (2.89) and (2.90)

$$\begin{aligned} \sigma_1 &= Ke \\ \sigma_2 &= \eta\dot{e} \end{aligned} \tag{2.97}$$

Since both elements are connected in parallel, the total stress is

$$\sigma = \sigma_1 + \sigma_2 \tag{2.98}$$

Again, Equations (2.97) and (2.98) contain four unknowns. Eliminating σ_1 and σ_2 among these equations yields the following equation between stress a and strain e

$$\dot{e} + \frac{K}{\eta}e = \frac{\sigma}{\eta} \tag{2.99}$$

The solution of Eq. (2.99) may be shown to have the following form for creep under a constant stress σ_0 applied at t = 0,

$$e = \frac{\sigma_0}{K}\left(1 - e^{-Kt/\eta}\right) \tag{2.100}$$

As shown in Fig. 2.10, the strain described by Eq. (2.100) increases with a decreasing rate and approaches asymptotically the value of σ_0/K when t tends to infinity. It should be noted that the Kelvin model does not show a time-dependent relaxation. Owing to the presence of the viscous element an abrupt change in strain e_0 can be accomplished only by an infinite stress which is impossible.

Neither the Maxwell nor Kelvin model described above accurately represents the behavior of most viscoelastic materials. For example, the Kelvin model does not exhibit time-independent strain on loading or unloading, nor does it describe a permanent strain after unloading. The Maxwell model shows no time-dependent recovery and does not show the decreasing strain rate under constant stress which is a characteristic of primary creep. Both models show a finite initial strain rate whereas the apparent initial strain rate for many materials is very rapid.

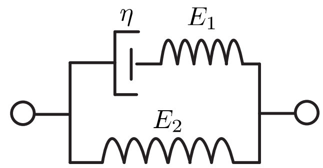

Figure 2.11: Schematic illustration of standard Linear Solid Model (SLS) Model.

2.7.4 Standard Linear Solid Model

We review the standard linear solid model (SLS) which is a method of modeling viscoelasticity using linear combinations of springs and dampers as shown in FIG. 2.11. The strain response from this model will be compared with that from the PFC-PCD simulation in order to extract viscoelastic quantities and properties. The governing differential equation for the SLS model is [41, 8]

$$(E_1 + E_2)\frac{de}{dt} + \frac{E_1 E_2}{\eta} e = \frac{E_1}{\eta}\sigma + \frac{d\sigma}{dt} \tag{2.101}$$

where e is the strain response from the applied stress σ. Equation (2.101) can be written in simple form as follows

$$\frac{de}{dt} + Ke = \sigma' + \tau\frac{d\sigma'}{dt} \tag{2.102}$$

where $K = E_1 E_2/(\eta(E_1 + E_2))$ and $\tau = \eta/E_1$. The variable σ' is the scaled quantity defined as $\sigma' = \sigma/\left(\tau(E_1 + E_2)\right)$.

For the creep behavior, we consider the case where the system (initially at zero stress and strain) is subject to constant stress.

$$\sigma'(t) = \bar{\sigma}'. \tag{2.103}$$

The corresponding strain is then

$$e(t) = e_\infty \left[1 - \exp\left(-\frac{t}{\tau_c}\right)\right] \tag{2.104}$$

where $e_\infty = \bar{\sigma}'/K$ is the deformation at $t = \infty$ and $\tau_c = 1/K$ is the relaxation time; the subscript "c" indicate the creep phenomena. The quantities e_∞ is the deformation at steady-state while τ_c relates to the rate at which the system reaches the steady-state deformation. The plot of the strain response is shown as an example in Fig. 2.12. For the hysteresis behavior, we consider the system induced by harmonic excitation given by

$$\sigma'(t) = \sigma'_A \sin(\omega t) \tag{2.105}$$

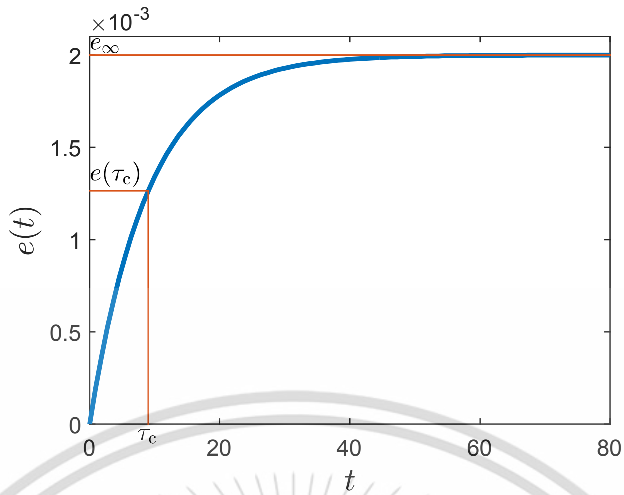

Figure 2.12: Viscoelastic creep under step load at the same $e_\infty = 2 \cdot 10^{-3}$ condition and $\tau_c = 9.0$.

where σ'_A is the stress amplitude, $\omega = 2\pi f$ is the angular frequency, and f is the frequency. At steady state, the strain response yield the solution:

$$e(t) = e_A \sin(\omega t - \delta) \tag{2.106}$$

where

$$e_A = \sigma'_A \sqrt{\frac{1 + (\tau\omega)^2}{K^2 + \omega^2}} \tag{2.107}$$

is the strain amplitude. As a result, the amplitude ratio, A_r, is

$$A_{\text{r}} = \frac{\sigma'_A}{\sigma_A} \sqrt{\frac{1 + (\tau\omega)^2}{K^2 + \omega^2}} \tag{2.108}$$

Also, the loss tangent factor,

$$\delta = \arctan\left[\left(\frac{1 - \tau K}{K + \tau\omega^2}\right)\omega\right], \tag{2.109}$$

defines the phase angle due to time-delayed response. From the solution the complex moduli (or dynamic modulus) can be defined from

$$G'_{\text{complex}} \equiv \frac{\sigma'}{e_A} = \frac{K + j\omega}{1 + j\tau\omega} = G'_{\text{storage}} + jG'_{\text{loss}}. \tag{2.110}$$

The quantity G'_{complex} is a property of viscoelastic materials and can be written further as $G'_{\text{complex}} = G'_{\text{storage}} + jG'_{\text{loss}}$, where G'_{storage} is the storage modulus and G'_{loss} is the loss modulus. The quantity G'_{storage} measures the stored energy and is an elastic response of material while G'_{loss} measures energy dissipation and is a viscous response of a material. The expressions for G'_{storage} and G'_{loss} can be obtained from rearranging the last equality in Eq. (2.110), yielding

$$G'_{\text{storage}} = \frac{K + \tau\omega^2}{1 + (\tau\omega)^2}, \qquad G'_{\text{loss}} = \frac{(1 - \tau K)\omega}{1 + (\tau\omega)^2}. \tag{2.111}$$

The loss tangent, tan(δ), is the ratio of storage and loss modulus or tan(δ) $= G'_{\text{loss}}/G'_{\text{storage}}$; this quantity is a measure of damping in the material.

The behavior of the SLS model a function of excitation frequency is shown in Fig. 2.13(a). At low frequencies, tan(δ) or δ is low, which indicates that the system behaves in an elastic manner. This is due to fact that the dashpot in Fig. 2.11 has sufficient time to displace, resulting in the stress and strain profiles that are almost in phase. The value of G'_{storage} is relatively small compared with that at higher frequencies due to large strain amplitude (Fig. 2.13(b)). At high frequencies, the system also behaves elastically as seen from small tan(δ); at this condition, the change in stress is too rapid for the dashpot to operate and thus the strain response is in phase with the stress profile. Due to small strain amplitude, the value of G'_{storage} is relatively large.

At intermediate frequencies, a considerable amount of phase lag occurs, as shown schematically in Fig. 2.13(c), showing a more viscous behavior, and the stress-strain profiles can be plotted to exhibit hysteresis loop as shown in Fig. 2.13(d) where the area inside the loop represent the energy loss. At the frequency where tan(δ) is maximum, the system exhibit the highest damping capacity and, in real materials, this condition is important for damping applications.

2.8 Literature Review

In 2002, Elder et al.[31] presented a new model of crystal growth that described the phenomena on atomic length and diffusive time scales. The former incorporates elastic and plastic deformation in a natural manner, and the latter enables access to time scales much larger than conventional atomic methods. Historically, many continuum models have been developed to describe certain aspects of crystal growth and liquid/solid transitions in general. At the simplest level called model A in the Halperin and Hohenberg [30] classification scheme has been used to describe liquid/ solid transitions. This model treats all solids equivalently and does not introduce any crystal anisotropy. Extensions to this basic model have been developed to incorporate a solid phase that has multiple states that represent multiple orientations [42, 43]. Other models [44, 45, 46] have sought to include elastic and plastic deformations, but cannot account for multiple orientations. Therefore, in this work, these limitations are overcome by considering a free energy that is minimized by a periodic hexagonal (i.e., solid) state. The model used in this work describes the statics and dynamics of a conserved field, ψ, by the following free energy and equation of motion:

$$\mathcal{F} = \int \left\{ \psi \left[\left(q_0^2 + \nabla^2\right)^2 - \epsilon \right] \frac{\psi}{2} + \frac{\psi^4}{4} \right\} \tag{2.112}$$

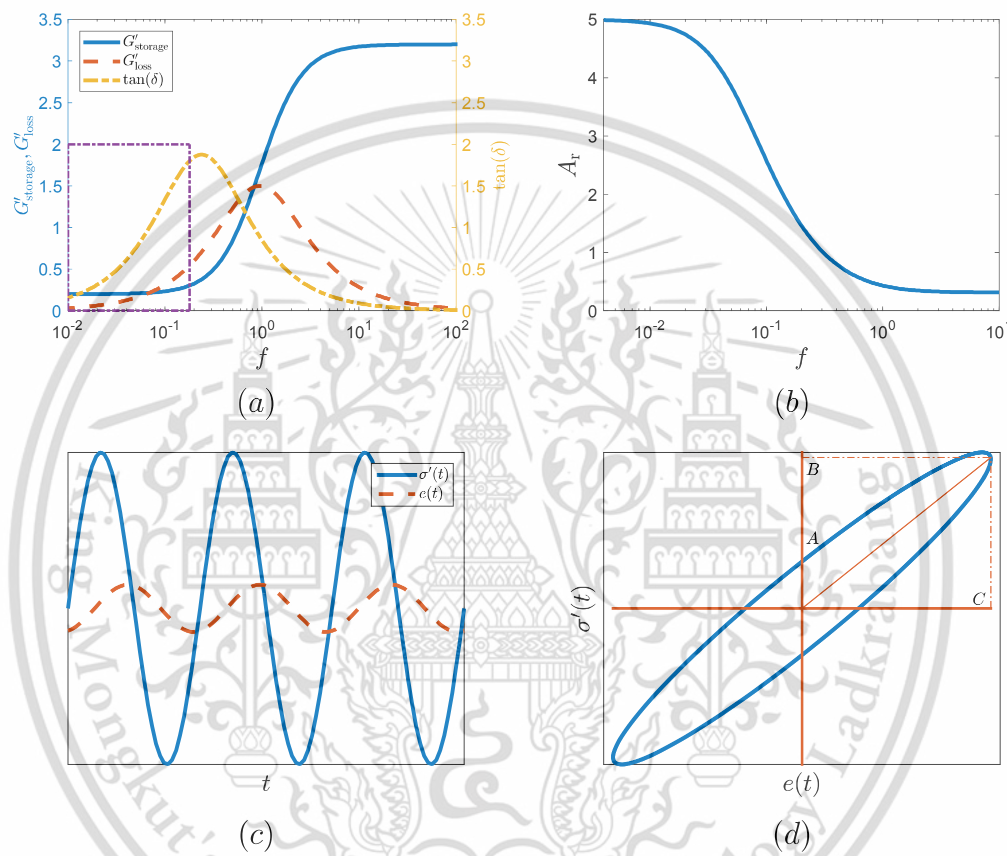

Figure 2.13: Hysteresis behavior regarding SLS model. (a) Complex Moduli G'_{storage} (solid-line), G'_{loss} (dash-line) and tan(δ) (densed dash-line) established by SLS model at condition $\sigma'_A = 0.00075$, $K = 0.3750$ and $\tau = 0.1667$ and f ranges between (0.01,100) (b) Amplitude ratio at f ranges between (0.004,10) (c) System response schematic demonstrates phase lag between $\sigma'(t)$ (solid-line) and $e(t)$ (dash-line) (d) Mechanical-Hysteresis schematic $e(t)$ vs $\sigma'(t)$ plot.

and

$$\frac{\partial \psi}{\partial t} = \nabla^2 \left(\frac{\delta \mathcal{F}}{\delta \psi} \right) + \eta \tag{2.113}$$

where η is a stochastic noise, with zero mean and correlations $< \eta(\mathbf{r}, t)\eta(\mathbf{r}', t') >= -G\nabla^2 \delta(\mathbf{r} - \mathbf{r}')\delta(t - t')$ and $G = 0$ hereafter, q_0 and ϵ are constants. The field ψ represents the local mass density. The specific free energy given in Eq. (2.112) was chosen as it is the simplest form that produces periodic states.

The simplicity is important, as it leads to computationally efficient numerical schemes. Producing periodic structures is crucial, as such states naturally allow for elastic and plastic deformations, multiple orientations, and can accommodate free surfaces, as required for a crystal phase. The dynamical equation of motion, Eq. (2.113), was chosen to conserve the local mass density. In 2D, this free energy is minimized by striped

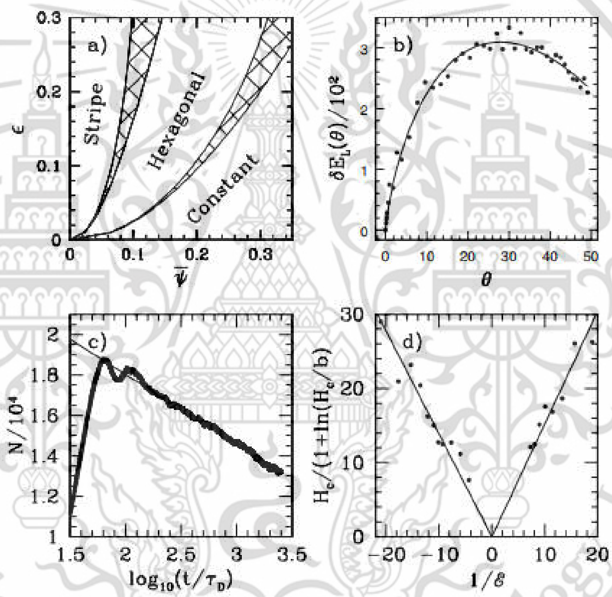

Figure 2.14: (a) Mean field phase diagram (b) Grain boundary energy. The points are from numerical simulations and the line a fit to the Read-Shockley equation. (c) Grain growth. In this figure, the number defects is plotted and the solid line is a guide to the eye. (d) Epitaxial growth. The points are from numerical simulations and the lines are best fits [17].

ψ_s, hexagonal ψ_h, and constant ψ_c states depending on the average value, $\bar{\psi}$, of ψ. To estimate the phase diagram, these states can be approximated by

$$\psi_s = A_s \sin(q_s x) + \bar{\psi}, \quad \psi_h = A_h \left[\cos(q_h x) \cos(\frac{q_h}{\sqrt{3}} y) + \frac{\cos(\frac{2 q_h y}{\sqrt{3}})}{2} \right] + \bar{\psi}, \quad \psi_c = \bar{\psi} \tag{2.114}$$

Substituting these expressions into Eq. (2.14) and minimizing subject to the constraint $\int d\mathbf{r}\psi = \bar{\psi}$ gives the values for the characteristic amplitudes A and wave number q and the phase diagram shown in Fig. 2.14(a). The energy per unit surface length, E_L, between grains that differ in orientation by an angle θ was determined numerically and, in Fig. 2.14(b), compared with the prediction of Read and Shockley [47], i.e., $E_L = E_M\theta[1 - \ln(\theta/\theta_M)]$, where E_M and θ_M are constants. The number of defects is shown in Fig. 2.14(c) as a function of the logarithm of time. Initially $[\log(t/\tau_D) < 1.7]$ the number of defects increases as the total droplet surface area increases. When the droplets impinge, the number of defects begins to decrease as local rearrangements take place. At later times $[\log(t/\tau_D) > 2.0]$, the grain boundaries evolve at a very slow rate. In these simulations, it is found that the number of defects decreases logarithmically at late times. The slow growth is distinctly different from foams and froths, where growth is mainly determined by the motion of triple junctions and curvature relaxation, and cannot be attributed to impurity pinning since these simulations were conducted for a pure material. The numerical results for H_c shown in Fig. 2.14(d) are consistent with the functional relationship proposed by Matthews and Blakeslee [48] where H_c is the critical height.

In 2004, this model, called phase-field crystal (PFC), was extended and discussed the basic properties of the model, and present several applications to technologically important non-equilibrium phenomena [19]. Many basic properties of the model are calculated analytically, and numerical simulations are presented for a number of important applications including, epitaxial growth, material hardness, grain growth, reconstructive phase transitions and crack propagation.

In many physical systems periodic structures emerge. Classic examples include block copolymers [49, 50], Abrikosov vortex lattices in superconductors [51], oil-water systems containing surfactants [52], and magnetic thin films [53, 54]. In addition many convective instabilities [55, 56], such as Rayleigh-Benard convection and a Margonoli instability, lead to periodic structures. To construct a free-energy functional for periodic systems, it is important to make the somewhat trivial observation that unlike uniform systems, these systems are minimized by spatial structures that contain spatial gradients. This simple observation implies that in a lowest-order gradient expansion the coefficient of $|\nabla\phi|^2$ in the free energy below,

$$\mathcal{F} = \int dV \left[f(\phi) + K|\nabla\phi|^2/2 \right], \tag{2.115}$$

is negative. By itself this term would lead to infinite gradients in ϕ so that the next-order term in the gradient expansion must be included, i.e. $|\nabla^2\phi|^2$. In addition to these two terms a bulk free energy with two wells is also needed, so that a generic free-energy functional that gives rise to periodic structures can be written

$$\mathcal{F} = \int dV \left(\frac{K}{\pi^2} \left[-|\nabla\phi|^2 + \frac{a_0^2}{8\pi^2}|\nabla^2\phi|^2 \right] + f(\phi) \right) \tag{2.116}$$

where K and a_0 are phenomenological constants. Insight into the influence of the gradient energy terms can be obtained by considering a solution for ϕ of the form

$\phi = A\sin(2\pi x/a)$. For this particular functional form for f the free energy becomes

$$\frac{\mathcal{F}}{a} = KA^2\left[-\frac{2}{a^2} + \frac{a_0^2}{a^4} + ...\right] + \frac{1}{a}\int dV f(\phi) \tag{2.117}$$

which can be approximated by

$$\frac{\mathcal{F}}{a} \approx -\frac{KA^2}{a_0^2} + \frac{4KA^2}{a_0^4}(\Delta a)^2 + \frac{1}{a}\int dV f(\phi) \tag{2.118}$$

where $\Delta a \equiv a - a_0$. At this level of simplification it can be seen that the free energy per unit length is minimized when $a = a_0$ or a_0 is the equilibrium periodicity of the system. Perhaps more importantly, it highlights the fact that the energy can be written in a Hooke's law form, i.e. $E = E_0 + (k\Delta a)^2$, which is so common in elastic phenomena. Thus, a generic feature of periodic systems is that for small perturbation, e.g., compression or expansion, away from the equilibrium they behave elastically.

In a liquid-solid transition the obvious field of interest is the density field since it is significantly different in the liquid and solid phases. More precisely the density is relatively homogeneous in the liquid phase and spatially periodic (i.e., crystalline) in the solid phase. The free-energy functional can then be approximated as

$$\mathcal{F} = \int d\mathbf{r}[H(\phi)] = \int d\mathbf{r}\left[f(\phi) + \frac{\phi}{2}G(\nabla^2)\phi\right] \tag{2.119}$$

where f and G are to be determined and f is the deviation of density from the average density. Under constant-volume conditions f is a conserved field, so that the dynamics is given by

$$\frac{\partial\phi}{\partial t} = \Gamma\nabla^2\frac{\delta F}{\delta\phi} + \eta \tag{2.120}$$

where η is a Gaussian random variable with zero mean and two-point correlation

$$< \eta(\mathbf{r},t)\eta(\mathbf{r}',t') >= \Gamma k_b\nabla^2\delta(\mathbf{r}-\mathbf{r}')\delta(t-t') \tag{2.121}$$

To determine the precise functional form of the operator $G(\nabla^2)$ it is useful to consider a simple liquid since ϕ is small and f can be expanded to lowest order in ϕ i.e.

$$f_{liq} = f^{(0)} + f^{(1)}\phi + \frac{f^{(2)}}{2!}\phi^2 + ..., \tag{2.122}$$

where $f^{(i)} \equiv (\partial^i f/\partial\phi^i)$. In this limit Eq. (2.120) takes the form

$$\frac{\partial\phi}{\partial t} = \Gamma\nabla^2\left[f^{(2)} + G(\nabla^2)\right]\phi + \eta \tag{2.123}$$

which can be easily solved to give

$$\hat{\phi}(\mathbf{q},t) = e^{-q^2\hat{\omega}_q\Gamma t}\hat{\phi}(\mathbf{q},0) + e^{-q^2\hat{\omega}_q\Gamma t}\int_0^t e^{q^2\hat{\omega}_q\Gamma t}\eta(\mathbf{q},t') \tag{2.124}$$

where **q** is the wave vector, $\hat{\omega}_q \equiv f^{(2)} + G(q^2)$, $\hat{\phi}$ is the Fourier transform of ϕ, i.e.,

$$S(q,t) = e^{-2q^2\hat{\omega}_q\Gamma t}S(q,0) + \frac{k_bT}{\hat{\omega}_q}(1 - e^{-q^2\hat{\omega}_q\Gamma t}) \tag{2.125}$$

In a liquid system the density is stable with respect to fluctuations which implies that $\hat{\omega}_q > 0$. The equilibrium liquid state structure factor $S^{eq}_{liq}(q) = S(q,\infty)$ then becomes

$$S^{eq}_{liq}(q) = \frac{k_BT}{\hat{\omega}_q} \tag{2.126}$$

This simple calculation indicates that the method can model a liquid state if the function $\hat{\omega}_q$ is replaced with $k_BT/S^{eq}_{liq}(q)$ or

$$G(q) = \frac{k_BT}{S^{eq}_{liq}} - f^{(2)} \tag{2.127}$$

A typical liquid-state structure factor and the corresponding $\hat{\omega}_q$ are shown in Fig. 2.15. Thus $G(\nabla^2)$ can be obtained for any pure material through Eq. (2.127).

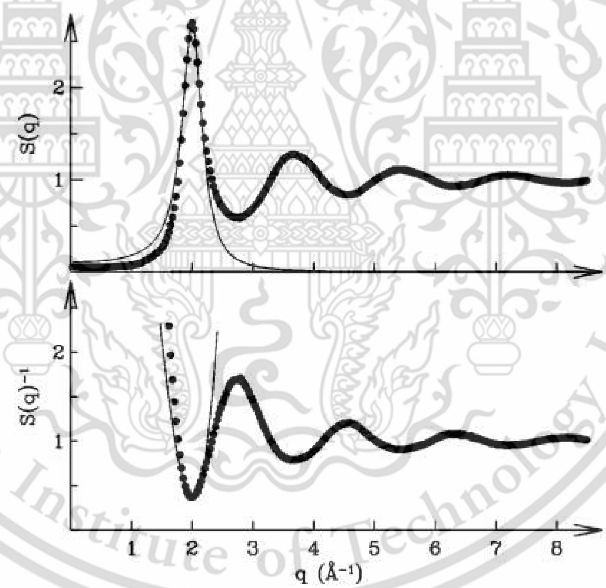

Figure 2.15: The points correspond to an experimental liquid structure factor for Ar^{36} at 85 K taken from [18]. The line corresponds to a best fit to Eq. (2.128) [19].

It was also argued that the basic physical features of elasticity are naturally incorporated by any free energy that is minimized by a spatially periodic function. The simplest possible free energy that produces periodic structures can be constructed by fitting the following functional form for G:

$$G(\nabla^2) = \lambda\left(q_0^2 + \nabla^2\right)^2, \tag{2.128}$$

to the first-order peak in an experimental structure factor. As an example such a fit is shown for argon in Fig. 2.15. At this level of simplification the minimal free-energy functional is given by

$$\mathcal{F} = \int d\mathbf{r} \left(\frac{\phi}{2} \left[a\Delta T + \lambda \left(q_0^2 + \nabla^2 \right)^2 \right] \phi + u \frac{\phi^4}{4} \right), \tag{2.129}$$

In principle other nonlinear terms, such as ϕ^3, can be included in the expansion but retaining only ϕ^4 simplifies calculations. The dynamics of ϕ is then described by the equation

$$\frac{\partial \phi}{\partial t} = \Gamma \nabla^2 \mu + \eta = \Gamma \nabla^2 \frac{\delta \mathcal{F}}{\delta \phi} \eta, \tag{2.130}$$

For convenience it is useful to rewrite the free energy in dimensionless units, i.e.

$$\mathbf{x} = \mathbf{r} q_0, \quad \psi = \phi \sqrt{\frac{u}{\lambda q_0^4}}, \quad r = \frac{a\Delta T}{\lambda q_0^4}, \quad \tau = \Gamma \lambda q_0^6 t \tag{2.131}$$

In dimensionless units the free energy becomes

$$F \equiv \frac{\mathcal{F}}{\mathcal{F}_0} = \int \left[\frac{\psi}{2} \omega(\nabla^2) \psi + \frac{\psi^4}{4} \right] \tag{2.132}$$

where $\mathcal{F}_0 \equiv \lambda^2 q_0^{8-d}$ and

$$\omega(\nabla^2) = r + \left(1 + \nabla^2\right)^2 \tag{2.133}$$

The dimensionless equation of motion becomes

$$\frac{\partial \psi}{\partial t} = \nabla^2 \left(\omega(\nabla^2) + \psi^3 \right) + \zeta \tag{2.134}$$

where $< \zeta(\mathbf{r}_1, \tau_1) \zeta(\mathbf{r}_2, \tau_2) >= \mathcal{D} \nabla^2 \delta(\mathbf{r}_1 - \mathbf{r}_2) \delta(\tau_1 - \tau_2)$ and $\mathcal{D} = u k_B T q_0^{d-4} / \lambda^2$. Equations (2.132), (2.133), and (2.134) describe a material with specific elastic properties.

In one dimension the free energy described by Eq. (2.132) is minimized by a periodic function when the average value of $\psi(\bar{\psi})$ is small and a constant when $\bar{\psi}$ is large. To determine the properties of the periodic state it is useful to make a one-mode approximation

$$\psi \approx A \sin(qx) + \bar{\psi} \tag{2.135}$$

which is valid in the small r limit. Substitution of this function into Eq. (2.132) gives

$$\begin{aligned} \frac{F^p}{L} &= \frac{q}{2\pi} \int_0^{2\pi/q} dx \left[\frac{\psi}{2} \omega(\partial_x^2) \psi + \frac{\psi^4}{4} \right] \\ &= \frac{\bar{\psi}^2}{2} \left[\hat{\omega}_0 + \frac{3A^2}{2} + \frac{\bar{\psi}^2}{2} \right] + \frac{A^2}{4} \left[\hat{\omega}_q + \frac{3A^2}{8} \right] \end{aligned} \tag{2.136}$$

where $\hat{\omega}_1$ is the Fourier transform of $\omega(\nabla^2)$, $\hat{\omega}_q = r + (1-q^2)^2$. Minimizing Eq. (2.136) with respect to q gives the selected wave vector $q^* = 1$. Minimizing $\mathcal{F}$ with respect to A gives $A^2 = -4\left(\hat{\omega}_{q^*}/3 + \bar{\psi}^2\right)$. The minimum free energy is then

$$\frac{F^p}{L} = -\frac{r^2}{6} + \frac{\bar{\psi}^2(1-r)}{2} - \frac{5\bar{\psi}^4}{4} \tag{2.137}$$

Equation (2.137) represents the free-energy density of a periodic solution in the one-mode approximation. To determine the phase diagram this energy must be compared to that for a constant state, i.e., the state for which $\psi^c = \bar{\psi}$, which is

$$\frac{F^c}{L} = \hat{\omega}_0\frac{\bar{\psi}^2}{2} + \frac{\bar{\psi}^4}{4} \tag{2.138}$$

In two dimension case, F is minimized by three distinct solutions for ψ. These solutions are periodic in either zero dimensions (i.e. a constant), one dimension (i.e., stripes), or two dimensions (i.e., triangular distributions of drops or "particles"). The free-energy density for the constant and stripe solutions are identical to the periodic and constant solution discussed in the preceding section. The two-dimensional solution can be written in the general form

$$\psi(\mathbf{r}) = \sum_{n,m} a_{nm} e^{i\mathbf{G}\cdot\mathbf{r}} + \bar{\psi} \tag{2.139}$$

where $\mathbf{G} \equiv n\mathbf{b}_1 + m\mathbf{b}_2$ and the vectors $\mathbf{b}_1$ and $\mathbf{b}_2$ are reciprocal lattice vectors. For a triangular lattice the reciprocal lattice vectors can be written

$$\begin{aligned} \mathbf{b}_1 &= \frac{2\pi}{a\sqrt{3}/2}\left(\frac{\sqrt{3}}{2}\hat{x} + \frac{1}{2}\hat{y}\right) \\ \mathbf{b}_2 &= \frac{2\pi}{a\sqrt{3}/2}\hat{y} \end{aligned} \tag{2.140}$$

where a is the distance between nearest-neighbor local maxima of ψ. In analogy with the one-dimensional calculations presented a one-mode approximation will be made to evaluate the phase diagram and elastic constants. In a two-dimensional triangular system a one-mode approximation corresponds to retaining all Fourier components that have the same length. More precisely the lowest-order harmonics consists of all (n,m) pairs such that the vector $\mathbf{G}$ has length $2\pi/(a\sqrt{3}/2)$. This set of vectors includes (n,m) = $(\pm1,0)$, $(0,\pm1)$, $(1,-1)$ and $(-1,1)$. It is easy to show that in the lowest-order harmonic expansion c can be represented by

$$\psi_t = A_t\left[\cos(q_t x)\cos(\frac{q_t y}{\sqrt{3}}) - \frac{1}{2}\cos(\frac{2q_t y}{\sqrt{3}})\right] + \bar{\psi} \tag{2.141}$$

where A_t is an unknown constant and $q_t = 2\pi/a$. Substituting Eq. (2.141) into Eq.

(2.129) and minimizing with respect to A_t and q_t gives

$$\begin{aligned}\frac{F^t}{S} &= \int_0^{\frac{a}{2}} \frac{dx}{a/2} \int_0^{\frac{\sqrt{3}}{2}a} \frac{dy}{a\sqrt{3}/2} \left[\frac{\psi}{2}\omega(\nabla^2)\psi + \frac{\psi^4}{4}\right] \\ &= -\frac{1}{10}\left(r^2 + \frac{13}{50}\bar{\psi}^4\right) + \frac{\bar{\psi}^2}{2}\left(1 + \frac{7}{25}r\right) \\ &+ \frac{4\bar{\psi}}{25}\sqrt{-15r - 36\bar{\psi}^2}\left(\frac{4\bar{\psi}^2}{5} + \frac{r}{3}\right)\end{aligned} \tag{2.142}$$

$$A_t = \frac{4}{5}\left(\bar{\psi} + \frac{1}{3}\sqrt{-15r - 36\bar{\psi}^2}\right) \tag{2.143}$$

where $q_t = \sqrt{3}/2$, and S is a unit area. The phase diagram of one-dimensional and two-dimensional case are given in Fig. 2.16.

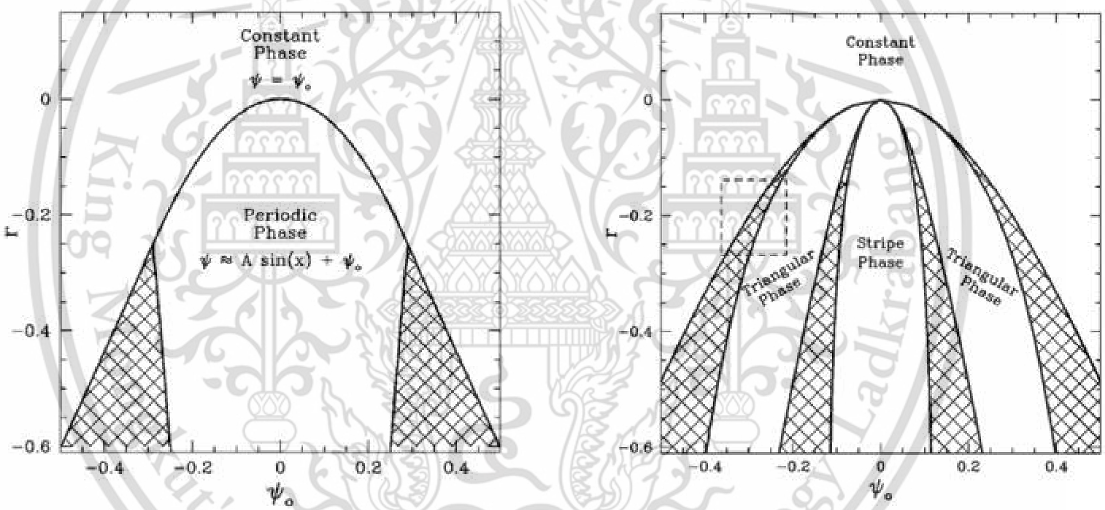

Figure 2.16: One-dimensional and Two-dimensional phase diagram in the one-mode approximation. The solid line is the boundary separating constant between liquid and solid phase. The hatched region is liquid-crystal coexistence. (a) One-dimensional phase diagram (b) Two-dimensional phase diagram. To obtain the equilibrium states the Maxwell equal-area construction rule must be satisfied, $\int_{\bar{\psi}_1}^{\bar{\psi}_1} d\psi \left[\mu(\bar{\psi}) - \mu_{eq}\right] = 0$ [19].

For elastic constant calculation, it is also relatively easy to calculate the elastic energy in the one-mode approximation. If $a \equiv 2\pi/q$ is defined as the one-dimensional lattice parameter, then the $\mathcal{F}$ can be written

$$\frac{F^p}{L} = \frac{F^p_{min}}{L} + K\frac{u^2}{2} + \mathcal{O}(u^3) + ... \tag{2.144}$$

where $u \equiv (a - a_0)/a_0$ is the strain and K is the bulk modulus and is equal to

$$K = -\left(\bar{\psi}^2 + \frac{\hat{\omega}_{q^*}}{3}\right) \frac{d^2\hat{\omega}_q}{dq^2}\bigg|_{q=q^*} \tag{2.145}$$

or for the particular dispersion relationship used here, $K = -8(r + 3\bar{\psi}^2)/3$. The elastic properties of the two-dimensional triangular state can be obtained by considering the energy costs for deforming the equilibrium state. The free-energy density associated with bulk, shear, and deviatoric deformations can be calculated by considering modified forms of Eq. 2.141.

$$\psi_t\left(\frac{x}{1+\xi}, \frac{y}{1+\xi}\right)_{\text{bulk}}, \quad \psi_t\left(x + \xi y, y\right)_{\text{shear}}, \quad \psi_t\left(x(1+\xi), y(1-\xi)\right)_{\text{deviatoric}} \tag{2.146}$$

In such calculations ξ represents the dimensionless deformation, $q_t = \sqrt{3}/2$ and A_t is obtained by minimizing F. The results of these calculations are

$$\begin{aligned} \frac{F_{bulk}}{A} &= F^t_{min} + \alpha\xi^2 + ... \\ \frac{F_{shear}}{A} &= F^t_{min} + \frac{\alpha}{8}\xi^2 + ... \\ \frac{F_{deviatoric}}{A} &= F^t_{min} + \frac{\alpha}{2}\xi^2 + ... \end{aligned} \tag{2.147}$$

where $\alpha = (q_t A_t)^2/3$. These results can be used to determine the elastic constants by noting that, for a two-dimensional system [57, 58],

$$\begin{aligned} \frac{F_{bulk}}{A} &= F^t_{min} + [C_{11} + C_{12}]\,\xi^2 + ... \\ \frac{F_{shear}}{A} &= F^t_{min} + \frac{C_{44}}{2}\xi^2 + ... \\ \frac{F_{deviatoric}}{A} &= F^t_{min} + [C_{11} - C_{12}]\,\xi^2 + ... \end{aligned} \tag{2.148}$$

The elastic constants are then

$$\frac{C_{11}}{3} = C_{12} = C_{44} = \frac{\alpha}{4} \tag{2.149}$$

These results are consistent with the symmetries of a two-dimensional triangular system i.e., $C_{11} = C_{12} + 2C_{44}$. In two dimensions this implies a bulk modulus of $B = \alpha/2$, a shear modules of $\mu = \alpha/4$, a Poisson's ratio of $\sigma = 1/3$, and a two-dimensional, i.e. $Y_2 = 4B\mu/(B + \mu)$, Young's modulus of $Y_2 = 2\alpha/3$. The results, shown in Fig. 2.17, indicate that the approximation is quite good in the small r limit. These calculations highlight the strengths and limitations of the simplistic model described by Eq. (2.129). On the positive side the model contains all the expected elastic properties (with the correct symmetries) and the elastic constants can be approximated analytically within a one mode analysis. On the negative side, the model as written can only describe

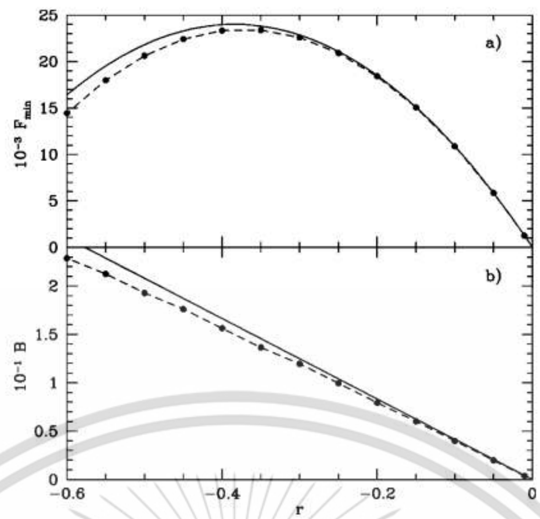

Figure 2.17: In (a) the minimum of the free energy is plotted as a function of r for $\bar{\psi} = \sqrt{-r}/2$. The solid line is Eq. 2.142 and the points are from numerical simulations. In (b) the bulk modulus is plotted as a function of r for $\bar{\psi} = \sqrt{-r}/2$. The solid line is an analytic calculation $[(q_t A_t)^2/6]$ and the points are from numerical simulations [19].

a system where $C_{11} = 3C_{12}$. Thus parameters in the free energy can be chosen to produce any C_{11}, but C_{12} cannot be varied independently.

The free-energy density of a boundary between two grains that differ in orientation is largely controlled by geometry. In a finite-size two-dimensional system the parameters that control this energy are the orientational mismatch θ and an offset distance Δ or alternatively a disclination angle, as shown in Fig. 2.18.

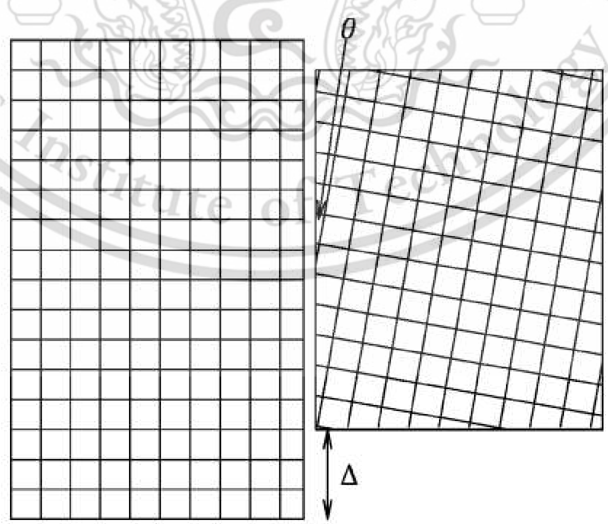

Figure 2.18: Schematic of a grain boundary [19].

For small θ, θ controls the number of dislocations per unit length and Δ controls the average core energy. For an infinite grain boundary Δ becomes irrelevant, unless the distance between dislocation is an integer number of lattice constants (and the integer is relatively small). Nevertheless, it is straightforward to determine a lower bound on the grain boundary energy in the small-θ limit, by directly relating the dislocation density to θ and assuming that the dislocation cores can always find the minimum-energy location. The latter assumption restricts the calculation to providing a lower bound on the grain boundary energy.Read and Shockley [47] were able to derive an expression for the grain boundary energy, assuming the dislocation core energy was a constant independent of geometry. In two dimensions the energy/length of the grain boundary is [57]

$$\frac{F}{L} = E_{core} + \frac{b^2 Y_2}{8\pi d}\left[1 - \ln\left(\frac{2\pi a}{d}\right)\right] \tag{2.150}$$

where b is the magnitude of the Burger's vector, a is the size of the dislocation core, d is the distance between dislocations, Y_2 is the two-dimensional Young's modulus, and E_{core} is the energy/length of the dislocation core. The core energy is proportional to the size of the core [57] i.e. $E_{core} = Ba^2$, where B is unknown constant. The total energy/length then becomes

$$\frac{F}{L} = Ba^2 + \frac{b^2 Y_2}{8\pi d}\left[1 - \ln\left(\frac{2\pi a}{d}\right)\right] \tag{2.151}$$

To minimize F/L, B is chosen to satisfy $d(F/L)da = 0$ which gives $Ba^2 = b^2 Y_2/16\pi d$. Furthermore, from purely geometrical considerations, the distance between dislocations is $d = a/\tan(\theta)$, where $theta$ is the orientational mismatch. Finally in the small-angle limit, $\tan(\delta) \approx \theta$. Equation (2.151) reduces to

$$\frac{F}{L} = \frac{bY_2}{8\pi}\theta\left(\frac{3}{2} - \ln(2\pi\theta)\right) \tag{2.152}$$

where the dislocation core size b was assumed to be equal to the lattice constant a. Small portions of sample configurations are shown in Fig. 2.19 for $\theta = 5.8^o$ and $\theta = 34.2^o$ (the grain boundary energy is symmetric around 30^o). As expected the Read-Shockley description of a grain boundary is consistent with the small-angle configuration. In contrast the large-angle grain boundary is much more complicated and harder to identify individual dislocations. The measured grain boundary energy is compared with Eq. (2.152) in Fig. 2.20. As expected Eq. (2.152) provides an adequate description for small angles but not for large angles The Read-Shockley equation does fit the measured result for all θ reasonably well if the coefficients that enter the equation are adjusted, as has been observed in experiment [20, 21]. This fit is shown in Fig. 2.21.

As the polycrystalline sample is pulled the total free energy was monitored and used to calculate the stress, σ, i.e. $\sigma \equiv dF/d\xi$, where ξ is the relative change in the width of the crystal. Stress-strain curves are shown in Fig. 2.22 as a function of grain size and strain rate. In all cases the stress is initially a linear of function of strain until

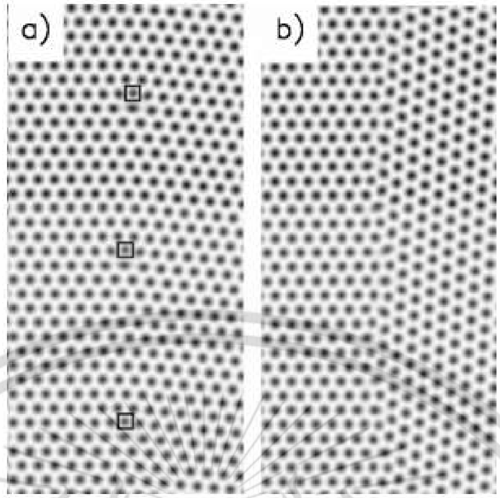

Figure 2.19: The grey scale corresponds to the magnitude of the field ψ for a grain boundary mismatch of $\theta = 5.8^o$ and $\theta = 34.2^o$ in (a) and (b), respectively. In (a) squares have been placed at defect sites [19].

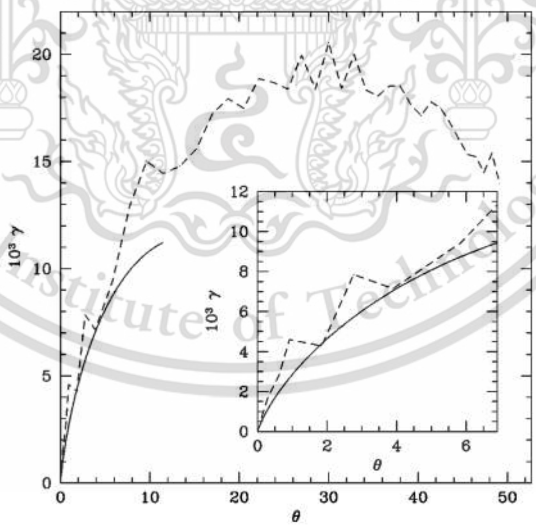

Figure 2.20: The grain boundary energy is plotted as a function of mismatch orientation. The points correspond to numerical simulations of the PFC model and the solid line corresponds to Eq. (2.152) [19].

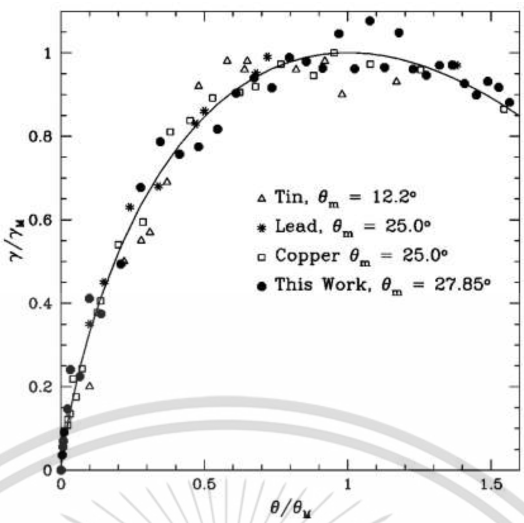

Figure 2.21: The grain boundary energy of the PFC model is compared with experiments on tin [20], lead [20], and copper [21]. This figure is from [19].

plastic deformation occurs and the slope of the stress-strain curve decreases. In Fig. 2.22(a) the influence of strain rate is examined for the initial configuration. It is clear from this figure that the strain rate plays a strong role in determining the maximum stress that a sample can reach, or the yield stress, as has been observed in experiments [59]. The yield strength increases as the strain rate increases as would be expected.

The influence of grain size on the stress-strain relationship is shown in Fig. 2.22(b) for four grain sizes. The initial slope of the stress-strain curve, which will be denoted Y_0 in what follows, increases with increasing grain size as does the maximum stress, or yield stress, sustained by the sample. The yield strength and elastic moduli, Y_0, are plotted as a function of inverse grain size in Fig. (a) and (b), respectively, for several strain rates. The constant of proportionality decreases with decreasing strain rate. Thus the PFC approach is able to reproduce the inverse Hall-Petch effect or the softening of nanocrystalline materials.

It would be interesting to observe the crossover to the normal Hall-Petch effect where the yield stress decreases with increasing grain size. However, it is important to note that the initial conditions in these simulations was set up to explicitly remove the Hall-Petch mechanism; i.e., each nanocrystal was defect free. In addition thermal fluctuations were not included in the simulations. Nevertheless it is unclear whether or not a crossover may occur, due to the fact that low-angle grain boundaries may act as sources of movable dislocations. Further study of this interesting phenomenon for larger grain sizes would be of great interest.

The PFC model was also used to examine the heterogeneous nucleation of a polycrystalline sample from a supercooled liquid state. A simulation containing 50 initial seeds (or nucleation sites) was conducted.

The results of the simulations are shown in Fig. 2.24. Comparison of Figs. 2.24(b) and 2.24(c) shows that there is a wide distribution of grain boundaries each with a

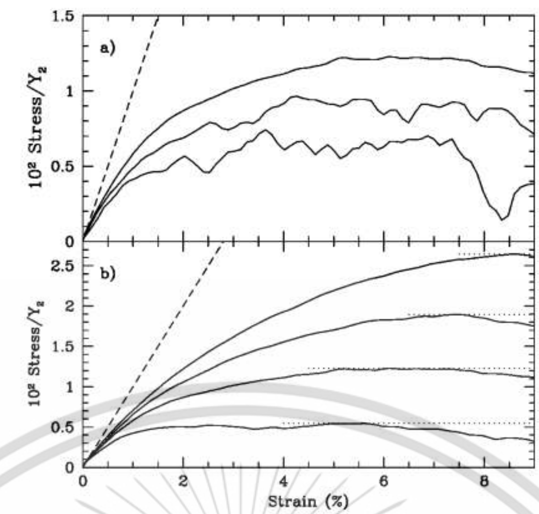

Figure 2.22: In (a) the stress is plotted as a function of strain for a system with an average grain radius of 35 particles. The solid lines from top to bottom in (a) correspond to strain rates of 24×10^{-6}, 12×10^{-6}, and 6×10^{-6}, respectively. In (b) the solid lines from top to bottom correspond to systems with average grain sizes of 70, 50, 35, and 18 particles, respectively. In both (a) and (b) the dashed line corresponds to a unit slope [19].

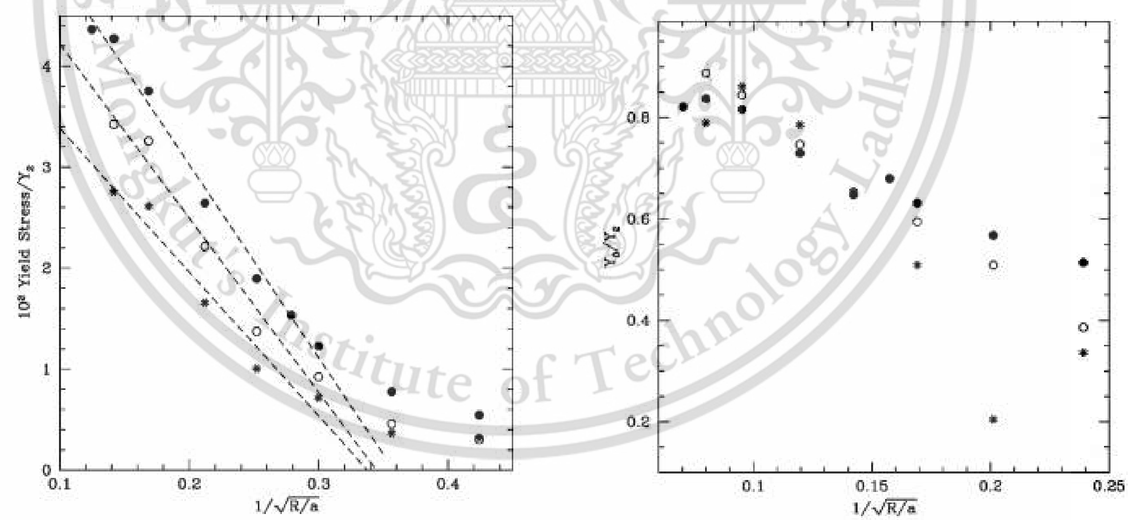

(a) (b)

Figure 2.23: (a) The yield stress is plotted as a function of average grain radius. The solid, open, and starred points correspond to strain rates of 24×10^{-6}, 12×10^{-6}, and 6×10^{-6}, respectively. The dashed lines are guides to the eye; (b) The elastic moduli Y_0 (see text) are plotted as a function grain radius. The solid, open, and starred points correspond to strain rates of 24×10^{-6}, 12×10^{-6}, and 6×10^{-6}, respectively [19].

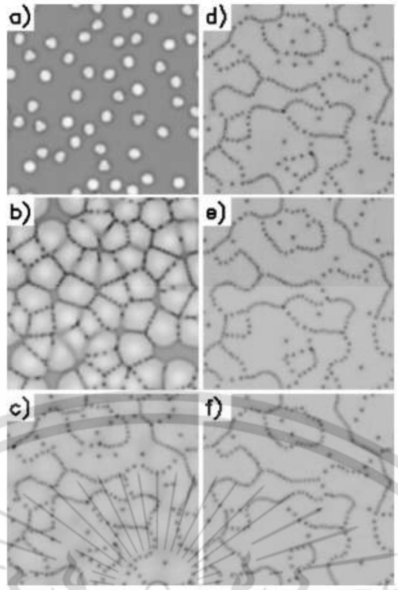

Figure 2.24: Heterogeneous nucleation and grain growth. In this figure the grey scale corresponds to the smoothed local free energy. (a), (b), (c), (d), (e), and (f) correspond to times 50, 200, $1,000$, $3,000$, $15,000$, and $50,000$, respectively [19].

different density of dislocations (which appear as black dots in the figure). Comparison of Fig. 2.24(c) with later configurations indicates that the low-angle grain boundaries disappear much more rapidly than the large-angle ones. The simple reason is that it is easy for one or two dislocations to glide in such a manner as to reduce the overall energy (this is usually accompanied with some grain rotation).

The PFC model can be used to study the propagation of a crack in ductile (but not brittle) material. To illustrate this phenomena a numerical simulation was conducted on a periodic system of size s4096Dx,1024Dxd for the parameters $(r, \bar{\psi}, \Delta x, \Delta t) = (-1.0, 0.49, p/3, 0.05)$. A notch of size $20\Delta x \times 10\Delta x$ was cut out of the center of the simulation cell and replaced with a coexisting liquid ($\psi = 0.79$). The notch provides a nucleating cite for a crack to start propagating. A sample simulation is shown in Fig. 2.25.

Phase diagram of three-dimensional crystal structure with a continuum phase-field was first introduced by Wu et al. [22]. Since the crystal density field of the PFC model is dominated by the principal reciprocal lattice vectors, they expected this model to yield similar predictions of BCC-liquid interfacial properties as Ginsburg-Landau theory. To establish BCC-liquid phase diagram, the simplest PFC model was defined by the free energy functional

$$F = \int d\mathbf{r} \left\{ \frac{\phi}{2} \left[a + \lambda \left(q_0^2 + \nabla^2 \right)^2 \right] \phi + g \frac{\phi^4}{4} \right\} \qquad (2.153)$$

which is a transposition to crystalline solids of the Swift-Hohenberg model of pattern formation [55]. The conserved order parameter ϕ is a dimensionless measure of the

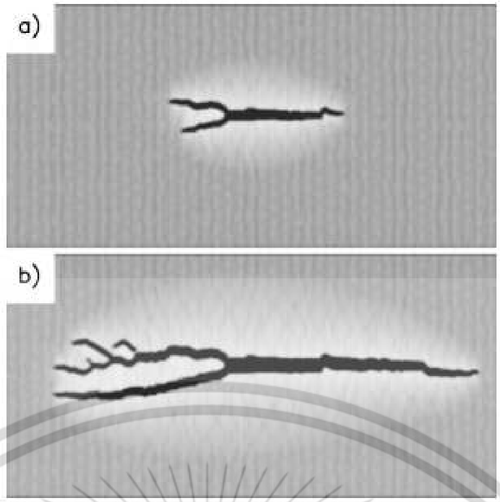

Figure 2.25: A portion of a simulation is shown where the grey scale corresponds to the local energy density. The size of both figures is $2048\Delta x \times 1024\Delta x$, where $\Delta x = \pi/3$. (a) and (b) are at times t= $25,000$ and $65,000$ after the rip was initiated, respectively [19].

crystal density field measured from some constant reference value. The wave number q_0 sets the magnitude K_i of the principal reciprocal lattice vectors that correspond to the first peak of the liquid structure factor $S(K)$ at melting, and hence sets the scale of the ordered crystalline pattern $\sim q_0^{-1}$. The parameters a and λ determine the shape of the polynomial approximation of the liquid structure factor $S(K)$ in the PFC model.

To render the calculations less cumbersome, it is useful to rewrite the free-energy functional in dimensionless form by defining the parameter

$$-\frac{a}{\lambda q_0^4} = \epsilon, \quad q_0\mathsf{r} = \tilde{\mathsf{r}}, \quad \sqrt{\frac{g}{\lambda q_0^4}}\phi = \psi, \quad \frac{g}{\lambda^2 q_0^5}F = \mathcal{F} \tag{2.154}$$

where all the transformed quantities to the right of the arrows are dimensionless and

$$\mathcal{F} = \int d\tilde{\mathsf{r}} \left\{ \frac{\psi}{2}\left[-\epsilon + \left(\nabla^2 + 1\right)^2\right]\psi + \frac{1}{4}\psi^4 \right\} \tag{2.155}$$

The condition that the chemical potential must be spatially uniform in equilibrium yields the equation

$$\mu_E = \frac{\delta \mathcal{F}}{\delta \psi} = -\epsilon\psi + \left(\nabla^2 + 1\right)^2\psi + \psi^3 \tag{2.156}$$

which is the starting point of the present study. To establish phase diagram, the free energy density, free-energy per unit volume, as a function of the mean density $\bar{\psi}$ in solid, denoted by $f_s(\bar{\psi})$, and liquid $f_l(\bar{\psi})$ using Eq. (2.155). Then, the standard common tangent construction was used. This method was equivalent to equating the chemical potentials and grand potentials of the two phases. Since the density is constant in the liquid, f_l is obtained directly from Eq. (2.155)

$$f_l = -(\epsilon - 1)\frac{\bar{\psi}^2}{2} + \frac{\bar{\psi}^4}{4} \tag{2.157}$$

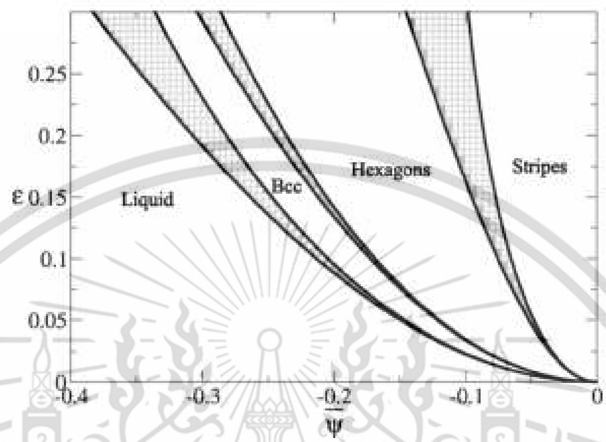

Figure 2.26: Phase diagram of the PFC model obtained under the approximation that the crystal density field is as a sum of density waves corresponding to the set of principal reciprocal lattice vectors for a given crystal structure [22].

To derive free energy density of solid phase, f_s, the density field was constructed by using density expansion form below

$$\psi(\tilde{\mathbf{r}}) \approx \bar{\psi} + \sum_i A_i e^{i\mathbf{K}_i\cdot\tilde{\mathbf{r}}} \tag{2.158}$$

where $\mathbf{K}_i$ is reciprocal lattice vectors which can be written as $\mathbf{K}_i = m\mathbf{b}_1 + n\mathbf{b}_2 + k\mathbf{b}_3$. It should be noted that $\mathbf{b}_i$ and (m, n, k) are the principal reciprocal lattice vectors describing a specific crystalline symmetry and set of integer, respectively. For a BCC crystal, $\mathbf{K}_i$ can be written in terms of the following set of principal reciprocal lattice vectors

$$\mathbf{b}_1 = \frac{2\pi}{a}\left(\frac{\hat{x}+\hat{y}}{\sqrt{2}}\right), \quad \mathbf{b}_2 = \frac{2\pi}{a}\left(\frac{\hat{x}+\hat{z}}{\sqrt{2}}\right), \quad \mathbf{b}_3 = \frac{2\pi}{a}\left(\frac{\hat{y}+\hat{z}}{\sqrt{2}}\right) \tag{2.159}$$

where a is the lattice constant. The values of (m, n, k) which correspond to a one-mode approximation are $(1, 0, 0)$, $(0, 1, 0)$, $(0, 0, 1)$, $(1, -1, 0)$, (0,1,-1) and $(-1, 0, 1)$. Then, the crystal density field can be written as

$$\psi(\mathbf{r}) \approx \bar{\psi} + 4A_s\left(\cos(qx)\cos(qy) + \cos(qx)\cos(qz) + \cos(qy)\cos(qz)\right) \tag{2.160}$$

where we have used the fact that all density waves have the same amplitude ($|A_i| = A_s$) and all principal reciprocal lattice vectors of the BCC structure have the same magnitude ($|\mathbf{K}_{110}| = |\mathbf{K}_{1-10}| = ... = \sqrt{2}q$). The parameters As and q are solved by substituting Eq. (2.160) into Eq. (2.155) and minimizing the resulting free-energy with respect to A_s and q, which yields

$$A_s = -\frac{2}{15} + \frac{1}{15}\sqrt{5\epsilon - 11\bar{\psi}^2} \tag{2.161}$$

and $q = 1/\sqrt{2}$, together with the expression for the solid free energy density

$$f_s = -(\epsilon - 1)\frac{\bar{\psi}^2}{2} + \frac{\bar{\psi}^4}{4} - 6\epsilon A_s^2 + 18\bar{\psi}_s^2 + 48\bar{\psi}A_s^3 + 135A_s^4 \tag{2.162}$$

Applying the common tangent construction, which is detailed below in the small ϵ limit, yields the BCC-liquid coexistence region in the phase diagram of Fig. 2.26.

In 2007, K.R. Elder and N. Provatas [17] linked PFC free energy to classical density functional theory of freezing proposed by Ramakrishnan and Yussouff [60]. Their free energy functional are given as

$$\frac{F}{k_BT} = \int d\vec{r}\left[\rho ln\left(\frac{\rho}{\rho_l}\right) - \delta\rho\right] - \frac{1}{2}\int d\vec{r}d\vec{r}\delta\rho C(\vec{r},\vec{r})\delta\rho' \tag{2.163}$$

By using taylor expansion, equation (2.163) can be simplified as

$$\frac{\Delta F}{k_BT} = \int d\vec{r}\left(n\frac{1-\bar{\rho}C}{2}n - \frac{n^3}{6} + \frac{n^4}{12} - ...\right) \tag{2.164}$$

where $\Delta F \equiv F - F_0$, F_0 represents free energy functional at constant density (i.e., $\rho = \bar{\rho}$) and $n \equiv \frac{\rho-\bar{\rho}}{\bar{\rho}}$ represent normalized density function and in real space

$$C = (C_0 - C_2\nabla^2 + C_4\nabla^4 - ...)\delta(\vec{r} - \vec{r}') \tag{2.165}$$

We can also develop free energy functional for binary alloys system by extending equation (2.163) to two component system and using taylor expansion. Finally, we obtain free energy functional as

$$\frac{F}{k_BT} = \int d\vec{r}\left(\frac{n}{2}\left[B_l + B_s(2R^2\Delta^2 + R^4\Delta^4)\right]n + \frac{t}{3}n^3 - \frac{v}{4}n^4 + \gamma\delta N + \frac{w}{2}\delta N^2 + ...\right) \tag{2.166}$$

where

$$n_A = \frac{\rho_A - \bar{\rho}_A}{\bar{\rho}} \tag{2.167}$$

$$n_B = \frac{\rho_B - \bar{\rho}_B}{\bar{\rho}} \tag{2.168}$$

$$n = n_A + n_B \tag{2.169}$$

$$\delta N = (n_A - n_B) + \frac{\rho_B - \rho_A}{\bar{\rho}} \tag{2.170}$$

with equation (2.166) and proper dynamic equations as below

$$\frac{\partial n}{\partial t} = M_e \nabla^2 \frac{\delta F}{\delta n} \tag{2.171}$$

$$\frac{\partial(\delta N)}{\partial t} = M_e \nabla^2 \frac{\delta F}{\delta(\delta N)} \tag{2.172}$$

Binary alloys simulation can be thoroughly investigated.

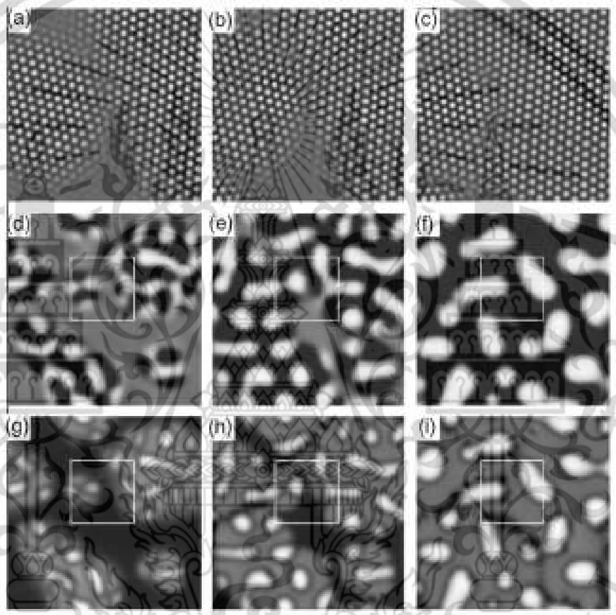

Figure 2.27: Binary alloys simulation Density (n) are illustrated in (a,b,c), concentration (δN) are illustrated in (d,e,f) and local energy density are illustrated in (g,h,i) [17].

In 2009, a new numerical technique for PFC deformation simulation that could maintain a constant volume during plastic deformation was introduced by Hirouchi et al. [23]. Unlike the previous work using the PFC method, the tensile deformation simulations had been performed under conditions where the volume increases during plastic deformation [19]. The volume of a polycrystalline structure increases during plastic deformation simulation because of the difficulty in setting the boundary conditions appropriately. Therefore, it is of great importance to develop an appropriate numerical scheme for PFC deformation simulation.

Figure 2.28 provides a schematic illustration of the proposed technique for deformation simulation in one-dimension. To simulate tensile deformation, the sizes of finite difference grids are increased by the displacement increment $d = \dot{\varepsilon}\Delta x \Delta t$ at every dimensionless time step Δt. Here, Δx is the initial grid size and $\dot{\varepsilon}$ is the di-

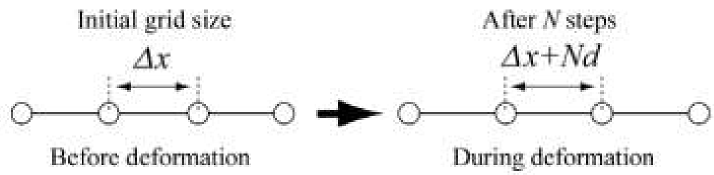

Figure 2.28: Numerical technique of tensile deformation in one-dimensional problem [23].

mensionless strain rate. Therefore, since a constant strain rate is applied to all atoms, the deformation state becomes the affine deformation state, and periodic boundary conditions can be used as boundary conditions.

Figure 2.29 shows the computational model of the one-dimensional crystal and the phase field profile at the initial state. The computational domain size is set to be $16a$, where a is the initial distance between adjacent atoms. To investigate the effects of computational grid size $\Delta x = a/n$ on the accuracy of stress evaluation, the number of meshings n is varied to 8, 10, 12, 14 and 16. The dimensionless stress σ at every time step is calculated following $\sigma = \Delta f/\Delta\varepsilon$, where Δf is the change in free energy density and $\Delta\varepsilon$ is the strain increment during the time step Δt.

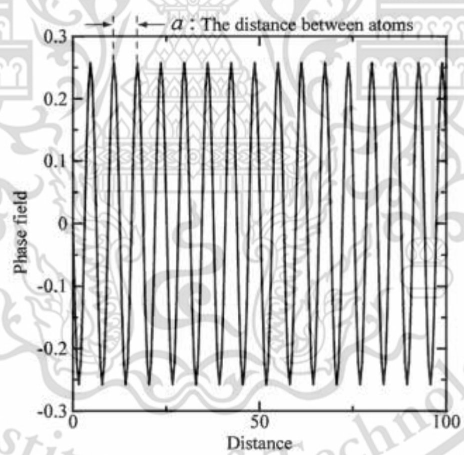

Figure 2.29: Computational model in one-dimension and phase field profile at initial state [23].

Fig. 2.30 shows stress–strain curves where solid lines indicate numerical results and a dashed line indicates the theoretical value. The theoretical value is derived from the difference in free energy density calculated from the equilibrium profiles, or $\phi = A\sin(q_i x)$, obtained before and after applying the strain increment $\Delta\varepsilon$. These results confirm that as n increases or numerical grids become finer, the calculated stresses approach the theoretical value. Additionally, as the strain increases, the calculated stresses deviate from the theoretical value, because the increased grid sizes reduce the accuracy of stress evaluation.

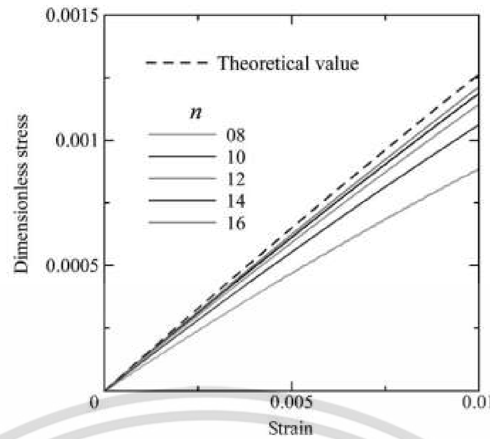

Figure 2.30: Stress–strain curves for one-dimensional crystal [23].

Fig. 2.31 schematically shows the proposed numerical scheme for the PFC deformation simulation in two-dimensions. Here, the grid size in the x-direction increases by $d = \dot{\varepsilon}\Delta x \Delta y$ at every time step similarly to the one-dimensional case. The grid size in the y-direction varies as $\Delta y' = (\Delta x \Delta y)/\Delta x'$, where $\Delta x' = \Delta x + Nd$, keeping a constant volume during deformation. Here, Δx and Δy are the initial grid sizes in the $x-$ and $y-$directions, respectively.

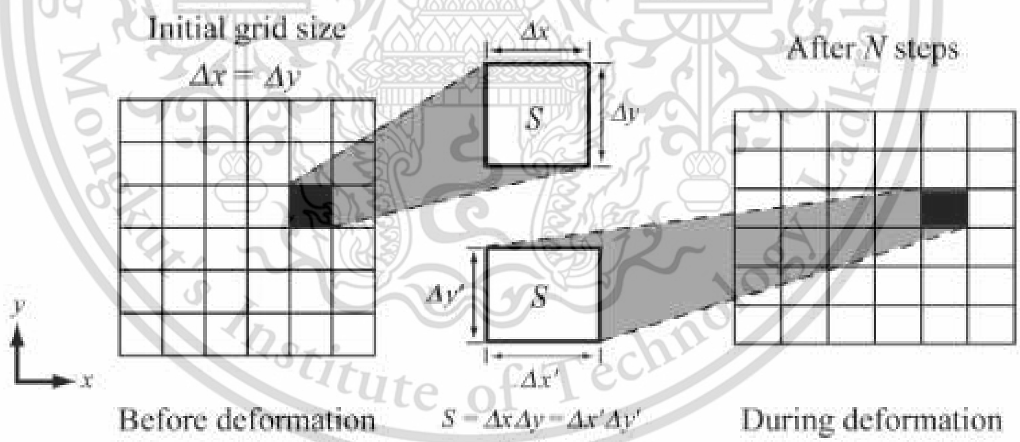

Figure 2.31: Numerical scheme of tensile deformation simulation in two-dimensions [23].

To investigate the elastic response of a single-crystal structure, we prepare a computational model of a single-crystal structure with an initial phase field profile, as shown in Fig. 2.32. To restrict the displacement of atoms in the x-direction, atoms are arranged parallel to the tensile direction. The computational domain is $60a \times 3a$ (600×30 lattices), where a is the distance between the nearest-neighboring atoms, as shown in Fig. 2.32. To simulate quasi-static deformation, the dimensionless strain rate is set to be $\dot{\varepsilon} = 5.17 \times 10^{-6}$, which corresponds to realistic strain rates of about $10^1 s^{-1}$ to $10^2 s^{-1}$ [19, 61]. The time step Δt is 3.2×10^{-3}. Model parameters are set to be $(\alpha, \phi_0) = (-0.25, -0.285)$ at a near-melting temperature [61]. Periodic boundary conditions are adopted in all directions.

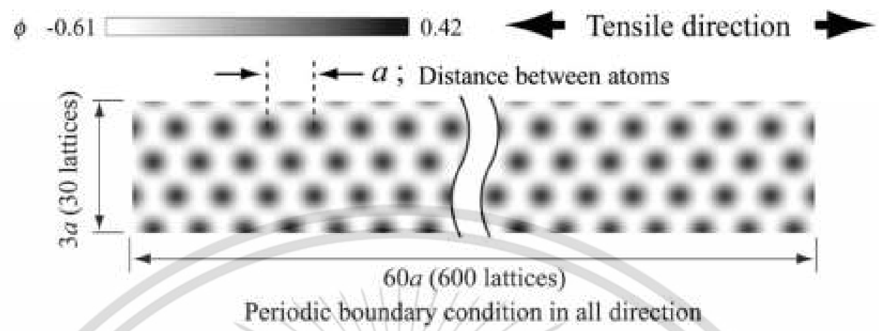

Figure 2.32: Computational model of single-crystal structure and initial phase field profile [23].

Fig. 2.33 shows calculated atomic displacements of single-crystal structures at tensile strains of 0.002, 0.004 and 0.006. Dashed lines indicate analytical values. From these results, we confirm that the response of the system demonstrates linear elasticity.

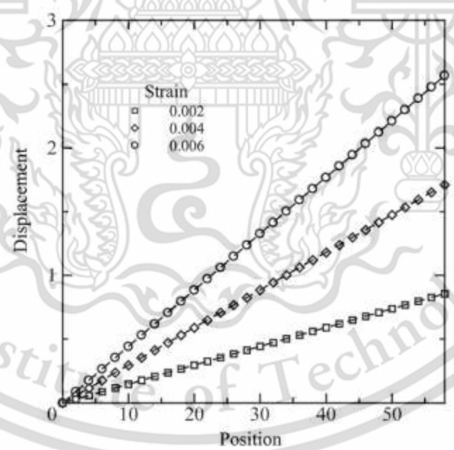

Figure 2.33: Atomic displacement distributions at dimensionless strain rate of 5.17×10^{-6} [23].

To confirm that the PFC deformation simulation technique employing the numerical scheme proposed in this study can express reasonable plastic deformation behaviors, we perform the deformation simulation of a bicrystal. Figure 2.34 shows computational models with a square domain of $60a \times 60a$ (600×600 lattices) and the initial configurations of atoms and grain boundaries displayed by local free energy distributions to facilitate the viewing of defect structures.

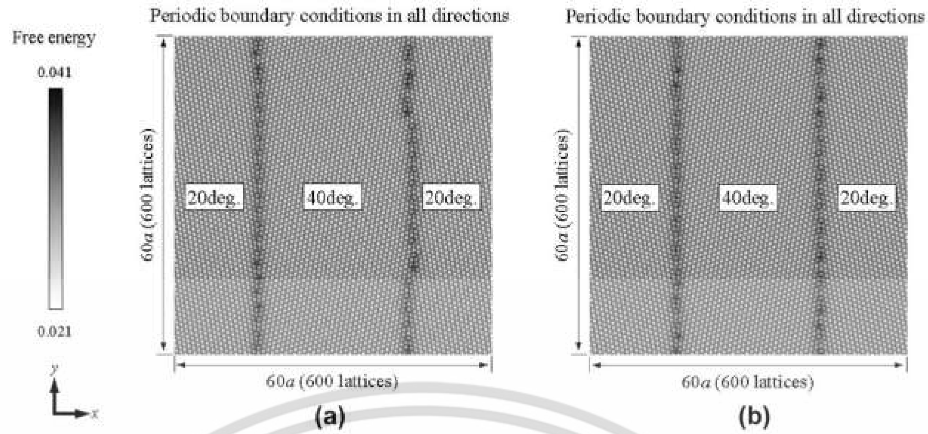

Figure 2.34: Computational models for bicrystals with (a) ‘stepped’ and (b) ‘planar’ grain boundaries [23].

Therefore, in Fig. 2.34, high-energy fields correspond to lattice defects, such as grain boundaries and dislocations. To investigate the effects of grain boundary configuration during plastic deformation, Two bicrystalline structures were prepared with ‘stepped’ and ‘planar’ grain boundaries. Crystal orientations of 20 and 40 degrees were selected to construct large-angle grain boundaries.

The deformation behaviors of the bicrystal with stepped grain boundaries are shown in Fig. 2.35. As deformation proceeds, the stepped parts of grain boundaries become sharp (Fig. 2.35(a)) and result in dislocation emissions (Fig. 2.35(b)) because of the high stress concentration. Moreover, dislocation ‘‘A” generated from a grain boundary migrates inside the crystal and is absorbed by the opposite grain boundary (Figs. 2.35(b)–(d)). In Figs. 2.35(d) and (e), it was observed that dislocations at grain boundaries migrate and some subgrains are formed.

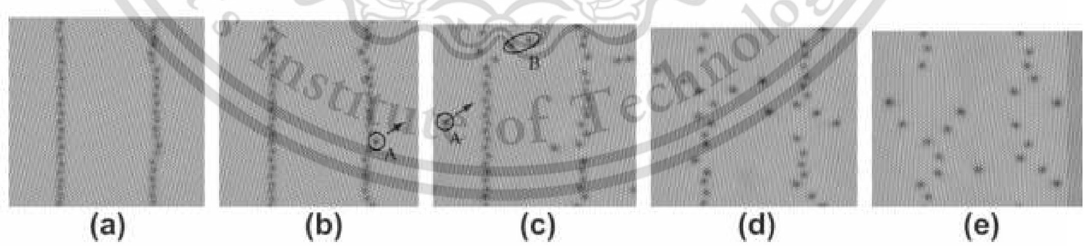

Figure 2.35: Deformation behaviors of bicrystal with ‘stepped’ grain boundaries shown in Fig. 2.34(a) at strains $\varepsilon =$ (a) 0.02, (b) 0.04, (c) 0.06, (d) 0.08 and (e) 0.10 [23].

Figure. 2.36 indicates the results for the bicrystal with planar grain boundaries. These results also confirm that the grain boundary serves as the source of dislocations (Fig. 2.36(b) and (c)) and dislocation annihilation (Fig. 2.36(d) and (e)). Unlike the case shown in Fig. 2.35, dislocations are generated at narrow intervals at grain boundaries. It is considered that these phenomena result from periodic arrangements of dislocations at a planar grain boundary.

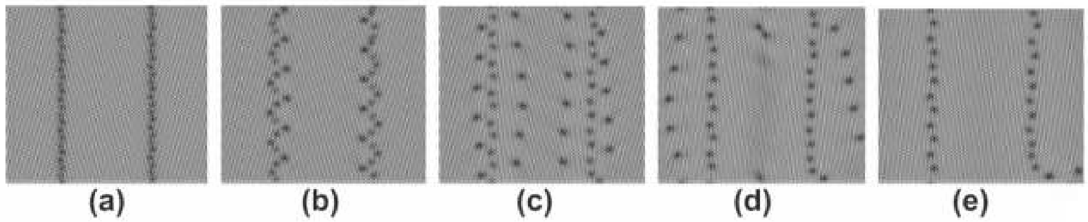

Figure 2.36: Deformation behaviors of bicrystal with 'planar' grain boundaries shown in Fig. 2.34(b) at strains $\varepsilon =$ (a) 0.060, (b) 0.080, (c) 0.085, (d) 0.091 and (e) 0.100 [23].

Moreover, by comparing strains from which dislocations begin to form, we can confirm that a stepped grain boundary is a more favorable dislocation source than a planar grain boundary. This phenomenon is also confirmed in MD simulation [62]. Thus, we conclude that the PFC deformation simulation technique with the proposed numerical scheme can reproduce plastic deformation reasonably.

Fig. 2.37 shows the schematic illustration of the desired nanopolycrystalline structure with regular hexagonal grains with a distance between two sides of approximately 14 atoms. The predefined crystal orientations of each grain are shown at the center of each grain. The computational domain size is set to be $50a \times 44a$ $(500 \times 440$ lattices).

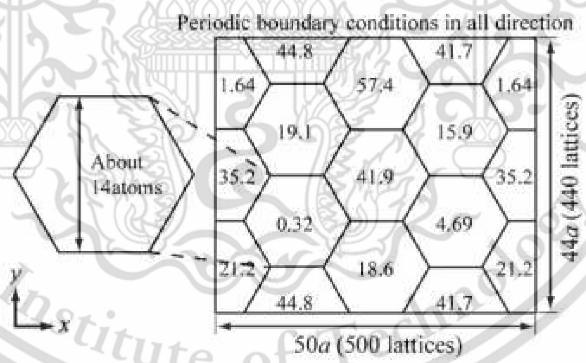

Figure 2.37: Computational model of nanopolycrystalline structure [23].

The initial structure is formed by solidification simulation that starts from nuclei with predefined crystal orientations. As a result of this simulation, the initial structure shown in Fig. 2.38(a) is obtained. Tensile deformation simulation is performed under a constant dimensionless strain rate of 1.72×10^{-6} and using the dimensionless time step $\Delta t = 3.2 \times 10^{-3}$. Periodic boundary conditions are used in all directions.

Fig. 2.38 indicates the deformation states of the nanocrystalline structure during tensile deformation. As the strain increases, grain rotations occur and cause the motions of dislocation at grain boundaries, as shown by arrows in Fig. 2.38. It is also

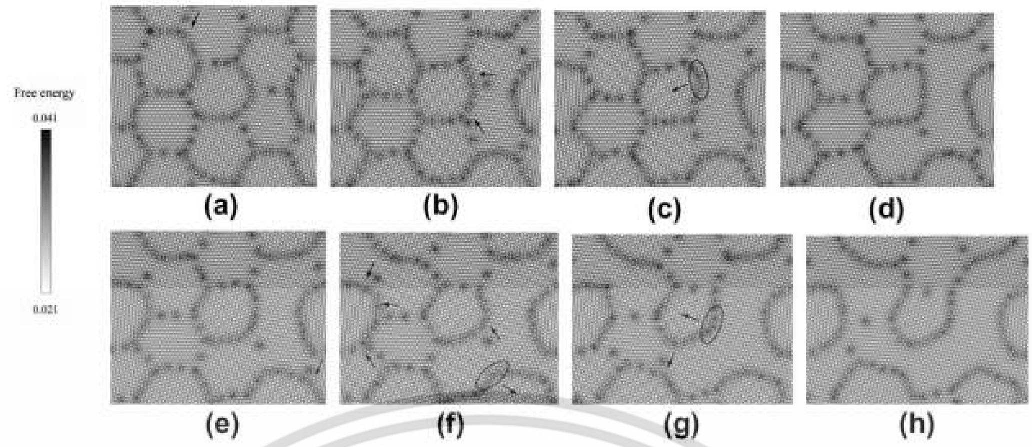

Figure 2.38: Nanopolycrystalline structure at (a) initial state and deformed states with strains $\varepsilon =$ (b) 0.02, (c) 0.03, (d) 0.04, (e) 0.05, (f) 0.06, (g) 0.07 and (h) 0.08 [23].

observed that grain rotation occurs between two neighboring grains with a relatively small misorientation (Fig. 2.38(b)). As a result of coalescence due to grain rotation, the grain boundary between integrated grains disappears and the grain migration driven by curvature is accelerated (Fig. 2.38(c) and (d)). With further deformation, grain rotations and grain boundary migrations occur continuously in other grains (Fig. 2.38(e)–(h)). On the other hand, we cannot observe phenomena indicating that dislocations penetrate into grains from grain boundaries and pass through grains. This is considered to be due to the fact that the grain size is too small for dislocations to penetrate into grains. From these results, we confirm that grain rotation and grain growth, or intergranular plastic deformations [63, 64], are the dominant deformation mechanisms under these conditions. In MD simulations [65, 66] for nanopolycrystalline structures at high temperatures, grain coalescence due to grain rotation and grain growth is observed. In summary, the PFC model with this technique can reproduce the plastic deformation behaviors of nanopolycrystalline structures at high temperatures.

In 2015, a new density functional approach was introduced to investigate a full spectrum of solid-liquid-vapor transitions in pure materials within the framework of a single density order parameter [15]. Consider classical Density Functional Theory (c-DFT), the free energy of interacting liquid is generally written as

$$\frac{F_{\text{CDFT}}[\rho]}{k_B T} = F_{\text{id}}[\rho] + \Phi[\rho] \tag{2.173}$$

where $F_{\text{id}}[\rho]$ is the energy of an ideal gas and $\Phi[\rho]$ is the contribution due to interaction. Φ is then treated by functional expansion around a reference density $\bar{\rho}$, in a power series of $n = (\rho - \bar{\rho})/\bar{\rho}$ and interactions are described by a sequence of n-point correlations $C^{(n)}(\mathbf{r}_1, ..., \mathbf{r}_n)$. While these correlation functions are not known in general, a truncation of the series to second order along with a suitable ansatz of $C^{(2)}$ has been shown to separately describe both vapor-liquid interfaces [36] or solidification problems [60] with success.

To overcome the limitations of two-point correlations on multi-phase behavior, we introduce here a theory that relies on higher order correlations. Consider the Van derWaals theory for the liquid vapor transition [67]. Its improvement to the Ideal gas law is based on two simple mean-field postulates: the attraction between particles is proportional to the average surrounding density, and each particle proportionally reduces the free volume available to other particles. At the field theory level for the spatially varying coarse grained field ρ, such improvements can be described by the free energy

$$\frac{F_{\mathrm{VdW}}[\rho]}{k_B T} = F_{\mathrm{id}}[\rho] - \int dr \left[\rho_{mf} \ln(1-\rho_{mf} b) + \frac{a}{k_B T}\rho_{mf}^2\right] \tag{2.174}$$

where $\rho_{mf}(\mathbf{r}) = \int d\mathbf{r}\chi(\mathbf{r}-\mathbf{r}')\rho(\mathbf{r})$ is a local spatial average of the density field ρ, with χ a local smoothing kernel. This free energy reduces to the standard Van derWaals free energy, where a and b respectively control the magnitude of the attraction and repulsion between atoms. In the following they introduced a formulation that incorporates all the qualitative contributions from the Van derWaals theory into the free energy of the standard PFC-expanded formalism as

$$\begin{aligned}\mathcal{F} = &\int d\mathbf{r}\left[\frac{n(\mathbf{r}^2)}{2} - \frac{n(\mathbf{r}^3)}{6} + \frac{n(\mathbf{r}^4)}{12}\right] \\ &- \frac{1}{2}\int d\mathbf{r}_1 d\mathbf{r}_2 C^{(2)}(\mathbf{r}_1-\mathbf{r}_2)n(\mathbf{r}_1)n(\mathbf{r}_2) \\ &+ \sum_{m=3}^{4}\frac{1}{m}\left[\int d\mathbf{r}_1 \ldots d\mathbf{r}_m \chi^{(m)}(\mathbf{r}_1,\ldots,\mathbf{r}_m)n(\mathbf{r}_1)\ldots n(\mathbf{r}_m)\right]\end{aligned} \tag{2.175}$$

where $\mathcal{F} = F/\bar{\rho}k_B T$. The first line results from the expansion of the ideal gas free energy $F_{\mathrm{id}}[\rho]$, while the second line adds a multi-peaked two-point correlation function. The choice of the latter term determines the structure and properties of the solid phase. While elaborate choices can be made for this term (to target specific two-dimensional or three-dimensional structures [68, 69]), for simplicity, we choose a kernel that yields triangular structure in two-dimension and BCC structure in three-dimension [31]

$$C^{(2)}(\mathbf{r}_1-\mathbf{r}_2) = 1 - r - B_x(1-\nabla^2)^2 \tag{2.176}$$

Here, B_x controls both the bulk compressibility and the strength of the anisotropy in the periodic phase, while r acts as an effective temperature parameter. Vapor-liquid transformations are controlled by the $\chi^{(3)}$ and $\chi^{(4)}$ functions. These are effective $3-$ and $4-$ point correlation functions, given by

$$\begin{aligned}\chi^{(3)} &= (ar+b)\chi(\mathbf{r}_1-\mathbf{r}_2)\chi(\mathbf{r}_1-\mathbf{r}_3) \\ \chi^{(4)} &= c\chi(\mathbf{r}_1-\mathbf{r}_2)\chi(\mathbf{r}_1-\mathbf{r}_3)\chi(\mathbf{r}_1-\mathbf{r}_4)\end{aligned} \tag{2.177}$$

where $\chi(k) = exp(-k^2/(2\lambda))$ in reciprocal space. χ affects low k modes, only picking up density contributions at long wavelengths. The a, b and c parameters determine the

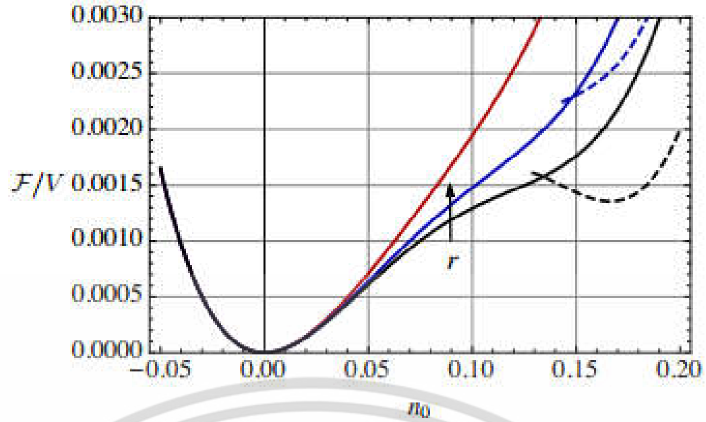

Figure 2.39: 2D Free energy landscapes (vs. average density) for different effective temperatures r. Uniform phases: continuous lines, periodic phases: dashed. Black: $r = 0.14$, blue: $r \approx 0 : 148$ (triple point), red: $r = 0.17$. Other parameters: $a = 50$, $b = -19$, $c = 50$, $B_x = 0.7$ [15].

bulk properties of the uniform phases, while λ affects surface energetics. Substituting a uniform $n(r) = n_0$ into Eq. (2.175) yields a Landau free energy in terms of no for uniform phases (liquid/vapor). This is shown in Fig. 2.39. The phase diagram can be computed by performing common tangent constructions on the Landau theory for different pressures as shown in Fig. 2.40.

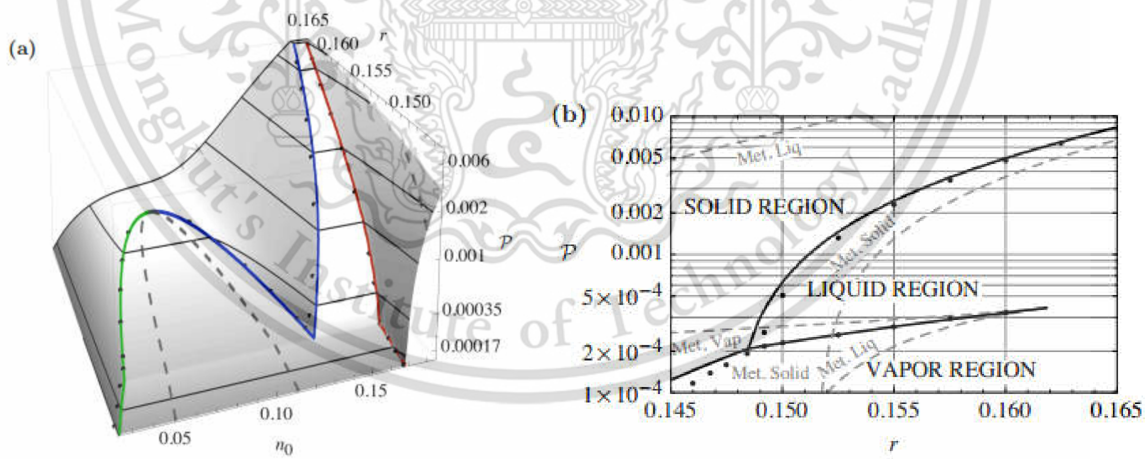

Figure 2.40: (a) Density-temperature-pressure and (b) pressure temperature phase diagrams of model [15].

Figure 2.40(a) shows the density-temperature-pressure phase diagram of Eq. (2.175). It features solid-liquid, solid-vapor and vapor-liquid coexistence regions, and is in excellent qualitative agreement with experimental phase diagrams for pure materials [67, 70]. The vapor-liquid phase separation is parabolic, due to the expanded nature of the theory. Higher order long range correlation terms may be added systematically to fine-tune this behavior. The Pressure-Temperature phase diagram, as shown in Fig. 2.40(b), also shows a behavior consistent with experiments. Along with the equilibrium phase boundaries, Figure 2.40(b) also shows analytical estimates for the metastability regions of the different phases (dashed lines).

Figure 2.40 demonstrates that the coexistence densities, as shown in (a), and pressures, as shown in (b), from direct simulation are in excellent qualitative agreement with our analytical $r - n_o - P$ and $r - P$ space calculations, respectively. Deviations at low average density are in part due to finite size effects, and due to surface energetics not captured in the phase diagram analysis.

To probe the 3-phase kinetics at fixed volume, another simulation was performed where a uniform liquid was quenched into solid-vapor coexistence. The metastable liquid is seeded with a crystal, which grows (Fig. 2.41(a)). As the solid depletes the surrounding liquid density, vapor pockets nucleate in high depletion areas (Fig. 2.41(b)). Due to the different growth rates into liquid and vapor, long faceted solid branches are created (Fig. 2.41(c)), and the resulting structure is a seaweed-like dendrite (Fig. 2.41(d)).

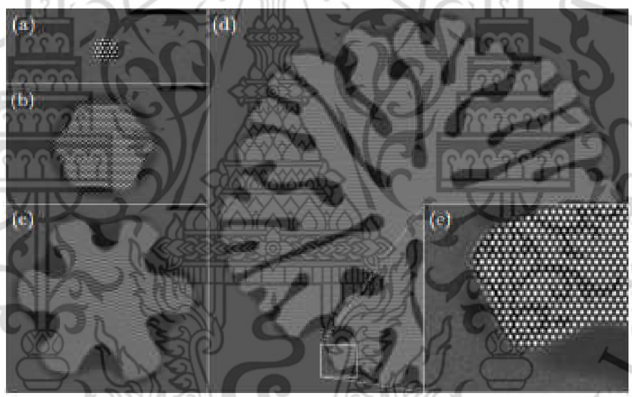

Figure 2.41: 3-phase dendritic growth. A solid seed (periodic regions) grows into a metastable liquid (gray uniform areas). High depletion areas nucleate vapor pockets (black regions). a) $t = 100$, b) $t = 4177$, c) $t = 10293$, d) $t = 36797$, e) inset of d) Scale bar: 20 lattice units. Model parameters: $a = 35$, $b = -12.01$, $c = 33.5$, $B_x = 0.3$, $n_0 = 0.125$, $N_a = 0.01$, $r = 0.145$ [15].

Changes in system volume $V = dx^2 N_x N_y$, for a 2D N_x by N_y grid, can be induced by modifying dx. As V changes one also modifies the average density, no, so that $N = n_0 \cdot V$ remains constant. In practice this is done by adding a uniform density flux J_V everywhere such as to recover the correct n_0. To control the system pressure, an equation of motion for the volume of the system was derived below

$$\frac{\partial V}{\partial t} = M\left(\omega - \mathcal{P}_0\right) \tag{2.178}$$

where $\omega = \int_V d\mathbf{r}\,(-f + \mu\rho)\,/(\bar{\rho}k_BTV)$ emerges as the a dimensional functional generalization. $\mathcal{P}_0 = P_0/(\bar{\rho}k_BT)$ where P_0 is externally imposed pressure. Simulations of

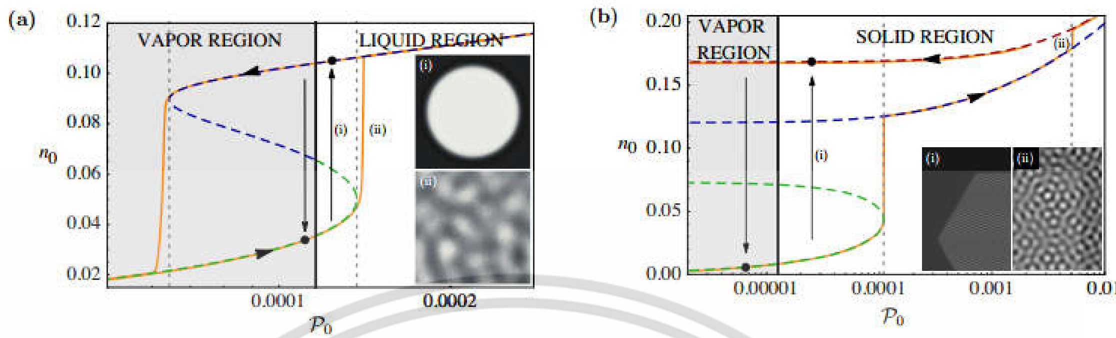

Figure 2.42: Pressure controlled vapor-liquid ((a), $r = 0.155$) and vapor-solid ((b), $r = 0.147$) transformations. Thick vertical black line: equilibrium condensation/deposition point. Dashed green/blue/red lines: average density vs. pressure for vapor/liquid/periodic phases. Continuous orange lines: system under pressure that is continuously increased/decreased (arrows show direction, $N_a = 0.01$). Vertical black arrows: seeded growth of a stable phase out of a metastable phase ($N_a = 0$) [15].

pressure induced transformation were first tested on vapor-liquid systems (Fig. 2.42(a)). The initialization is done in either of the uniform phases, and stabilized to an initial pressure over 5000 time steps. The target pressure P0 is then ramped up/down continuously, at a rate of $\pm 2.7027 \times 10^{-10}$. The vapor-solid transition was also tested in a similar manner (Fig. 2.42(b)). Using $M = (N_xN_y) = 15$, the vapor phase pressure is continuously increased into the solid region, at a rate of 7.375×10^{-11} up to $P_0 = 0.00012$, and then a rate of 2.48866×10^{-8} to $P_0 = 0.01$.

Despite a several studies on material phenomena using the phase-field crystal method, the investigation of viscoelastic properties of material by using such method is still limited and not thoroughly explored. Viscoelasticity is the behavior with both viscous and elastic characteristics; thus materials with viscoelastic behavior can return to its original configuration when unloaded but does so in a time dependent manner. The viscous property also leads to the fact that materials response depends on the rate at which it is deformed [41, 11]. Viscoelastic effect has played significant roles in many materials ranging from amorphous polymers [71], semi-crystalline polymers [72], biopolymers [73], bitumen materials [74] to metals at very high temperature [75]. Furthermore, viscoelasticity governs many engineering applications in various fields including shape-memory ceramics and polymers [76], piezoelectric material [77], self-healing materials [78], viscoelastic gel in surgery application [79], low-loss materials [80], nanoscale resonators [81, 82], in particular, in damping capacity for damping material design. Damping capacity is the property that measures how much damping materials dissipate the energy during their deformation process which can be obtained from mechanical-hysteresis curve. This property has played a key role in approximating the damping performance of damping materials which contributes to numerous engineering applications e.g. noise reduction and vibration isolation [83, 84] and vibration control in engineering structure [85].

In quantifying the viscoelasticity, there are three types of studies: viscoelastic-creep, stress relaxation and mechanical-hysteresis which is related to damping capacity properties in damping materials [7, 8]. Since the studies of viscoelastic-creep and mechanical-hysteresis involve measuring the strain response from an applied stress, we also need a method to control the applied stress and thus we employ the PFC model that is incorporated with previously-proposed pressure-controlled dynamics (PCD) equation [15]. The use of the PCD equation enables convenient control of deformation using external pressure which allows studies of experimentally-observed phenomena involving a system under different types of applied pressure; we will refer to this particular PFC method as PFC-PCD method. This is in contrast to a previously proposed scheme by Hirouchi et al. [23] where the deformation was controlled by specifying the grid spacing as an input variable which is suitable for studying stress relaxation problem. Regarding the advantage of the PFC-PCD method, although this particular method had the potential to implement in the viscoelastic study, however, it was solely used to investigate the triple-phase transition problem since viscoelastic study was not focus area and addressed in earlier work [15].

Therefore, we provided the preliminary study in viscoelastic-creep behavior in the one-dimensional crystal structure using PFC-PCD method. This study can be found in our previous work [25, 26]. It should be noted that the PCD equation used in our study was slightly different to the original PCD version proposed by Kocher and Provatas [15] in that we established the PCD equation regarding thermodynamic of hydrostatically-stressed crystal solid proposed by Larche' and Cahn [39, 40] and classical irreversible thermodynamic frameworks [86, 87, 88]. As a result, although the strain responses under step pressure produced by both methods were slightly different, both of them demonstrated time-delayed strain response which was indicative of viscoelastic-creep behavior. Despite this success, we need results that represent a more realistic crystal structure that allows us to predict more practical viscoelastic behavior. Therefore, we should not limit our study to the one-dimensional case.

We extend our investigation to the viscoelastic-creep behavior and its related properties in three-dimensional BCC crystal structure under step pressure, in particular, the mechanical-hysteresis behavior and its related properties under sinusoidal pressure oscillation in BCC crystal structure. We simulate a hydrostatic stress in BCC unit cell subjected to two types of applied pressure: constant pressure for the viscoelastic-creep study and sinusoidal pressure oscillation for mechanical-hysteresis study. We find that, in both cases, the solid exhibits delayed strain responses from the applied pressure which is indicative of viscoelasticity; and the degree of viscoelasticity can be controlled by the parameter in the PCD equation. Furthermore, the strain responses from the simulations can be compared with functional forms of the solutions to the standard linear solid model to extract viscoelastic quantities and properties. These properties includes relaxation time of viscoelastic creep, and the complex moduli from the hysteresis. The parametric studies show that the relaxation time is proportional to temperature while the magnitude of deformation at steady-state condition is proportional to both temperature and atomic density. Also, the dynamic behavior, mechanical hysteresis and complex moduli predicted by PFC-PCD equation under sinusoidal pressure oscillation is consistent to that of standard linear solid model at certain frequency range. However, at very frequency, the behavior exhibited by the PFC-PCD model differs from that of standard linear solid model which is typically used to investigate viscoelasticity in solid materials [41, 8, 89].

To predict mechanical-hysteresis behavior more accurately, we also propose the modified PFC-PCD method to address this limitation. We modify the pressure-control by adding pressure time derivative term to the existing PCD equation, referred to as MPCD equation. This additional term comes from comparing the Taylor expansion of the existing PCD equation with the SLS model. According to the numerical study, the results demonstrate that the PFC model which incorporates MPCD equation, referred to as PFC-MPCD method, can predict mechanical-hysteresis behavior and complex moduli parameters consistent with SLS model at the broaden pressure-oscillation frequency range. This is in contrast to PFC-PCD method which produces the results inconsistent with SLS model, in particular, at the high-frequency range. We expect that this new PFC-MPCD method can be extended to more complex system with microstructural features such as grain boundary, dislocation or surface and still be capable to exhibit the accurate mechanical-hysteresis behavior and complex moduli parameters which results in predicting more reliable damping capacity parameter in viscoelastic and damping material design.

CHAPTER 3

Methodology

3.1 PFC Method

To simplify the expressions in Eq. (2.40), one can non-dimensionalize the variables by using the following substitutions [19]:

$$\tilde{\mathsf{r}} \equiv q_0 \mathsf{r}, \quad \tilde{\epsilon} \equiv -\frac{a_t}{\lambda q_0^4}, \quad \tilde{\rho} \equiv \sqrt{\frac{g_t}{\lambda q_0^4}}\rho, \quad \tilde{\mathcal{F}} \equiv \frac{g_t}{\lambda^2 q_0^{8-d}}\mathcal{F}, \quad \tilde{w} \equiv \frac{g_t}{\lambda^2 q_0^8} w, \tag{3.1}$$

where the quantities with tildes are non-dimensional and $d = 3$ is the dimensionality of the problem. The expressions in Eq. (2.40) simplifies to

$$\tilde{\mathcal{F}} = \int \tilde{w}\left(\tilde{\rho}\right)\ d\tilde{\mathsf{r}}, \quad \tilde{w}\left(\tilde{\rho}\right) = \frac{\tilde{\rho}}{2}\left[-\tilde{\epsilon} + \left(1 + \tilde{\nabla}^2\right)^2\right]\tilde{\rho} + \frac{\tilde{\rho}^4}{4}. \tag{3.2}$$

where ϵ can be interpreted as the degree of undercooling which is inversely proportional to temperature. The one-mode approximation of the BCC crystal becomes

$$\tilde{\rho}_{\text{one}} = \bar{\tilde{\rho}} + 4\tilde{A}_s\left[\cos\left(\tilde{q}_a\tilde{r}_1\right)\cos\left(\tilde{q}_a\tilde{r}_2\right) + \cos\left(\tilde{q}_a\tilde{r}_1\right)\cos\left(\tilde{q}_a\tilde{r}_3\right) + \cos\left(\tilde{q}_a\tilde{r}_2\right)\cos\left(\tilde{q}_a\tilde{r}_3\right)\right], \tag{3.3}$$

where $\tilde{q}_a = q_a/q_0 = 2\pi/(L_a q_0) = 2\pi/\tilde{L}_a$. The value of $\tilde{q}_a$ can be determined from minimization of the free energy density [16] leading to $\tilde{q}_a = 1/\sqrt{2}$ and, consequently, $\tilde{L}_a = 2\pi\sqrt{2}$.

One can also approximate the ranges of $\tilde{\epsilon}$ and $\bar{\tilde{\rho}}$ where the BCC solid is stable. This is achieved by calculating the free energy density of the solids using the one-mode approximations for stripes, hexagonal, and BCC structures and the free energy of the liquid using a uniform density. Then the phase diagram can be determined from the common tangent construction and the ranges of $\tilde{\epsilon}$ and $\bar{\tilde{\rho}}$ where the BCC solid is stable can be obtained [22]. It should be noted that the alternative free energy functional forms should be used if we need to study the material problem in the other crystal structure than BCC structure such as FCC structure [90], liquid crystal structure [91] or more general form by using CDFT functional form which can be found in [17, 32, 33, 34, 35, 36].

The evolution equation for $\tilde{\rho}$ is the Cahn-Hilliard type which involves dissipative dynamics and mass conservation [19]

$$\frac{\partial\tilde{\rho}}{\partial\tilde{t}} = \tilde{L}_\mu\tilde{\nabla}^2\tilde{\mu}, \quad \tilde{\mu} = (1-\tilde{\epsilon})\tilde{\rho} + \tilde{\rho}^3 + 2\tilde{\nabla}^2\tilde{\rho} + \tilde{\nabla}^4\tilde{\rho} \tag{3.4}$$

where $\tilde{L}_\mu$ is the mobility coefficient and $\tilde{\mu} = \delta\tilde{\mathcal{F}}/\delta\tilde{\rho}$ is the diffusion potential. This equation can be used to simulate evolution of $\tilde{\rho}$ under specified (or fixed) temperature (from the value of $\tilde{\epsilon}$), mass (from the value of $\bar{\tilde{\rho}}$), and volume (from value of grid spacing); typical simulations under this condition are solidification and microstructural evolution. One can also vary the grid spacing to simulate the evolution of the density profile under specified time-dependent deformation [23]. In the context of the viscoelastic behavior, this technique would be appropriate for the stress-relaxation calculation; however for the viscoelastic-creep and mechanical-hysteresis studies, where the system is subjected to specified external stress, additional dynamic equation is needed. Note: From now on, we will drop tilde sign for simplicity.

3.2 Pressure-Controlled Dynamic Equation

The study of viscoelastic creep and mechanical hysteresis involve specifying the external stress, or, in this study, external pressure, and investigate how the (average) internal pressure

$$\bar{P}_{\text{int}} = \frac{1}{V}\int(-f+\mu\rho)\,d\mathbf{r} \tag{3.5}$$

changes temporally; this requires the dynamic equation that contains external pressure as an independent variable. Such equation, referred to as the pressure-controlled dynamic (PCD) equation, was first introduced by Kocher and Provatas [15] expressed as

$$\frac{dV}{dt} = L_{\text{def}}\left(\bar{P}_{\text{int}} - \bar{P}_{\text{ext}}\right), \tag{3.6}$$

where $\bar{P}_{\text{ext}}$ is the externally applied pressure, and $\tilde{L}'_{\text{def}}$ is the mobility coefficient. This equation can be used in conjunction with Eq. (3.4) to simulate the system under specified $\tilde{\bar{P}}_{\text{ext}}$. If the external pressure is higher (lower) than the internal pressure, or $\bar{P}_{\text{ext}} > \bar{P}_{\text{int}}$ ($\bar{P}_{\text{ext}} < \bar{P}_{\text{int}}$), the value of dV/dt will be negative (positive) which indicates that the system will undergo compressive (tensile) deformation.

A slightly modified version of the PCD was recently proposed by Em-Udom and Pisutha-Arnond [25]. The equation is expressed as

$$\frac{dV}{dt} = L_{\text{def}}V(\bar{P}_{\text{int}} - \bar{P}_{\text{ext}}), \tag{3.7}$$

where $\tilde{L}_{\text{def}}$ is the mobility coefficient. This equation was developed using the principle of thermodynamics of hydrostatically-stressed solid [40] and classical irreversible thermodynamic framework [86, 87, 88] and the derivation was summarized in the next section. The comparison between results between equation (3.6) and (3.7) shows that the steady-state behavior obtained from both equations are identical; however, the non-equilibrium behaviors are different. This difference is due to the extra volume term (V) on the right-hand side of Eq. (3.7). This extra volume terms results in higher deformation rate in tension (due to increasing V) than the deformation rate in compression (due to decreasing V). Nevertheless, for small deformation, the numerical difference from the Eqs. (3.6) and (3.7) is unlikely to change the qualitative interpretation of the results. Despite the fact that we employ Eq. (3.6) in this work, the choice of the PCD equation is immaterial for this study. Hereafter, we will refer to the PFC method that incorporates the PCD equation as PFC-PCD model. Lastly, the tilde notation will also be omitted for simplicity.

3.3 Derivation of Pressure-Controlled Dynamic Equation

3.3.1 Thermodynamics of Solids

We first introduce the thermodynamic description of solids proposed by Larché and Cahn [39] which considers the solids as networks of lattices occupied by atomic species and vacancies. For a hydrostatically-stressed, single-component solid, the number of lattices sites (N_L) can be written as

$$N_L = N_A + N_v, \tag{3.8}$$

where N_A and N_v are the numbers of lattices occupied by the atomic species and vacancies, respectively. The internal energy, E, is then postulated to have the following functional dependence: $E(S, V, N_A, N_v)$, where S is the entropy and V is the volume. We can then write the differential of E as [40]

$$dE = TdS - PdV + \mu_A dN_A + \mu_v dN_v, \tag{3.9}$$

where T is temperature, μ_A and μ_v are the chemical potentials. Next, we consider the energy density $e_{V'} = E/V'$, where V' is the volume at the undeformed state. It can be shown using the standard thermodynamic relationships such as the Euler relation and Gibbs-Duhem equation that [40]

$$de_{V'} = Tds_{V'} - PdJ + \mu_{Av} d\rho_{A'}, \tag{3.10}$$

where $s_{V'} = S/V'$, $\rho_{A'} = N_A/V'$, $J = V/V'$, and $\mu_{Av} = \mu_A - \mu_v$. In arriving at the expression for $de_{V'}$, we use the assumption that the network is conserved or $\rho_{A'} + \rho_{v'} = \rho_{L'} \equiv$ Constant, where $\rho_{v'} = N_v/V'$ and $\rho_{L'} = N_L/V'$. Alternative to $e_{V'}$ which is defined by the undeformed volume (Lagrangian frame), we can define $e_V = E/V = e_{V'}/J$ which is the energy density defined by the deformed volume

(Eulerian frame). By using the transformations, $e_{V'} = Je_V$, $\rho_{A'} = J\rho_A$, and $s_{V'} = Js_V$, we obtain the differential of e_V:

$$de_V = Tds_V - \frac{(P + f_v - \mu_{Av}\rho_A)}{J}dJ + \mu_{Av}d\rho_A, \tag{3.11}$$

where $f_V = e_V - Ts_V$ is the Helmhotlz free energy density (Eulerian frame). Finally, we rearrange the expression of de_V to arrive at the differential of s_V:

$$Tds_V = de_V + \frac{(P + f_V - \mu_{Av}\rho_A)}{J}dJ - \mu_{Av}d\rho_A. \tag{3.12}$$

3.3.2 Balance Equations

Here, we introduce the balance equations for mass, internal energy and entropy. We centralize the description of deformation by using a lattice velocity field, $\vec{v}_L$, which is the velocity of the imaginary network of indestructible sites called "markers" [87]. Consequently, the relationship between the lattice material time derivative and the partial derivative can be written as

$$\frac{d^L}{dt} = \frac{\partial}{\partial t} + \vec{v}_L \cdot \nabla. \tag{3.13}$$

Let us first consider the mass balance equation. In the absence of site creation and annihilation, the density of the material species i, where i can be A or v, changes through the equation:

$$\frac{\partial \rho_i}{\partial t} + \nabla \cdot \left(\rho_i \vec{v}_L + \vec{J}_i^L\right) = 0, \tag{3.14}$$

where $\vec{J}_i^L$ is the flux of the species i relative to the lattice. Using equation (3.13), we arrive at [87]

$$\frac{d^L \rho_i}{dt} + \rho_i \nabla \cdot \vec{v}_L + \nabla \cdot \vec{J}_i^L = 0. \tag{3.15}$$

For the energy balance equation, we first consider the fact that the total energy of the system comprises of the internal, kinetic, and potential energies; however, the latter two can be neglected if the system is stationary and is not influenced by an external field such as gravity. Therefore, the balance equation for the energy is [87]

$$\frac{\partial e_V}{\partial t} + \nabla \cdot \left(e_V \vec{v}_L + \vec{J}_E^L\right) = \dot{w}, \tag{3.16}$$

where $\dot{w}$ is the rate of mechanical work per unit volume and $\vec{J}_E^L$ is the flux of the internal energy relative to the lattice [87]. In the absence of an applied field and the assumption of the mechanical equilibrium, we have $\dot{w} = \sigma : \nabla\vec{v}_L$, where σ is the Cauchy stress tensor. Furthermore, for a system under hydrostatic pressure, $\bar{P}_{ext}$, the stress tensor becomes $\sigma = -\bar{P}_{ext}I$, where I is the identity tensor. The mechanical work then reduces to $\dot{w} = -\bar{P}_{ext}\nabla\cdot\vec{v}_L$. Using the expression for $\dot{w}$ and equation (3.13), the energy balance equation becomes [87]

$$\frac{d^L e_V}{dt} + e_V\nabla\cdot\vec{v}_L + \nabla\cdot\vec{J}_E^L = -\bar{P}_{ext}\nabla\cdot\vec{v}_L. \tag{3.17}$$

Lastly, the entropy balance is postulated to be [87]

$$\frac{\partial s_V}{\partial t} + \nabla\cdot\left(s_V\vec{v}_L + \vec{J}_S^L\right) = \dot{s}, \tag{3.18}$$

where the entropy change is affected by the entropy flux relative to the lattice, $\vec{J}_S^L$, and entropy generation, $\dot{s}$, due to irreversibility. Using equation (3.13), we arrive at [87]

$$\frac{d^L s_V}{dt} + s_V\nabla\cdot\vec{v}_L + \nabla\cdot\vec{J}_S^L = \dot{s}. \tag{3.19}$$

3.3.3 Entropy Production

In this section, we derive the expression for the entropy production, $\dot{s}$, which will be used to identify the corresponding flux and force for the phenomenological relation in the next subsection. We consider the fundamental equation (3.12) derived earlier and replace the differential with the lattice material time derivative to obtain

$$T\frac{d^L s_V}{dt} = \frac{d^L e_V}{dt} + \frac{(P + f_V - \mu_{Av}\rho_A)}{J}\frac{d^L J}{dt} - \mu_{Av}\frac{d^L\rho_A}{dt}. \tag{3.20}$$

Using the balance equations (3.15) and (3.17), and the identity $d^L J/dt = J\nabla\cdot\vec{v}_L$, we arrive through lengthy but straightforward derivation

$$\frac{d^L s_V}{dt} + s_V\nabla\cdot\vec{v}_L + \nabla\cdot\vec{J}_S^L = -\vec{J}_Q^L\cdot\frac{\nabla T}{T^2} - \vec{J}_A^L\cdot\frac{\nabla\mu_{Av}}{T} + (P - \bar{P}_{ext})\frac{\nabla\cdot\vec{v}_L}{T}, \tag{3.21}$$

where $\vec{J}_Q^L = T\vec{J}_S^L = \vec{J}_E^L - \mu_{Av}\vec{J}_A^L$ is the heat flux relative to the lattice. Compared the above equation with equation (3.19), we can identify the entropy production to be

$$T\dot{s} = -\vec{J}_Q^L\cdot\frac{\nabla T}{T} - \vec{J}_A^L\cdot\nabla\mu_{Av} + \nabla\cdot\vec{v}_L(P - \bar{P}_{ext}). \tag{3.22}$$

Following Ref. [86, 1], the form of the above equation allows us to identify that one of the fluxes is $\nabla\cdot\vec{v}_L$ and the corresponding force is $P - \bar{P}_{ext}$.

3.3.4 Phenomenological Relations and Pressure-Controlled Dynamic Equation

Based on the classical irreversible thermodynamics framework, it is postulated that the forces and fluxes are related by the phenomenological (linear) law [86, 1]:

$$J_\alpha = \sum_\beta L_{\alpha\beta}X_\beta, \tag{3.23}$$

where J_α represents thermodynamic fluxes, X_β represents thermodynamic forces and $L_{\alpha\beta}$ represents phenomenological coefficients. Using the assumption of symmetry properties of materials [87], the linear law reduces to

$$J_\alpha = L_{\alpha\alpha} X_\alpha. \tag{3.24}$$

Considering the flux and force identified in the previous subsection, we can write the phenomenological relation as

$$\nabla \cdot \vec{v}_L = L_P \cdot (P - \bar{P}_{ext}), \tag{3.25}$$

where L_P is the phenomenological coefficient. From the Reynolds transport theorem [92, 93], we can write the balance law as

$$\frac{dV}{dt} = \int_V (\nabla \cdot \vec{v}_L) d\mathbf{r}. \tag{3.26}$$

Substituting equation (3.25) into equation (3.26), we finally arrive at the pressure-controlled dynamic equation:

$$\frac{dV}{dt} = L_P \int_V (P_{\text{int}} - \bar{P}_{ext}) d\mathbf{r}. \tag{3.27}$$

Denote that $P = P_{\text{int}}$.

3.4 Modified Pressure-Controlled Dynamics Equation

3.4.1 MPCD Equation

Mechanical-hysteresis is one of the behaviors which characterizes viscoelasticity. This behavior requires sinusoidal pressure oscillation as an input to establish mechanical-hysteresis curve. According to our previous study [94], we found the existing PFC-PCD method predicted mechanical-hysteresis curve inaccurately, in particular, at high pressure oscillation frequency when compared to the SLS model. With regard to the Taylor expansion [94], we observed that the PCD equation closely resembled Kelvin-Voigt model which can only exhibit viscoelastic-creep but not mechanical-hysteresis in solid material, in particular, at high frequency range.This inaccuracy arose from the missing pressure time derivative term in the existing PCD equation. Therefore, we have introduced this pressure time derivative term to the existing equation. We refer to this new modified PCD version as MPCD equation as shown below

$$\frac{dV}{dt} = L_{\text{def}} \left(\bar{P}_{\text{int}} - \bar{P}_{\text{ext}} - \tau \frac{d\bar{P}_{\text{ext}}}{dt} \right), \tag{3.28}$$

where $d\bar{P}_{\text{ext}}/dt$ is the time pressure derivative term which is introduced to the existing PCD equation. τ is the shape factor coefficient that enables us to adjust the magnitude of peak in the loss factor parameters. This additional term helps MPCD equation in producing mechanical-hysteresis behavior consistent with SLS model, in particular, at high pressure oscillation frequency where the existing version is failed. It should be noted that the MPCD equation is established according to the SLS model (Zener model) which restricts the model to describing viscoelastic-creep and relaxation in exponential manner [8]. Therefore, this limitation also applies to the MPCD equation.

3.4.2 Approximated Dynamics Behavior of MPCD Equation

In this section, we aim to demonstrate that the approximation behavior of MPCD equation is consistent with SLS model. We begin with the definition of V

$$V(t) = L(t)^3, \quad L(t) = L_a\left(1 + e(t)\right) \tag{3.29}$$

where $V(t)$ is current volume at time t. L_a is the length of unit cell in the reference state. $L(t)$ is the length of unit cell at time t. $e(t)$ is strain at time t. It is obvious that we can alter volume time derivative term to strain time derivative term by chain's rule.

$$\frac{dV}{dt} = \frac{dV}{dL} \cdot \frac{dL}{de} \cdot \frac{de}{dt} \tag{3.30}$$

where $dV/dt = 3L^2$, $dL/de = L_a$. Substitute Eq. (3.30) into Eq. (3.28), we obtain

$$3L^2 L_a \frac{de}{dt} = L_{\text{def}}\left(\bar{P}_{\text{int}} - \bar{P}_{\text{ext}} - \tau \frac{d\bar{P}_{\text{ext}}}{dt}\right), \tag{3.31}$$

Note that $\mathcal{P}_{\text{int}} = -f + \mu\rho$, The equation (3.5) becomes

$$\bar{P}_{\text{int}} = \frac{1}{V}\int_V P_{\text{int}}\, d\mathbf{r} \tag{3.32}$$

Since $\bar{P}_{\text{int}}$ changes its value with $e(t)$, therefore, $\bar{P}_{\text{int}}$ can be written as a function of $e(t)$. However, if the small deformation is postulated around the undeformed state, $e_0 = 0$, $\bar{P}_{\text{int}}$ can be written in Taylor expansion form [95] as

$$\bar{P}_{\text{int}}(e_0 + \Delta e) = \bar{P}_{\text{int}}(e_0) + \left.\frac{d\bar{P}_{\text{int}}}{de}\right|_{e=e_0} \Delta e + \frac{1}{2!}\left.\frac{d^2\bar{P}_{\text{int}}}{de^2}\right|_{e=e_0} \Delta e^2 + \ldots \tag{3.33}$$

where $e = e_0 + \Delta e$ and $\bar{P}_{\text{int}}(e_0)$ is average internal pressure at undeformed state. If we approximate $\bar{P}_{\text{int}}(e_0 + \Delta e)$ only at first derivative expansion, equation (3.33) yields

$$\bar{P}_{\text{int}}(e_0 + \Delta e) \approx \bar{P}_0 + \left.\frac{d\bar{P}_{\text{int}}}{de}\right|_{e=e_0} \Delta e, \qquad \bar{P}_0 = \bar{P}_{\text{int}}(e_0) \tag{3.34}$$

Substitute Eq. (3.34) into Eq. (3.31), we obtain

$$\frac{de}{dt} = \frac{1}{3}\frac{L_{\text{def}}}{L_a^3}\left(1 + \Delta e\right)^{-2}\left(\Delta\bar{P}_{\text{ext}} + \tau\frac{d\Delta\bar{P}_{\text{ext}}}{dt} + \left.\frac{d\bar{P}_{\text{int}}}{de}\right|_{e=e_0}\Delta e\right) \tag{3.35}$$

Note that $\Delta\bar{P}_{\text{ext}} = \bar{P}_0 - \bar{P}_{\text{ext}}$ and $\Delta e \equiv e$ since $e_0 = 0$. Regarding the binomial series of $(1+\Delta e)^{-2} = 1 - 2\Delta e + 3\Delta e^2 - \ldots$ Ref. [95]. Consider only the first term of the expansion; $(1+\Delta e)^{-2} \approx 1 - 2\Delta e$. Substitute this relation into Eq. (3.35). We obtain

$$\frac{de}{dt} - \frac{1}{3}\frac{L_{\text{def}}}{L_a^3}\frac{d\bar{P}_{\text{int}}}{de}\bigg|_{e=e_0} e = \frac{1}{3}\frac{L_{\text{def}}}{L_a^3}\Delta\bar{P}_{\text{ext}} + \frac{\tau}{3}\frac{L_{\text{def}}}{L_a^3}\frac{d\Delta\bar{P}_{\text{ext}}}{dt} \tag{3.36}$$

It should be noted that $d\bar{P}_{\text{int}}/de|_{e=e_0} < 0$. If we denote $d\bar{P}_{\text{int}}/de|_{e=e_0} = -K_P$, where, $K_P > 0$. Finally, Eq. (3.36) becomes

$$\frac{de}{dt} + \frac{K_P}{3}\frac{L_{\text{def}}}{L_a^3}\, e = \frac{1}{3}\frac{L_{\text{def}}}{L_a^3}\Delta\bar{P}_{\text{ext}} + \frac{\tau}{3}\frac{L_{\text{def}}}{L_a^3}\frac{d\Delta\bar{P}_{\text{ext}}}{dt} \tag{3.37}$$

Equation (3.37) has the structure like SLS model Eq. (2.102) where the pressure time derivative term is included on the right hand side of the equation. Nonetheless, the viscoelastic behavior stems from the MPCD equation not from PFC free energy. According to Eq. (3.37), it is obvious that the PFC free energy only influences the K_P variable, the second term on the left-hand side of Eq. (3.37), but not the structure of the equation. Therefore, the alternative choices of PFC free energy Eq. (3.2) can be applied and the PFC-MPCD method should still produce similar viscoelastic behavior correspond to those PFC free energy choices.

It should be noted that although the MPCD equation has a functional form like that of the SLS model, the MPCD equation derives from PFC free energy function where K_P parameter depends on ϵ and $\bar{\rho}_0$ variables. The former variable represents the temperature in the solid system under consideration while the latter variable represents the average atomic density. This allows the MPCD equation to study the impact of temperature and average atomic density on viscoelastic behavior including its related parameters whereas the SLS model is impractical.

3.5 Numerical Simulation

3.5.1 One-Dimensional Crystal Structure

In this section, we describe the method to simulate, analyze and study the viscoelastic-creep behavior in the PFC model. To simulate the viscoelastic-creep behavior, we consider a one-dimensional crystalline phase with the density field

$$\rho(x,t) = \bar{\rho}(t) + \sum_j A_j(t)\cos(G_j x), \tag{3.38}$$

where x is the spatial coordinate.
The system is initially at equilibrium and this state of the system is characterized by three state variables. First is the mass per unit-cell

$$N_0 = \bar{\rho}_0 L_0, \tag{3.39}$$

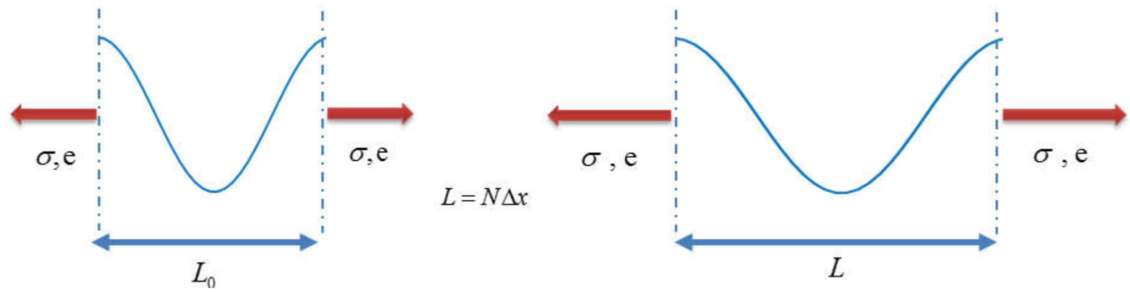

Figure 3.1: One-dimensional deformation schematic.

where L_0 is the initial unit-cell length and $\bar{\rho}_0 \equiv \bar{\rho}(0)$ is the initial average density. The second state variable is the average pressure

$$\bar{P}_0 = \frac{1}{L_0}\int_{L_0} P dx, \tag{3.40}$$

and the third is the temperature which is related to the model parameter ϵ. Then, the system is subjected to step changes in the average pressure quantified by $\Delta\bar{P} = \bar{P}_0 - \bar{P}_{ext}$. From equation (3.27), the nonzero $\Delta\bar{P}$ will lead to deformation characterized by the change in the unit-cell length $L(t)$ and the strain

$$e(t) = \frac{L(t) - L_0}{L_0}. \tag{3.41}$$

During the deformation, we enforce mass conservation by changing the average density according to

$$\bar{\rho}(t) = \frac{N_0}{L(t)} = \frac{\bar{\rho}_0 L_0}{L(t)}, \tag{3.42}$$

and we also allow the system to attain the equilibrium condition in all deformation states by evolving the density profile using equation (3.4) until a steady state is reached for each value of $L(t)$.

3.5.2 Three-Dimensional Crystal Structure

In this section, we describe the setup and method of simulations. In all simulations, we construct a BCC unit-cell with a periodic $N \times N \times N$ grid where $N = 16$ and the lattice parameter $L_a = 2\pi\sqrt{2}$; this results in the reference grid spacing, $\Delta r_0 = \sqrt{2}\pi/8$ in all dimensions, and the reference volume $V_0 = (2\pi\sqrt{2})^3$. The initial density profile is constructed with the one-mode approximation in Eq. (3.3), where the reference density, $\bar{\rho}_0$, is specified. The profile is then relaxed using the evolution equation (Eq. (3.4)), while fixing $\Delta r = \Delta r_0$ and $\bar{\rho} = \bar{\rho}_0$, until the equilibrium density profile is reached. At this state, the reference internal pressure, $\bar{P}_0$, can be calculated using Eq. (3.5). Also, the numerical method employed to solve the evolution equation, and also the PCD equation (Eq. (3.7)), is the Fourier pseudo-spectral method where Fourier transform is used to calculate spatial derivatives and the forward finite difference scheme is used to discretize the time derivative. For the viscoelastic simulations, the PCD equation

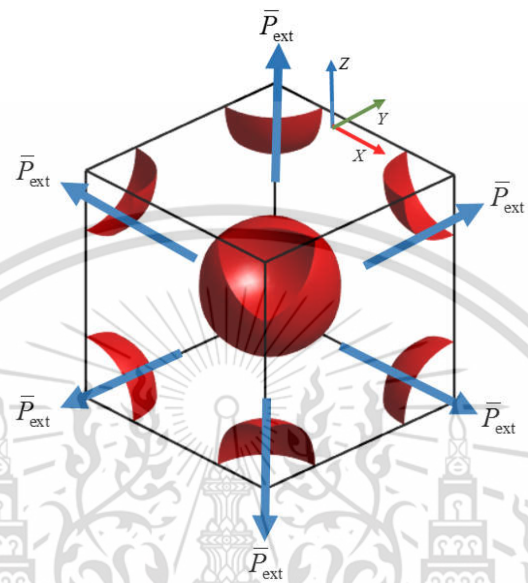

Figure 3.2: BCC unit-cell under hydrostatic pressure schematic using isosurface construction; $\sigma_{\text{ii}} = \bar{P}_{\text{ext}}$ depicts stress in $\{\text{ii}\}$ direction where all σ_{ij} components, shear stress components $\{\text{i} \neq \text{j}\}$, are equal to zero.

is employed where different profiles of $\bar{P}_{\text{ext}}(t)$ are specified and the change in the volume is used to update the grid spacing through the relation

$$\Delta r(t) = \left(\frac{V(t)}{N^3}\right)^{\frac{1}{3}}. \tag{3.43}$$

We note that the grid spacing $\Delta r(t)$ is identical in all directions due to the assumption of crystal under hydrostatic stress Fig 3.3. During the simulation, the mass conservation is imposed by changing the average density through

$$\bar{\rho}(t) = \bar{\rho}_0 \frac{V_0}{V(t)}. \tag{3.44}$$

Also, the mechanical equilibrium is maintained throughout the deformation process; this is accomplished by relaxing the system using the evolution equation at every time step of the time evolution from the PCD equation. The system response is characterized by the strain defined by

$$e(t) = \frac{\Delta r(t) - \Delta r_0}{\Delta r_0}, \tag{3.45}$$

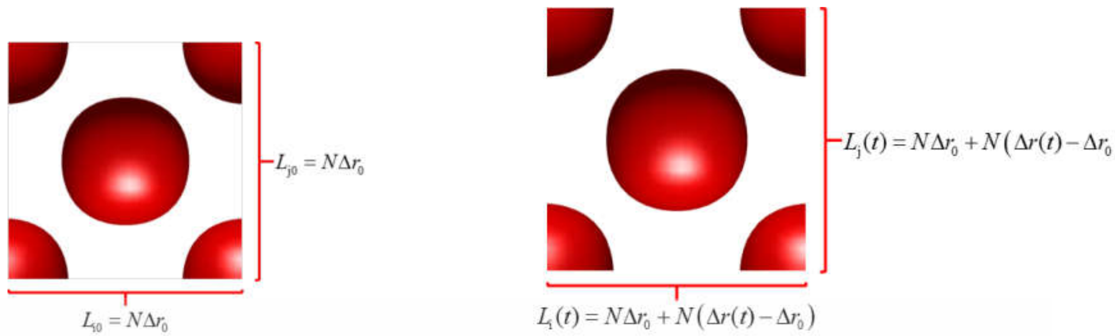

Figure 3.3: Deformation schematic for BCC unit-cell under hydrostatic pressure regarding family plane $\{100\}$ view; (a) Undeformed configuration, original crystal length $L_{\text{i}0}, L_{\text{j}0} = N\Delta r_0$ (b) Deformed configuration, deformed crystal length $L_{\text{i}}(t), L_{\text{j}}(t) = N\Delta r_0 + N\left(\Delta r(t) - \Delta r_0\right)$ where $\{\text{ij}\}$ subscription denotes i, j direction, respectively. The deformation scheme for each Cartesian direction in BCC unit-cell is identical.

which is identical in all directions. The profiles of $e(t)$ and $\bar{P}_{\text{ext}}(t)$ is then used to quantify the viscoelastic behavior predicted form the PFC-PCD method.

Two types of $\bar{P}_{\text{ext}}(t)$ are used in this study. For the viscoelastic creep simulation, the applied pressure is set to

$$\bar{P}_{\text{ext}}(t) = \bar{\mathcal{P}}_{\text{ext}}, \tag{3.46}$$

where $\bar{\mathcal{P}}_{\text{ext}}$ is a constant. The values of $\bar{\mathcal{P}}_{\text{ext}}$ are chosen such that the pressure deviation from the reference pressure

$$\Delta\bar{P}_0 \equiv \frac{\bar{P}_0 - \bar{\mathcal{P}}_{\text{ext}}}{\bar{P}_0} \tag{3.47}$$

is positive or negative; the former leads to tensile deformation while the latter results in compressive deformation. The quantities e_∞ and τ_c are numerically extracted from the strain response, $e(t)$, where e_∞ is the values of $e(t)$ at large t, and τ_c is the value of t at $e(\tau_c) = e_\infty(1 - \exp(-1)) \approx 0.6321 e_\infty$ (see Eq. (2.104) and Fig. 2.12).

For the hysteresis simulation, the applied pressure is set to

$$\bar{P}_{\text{ext}}(t) = \bar{P}_0 - \bar{P}_A \sin(\omega t), \tag{3.48}$$

where $\bar{P}_A$ is the pressure amplitude. The pressure deviation from the reference pressure will then be

$$\Delta\bar{P}_0(t) \equiv \frac{\bar{P}_0 - \bar{P}_{\text{ext}}(t)}{\bar{P}_0} = \frac{\bar{P}_A}{\bar{P}_0}\sin(\omega t). \tag{3.49}$$

With this type of pressure function, the system is then allowed to evolve temporally until the steady-stead strain-response is reached. The strain response profile at steady state will exhibit the sinusoidal behavior similar to Fig. 2.13(a) and we can numerically measure the strain amplitude e_A in order to calculate the amplitude ratio $A_r = e_A/\bar{P}_A$.

When plotting the hysteresis loop as in Fig. 2.13(d), the complex moduli and loss tangent can be calculated by numerically identify the values of A (pressure value at zero strain), B (pressure value at maximum strain), and C (maximum strain value). Then we evaluate the expressions: $G'_{\text{storage}} = B/C$, $G'_{\text{loss}} = A/C$, and $\tan(\delta) = G'_{\text{loss}}/G'_{\text{storage}}$. We note that in all hysteresis simulations, $\bar{P}_A$ is set to $0.02\bar{P}_0$.

Finally, the values of $\bar{P}_0$ and ϵ in all simulations are restricted to the range of $(-0.248, -0.260)$ and $(0.175, 0.200)$, respectively. This values of $\bar{P}_0$ and ϵ ensures the stability of the BCC crystal as shown in the phase diagram in Fig. 2.26, Ref. [22].

3.5.3 Numerical Scheme

The PFC-PCD equation consists of two governing equations; Cahn-Hilliard (CH) type equation and pressure-controlled dynamics (PCD) equation. The first equation is involved dissipative dynamics and mass conservation equation Ref. [19] formulated in partial differential equation (PDE) with four independent variables (t, r_1, r_2, r_3); time variable with three spatial coordinate variables

$$\frac{\partial \rho}{\partial t} = L_\mu \nabla^2 \frac{\delta \mathcal{F}}{\delta \rho} \tag{3.50}$$

where $\rho \equiv \rho(t, r_1, r_2, r_3)$ is density field variable in three dimensional space. L_μ is the mobility coefficient. $\nabla^2(\cdot) = \partial^2(\cdot)/\partial r_1^2 + \partial^2(\cdot)/\partial r_2^2 + \partial^2(\cdot)/\partial r_3^2$ is three dimensional Laplacian operator. $\delta\tilde{\mathcal{F}}/\delta\rho \equiv \mu$ is the variational derivative of $\tilde{\mathcal{F}}$ by ρ which defines a chemical potential μ. The free energy functional $\mathcal{F}$ can be expressed

$$\mathcal{F} = \int \frac{\rho}{2}\left[-\epsilon + \left(1 + \nabla^2\right)^2\right]\rho + \frac{\rho^4}{4}\; d\mathbf{r} \tag{3.51}$$

or in alternative form

$$\mathcal{F} = \int w\left(\rho\right)\; d\mathbf{r}, \quad \mathcal{F} = \int \left[\left(1-\epsilon\right)\frac{\rho^2}{2} + \frac{\rho^4}{4} + \rho\nabla^2\rho + \frac{\rho}{2}\nabla^4\rho\right]\; d\mathbf{r} \tag{3.52}$$

where $\nabla^4(\cdot) = \partial^4(\cdot)/\partial r_1^4 + \partial^4(\cdot)/\partial r_2^4 + \partial^4(\cdot)/\partial r_3^4 + 2\partial^4(\cdot)/\partial r_1^2\partial r_2^2 + 2\partial^4(\cdot)/\partial r_1^2\partial r_3^2 + 2\partial^4(\cdot)/\partial r_2^2\partial r_3^2$. The free energy density variable, $w\left(\rho\right)$, can be expressed in expansion form as

$$\begin{aligned}\tilde{w}\left(\rho\right) = {} & \left(1-\epsilon\right)\frac{\rho^2}{2} + \frac{\rho^4}{4} + \rho\frac{\partial^2\rho}{\partial r_1^2} + \rho\frac{\partial^2\rho}{\partial r_2^2} + \rho\frac{\partial^2\rho}{\partial r_3^2} + \frac{\rho}{2}\frac{\partial^4\rho}{\partial r_1^4} + \frac{\rho}{2}\frac{\partial^4\rho}{\partial r_2^4} + \frac{\rho}{2}\frac{\partial^4\rho}{\partial r_3^4} \\ & + \rho\frac{\partial^4\rho}{\partial r_1^2\partial r_2^2} + \tilde{\rho}\frac{\partial^4\rho}{\partial r_1^2\partial r_3^2} + \rho\frac{\partial^4\rho}{\partial r_2^2\partial r_3^2}\end{aligned} \tag{3.53}$$

Denote that $w(\rho) \equiv f(\rho, \rho_{r_1r_1}, \rho_{r_2r_2}, \rho_{r_3r_3}, \rho_{r_1r_1r_1r_1}, \rho_{r_2r_2r_2r_2}, \rho_{r_3r_3r_3r_3}, \rho_{r_1r_1r_2r_2}, \rho_{r_1r_1r_3r_3}, \rho_{r_2r_2r_3r_3})$ where each independent variable of f is defined by

$$\begin{gathered}
\rho_{r_1r_1} = \frac{\partial^2\rho}{\partial r_1^2}, \quad \rho_{r_2r_2} = \frac{\partial^2\rho}{\partial r_2^2}, \quad \tilde{\rho}_{r_3r_3} = \frac{\partial^2\rho}{\partial r_3^2} \\
\rho_{r_1r_1r_1r_1} = \frac{\partial^4\rho}{\partial r_1^4}, \quad \rho_{r_2r_2r_2r_2} = \frac{\partial^4\rho}{\partial r_2^4}, \quad \rho_{r_3r_3r_3r_3} = \frac{\partial^4\rho}{\partial r_3^4} \\
\rho_{r_1r_1r_2r_2} = \frac{\partial^4\rho}{\partial r_1^2\partial r_2^2}, \quad \rho_{r_1r_1r_3r_3} = \frac{\partial^4\rho}{\partial r_1^2\partial r_3^2}, \quad \rho_{r_2r_2r_3r_3} = \frac{\partial^4\rho}{\partial r_2^2\partial r_3^2}
\end{gathered} \tag{3.54}$$

To solve equation (3.50), μ variable must be reformulated as a function of ρ and its derivative. Therefore, we need to find $\delta\mathcal{F}/\delta\rho$ by using functional derivative definition

$$\begin{aligned}
\frac{\delta\mathcal{F}}{\delta\rho} = \frac{\partial f}{\partial\rho} &+ \frac{\partial^2}{\partial r_1^2}\left(\frac{\partial f}{\partial\rho_{r_1r_1}}\right) + \frac{\partial^2}{\partial r_2^2}\left(\frac{\partial f}{\partial\rho_{r_2r_2}}\right) + \frac{\partial^2}{\partial r_3^2}\left(\frac{\partial f}{\partial\rho_{r_3r_3}}\right) + \frac{\partial^4}{\partial r_1^4}\left(\frac{\partial f}{\partial\rho_{r_1r_1r_1r_1}}\right) \\
&+ \frac{\partial^4}{\partial r_2^4}\left(\frac{\partial f}{\partial\rho_{r_2r_2r_2r_2}}\right) + \frac{\partial^4}{\partial r_3^4}\left(\frac{\partial f}{\partial\rho_{r_3r_3r_3r_3}}\right) + \frac{\partial^4}{\partial r_1^2 r_2^2}\left(\frac{\partial f}{\partial\rho_{r_1r_1r_2r_2}}\right) \\
&+ \frac{\partial^4}{\partial r_1^2 r_3^2}\left(\frac{\partial f}{\partial\rho_{r_1r_1r_3r_3}}\right) + \frac{\partial^4}{\partial r_2^2 r_3^2}\left(\frac{\partial f}{\partial\rho_{r_2r_2r_3r_3}}\right)
\end{aligned} \tag{3.55}$$

Evaluate each derivative term on the right hand side of equation (3.55)

$$\begin{aligned}
\frac{\partial f}{\partial\rho} = (1-\epsilon)\rho + \rho^3 &+ \frac{\partial^2\rho}{\partial r_1^2} + \frac{\partial^2\rho}{\partial r_2^2} + \frac{\partial^2\rho}{\partial r_3^2} \\
&+ \frac{1}{2}\left(\frac{\partial^4\rho}{\partial r_1^4} + \frac{\partial^4\rho}{\partial r_2^4} + \frac{\partial^4\rho}{\partial r_3^4} + 2\frac{\partial^4\rho}{\partial r_1^2\partial r_2^2} + 2\frac{\partial^4\rho}{\partial r_1^2\partial r_3^2} + 2\frac{\partial^4\rho}{\partial r_2^2\partial r_3^2}\right)
\end{aligned} \tag{3.56}$$

where

$$\begin{aligned}
&\frac{\partial^2}{\partial r_1^2}\left(\frac{\partial f}{\partial\rho_{r_1r_1}}\right) = \frac{\partial^2\rho}{\partial r_1^2}, \quad \frac{\partial^2}{\partial r_2^2}\left(\frac{\partial f}{\partial\rho_{r_2r_2}}\right) = \frac{\partial^2\rho}{\partial r_2^2}, \quad \frac{\partial^2}{\partial r_3^2}\left(\frac{\partial f}{\partial\rho_{r_3r_3}}\right) = \frac{\partial^2\rho}{\partial r_3^2} \\
&\frac{\partial^4}{\partial r_1^4}\left(\frac{\partial f}{\partial\rho_{r_1r_1r_1r_1}}\right) = \frac{1}{2}\frac{\partial^4\rho}{\partial r_1^4}, \quad \frac{\partial^4}{\partial r_2^4}\left(\frac{\partial f}{\partial\rho_{r_2r_2r_2r_2}}\right) = \frac{1}{2}\frac{\partial^4\rho}{\partial r_2^4}, \quad \frac{\partial^4}{\partial r_3^4}\left(\frac{\partial f}{\partial\rho_{r_3r_3r_3r_3}}\right) = \frac{1}{2}\frac{\partial^4\rho}{\partial r_3^4} \\
&\frac{\partial^4}{\partial r_1^2 r_2^2}\left(\frac{\partial f}{\partial\rho_{r_1r_1r_2r_2}}\right) = \frac{\partial^4\rho}{\partial r_1^2\partial r_2^2}, \quad \frac{\partial^4}{\partial r_1^2 r_3^2}\left(\frac{\partial f}{\partial\rho_{r_1r_1r_3r_3}}\right) = \frac{\partial^4\rho}{\partial r_1^2\partial r_3^2} \\
&\frac{\partial^4}{\partial r_2^2 r_3^2}\left(\frac{\partial f}{\partial\rho_{r_2r_2r_3r_3}}\right) = \frac{\partial^4\rho}{\partial r_2^2\partial r_3^2}
\end{aligned} \tag{3.57}$$

Substitute each term of equation (3.56) into equation (3.55). Then, the chemical potential μ is literally obtained

$$\mu = (1-\epsilon)\rho + \rho^3 + 2\nabla^2\rho + \nabla^4\rho \tag{3.58}$$

Finally, the equation (3.50) becomes

$$\frac{\partial\rho}{\partial t} = L_\mu\left[(1-\epsilon)\nabla^2\rho + \nabla^2\rho^3 + 2\nabla^4\rho + \nabla^6\rho\right] \tag{3.59}$$

where $\nabla^6(\cdot) = \partial^6(\cdot)/\partial r_1^6 + \partial^6(\cdot)/\partial r_2^6 + \partial^6(\cdot)/\partial r_3^6 + 3\partial^6(\cdot)/\partial r_1^2\partial r_2^4 + 3\partial^6(\cdot)/\partial r_1^2\partial r_3^4 + 3\partial^6(\cdot)/\partial r_2^2\partial r_3^4 + 3\partial^6(\cdot)/\partial r_1^4\partial r_2^2 + 3\partial^6(\cdot)/\partial r_1^4\partial r_3^2 + 3\partial^6(\cdot)/\partial r_2^4\partial r_3^2 + 6\partial^6(\cdot)/\partial r_1^2\partial r_2^2\partial r_3^2$. It is obvious that equation (3.59) is the sixth-order nonlinear partial differential equation (6OD-NPDE) which can be expressed in a full description as

$$\begin{aligned}
\frac{\partial \rho}{\partial t} &= L_\mu \left[(1-\epsilon)\left(\frac{\partial^2 \rho}{\partial r_1^2} + \frac{\partial^2 \rho}{\partial r_2^2} + \frac{\partial^2 \rho}{\partial r_3^2}\right) + \left(\frac{\partial^2 \rho^3}{\partial r_1^2} + \frac{\partial^2 \rho^3}{\partial r_2^2} + \frac{\partial^2 \rho^3}{\partial r_3^2}\right)\right] \\
&+ 2\left(\frac{\partial^4 \rho}{\partial r_1^4} + \frac{\partial^4 \rho}{\partial r_2^4} + \frac{\partial^4 \rho}{\partial r_3^4}\right) \\
&+ L_\mu \left[2\left(2\frac{\partial^4 \rho}{\partial r_1^2 \partial r_2^2} + 2\frac{\partial^4 \rho}{\partial r_1^2 \partial r_3^2} + 2\frac{\partial^4 \rho}{\partial r_2^2 \partial r_3^2}\right) + \left(\frac{\partial^6 \rho}{\partial r_1^6} + \frac{\partial^6 \rho}{\partial r_2^6} + \frac{\partial^6 \rho}{\partial r_3^6}\right)\right] \\
&+ L_\mu \left[3\frac{\partial^6 \rho}{\partial r_1^2 \partial r_2^4} + 3\frac{\partial^6 \rho}{\partial r_1^2 \partial r_3^4} + 3\frac{\partial^6 \rho}{\partial r_2^2 \partial r_3^4} + 3\frac{\partial^6 \rho}{\partial r_1^4 \partial r_2^2} + 3\frac{\partial^6 \rho}{\partial r_1^4 \partial r_3^2}\right] \\
&+ 3\frac{\partial^6 \rho}{\partial r_2^4 \partial r_3^2} + 6\frac{\partial^6 \rho}{\partial r_1^2 \partial r_2^2 \partial r_3^2}
\end{aligned} \tag{3.60}$$

In order to solve equation (3.60) numerically, there are two options which can be employed; finite difference method (FD) [96, 97, 14] and fourier spectral method (FSM) [98, 99, 100, 14]. In this study, not only the periodic boundary condition is governed but also the equation itself has a very high derivative order in spatial coordinate which demands a lot of numerical expense if FD scheme is used. Therefore, FSM method is more appropriate than FD in terms of numerical accuracy and numerical expense to solve equation (3.60). To employ FSM scheme, we begin with equation (3.59). If we apply fourier transform both sides, we obtain

$$\frac{d\hat{\rho}}{dt} = L_\mu \left[-(1-\epsilon)|\mathbf{K}|^2\hat{\rho} - |\mathbf{K}|^2\hat{\rho}^3 + 2|\mathbf{K}|^4\hat{\rho} - |\mathbf{K}|^6\hat{\rho}\right] \tag{3.61}$$

Then, the 6OD-NPDE is literally reduced to empirical ordinary differential equation which depends on time constraint only; where $\hat{\rho} \equiv \hat{\rho}(\mathbf{K}, t)$ is fourier transform of ρ. $\hat{\rho}^3 \equiv \hat{\rho}^3(\mathbf{K}, t)$ is fourier transform of ρ^3 which can be described as below

$$\begin{aligned}
\hat{\rho}(\mathbf{K}, t) &= \int_{-\infty}^{+\infty} \rho(\mathbf{r}, t) e^{-j\mathbf{K}\cdot\mathbf{r}} d\mathbf{r} \\
\hat{\rho}^3(\mathbf{K}, t) &= \int_{-\infty}^{+\infty} \rho^3(\mathbf{r}, t) e^{-j\mathbf{K}\cdot\mathbf{r}} d\mathbf{r}
\end{aligned} \tag{3.62}$$

$\mathbf{K} \equiv \mathbf{K}(\mathbf{k}_{r_1}, \mathbf{k}_{r_2}, \mathbf{k}_{r_3})$ is a vector in fourier space and each fourier wave vector component $\mathbf{k}_{r_i}$ is defined by

$$\mathbf{k}_{r_i} = \frac{2\pi}{L_{r_i}}\left[0, 1, 2, ..., \frac{N_{r_i}}{2} - 1, -\frac{N_{r_i}}{2}, -\frac{N_{r_i}}{2} + 1, -\frac{N_{r_i}}{2} + 2, .., -1\right], \quad \forall i \in \{1, 2, 3\} \tag{3.63}$$

where L_{r_i} is lattice parameter along r_i direction and our study uses $L_{r_i} = 2\pi\sqrt{2}$ for $\forall i \in \{1, 2, 3\}$. N_{r_i} is number of grid points along r_i direction which we employ $r_i = 16$

for $\forall i \in \{1, 2, 3\}$. It should be noted that

$$
\begin{aligned}
&|\mathsf{K}|^2 = \mathsf{k}_{r_1}^2 + \mathsf{k}_{r_2}^2 + \mathsf{k}_{r_3}^2 \\
&|\mathsf{K}|^4 = \mathsf{k}_{r_1}^4 + \mathsf{k}_{r_2}^4 + \mathsf{k}_{r_3}^4 + 2\mathsf{k}_{r_1}^2\mathsf{k}_{r_2}^2 + 2\mathsf{k}_{r_1}^2\mathsf{k}_{r_3}^2 + +2\mathsf{k}_{r_2}^2\mathsf{k}_{r_3}^2 \\
&|\mathsf{K}|^6 = \mathsf{k}_{r_1}^6 + \mathsf{k}_{r_2}^6 + \mathsf{k}_{r_3}^6 + 3\mathsf{k}_{r_1}^2\mathsf{k}_{r_2}^4 + 3\mathsf{k}_{r_1}^2\mathsf{k}_{r_3}^4 + 3\mathsf{k}_{r_2}^2\mathsf{k}_{r_3}^4 + 3\mathsf{k}_{r_1}^4\mathsf{k}_{r_2}^2 + 3\mathsf{k}_{r_1}^4\mathsf{k}_{r_3}^2 \\
&\qquad + 3\mathsf{k}_{r_2}^4\mathsf{k}_{r_3}^2 + 6\mathsf{k}_{r_1}^2\mathsf{k}_{r_2}^2\mathsf{k}_{r_3}^2
\end{aligned}
\tag{3.64}
$$

We employ semi-implicit scheme [98] to solve equation (3.61). The forward difference approximation for time derivative term is given as

$$\frac{d\hat{\rho}}{dt} = \frac{\hat{\rho}^{n+1} - \hat{\rho}^n}{\Delta t} \tag{3.65}$$

where $\hat{\rho}^{n+1}$ and $\hat{\tilde{\rho}}^n$ denote $\hat{\rho}$ at time $t + \Delta t$ and t, respectively. Substitute equation (3.65) in equation (3.61)

$$\frac{\hat{\rho}^{n+1} - \hat{\rho}^n}{\Delta t} = L_\mu \left[- (1 - \epsilon) |\mathsf{K}|^2 \hat{\rho}^{n+1} - |\mathsf{K}|^2 \hat{\rho}^{3n} + 2|\mathsf{K}|^4 \hat{\rho}^{n+1} - |\mathsf{K}|^6 \hat{\rho}^{n+1} \right] \tag{3.66}$$

where $\hat{\rho}^{n+1}$ and $\hat{\rho}^{3n}$ are $\hat{\rho}$ at time $t + \Delta t$ and $\hat{\rho}^3$ at time t, respectively. Rearrange above equation, we obtain

$$\left[1 + \Delta t L_\mu \left[(1 - \epsilon) |\mathsf{K}|^2 - 2|\mathsf{K}|^4 + |\mathsf{K}|^6\right]\right] \hat{\rho}^{n+1} = \hat{\rho}^n - \Delta t L_\mu |\mathsf{K}|^2 \hat{\rho}^{3n} \tag{3.67}$$

and it yields

$$\hat{\rho}^{n+1} = \frac{\hat{\rho}^n - \Delta t L_\mu |\mathsf{K}|^2 \hat{\rho}^{3n}}{\left[1 + \Delta t L_\mu \left[(1 - \epsilon) |\mathsf{K}|^2 - 2|\mathsf{K}|^4 + |\mathsf{K}|^6\right]\right]} \tag{3.68}$$

Finally, $\hat{\rho}^{n+1}$ variable which is in reciprocal space can be converted into the real space variable by using inverse fourier transform

$$\rho^{n+1}(\mathsf{r}) = \frac{1}{(2\pi)^d} \int_{-\infty}^{+\infty} \hat{\rho}^{n+1}(\mathsf{K}) e^{j\mathsf{K}\cdot\mathsf{r}} d\mathsf{K} \tag{3.69}$$

where d is dimensionality of the problem. This variable will be used to calculate $\bar{P}_{\text{int}}$ in pressure-controlled dynamics equation further. Next, the second important equation is the PCD equation which was developed regarding thermodynamic of hydrostatically-stressed crystal solid [39] and classical irreversible thermodynamic frameworks [86, 87, 88]. The advantage of this equation is that it allows to create the deformation in PFC model by specifying external pressure as an input variable unlike the conventional PFC simulations where volume, or grid spacing, is an input variable [23]. This equation is given as below

$$\frac{dV}{dt} = L_{\text{def}} V (\bar{P}_{\text{int}} - \bar{P}_{\text{ext}}) \tag{3.70}$$

To solve PCD equation, we use forward difference scheme for time derivative term.

$$\frac{dV}{dt} = \frac{V^{n+1} - V^{n}}{\Delta t} \tag{3.71}$$

Then, equation (3.70) becomes

$$\frac{V^{n+1} - V^{n}}{\Delta t} = L_{\text{def}} V^{n} \left(\bar{P}^{n}_{\text{int}} - \bar{P}^{n}_{\text{ext}}\right) \tag{3.72}$$

where V^{n+1} and V^{n} is volume at time $t + \Delta t$ and t, respectively. Also, $\bar{P}^{n}_{\text{int}}$ and $\bar{P}^{n}_{\text{ext}}$ is $\bar{P}_{\text{int}}$ and $\bar{P}_{\text{ext}}$ at time t. Then, the equation (3.72) yields

$$V^{n+1} = V^{n} + \Delta t L_{\text{def}} V^{n} \left(\bar{P}^{n}_{\text{int}} - \bar{P}^{n}_{\text{ext}}\right) \tag{3.73}$$

For MPCD equation, the numerical scheme is given below

$$V^{n+1} = V^{n} + \Delta t L_{\text{def}} V^{n} \left(\bar{P}^{n}_{\text{int}} - \bar{P}^{n}_{\text{ext}} - \tau \left[\frac{d\bar{P}_{\text{ext}}}{dt}\right]^{n}\right) \tag{3.74}$$

where $[d\bar{P}_{\text{ext}}/dt]^{n}$ is pressure time derivative time at time t. Finally, we literally obtain a new volume value at next time step as we required. It should be noted that $\bar{P}^{n}_{\text{int}}$ is

$$\bar{P}^{n}_{\text{int}} = \frac{1}{V^{n}} \int \left(-f^{n} + \mu^{n} \rho^{n}\right) d\mathbf{r} \tag{3.75}$$

where

$$\begin{aligned} f^{n} &= (1-\epsilon)\frac{\rho^{2n}}{2} + \frac{\rho^{4n}}{4} + \rho^{n}\left[\nabla^{2}\rho\right]^{n} + \frac{\rho^{n}}{2}\left[\nabla^{4}\rho\right]^{n} \\ \mu^{n} &= (1-\epsilon)\rho^{n} + \rho^{3n} + 2\left[\nabla^{2}\rho\right]^{n} + \left[\nabla^{4}\rho\right]^{n} \end{aligned} \tag{3.76}$$

All superscripts, n, regarding equation (3.76) which appear in all $(\cdot)^{n}$ represent those physical quantities, $(\cdot)$, at time t.

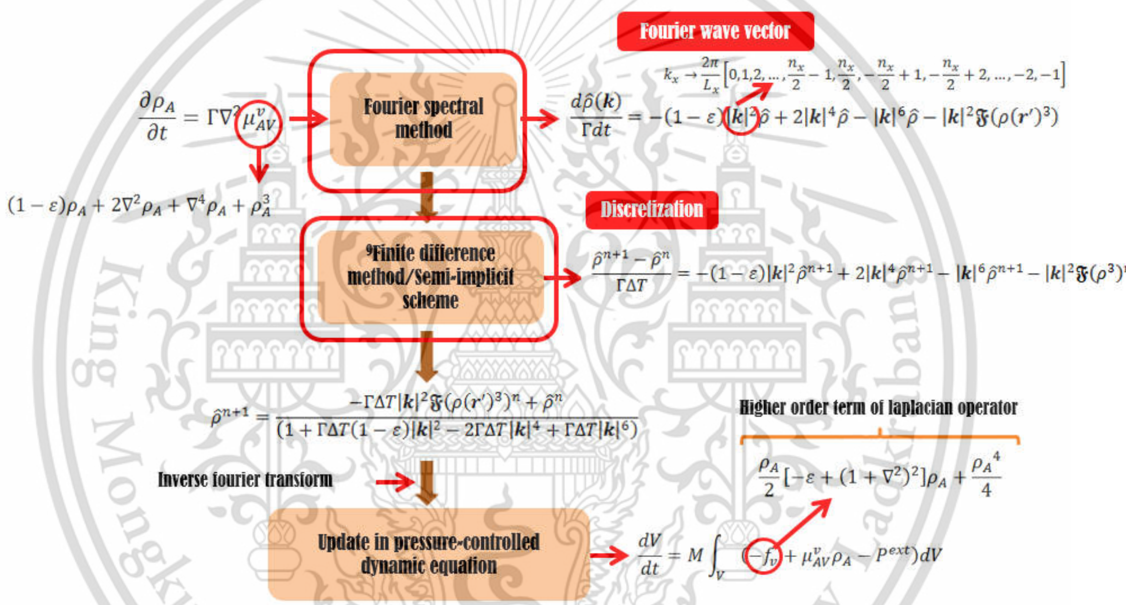

Figure 3.4: Numerical scheme for PFC-PCD equation.

CHAPTER 4

Results and Discussion

4.1 Preliminary Discussion

Damping materials have been used in many engineering applications and, in particular, in energy absorption such as vibration isolation and impact absorber. One of the most important properties that plays a key role in energy absorption is the damping capacity of material. This parameter indicates the ability of material in dissipating energy during the deformation which can be measured through mechanical-hysteresis curve of viscoelasticity. This mechanical behavior is characterized by three phenomena; viscoelastic-creep, stress relaxation and mechanical-hysteresis behavior. To select the appropriate materials in specific tasks, therefore, we need to predict these properties accurately and know the suitable working condition of these damping materials.

In the past few decades, computational materials science has emerged as an alternative choice to predict various material properties and phenomena. This new technique can help speeding up the design process and reducing the cost of the real experimental study. To predict this damping capacity accurately, we need a computational technique that incorporates microstructures which influences the material properties and can reproduce a correct mechanical-hysteresis behavior.

In the last decade, the PFC method has emerged as a robust tool to study various material phenomena. The PFC method was first introduced by Elder et.al. [31] which its free energy functional was minimized by periodic density field which was found in crystalline structure. This gives rise to numerous physical features that occurs due to the periodicity of crystalline phases e.g. spatial symmetry, elastic and plastic interaction, the nucleation, multiple crystal orientations and the motion of dislocations.

This method has been extensively used to study materials phenomena and behavior ranging from phase transformation [17, 101, 102], topological defect dynamics (vacancy [103], grain-boundary [104, 105, 106], dislocation [31, 19, 61, 107, 108], crack [109]) to elasticity and elastic constants [110, 111, 112], plasticity [108, 113] and segregation induced grain boundary premelting [114] in binary alloys.

Although there were numerous successful studies using PFC method. The investigation of viscoelastic behavior and the related properties predicted by the PFC model is still limited. Thus, it is of interest to study the capability of the PFC model to predict this phenomena. As mention earlier, viscoelasticity is characterized by viscoelastic-creep, stress relaxation and mechanical-hysteresis. However, in this work, we only focus our investigation on viscoelastic-creep and mechanical-hysteresis behavior which is directly related to damping capacity that is crucial for damping material design. Since the studies of viscoelastic-creep and mechanical-hysteresis involve measuring the strain response from an externally applied stress, therefore, we need a method which is able to produce the deformation from externally applied load. This is in contrast to a previously proposed method to control the deformation by Hirouchi et al. [23] where the deformation was controlled by specifying the grid spacing as an input variable which is suitable for studying stress relaxation problem which is not focused in our study.

Recently, the pressure-controlled-dynamics (PCD) equation was first introduced by Kocher and Provatas [15]. This equation allows us to measure the strain by specifying externally applied stress which is suitable for using to study viscoelastic-creep, mechanical-hysteresis behavior and complex moduli parameters. With incorporating the PFC method, this method is referred to as PFC-PCD method. Although they used this particular method to investigate the full spectrum of solid-liquid-vapor transitions, unfortunately, the viscoelastic-creep, mechanical-hysteresis behavior and complex moduli parameters which can be reproduced from that equation were not focused area and, of course, not addressed in their work [15]. We implemented this PFC-PCD method to study viscoelastic-creep behavior in one-dimensional crystal structure in our preliminary study. The full results and discussion are provided in the Appendix A.

Then, we extended our work to investigate viscoelastic-creep and mechanical hysteresis behavior for a body-centered-cubic (BCC) crystal structure in [94]. According to the results, although the PFC-PCD could reproduce viscoelastic-creep behavior correctly, it was inaccurate in predicting mechanical-hysteresis behavior and complex moduli parameters, in particular, at the high-pressure oscillation frequency region when compared with the standard linear solid (SLS) model [41, 8] which is typically used to investigate viscoelasticity in solid materials and theoretical perspective suggested by [9]. This inaccuracy was analyzed further by conducting the Taylor's expansion [95] on PCD equation. This analysis demonstrated that this inaccuracy arose from the missing pressure time derivative term in the existing PCD equation. This explained why the PFC-PCD model could reproduce creep phenomena, but not the mechanical-hystersis behavior similar to the SLS model. As a result, the modification to the existing PFC-PCD method is crucial in order to reproduce more accurate mechanical-hysteresis behavior.

Therefore, we proposed the modified PFC-PCD method to address this limitation in our latest work [115]. We modified the pressure-control by adding pressure time derivative term to the existing PCD equation, referred to as MPCD equation. This additional term comes from comparing the Taylor's expansion of the existing PCD equation with the SLS model. This pressure time derivative term helps MPCD equation in producing mechanical-hysteresis behavior consistent with SLS model, in particular, at high pressure oscillation frequency where the existing version is failed. According to the numerical study, the results demonstrate that the PFC model which incorporates MPCD equation, referred to as PFC-MPCD method, can predict mechanical-hysteresis behavior and complex moduli parameters consistent with SLS model and the real solid materials [9] at the broaden pressure oscillation frequency range. In particular, the complex moduli predicted by our method are in good agreement with the experimental observations which can be found in numerous sources e.g. [116, 117, 118] for alloy, [119, 120, 121] for rubber and [122] for elastomer. This is in contrast to PFC-PCD method which produces the results inconsistent with SLS model and experimental observations, especially, at the high-frequency range.

This chapter is organized as follows. In part (4.2), we present the results and discussion on viscoelastic-creep and parametric study of BCC crystal structure produced by PFC-PCD method [94]. In part (4.3), we study the influence of PFC and PCD parameters on dynamic response, mechanical-hysteresis behavior and complex moduli parameters of BCC crystal structure produced by PFC-PCD method [94]. In part (4.4), we provide the results and discussion on mechanical-hysteresis behavior and complex moduli parameters of BCC crystal structure predicted by both PFC-PCD and PCD-MPCD methods [115].

4.2 Viscoelastic-Creep and Parametric Study of BCC Solid

In this part, we show the viscoelastic-creep behavior exhibited by the PFC-PCD model and demonstrate the dependence of this behavior on $\Delta\bar{P}_0$ and L_{def}. Figure 4.1 shows the strain response from different values of $\Delta\bar{P}_0$. The graphs show the strain, initially at zero, increase or decrease gradually until the steady-state values (denoted as e_∞) are reached. This delayed responses obtained from the simulations are indicative of the viscoelastic-creep behavior; this means that the PFC model combined with the PCD equation is capable of modeling viscoelastic behavior. Also, depending on the values of $\Delta\bar{P}_0$ either tensile or compressive deformations are realized. When $\Delta\bar{P}_0 > 0$, or $\bar{\mathcal{P}}_{\text{ext}} < \bar{P}_0$, tensile deformation is obtained while $\Delta\bar{P}_0 < 0$, or $\bar{\mathcal{P}}_{\text{ext}} > \bar{P}_0$, results in compressive deformation. The magnitudes of e_∞ (steady-state deformation) also scale with the magnitudes of $\Delta\bar{P}_0$, as expected from the elastic effect in the PFC model (Eq. (2.40)).

Next, Fig. 4.2 shows how viscoelastic behavior is affected by L_{def}. From the figure, the increase in L_{def} results in $e(t)$ approaching e_∞ in a faster rate, or smaller τ_c; this means that the increase in L_{def} leads to the faster strain response or higher degree of elasticity. This results demonstrates that L_{def} can be used to adjusted the degree of viscoelasticity ranging from highly viscous to highly elastic. The capability to control the degree of viscoelastic creep can be used to tune the PFC-PCD model to different types of materials.

The degree of viscoelasticity is also affected by ϵ (inverse of temperature), as shown in Fig. 4.3. From the figure, the values of τ_c decreases as the values of ϵ increases for the range of $\bar{\rho}_0$ where solid is stable. Since ϵ is inversely proportional to temperature, this indicates that the system response faster, or becomes more elastic, as temperature decreases; this prediction agrees with the experimental observation where relaxation time in creep phenomena decreases with temperature.

We note that the results from Fig. 4.2 and Fig. 4.3 assume that L_{def} and ϵ are independent from one another. Nevertheless, since both L_{def} and ϵ both affects the

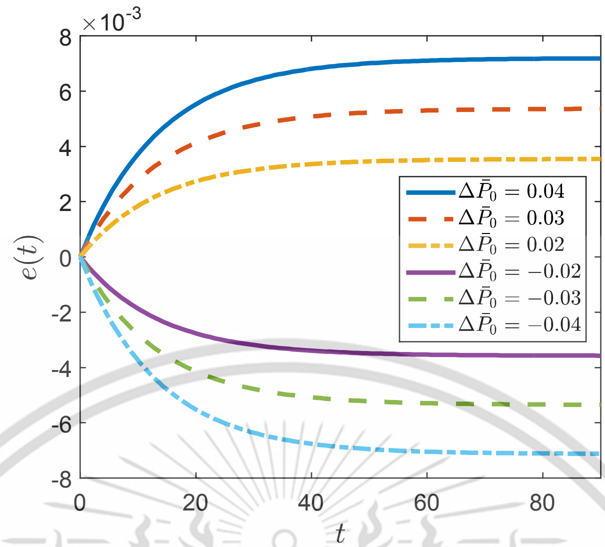

Figure 4.1: Viscoelastic-creep behaviors, $e(t)$, under different values of constant pressure, $\Delta\bar{P}_0$, at condition $|\bar{\rho}_0| = 0.2600$, $\epsilon = 0.2000$ and $L_{\text{def}} = 1$. The results show the capability of PCD equation to control e_∞ through $\Delta\bar{P}_0$. Note: All physical variables are in non-dimensionalized quantities.

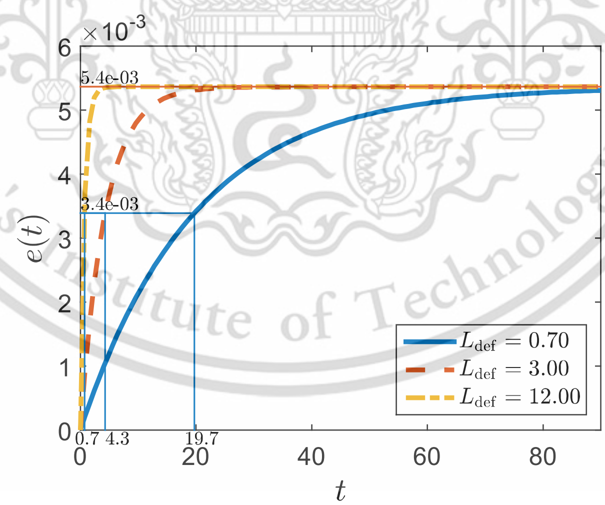

Figure 4.2: Viscoelastic-creep behaviors, $e(t)$, under different values of L_{def} at condition $|\bar{\rho}_0| = 0.2600$, $\epsilon = 0.2000$ and $\Delta\bar{P}_0 = 0.03$. The results demonstrate the capability of PCD equation to control relaxation time, τ_c, through L_{def}. Note: All physical variables are in non-dimensionalized quantities.

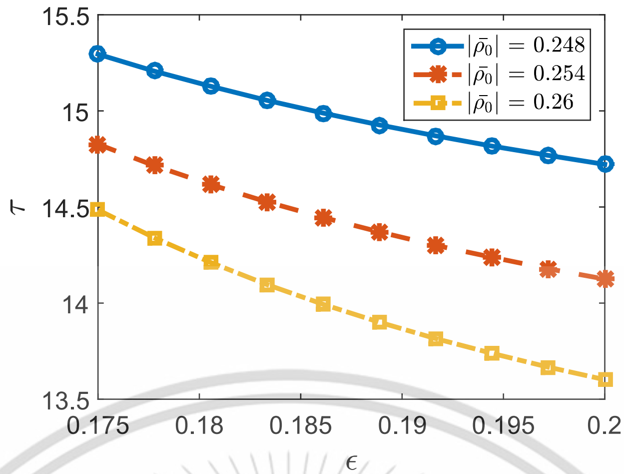

Figure 4.3: Viscoelastic-creep parametric study under step pressure; Influence of ϵ parameter on τ_c parameter at ϵ parameter ranges between $(0.175, 0.200)$ with three different $|\bar{\rho}_0|$ values. All numerical experiments are based on step pressure input ($\Delta\bar{P}_0 = 0.02$). Note: All physical variables are in non-dimensionalized quantities.

viscoelasticity behavior, it is likely that L_{def} and ϵ (or temperature) are related. It should be noted that L_{def} originates from linear phenomenological law in the classical irreversible thermodynamic framework. Therefore, the dependence of L_{def} on temperature could be introduced by considering a more rigorous treatment of this phenomenological law.

Lastly, we report how the stiffness changes with ϵ and $\bar{\rho}_0$. This is shown in Fig. 4.4(a) and 4.4(b), where the values of e_∞ are plot as functions of ϵ and $\bar{\rho}_0$, respectively. Since $\Delta\bar{P}_0$ is the same in all simulations, lower e_∞ values indicates higher stiffness and vice versa. From Fig. 4.4(a), e_∞ decreases as ϵ increases while, from Fig. 4.4(b) e_∞ increases as $|\bar{\rho}_0|$ increases. This indicates that the stiffness is higher at lower temperature and lower atomic densities. These results are qualitatively consistent with theoretical framework [110, 123] and experimental observations [124, 125, 126].

We note that stiffness is not a viscoelastic property and the consistency of the stiffness-variation with ϵ and $\bar{\rho}_0$ originates from the PFC free energy (Eq. (2.40)), not the PCD equation. Nevertheless, these stiffness results demonstrate the application of the PCD equation since it allows convenient calculation of e_∞ from specified values of $\Delta\bar{P}_0$. According to the results obtained from numerical study, we found that the our proposed PFC-PCD method has the significant potential to predict viscoelastic-creep behavior and its related parameters under step pressure input.

To characterize the viscoelastic behavior and its related parameters including the validation of prediction capability of the PFC-PCD method on viscoelastic behavior in a full spectrum, not only we need to investigate the viscoelastic behavior under step pressure but the investigation of such behavior under sinusoidal pressure oscillation is also required. This type of investigation enables us to study dynamic response and

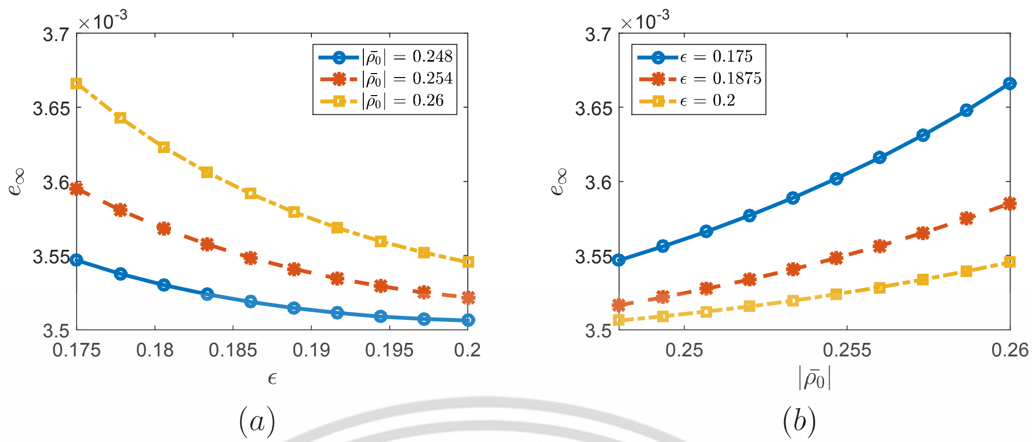

Figure 4.4: Viscoelastic-creep parametric study under step pressure; (a) Influence of ϵ parameter on e_∞ at ϵ parameter ranges between $(0.175, 0.200)$ with three different $|\bar{\rho}_0|$ values (b) Influence of $\bar{\rho}_0$ parameter on e_∞ at $|\bar{\rho}_0|$ parameter ranges between $(0.248, 0.260)$ with three different ϵ values. All numerical experiments are based on step pressure input ($\Delta\bar{P}_0 = 0.02$). Note: All physical variables are in non-dimensionalized quantities.

mechanical-hysteresis behavior of solid material under sinusoidal pressure oscillation. This allows us to determine the complex moduli parameters which is necessary for estimating the damping capacity parameter in damping material design. In next part, we provide the results and discussion on these dynamic behaviors established by the PFC-PCD method and determine the limitation for applying this method in predicting these dynamic behaviors. Also, we introduce our recently developed the PFC-MPCD method to predict dynamic response, mechanical-hysteresis behavior and complex moduli parameters which cannot be produced by the PFC-PCD method accurately.

4.3 Influence of PFC and PCD Parameters on Dynamic Response and Mechanical-Hysteresis Behavior in BCC solid

We divide our investigation into two parts. In the first part, we need to study the influence of PCD parameter, L_{def}, on dynamic response and mechanical-hysteresis behavior under sinusoidal pressure oscillation. This investigation is motivated by the results obtained from the study of the impact of L_{def} parameter on viscoelastic-creep behavior under step pressure. According to that study, we found the L_{def} parameter can be used to control the degree of viscoelasticity ranging from highly viscous to highly elastic which allows us to tune the PFC-PCD model to different types of materials.

Therefore, we extend our study to investigate how this parameter influences system response under sinusoidal pressure oscillation other than step pressure.

In the second part, we focus our study on how PFC parameters i.e. ϵ, which represents temperature, influences complex moduli parameters. The motivation of this study stems from the temperature dependence of damping capacity in viscoelastic materials which is crucial for damping material design. Thus, we need to know how PFC-PCD method can well predict this phenomena when compares the numerical results obtained from our method with the numerous experimental observations.

According to the first study, the results obtained from the simulation demonstrate the similarity to the those of the viscoelastic-creep study, the PCD parameter L_{def} can be used to control the degree of viscoelasticity. Figures 4.5(a) and (b) show the

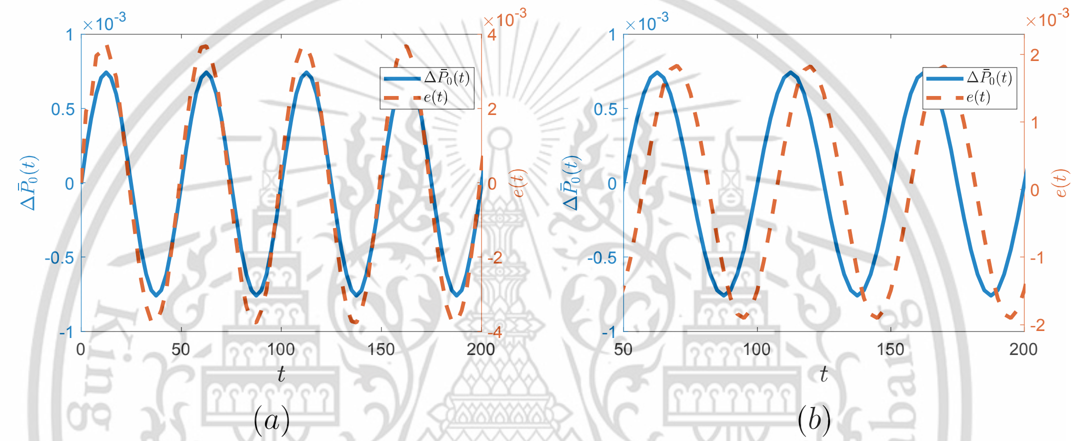

Figure 4.5: Influence of L_{def} parameter on system response; sinusoidal pressure input $\Delta\bar{P}_0(t)$ (solid-line on y-axis) and strain response $e(t)$ (dash-line on y-axis) at time t (x-axis); (a) $L_{\text{def}} = 10$ (b) $L_{\text{def}} = 1$; at $|\bar{\rho}_0| = 0.2600$, $\epsilon = 0.1750$ and $f = 0.02$. Note: All physical variables are in non-dimensionalized quantities.

strain response with different values of L_{def} at fixed pressure-oscillation frequency. The hysteresis loops from these results are also shown in Fig. 4.6. The results show that decreasing the value of L_{def} lead to higher phase lag (Fig. 4.5) and higher damping capacity (Fig. 4.6). This indicates that lowering L_{def} value leads to the system having in a more viscous manner. The opposite is also true where increasing L_{def} leads to a more elastic response from the system.

The influence of ϵ on G'_{storage}, G'_{loss}, and tan(δ) is shown in Fig. 4.7. Figure 4.7(a) shows that an increase in ϵ (decrease in temperature) leads to an increase in G'_{storage} and a decrease in G'_{loss}. As tan(δ) $= G'_{\text{loss}}/G'_{\text{storage}}$, the values of tan($\delta$) decreases with increasing ϵ, as shown in Fig. 4.7(b). The results show that as temperature decreases, the system behaves in a more stiffness and a less viscous manner and with reducing damping capacity. These trends qualitatively agree with numerous experimental observations for storage modulus in polymeric materials [127, 128, 129, 130] and in alloys [131, 132, 133, 134] and for loss tangent factor in polymeric materials below glass transition [133, 135, 136, 137, 138, 139] and metals such as alloys

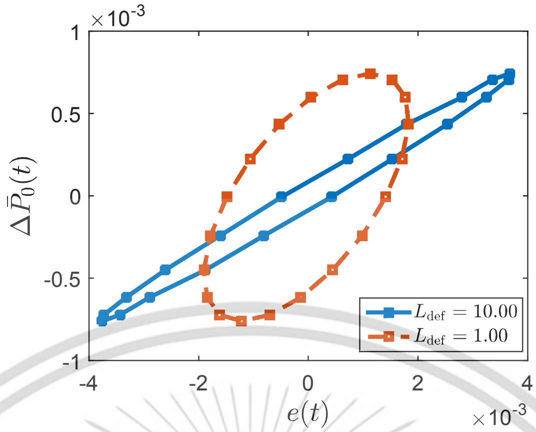

Figure 4.6: Influence of L_{def} on Mechanical-Hysteresis behavior at condition $|\bar{\rho}_0| = 0.2600$, $\epsilon = 0.1750$ and $f = 0.02$ where $e(t)$ (x-axis) is strain response at time t and $\Delta \bar{P}_0(t)$ (y-axis) is pressure input at time t established by PCD equation. Note: All physical variables are in non-dimensionalized quantities.

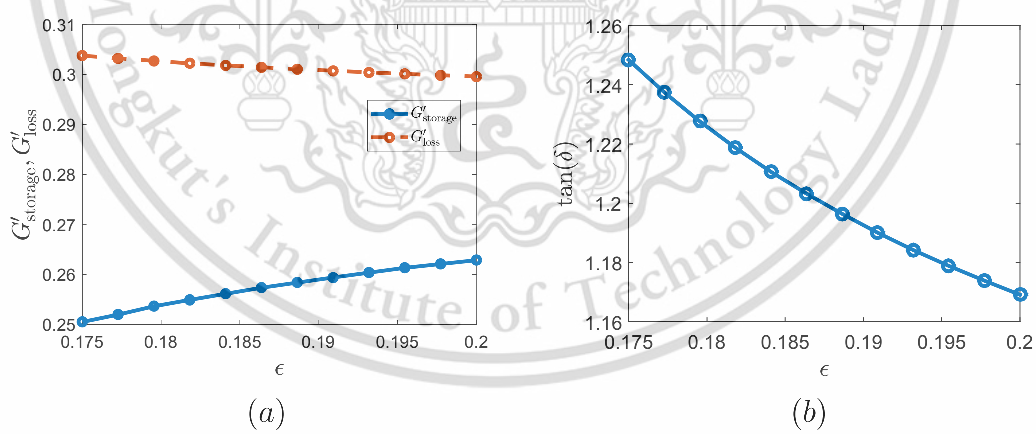

Figure 4.7: Influence of temperature, ϵ (x-axis), parameter on (a) Storage modulus, G'_{storage} (solid-line on y-axis), and loss modulus, G'_{loss} (dash-line on y-axis), and (b) Loss tangent factor, tan(δ) (y-axis), at $|\bar{\rho}_0| = 0.2600$ and $f = 0.02$. It should be noted that the ϵ parameter is inversely related to temperature. Note: All physical variables are in non-dimensionalized quantities.

[75, 140, 141, 142, 143, 144]. These consistencies demonstrate the capability of our method in predicting temperature dependence of complex moduli parameters. We expect that our proposed method can be extended to investigate the problems in a more complex situation when microstructures and defects are presented.

4.4 Mechanical-Hysteresis behavior in BCC solid based on PFC-PCD and PFC-MPCD method

4.4.1 Strain Response and Mechanical-Hysteresis Behavior

In this part, we demonstrate the strain response under sinusoidal pressure oscillation and its mechanical-hysteresis behavior exhibited by PFC-MPCD and PFC-PCD methods. The steady-state strain responses regarding the PFC-MPCD method are given Fig. 4.8(a)-(c) whereas the strain responses regarding the PFC-PCD method are shown in Fig. 4.8(d)-(f) for comparison.

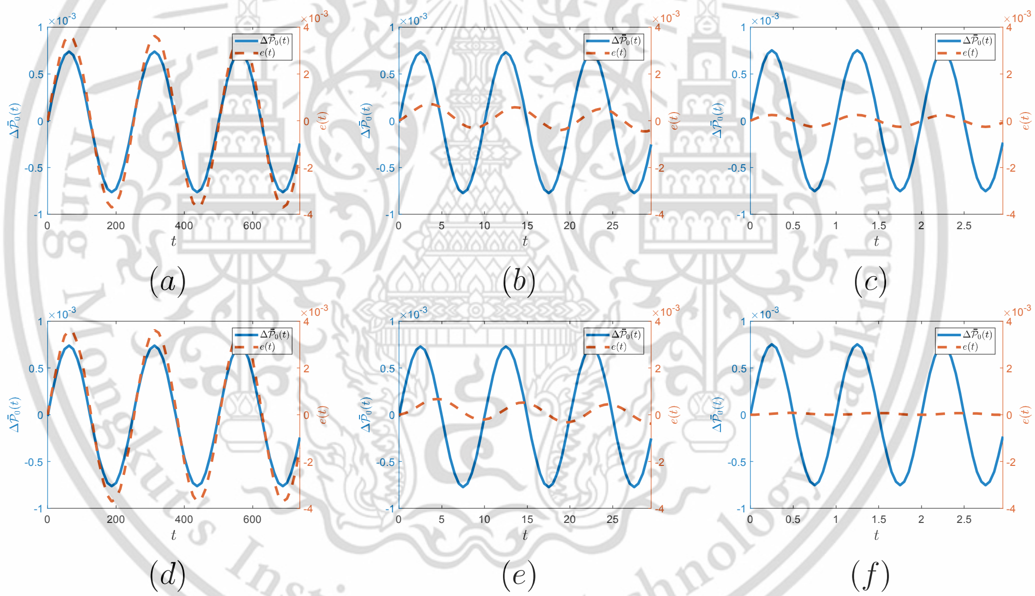

Figure 4.8: Influence of frequency, f, on system response; Sinusoidal pressure input $\Delta\bar{\mathcal{P}}_0(t)$ (solid-line) and strain response $e(t)$ (dash-line) established by PFC-MPCD method (a) $f = 0.004$ (b) $f = 0.1$ (c) $f = 1$ at $\tau = 0.9814$; Sinusoidal pressure input $\Delta\bar{\mathcal{P}}_0(t)$ (solid-line) and strain response $e(t)$ (dash-line) established by PFC-PCD method (d) $f = 0.004$ and (e) $f = 0.1$ (f) $f = 1$. Note that all simulation parameters are set at $|\bar{\rho}_0| = 0.2600$, $\epsilon = 0.1750$ and $L_{\text{def}} = (2\pi\sqrt{2})^3$. Note: All physical variables are in non-dimensionalized quantities.

According to the numerical results at oscillation frequency $f = 0.004$ and $f = 0.1$, the steady-state strain response predicted by both methods are in good agreement to each other. Both methods demonstrate the strain amplitude reduction and increased

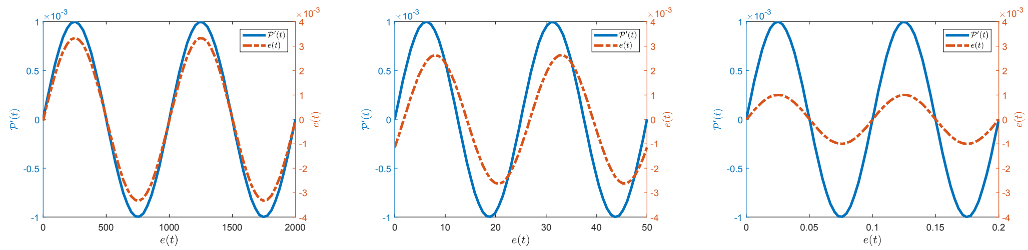

(a) (b) (c)

Figure 4.9: Influence of frequency, f, on system response; sinusoidal pressure oscillation $\mathcal{P}'(t)$ (solid-line) and strain response $e(t)$ (dash-line) established by SLS Model (a) $f = 0.001$ (b) $f = 0.04$ (c) $f = 10$; at parameter condition $\mathcal{P}'_{\mathrm{A}} = 0.001$, $K' = 0.3$ and $\tau' = 1$. These figures demonstrate that the amplitude and the phase angle of system response are influence by pressure oscillation frequency. Note: All physical variables are in non-dimensionalized quantities.

phase lag (phase angle) at elevated oscillation frequency. These results are qualitatively consistent with those of SLS model prediction in Fig. 4.9 (a)-(b). However, at oscillation frequency $f = 1$, both methods seem to behave differently. The amplitude of strain response exhibited by PFC-MPCD method tends to decline to the finite value while phase lag between strain response and pressure oscillation predicted by this method seems to be in-phase at this frequency. On the contrary, the amplitude of strain response exhibited by PFC-PCD method tends to vanish. Moreover, the phase lag between the strain response and pressure oscillation predicted by the PFC-PCD method becomes larger at this frequency which is contrast to SLS model prediction as shown Fig. 4.9(c).

To obtain more insight into these phenomena, we study the impact of frequency f on amplitude ratio A_{r} and phase lag (δ) exhibited by PFC-MPCD and PFC-PCD methods as indicated in Fig. 4.10(a)-(b). It is obvious that both methods exhibit amplitude ratio reduction with increasing frequency. However, this prediction according to the PFC-PCD method tends to vanishingly small at high-frequency range whereas the prediction regarding PFC-MPCD method remains at finite value. Besides, the phase lag predicted by both methods tends to increase at elevated frequency but until the certain value is reached. In particular, the result exhibited by PFC-MPCD method tends to reduce its magnitude with increasing frequency after its peak location, unlike PFC-PCD method prediction which tends to exhibit higher phase lag without the peak location. These results obtained from the numerical study indicate that the prediction demonstrated by both methods are consistent at low-frequency range but tends to differ at high frequency.

The magnitude of the amplitude ratio can also be illustrated in the mechanical-hysteresis loop according to Fig. 4.11(a)-(b) where the results in Fig. 4.8(a)-(f) are plotted on a pressure-strain axis. As the frequency increases, the hysteresis loops predicted by both methods rotate counter-clockwise, indicating smaller strain amplitude (or amplitude ratio). At frequency $f = 1$, the hysteresis loop predicted by the PFC-PCD method

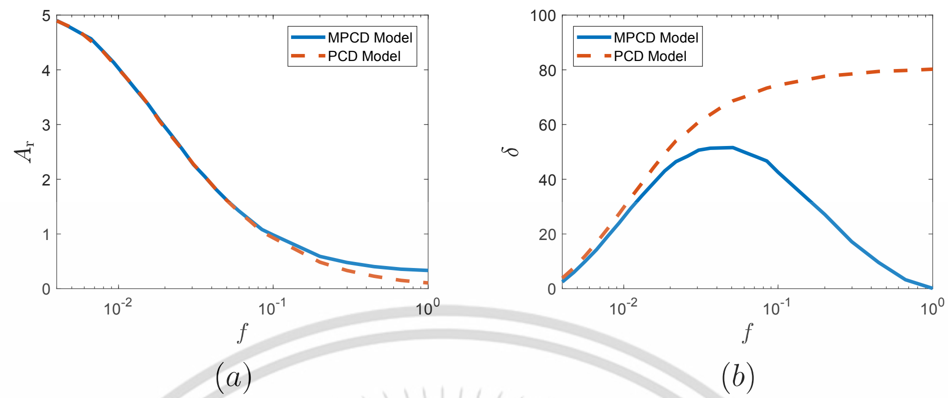

Figure 4.10: Influence of frequency, f, on (a) Amplitude ratio (A_r) predicted by PFC-MPCD method (solid-line) and PFC-PFC method (dash-line) and on (b) Phase angle (δ) or Phase lag predicted by PFC-MPCD method (solid-line) and PFC-PFC method (dash-line). Note that all simulation parameters are set at $|\bar{\rho}_0| = 0.2600$, $\epsilon = 0.1750$, $L_{\text{def}} = (2\pi\sqrt{2})^3$ and $\tau = 0.9814$ for PFC-MPCD method. Note: All physical variables are in non-dimensionalized quantities.

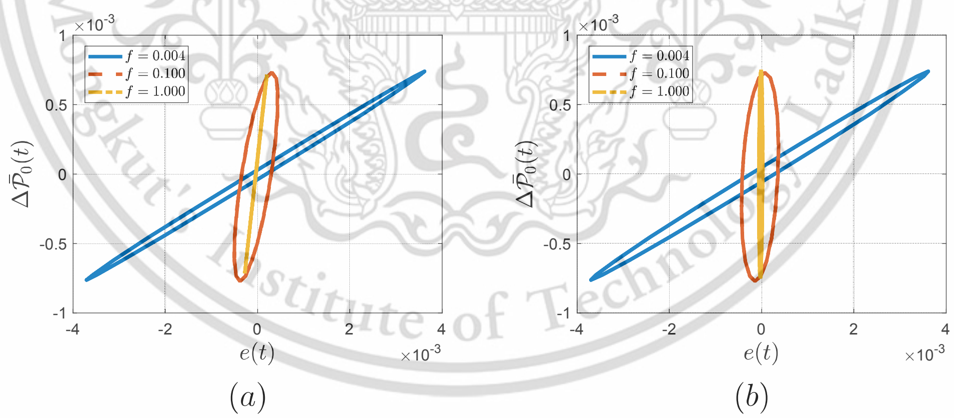

Figure 4.11: Influence of frequency, f, on mechanical-hysteresis behavior (a) Mechanical-hysteresis behavior predicted by PFC-MPCD method corresponding to Fig. 4.8 (a)-(c) at $\tau = 0.9814$; (b) Mechanical-hysteresis behavior predicted by PFC-PCD method corresponding to Fig. 4.8 (d)-(f). Note that all simulation parameters are set at $|\bar{\rho}_0| = 0.2600$, $\epsilon = 0.1750$ and $L_{\text{def}} = (2\pi\sqrt{2})^3$. Note: All physical variables are in non-dimensionalized quantities.

almost forms a vertical line with the y-axis in Fig. 4.11(b) because the amplitude ratio is driven to an extremely small value or almost zero amplitude. This is in contrast to the hysteresis loop predicted by PFC-MPCD method which remains tilted away from the y-axis as indicated by Fig. 4.11(a); this figure shows that strain amplitude has not been driven to zero amplitude at the high-frequency range.

In summary, the results demonstrated by PFC-MPCD method as shown in Fig. 4.10(a)-(b) and Fig. 4.11(a) qualitatively agree with the SLS model as indicated in Fig. 4.12(a)-(c). While, all those results exhibited by PFC-PCD method as illustrated in Fig. 4.10(a)-(b) and Fig. 4.11(b) tend to differ from the SLS model, in particular, at the high-frequency range as indicated in Fig. 4.12(a)-(c). It should be noted that although the dynamic behavior predicted by both methods is well consistent at low frequency range, it is substantial that the PFC-MPCD method is more suitable choice to investigate such behavior at the broader frequency. Therefore, the application of PFC-PCD method should be limited at certain frequency, in particular, at low frequency region.

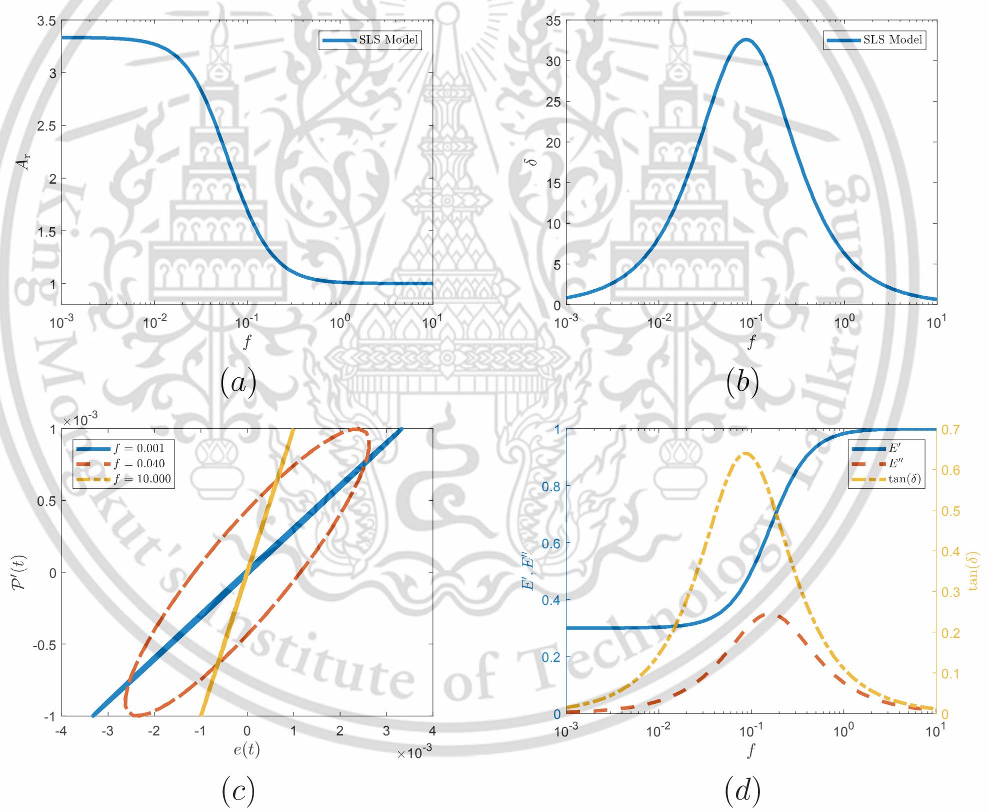

Figure 4.12: Influence of frequency, f, on (a) System amplitude ratio A_r defined by $E_A/\mathcal{P}'_A$ (b) Phase angle δ under pressure sinusoidal oscillation at parameter condition $\mathcal{P}'_\mathrm{A} = 0.001$, $K' = 0.3$ and $\tau' = 1$; (c) Mechanical-Hysteresis curve established by $e(t)$ vs. $\mathcal{P}'(t)$ corresponding to the response provided in Fig. 4.9 (d) Complex moduli parameters at parameter condition $\mathcal{P}'_\mathrm{A} = 0.001$, $K' = 0.3$ and $\tau' = 1$. Note: All physical variables are in non-dimensionalized quantities.

4.4.2 Prediction of Complex Moduli Parameters

In this part, we aim to demonstrate the difference in complex moduli parameters prediction between PFC-MPCD method and PFC-PCD method. All complex moduli parameters exhibited by the PFC-MPC method are illustrated in Fig. 4.13(a). while the results obtained from the PFC-PCD method are showed in Fig. 4.13(b) for comparison.

According to the numerical study, the storage modulus (E') predicted by PFC-MPCD tends to monotonically increased with increasing frequency and becomes constant at the certain frequency while loss modulus (E'') and loss tangent factor ($\tan(\delta)$) tends to increase in magnitude until their peak locations are reached. This is in good agreement with the SLS model prediction in Fig. 4.12(d) and consistent with real solid behavior [9]. In particular, all results predicted by PFC-MPCD method are agreeing with numerous experimental observations which can be found in [116, 117] for shear and young modulus, which are proportional to storage modulus, in In-Sn and Pb-Sn as well as for loss angle in some alloys [118] which is related to loss tangent factor. Besides, this consistency is even more pronounced in rubber [119, 120, 121] and in elastomer [122]. This is in contrast to the results obtained from PFC-PCD prediction in Fig. 4.13(b) where all complex moduli parameters monotonically increased with increasing frequency without peaks location for loss modulus (E'') and loss tangent factor ($\tan(\delta)$) as well as without the certain frequency value which allows storage modulus E' to become constant.

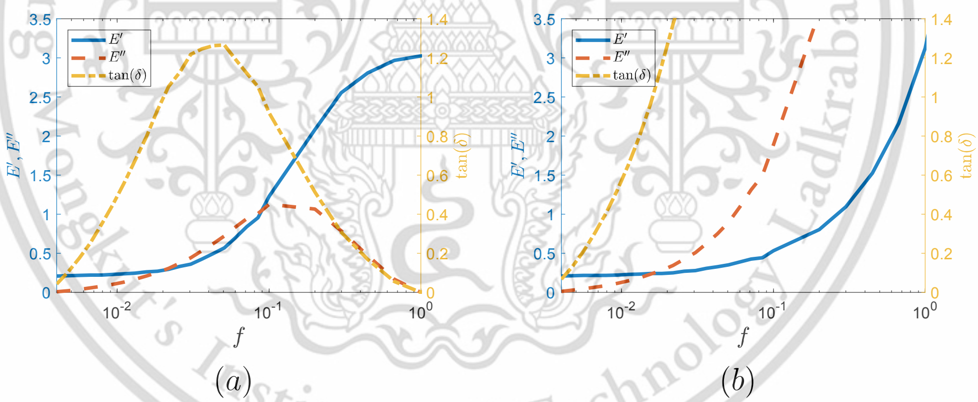

Figure 4.13: Influence of frequency, f, on complex moduli parameters (a) Predicted by PFC-MPCD method; Storage modulus (E') (solid-line), Loss modulus (E'') (dash-line) and Loss tangent factor ($\tan(\delta)$) (dense-dash-line) at $\tau = 0.9814$ (b) Predicted by PFC-PCD method; Storage modulus (E') (solid-line), Loss modulus (E'') (dash-line) and Loss tangent factor ($\tan(\delta)$) (dense-dash-line). Note that all simulation parameters are set at $|\bar{\rho_0}| = 0.2600$, $\epsilon = 0.1750$ and $L_{\text{def}} = (2\pi\sqrt{2})^3$. Note: All physical variables are in non-dimensionalized quantities.

To further investigate into the difference between the results predicted by PFC-MPCD and PFC-PCD methods, we compare each parameter exhibited by both methods in Fig. 4.14(a)-(c). It is obvious that the results obtained from both methods are in good

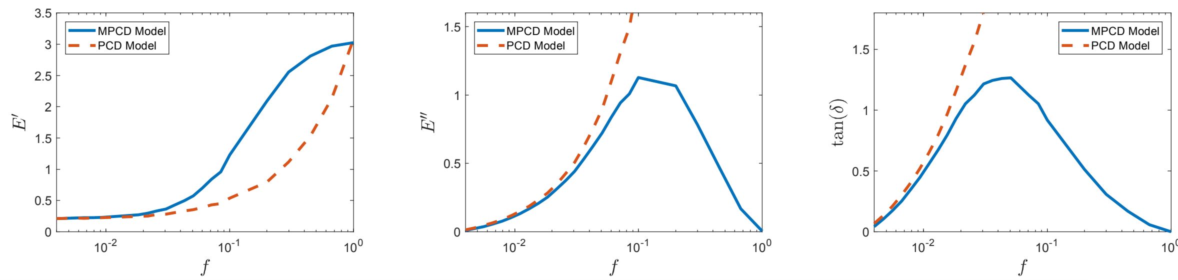

(a) (b) (c)

Figure 4.14: Influence of frequency, f, on complex moduli parameters (a) Storage modulus (E'); predicted by PFC-MPCD method (solid-line) and PFC-PCD method (dash-line) (b) Loss modulus (E''); predicted by PFC-MPCD method (solid-line) and PFC-PCD method (dash-line) (c) Loss tangent factor ($\tan(\delta)$) predicted by PFC-MPCD method (solid-line) and PFC-PCD method (dash-line). Note that all simulation parameters are set at $|\bar{\rho}_0| = 0.2600$, $\epsilon = 0.1750$, $L_{\text{def}} = (2\pi\sqrt{2})^3$ and $\tau = 0.9814$ for PFC-MPCD method. Note: All physical variables are in non-dimensionalized quantities.

agreement in a low-frequency range but tend to differ at very frequency. All complex moduli parameters obtained from PFC-PCD method prediction have increased as increasing frequency without the limit. This is unlike the results obtained from PFC-MPCD method prediction. Although all complex moduli predicted by the method increases as increasing frequency, they tend to become limited at a certain frequency value. In particular, all loss parameters, loss modulus (E'') and loss tangent factor ($\tan(\delta)$), predicted by the PFC-MPCD method can demonstrate at least one peak location. These observations are in good agreement with the real solid behavior suggested by Ref. [9] and experimental evidence that can be found in [116, 117, 118, 119, 120, 121, 122]. The peak location in loss modulus (E'') parameter also indicates the information on the suitable working frequency where the energy is most dissipated in damping material design. On the contrary, the PFC-PCD method cannot provide this information as indicated in Fig. 4.14(b). It should be noted that the particular form of the PFC free energy Eq. (3.2) is applicable to crystalline materials such as metals [22]; therefore, it might seem that the results from this work only restricts to these types of materials. However, since the viscoelastic behavior originates from the MPCD equation, not the PFC free energy, the alternative choices of PFC free energy Eq. (3.2) can be used and the PFC-MPCD method should still exhibit similar viscoelastic behavior correspond to those PFC free energy choices. The capability to generalize the PFC free energy enables us to model viscoelastic behavior in different types of materials such as polymeric materials and elastomer where viscoelasticity behavior is much more pronounced than that in metals.

CHAPTER 5

Research Summary

In this research, we propose a method that incorporates the pressure-controlled dynamic (PCD) equation with the phase-field crystal (PFC) model to investigate viscoelastic behavior [8, 11] which is crucial for studying damping capacity property in damping material design. We refer this particular method as PFC-PCD method. The use of the PCD equation enables convenient control of deformation using external pressure which allows studies of experimentally-observed phenomena involving a system under different types of applied pressure. This benefit provides us an opportunity to study time-dependent deformation behavior like viscoelastic-creep and mechanical hysteresis-behavior in crystalline solid structure under externally applied stress.

The original PCD version was proposed by Kocher and Provatas [15] to investigate a full spectrum of triple phase transition problem. This particular equation offers an opportunity to control the volume of substance by controlling externally applied pressure which can also be used to control the deformation in crystalline solid structure through specifying externally applied stress. Although this equation was successfully to be used to obtain equilibrium states of a system, the validity of the non-equilibrium behavior from this equation needs to be verified due to certain postulations that might not be fully consistent with the non-equilibrium thermodynamic framework. In our preliminary study, we developed the alternative PCD equation which was consistent with classical non-equilibrium thermodynamic framework [86, 88] and made a comparison of the strain responses under step pressure produced by both PCD versions. The results predicted by both methods were slightly different [25] and showed the time-delayed response with a reduction strain rate as time increasing which was indicative of viscoelasticity [26].

We extended our investigation to viscoelastic-creep and mechanical hysteresis behavior in a body-centered-cubic (BCC) crystal structure under hydrostatic pressure using the PFC-PCD method [94]. Although the model could produce viscoelastic-creep behavior accurately and the parametric study results were agreeing with theoretical framework [110, 123] and experimental observations [124, 125, 126], the mechanical-hysteresis behavior and complex moduli parameters predicted by this particular method were not consistent with the standard linear (SLS) model [41, 8] and theoretical perspective suggested by [9], in particular, at very frequency. We analyzed this inconsistency by applying the Taylor's expansion [95] on the existing PCD equation and found that the functional form of the equation is more like Kelvin-Voigt model [41, 7] than

SLS model. There was no the pressure time derivative term available in the present PCD equation. This explained why the existing model could not produced the accurate mechanical-hysteresis behavior and complex moduli parameters, especially, at the high pressure oscillation frequency.

To address this inaccuracy problem, we proposed the modified PCD equation by adding the pressure time derivative term into the existing PCD equation [115]. We referred to this particular equation as the modified pressure-controlled dynamic equation or the MPCD equation. This pressure time derivative term helps MPCD equation in producing mechanical-hysteresis behavior consistent with SLS model, in particular, at high pressure oscillation frequency where the PCD equation is failed. From the numerical study, the results demonstrated that the PFC model which incorporates MPCD equation, referred to as PFC-MPCD method, can predict mechanical-hysteresis behavior and complex moduli parameters consistent with SLS model, the real solid materials behavior suggested by [9] and numerous experimental evidence [116, 117, 118, 119, 120, 121, 122] at the broaden pressure oscillation frequency range.

Finally, It should be noted that the free energy functional form used in our work is limited to the formulation proposed by Wu [22] which is suitable for studying BCC solid structure. Furthermore, the crystal structure presented in our work is still limited to a perfect BCC unit cell. Yet, we expect that our method can be extended to a more complex system with microstructural features such as grain boundary, dislocation, surface or even with other free energy functional form where viscoelasticity behavior is much more pronounced and still be capable of exhibiting the accurate mechanical-hysteresis behavior and complex moduli parameters which allows us to predict more reliable damping capacity in damping material design.

Bibliography

[1] R. W. Balluffi, S. Allen, and W. C. Carter, *Kinetics of materials*. John Wiley & Sons, 2005.

[2] T. C. Steel, "Structural steel square pipe," *Thanasarn Central Steel Webpage*, vol. (Products), 2019.

[3] S. S. Structure, "Structural steel building," *Sanhe Steel Structure Webpage*, vol. (Products), 2019.

[4] N. N. Novitech, "Noise and vibration damping rubber," *Nyco Namyang Novitech Webpage*, vol. (Products), 2019.

[5] Farrat, "Isolated foundations," *Farrat Webpage*, vol. (Products), 2019.

[6] L. Dong and R. Lakes, "Advanced damper with high stiffness and high hysteresis damping based on negative structural stiffness," *International Journal of Solids and Structures*, vol. 50, no. 14-15, pp. 2416–2423, 2013.

[7] W. F. Hosford, *Mechanical behavior of materials*. Cambridge university press, 2010.

[8] R. Lakes and R. S. Lakes, *Viscoelastic materials*. Cambridge university press, 2009.

[9] T. Pritz, "Frequency dependences of complex moduli and complex poisson's ratio of real solid materials," *Journal of Sound and Vibration*, vol. 214, no. 1, pp. 83–104, 1998.

[10] Chem538w10grp1, "Dynamic mechanical analysis figure," *Wikepedia*, vol. (Dynamic mechanical analysis page), 2010.

[11] R. S. Lakes, *Viscoelastic solids*, vol. 9. CRC press, 1998.

[12] D. Raabe, "Computational materials science-the simulation of materials microstructures and properties," 1998.

[13] D. Raabe, F. Roters, F. Barlat, and L.-Q. Chen, *Continuum scale simulation of engineering materials: fundamentals-microstructures-process applications*. John Wiley & Sons, 2004.

[14] S. B. Biner, *Programming phase-field modeling*. Springer, 2017.

[15] G. Kocher and N. Provatas, "New density functional approach for solid-liquid-vapor transitions in pure materials," *Physical review letters*, vol. 114, no. 15, p. 155501, 2015.

[16] N. Provatas and K. Elder, *Phase-field methods in materials science and engineering*. John Wiley & Sons, 2011.

[17] K. Elder, N. Provatas, J. Berry, P. Stefanovic, and M. Grant, "Phase-field crystal modeling and classical density functional theory of freezing," *Physical Review B*, vol. 75, no. 6, p. 064107, 2007.

[18] J. Yarnell, M. Katz, R. G. Wenzel, and S. Koenig, "Structure factor and radial distribution function for liquid argon at 85 k," *Physical Review A*, vol. 7, no. 6, p. 2130, 1973.

[19] K. Elder and M. Grant, "Modeling elastic and plastic deformations in nonequilibrium processing using phase field crystals," *Physical Review E*, vol. 70, no. 5, p. 051605, 2004.

[20] K. Aust and B. Chalmers, "Metal interfaces," *American Society for Metals*, vol. 1, p. 153, 1952.

[21] N. A. Gjostein and F. Rhines, "Absolute interfacial energies of [001] tilt and twist grain boundaries in copper," *Acta Metallurgica*, vol. 7, no. 5, pp. 319–330, 1959.

[22] K.-A. Wu and A. Karma, "Phase-field crystal modeling of equilibrium bcc-liquid interfaces," *Physical Review B*, vol. 76, no. 18, p. 184107, 2007.

[23] T. Hirouchi, T. Takaki, and Y. Tomita, "Development of numerical scheme for phase field crystal deformation simulation," *Computational Materials Science*, vol. 44, no. 4, pp. 1192–1197, 2009.

[24] N. Provatas, J. Dantzig, B. Athreya, P. Chan, P. Stefanovic, N. Goldenfeld, and K. Elder, "Using the phase-field crystal method in the multi-scale modeling of microstructure evolution," *Jom*, vol. 59, no. 7, pp. 83–90, 2007.

[25] J. Em-Udom and N. Pisutha-Arnond, "Pressure-controlled dynamic equation for the phase-field crystal method," in *IOP Conference Series: Materials Science and Engineering*, vol. 361, p. 012006, IOP Publishing, 2018.

[26] J. Em-Udom and N. Pisutha-Arnond, "Investigation on viscoelastic-creep behavior of the phase-field crystal method," in *IOP Conference Series: Materials Science and Engineering*, vol. 361, p. 012009, IOP Publishing, 2018.

[27] J.-L. Barrat and J.-P. Hansen, *Basic concepts for simple and complex liquids*. Cambridge University Press, 2003.

[28] K. Huang, "Statistical mechanics, john wily & sons," *New York*, 1963.

[29] J. W. Cahn and J. E. Hilliard, "Free energy of a nonuniform system. i. interfacial free energy," *The Journal of chemical physics*, vol. 28, no. 2, pp. 258–267, 1958.

[30] P. C. Hohenberg and B. I. Halperin, "Theory of dynamic critical phenomena," *Reviews of Modern Physics*, vol. 49, no. 3, p. 435, 1977.

[31] K. Elder, M. Katakowski, M. Haataja, and M. Grant, "Modeling elasticity in crystal growth," *Physical review letters*, vol. 88, no. 24, p. 245701, 2002.

[32] I. R. McDonald and J. Hansen, *Theory of simple liquids*. Academic, 1976.

[33] S. P. Das, *Statistical physics of liquids at freezing and beyond*. Cambridge University Press, 2011.

[34] H. Emmerich, H. Löwen, R. Wittkowski, T. Gruhn, G. I. Tóth, G. Tegze, and L. Gránásy, "Phase-field-crystal models for condensed matter dynamics on atomic length and diffusive time scales: an overview," *Advances in Physics*, vol. 61, no. 6, pp. 665–743, 2012.

[35] A. Santos, "A concise course on the theory of classical liquids," *Lecture Notes in Physics*, vol. 923, 2016.

[36] R. Evans, "The nature of the liquid-vapour interface and other topics in the statistical mechanics of non-uniform, classical fluids," *Advances in Physics*, vol. 28, no. 2, pp. 143–200, 1979.

[37] N. Pisutha-Arnond, V. Chan, M. Iyer, V. Gavini, and K. Thornton, "Classical density functional theory and the phase-field crystal method using a rational function to describe the two-body direct correlation function," *Physical Review E*, vol. 87, no. 1, p. 013313, 2013.

[38] K.-A. Wu, A. Karma, J. J. Hoyt, and M. Asta, "Ginzburg-landau theory of crystalline anisotropy for bcc-liquid interfaces," *Physical Review B*, vol. 73, no. 9, p. 094101, 2006.

[39] F. Larché and J. W. Cahn, "A linear theory of thermochemical equilibrium of solids under stress," *Acta metallurgica*, vol. 21, no. 8, pp. 1051–1063, 1973.

[40] P. Voorhees and W. C. Johnson, "The thermodynamics of elastically stressed crystals," *Solid State Physics-Advances in Research and Applications*, vol. 59, no. C, pp. 1–201, 2004.

[41] W. N. Findley and F. A. Davis, *Creep and relaxation of nonlinear viscoelastic materials*. Courier Corporation, 2013.

[42] L.-Q. Chen and W. Yang, "Computer simulation of the domain dynamics of a quenched system with a large number of nonconserved order parameters: The grain-growth kinetics," *Physical Review B*, vol. 50, no. 21, p. 15752, 1994.

[43] B. Morin, K. R. Elder, M. Sutton, and M. Grant, "Model of the kinetics of polymorphous crystallization," *Physical review letters*, vol. 75, no. 11, p. 2156, 1995.

[44] A. Jacobs, "Landau theory of structures in tetragonal-orthorhombic ferroelastics," *Physical Review B*, vol. 61, no. 10, p. 6587, 2000.

[45] M. Sanati, A. Saxena, T. Lookman, and R. Albers, "Landau free energy for a bcc-hcp reconstructive phase transformation," *Physical Review B*, vol. 63, no. 22, p. 224114, 2001.

[46] Y. Wang, Y. Jin, A. Cuitino, and A. Khachaturyan, "Phase field microelasticity theory and modeling of multiple dislocation dynamics," *Applied Physics Letters*, vol. 78, no. 16, pp. 2324–2326, 2001.

[47] W. T. Read and W. Shockley, "Dislocation models of crystal grain boundaries," *Physical review*, vol. 78, no. 3, p. 275, 1950.

[48] J. Matthews and A. Blakeslee, "Defects in epitaxial multilayers: I. misfit dislocations," *Journal of Crystal growth*, vol. 27, pp. 118–125, 1974.

[49] C. Harrison, D. H. Adamson, Z. Cheng, J. M. Sebastian, S. Sethuraman, D. A. Huse, R. A. Register, and P. Chaikin, "Mechanisms of ordering in striped patterns," *Science*, vol. 290, no. 5496, pp. 1558–1560, 2000.

[50] D. Boyer and J. Vinals, "Weakly nonlinear theory of grain boundary motion in patterns with crystalline symmetry," *Physical review letters*, vol. 89, no. 5, p. 055501, 2002.

[51] F. Pardo, F. De La Cruz, P. Gammel, E. Bucher, and D. Bishop, "Observation of smectic and moving-bragg-glass phases in flowing vortex lattices," *Nature*, vol. 396, no. 6709, p. 348, 1998.

[52] M. Laradji, H. Guo, M. Grant, and M. J. Zuckermann, "Phase diagram of a lattice model for ternary mixtures of water, oil, and surfactants," *Physical Review A*, vol. 44, no. 12, p. 8184, 1991.

[53] C. Sagui and R. C. Desai, "Late-stage kinetics of systems with competing interactions quenched into the hexagonal phase," *Physical Review E*, vol. 52, no. 3, p. 2807, 1995.

[54] D. Orlikowski, C. Sagui, A. Somoza, and C. Roland, "Large-scale simulations of phase separation of elastically coherent binary alloy systems," *Physical Review B*, vol. 59, no. 13, p. 8646, 1999.

[55] J. Swift and P. C. Hohenberg, "Hydrodynamic fluctuations at the convective instability," *Physical Review A*, vol. 15, no. 1, p. 319, 1977.

[56] M. C. Cross and P. C. Hohenberg, "Pattern formation outside of equilibrium," *Reviews of modern physics*, vol. 65, no. 3, p. 851, 1993.

[57] P. M. Chaikin and T. C. Lubensky, *Principles of condensed matter physics*, vol. 1. Cambridge university press Cambridge, 2000.

[58] F. Seitz, *The modern theory of solids*, vol. 6. McGraw-Hill New York, 1940.

[59] R. Sreidel Jr and C. Makerov, "The tensile properties of some engineering materials at moderate rates of strain," tech. rep., Univ. of California, Livermore, 1960.

[60] T. Ramakrishnan and M. Yussouff, "First-principles order-parameter theory of freezing," *Physical Review B*, vol. 19, no. 5, p. 2775, 1979.

[61] J. Berry, M. Grant, and K. Elder, "Diffusive atomistic dynamics of edge dislocations in two dimensions," *Physical Review E*, vol. 73, no. 3, p. 031609, 2006.

[62] L. Capolungo, D. Spearot, M. Cherkaoui, D. McDowell, J. Qu, and K. Jacob, "Dislocation nucleation from bicrystal interfaces and grain boundary ledges: Relationship to nanocrystalline deformation," *Journal of the Mechanics and Physics of Solids*, vol. 55, no. 11, pp. 2300–2327, 2007.

[63] T. Shimokawa, A. Nakatani, and H. Kitagawa, "Grain-size dependence of the relationship between intergranular and intragranular deformation of nanocrystalline al by molecular dynamics simulations," *Physical Review B*, vol. 71, no. 22, p. 224110, 2005.

[64] J. Schiøtz and K. W. Jacobsen, "A maximum in the strength of nanocrystalline copper," *Science*, vol. 301, no. 5638, pp. 1357–1359, 2003.

[65] A. Haslam, D. Moldovan, V. Yamakov, D. Wolf, S. Phillpot, and H. Gleiter, "Stress-enhanced grain growth in a nanocrystalline material by molecular-dynamics simulation," *Acta Materialia*, vol. 51, no. 7, pp. 2097–2112, 2003.

[66] A. Haslam, V. Yamakov, D. Moldovan, D. Wolf, S. Phillpot, and H. Gleiter, "Effects of grain growth on grain-boundary diffusion creep by molecular-dynamics simulation," *Acta Materialia*, vol. 52, no. 7, pp. 1971–1987, 2004.

[67] M. Plischke and B. Bergersen, *Equilibrium statistical physics*. World Scientific Publishing Company, 2006.

[68] M. Greenwood, N. Provatas, and J. Rottler, "Free energy functionals for efficient phase field crystal modeling of structural phase transformations," *Physical review letters*, vol. 105, no. 4, p. 045702, 2010.

[69] S. Mkhonta, K. Elder, and Z.-F. Huang, "Exploring the complex world of two-dimensional ordering with three modes," *Physical review letters*, vol. 111, no. 3, p. 035501, 2013.

[70] S. M. Walas, *Phase equilibria in chemical engineering*. Butterworth-Heinemann, 2013.

[71] J. D. Ferry, *Viscoelastic properties of polymers*. John Wiley & Sons, 1980.

[72] A. Drozdov and J. d. Christiansen, “Viscoelasticity and viscoplasticity of semicrystalline polymers: Structure–property relations for high-density polyethylene,” *Computational materials science*, vol. 39, no. 4, pp. 729–751, 2007.

[73] E. Frey, K. Kroy, and J. Wilhelm, “Viscoelasticity of biopolymer networks and statistical mechanics of semiflexible polymers,” in *Advances in structural biology*, vol. 5, pp. 135–168, Elsevier, 1999.

[74] H. Di Benedetto, F. Olard, C. Sauzéat, and B. Delaporte, “Linear viscoelastic behaviour of bituminous materials: From binders to mixes,” *Road Materials and Pavement Design*, vol. 5, no. sup1, pp. 163–202, 2004.

[75] I. Ritchie, K. Sprungmann, and M. Sahoo, “Internal friction in sonoston-a high damping mn/cu-based alloy for marine propeller applications,” *Le Journal de Physique Colloques*, vol. 46, no. C10, pp. C10–409, 1985.

[76] K. Otsuka and C. M. Wayman, *Shape memory materials*. Cambridge university press, 1999.

[77] C. Rosen, B. V. Hiremath, and R. Newnham, *Piezoelectricity*. No. 5, Springer Science & Business Media, 1992.

[78] S. R. White, N. R. Sottos, P. H. Geubelle, J. S. Moore, M. Kessler, S. Sriram, E. Brown, and S. Viswanathan, “Autonomic healing of polymer composites,” *Nature*, vol. 409, no. 6822, p. 794, 2001.

[79] R. O. St, C. Weiss, J. L. Denlinger, and E. A. Balazs, “A preliminary assessment of na-hyaluronate injection into” no man’s land” for primary flexor tendon repair.,” *Clinical orthopaedics and related research*, no. 146, pp. 269–275, 1980.

[80] V. B. Braginsky, V. Mitrofanov, and V. I. Panov, *Systems with small dissipation*. University of Chicago Press, 1985.

[81] H. G. Craighead, “Nanoelectromechanical systems,” *Science*, vol. 290, no. 5496, pp. 1532–1535, 2000.

[82] R. Lifshitz and M. L. Roukes, “Thermoelastic damping in micro-and nanomechanical systems,” *Physical review B*, vol. 61, no. 8, p. 5600, 2000.

[83] J. Kim and J.-Y. Choi, “Performance test for transmitted noise reduction of smart panels using piezoelectric shunt damping,” *Smart materials and structures*, vol. 14, no. 4, p. 587, 2005.

[84] R. Fan, G. Meng, J. Yang, and C. He, “Experimental study of the effect of viscoelastic damping materials on noise and vibration reduction within railway vehicles,” *Journal of Sound and Vibration*, vol. 319, no. 1-2, pp. 58–76, 2009.

[85] S. Elias and V. Matsagar, "Research developments in vibration control of structures using passive tuned mass dampers," *Annual Reviews in Control*, vol. 44, pp. 129–156, 2017.

[86] S. R. De Groot and P. Mazur, *Non-equilibrium thermodynamics*. Courier Corporation, 2013.

[87] Y. Mishin, J. Warren, R. Sekerka, and W. Boettinger, "Irreversible thermodynamics of creep in crystalline solids," *Physical Review B*, vol. 88, no. 18, p. 184303, 2013.

[88] G. Lebon, D. Jou, and J. Casas-Vázquez, *Understanding non-equilibrium thermodynamics*, vol. 295. Springer, 2008.

[89] L. Dai and R. N. Jazar, *Nonlinear Approaches in Engineering Applications*. Springer, 2012.

[90] K.-A. Wu, A. Adland, and A. Karma, "Phase-field-crystal model for fcc ordering," *Physical review E*, vol. 81, no. 6, p. 061601, 2010.

[91] H. Löwen, "A phase-field-crystal model for liquid crystals," *Journal of Physics: Condensed Matter*, vol. 22, no. 36, p. 364105, 2010.

[92] L. E. Malvern, *Introduction to the Mechanics of a Continuous Medium*. No. Monograph, 1969.

[93] J. W. Rudnicki, *Fundamentals of continuum mechanics*. John Wiley & Sons, 2014.

[94] J. Em-Udom and N. Pisutha-Arnond, "Investigation of viscoelastic-creep and mechanical hysteresis behaviors of hydrostatically-stressed crystal using the phase field crystal method," *Advances in Mathematical Physics, Hindawi*, vol. (In Press), 2019.

[95] G. B. Arfken and H. J. Weber, *Mathematical methods for physicists*. AAPT, 1999.

[96] G. Sewell, *The numerical solution of ordinary and partial differential equations*, vol. 75. John Wiley & Sons, 2005.

[97] X.-S. Yang, *Introduction to computational mathematics*. World Scientific Publishing Company, 2014.

[98] L. Q. Chen and J. Shen, "Applications of semi-implicit fourier-spectral method to phase field equations," *Computer Physics Communications*, vol. 108, no. 2-3, pp. 147–158, 1998.

[99] L. N. Trefethen, *Spectral methods in MATLAB*, vol. 10. Siam, 2000.

[100] J. P. Boyd, *Chebyshev and Fourier spectral methods*. Courier Corporation, 2001.

[101] T. Pusztai, G. Tegze, G. I. Tóth, L. Környei, G. Bansel, Z. Fan, and L. Gránásy, "Phase-field approach to polycrystalline solidification including heterogeneous and homogeneous nucleation," *Journal of Physics: Condensed Matter*, vol. 20, no. 40, p. 404205, 2008.

[102] M. Greenwood, N. Ofori-Opoku, J. Rottler, and N. Provatas, "Modeling structural transformations in binary alloys with phase field crystals," *Physical Review B*, vol. 84, no. 6, p. 064104, 2011.

[103] P. Y. Chan, N. Goldenfeld, and J. Dantzig, "Molecular dynamics on diffusive time scales from the phase-field-crystal equation," *Physical Review E*, vol. 79, no. 3, p. 035701, 2009.

[104] T. Hirouchi, T. Takaki, and Y. Tomita, "Effects of temperature and grain size on phase-field-crystal deformation simulation," *International Journal of Mechanical Sciences*, vol. 52, no. 2, pp. 309–319, 2010.

[105] J. Berry, K. Elder, and M. Grant, "Melting at dislocations and grain boundaries: A phase field crystal study," *Physical Review B*, vol. 77, no. 22, p. 224114, 2008.

[106] J. Mellenthin, A. Karma, and M. Plapp, "Phase-field crystal study of grain-boundary premelting," *Physical Review B*, vol. 78, no. 18, p. 184110, 2008.

[107] P. Stefanovic, M. Haataja, and N. Provatas, "Phase-field crystals with elastic interactions," *Physical review letters*, vol. 96, no. 22, p. 225504, 2006.

[108] P. Y. Chan, G. Tsekenis, J. Dantzig, K. A. Dahmen, and N. Goldenfeld, "Plasticity and dislocation dynamics in a phase field crystal model," *Physical review letters*, vol. 105, no. 1, p. 015502, 2010.

[109] S. Hu and S. Wang, "The influences of crystal orientation and crack interaction on the initiation of growth and propagation mode of microcrack: A phase-field-crystal study," *Physica B: Condensed Matter*, vol. 552, pp. 104–109, 2019.

[110] N. Pisutha-Arnond, V. Chan, K. Elder, and K. Thornton, "Calculations of isothermal elastic constants in the phase-field crystal model," *Physical Review B*, vol. 87, no. 1, p. 014103, 2013.

[111] Z.-L. Wang, Z.-F. Huang, and Z. Liu, "Elastic constants of stressed and unstressed materials in the phase-field crystal model," *Physical Review B*, vol. 97, no. 14, p. 144112, 2018.

[112] W. Zhou, J. Wang, Z. Wang, Y. Huang, C. Guo, J. Li, and Y. Guo, "Elastic strain response in the modified phase-field-crystal model," *Chinese Physics B*, vol. 26, no. 9, p. 090702, 2017.

[113] P. Stefanovic, M. Haataja, and N. Provatas, "Phase field crystal study of deformation and plasticity in nanocrystalline materials," *Physical Review E*, vol. 80, no. 4, p. 046107, 2009.

[114] Y.-L. Lu, T.-T. Hu, G.-M. Lu, and Z. Chen, "Phase-field crystal study of segregation induced grain-boundary premelting in binary alloys," *Physica B: Condensed Matter*, vol. 451, pp. 128–133, 2014.

[115] J. Em-Udom and N. Pisutha-Arnond, "Prediction of mechanical-hysteresis behavior and complex moduli using the phase field crystal method with modifed pressure controlled dynamic equation," *Material Reserach Express, Institute of Physics, IOP Publishing*, vol. (In Press), 2019.

[116] R. Lakes and J. Quackenbush, "Viscoelastic behaviour in indium-tin alloys over a wide range of frequencies and times," *Philosophical Magazine Letters*, vol. 74, no. 4, pp. 227–232, 1996.

[117] P. Buechner, D. Stone, and R. Lakes, "Viscoelastic behavior of superplastic 37 wt% pb 63 wt% sn over a wide range of frequency and time," *Scripta materialia*, vol. 41, no. 5, pp. 561–567, 1999.

[118] G. Cagnoli, L. Gammaitoni, J. Kovalik, F. Marchesoni, and M. Punturo, "Low-frequency internal friction in clamped-free thin wires," *Physics Letters A*, vol. 255, no. 4-6, pp. 230–235, 1999.

[119] A. R. Payne and J. R. Scott, *Engineering design with rubber: the properties, testing, and design of rubber as an engineering material*. Maclaren, 1960.

[120] Y. Wada, R. Ito, and H. Ochiai, "Comparison between mechanical relaxations associated with volume and shear deformations in styrene-butadiene rubber," *Journal of the Physical Society of Japan*, vol. 17, no. 1, pp. 213–218, 1962.

[121] L. Rouleau, R. Pirk, B. Pluymers, and W. Desmet, "Characterization and modeling of the viscoelastic behavior of a self-adhesive rubber using dynamic mechanical analysis tests," *Journal of Aerospace Technology and Management*, vol. 7, no. 2, pp. 200–208, 2015.

[122] V. Sessner, A. Jackstadt, W. Liebig, L. Kärger, and K. Weidenmann, "Damping characterization of hybrid carbon fiber elastomer metal laminates using experimental and numerical dynamic mechanical analysis," *Journal of Composites Science*, vol. 3, no. 1, p. 3, 2019.

[123] J. Wachtman Jr, W. Tefft, D. Lam Jr, and C. Apstein, "Exponential temperature dependence of young's modulus for several oxides," *Physical review*, vol. 122, no. 6, p. 1754, 1961.

[124] P. M. Sutton, "The variation of the elastic constants of crystalline aluminum with temperature between 63 k and 773 k," *Physical Review*, vol. 91, no. 4, p. 816, 1953.

[125] W. Chancellor, A. Wolfenden, and G. Ludtka, "Temperature dependence of young's modulus and shear modulus in uranium-2.4 wt% niobium alloy," *Journal of Nuclear Materials*, vol. 171, no. 2-3, pp. 389–394, 1990.

[126] R. Bruls, H. Hintzen, G. De With, and R. Metselaar, “The temperature dependence of the young’s modulus of mgsin2, aln and si3n4,” *Journal of the European Ceramic Society*, vol. 21, no. 3, pp. 263–268, 2001.

[127] J. K. Pandey, A. P. Kumar, M. Misra, A. K. Mohanty, L. T. Drzal, and R. Palsingh, “Recent advances in biodegradable nanocomposites,” *Journal of Nanoscience and Nanotechnology*, vol. 5, no. 4, pp. 497–526, 2005.

[128] G. Kotzev, S. Djoumaliisky, M. Natova, and R. Benavente, “Vibration-assisted melt compounding of polypropylene/carbon black composites: Processability, filler dispersion and mechanical properties,” *Journal of Reinforced Plastics and Composites*, vol. 31, no. 20, pp. 1353–1363, 2012.

[129] S. R. Valandro, P. C. Lombardo, A. L. Poli, M. A. Horn Jr, M. G. Neumann, and C. C. S. Cavalheiro, “Thermal properties of poly (methyl methacrylate)/ organomodified montmorillonite nanocomposites obtained by in situ photopolymerization,” *Materials Research*, vol. 17, no. 1, pp. 265–270, 2014.

[130] M. Bastiurea, M. Rodeanu, D. Dima, M. Murarescu, and G. Andrei, “Thermal and mechanical properties of polyester composites with graphene oxide and graphite.,” *Digest Journal of Nanomaterials & Biostructures (DJNB)*, vol. 10, no. 2, 2015.

[131] W.-y. Wang, B. Liu, and V. Kodur, “Effect of temperature on strength and elastic modulus of high-strength steel,” *Journal of materials in civil engineering*, vol. 25, no. 2, pp. 174–182, 2012.

[132] Y. Ji, X. Ding, T. Lookman, K. Otsuka, and X. Ren, “Heterogeneities and strain glass behavior: Role of nanoscale precipitates in low-temperature-aged ti 48.7 ni 51.3 alloys,” *Physical Review B*, vol. 87, no. 10, p. 104110, 2013.

[133] J. Cox, D. Luong, V. Shunmugasamy, N. Gupta, O. Strbik, and K. Cho, “Dynamic and thermal properties of aluminum alloy a356/silicon carbide hollow particle syntactic foams,” *Metals*, vol. 4, no. 4, pp. 530–548, 2014.

[134] H. Ma, J. Yang, F. Lu, F. Qin, W. Xiao, and X. Zhao, “A fenimnc alloy with strain glass transition,” *Progress in Natural Science: Materials International*, vol. 28, no. 1, pp. 74–77, 2018.

[135] D. I. Jones, “Handbook of viscoelastic vibration damping,” *Handbook of viscoelastic vibration damping, John Wiley & Sons, (2001).*

[136] S. Iwayanagi and T. Hideshima, “Low frequency coupled oscillator and its application to high polymer study,” *Journal of the Physical Society of Japan*, vol. 8, no. 3, pp. 365–368, 1953.

[137] R. N. Capps and L. L. Beumel, “Dynamic mechanical testing: Application of polymer development to constrained-layer damping,” ACS Publications, 1990.

[138] Y. Zhang, R. Adams, and L. F. Da Silva, “A rapid method of measuring the glass transition temperature using a novel dynamic mechanical analysis method,” *The Journal of Adhesion*, vol. 89, no. 10, pp. 785–806, 2013.

[139] M. Verma, D. Patidar, M. Baboo, K. Sharma, and N. Saxena, “Storage modulus and glass transition temperature of mwnt/pmma polymer nanocomposite films with different wt% of mwnt,”

[140] T.-S. Kê, “Experimental evidence of the viscous behavior of grain boundaries in metals,” *Phys. Rev.*, vol. 71, pp. 533–546, 1947.

[141] T.-S. Kê, “Viscous slip along grain boundaries and diffusion of zinc in alpha-brass,” *Journal of Applied Physics*, vol. 19, no. 3, pp. 285–290, 1948.

[142] S. Huang, N. Li, Y. Wen, J. Teng, Y. Xu, and S. Ding, “Temperature dependence of the damping capacity in fe–19.35 mn alloy,” *Journal of Alloys and Compounds*, vol. 455, no. 1-2, pp. 225–230, 2008.

[143] Y.-Q. Jiao, Y.-H. Wen, L. Ning, J.-Q. He, and T. Jin, “Effect of environmental temperature on damping capacity of cu-al-mn alloy,” *Transactions of Nonferrous Metals Society of China*, vol. 19, no. 3, pp. 616–619, 2009.

[144] L. Licitra, D. D. Luong, O. M. Strbik III, and N. Gupta, “Dynamic properties of alumina hollow particle filled aluminum alloy a356 matrix syntactic foams,” *Materials & Design*, vol. 66, pp. 504–515, 2015.

[145] J. Zhang, R. Perez, and E. Lavernia, “Documentation of damping capacity of metallic, ceramic and metal-matrix composite materials,” *Journal of Materials Science*, vol. 28, no. 9, pp. 2395–2404, 1993.

APPENDIX

APPENDIX A

Preliminary Study in One-Dimensional Crystal Structure

The pressure-controlled-dynamics (PCD) equation was first introduced by Kocher and Provatas [15]. This equation allows us to measure the strain by specifying externally applied stress which is suitable for using to study viscoelastic-creep, mechanical-hysteresis behavior and complex moduli parameters. With incorporating the PFC method, this method is referred to as PFC-PCD method. Although they used this particular method to investigate the full spectrum of solid-liquid-vapor transitions, unfortunately, the viscoelastic-creep, mechanical-hysteresis behavior and complex moduli parameters which can be reproduced from that equation were not focused area and, of course, not addressed in their work [15].

We first implemented this particular technique to investigate the strain response under step pressure in one-dimensional crystal structure in our previous work [25, 26]. According to the result, the strain response predicted by the method showed time-delayed response which was indicative of viscoelastic-creep behavior as we expected. Therefore, we extend our study to the three-dimensional BCC crystal structure to obtain a more practical viscoelastic behavior.

In this appendix, we provide the preliminary study results of viscoelastic-creep behavior in one-dimensional crystal structure. This appendix is organized as follows. In part (A.1), we compare the numerical simulation of time-dependent deformation behavior of one-dimensional crystal structure under step pressure predicted by KP-PCD and EP-PCD equation [25]. It should be noted that the motivation of this part arose from the validity of the non-equilibrium behavior of PCD equation proposed by Kocher and Provatas [15] need to be valdiated due to certain postulations that might not be fully consistent with the established non-equilibrium thermodynamic framework. We referred to this PCD equation as KP-PCD equation. Therefore, we proposed an alternative PCD equation that is consistent with the non-equilibrium thermodynamic framework [86, 87, 88]. The equation is also based on the thermodynamic description of solids by Larché and Cahn [39, 40]. We referred to this PCD equation as EP-PCD equation. Finally, in part (A.2), we provide viscoelastic-creep study and the parametric prediction of one-dimensional crystal structure produced by EP-PCD equation [26].

A.1 PCD Equation Validation One-Dimensional Solid

To highlight the difference between KP equation and EP equation, we set $M = L_p V'$ (time scaling) and rearrange the KP equation to obtain

$$\frac{dJ}{dt} = L_P \left(\bar{P}_{int} - \bar{P}_{ext}\right) = L_P \Delta \bar{P}, \tag{A.1}$$

where $J = V/V'$ and V' is the volume at the initial state. For the EP equation, we assume that $P = -f + \mu\rho$ and thus the EP equation becomes

$$\frac{dJ}{dt} = J L_P \left(\bar{P}_{int} - \bar{P}_{ext}\right) = J L_P \Delta \bar{P}. \tag{A.2}$$

From these alternative expressions of the KP and EP equations, one can see the extra J factor in the right-hand side of the EP equation. This extra factor causes the rate of deformation (dJ/dt) from the EP equation to be different from that of the KP equation. For tensile deformation from the initial state ($J(0) = 1$), one can see that $J(t) > 1$ and the deformation rate from the EP equation will be higher than that from the KP equation. On the other hand, for compressive deformation, $J(t) < 1$ and the deformation rate from the EP equation will be lower than that from the KP equation. This behavior can also be shown from numerical calculations in figure A.1. In figure A. 1(a), the system undergoes tensile deformation ($\Delta\bar{P} > 0$) and the rate of increase in J from the EP equation is greater than that from the KP equation. In figure A.1(b), the system is subjected to compressive deformation ($\Delta\bar{P} < 0$) and the rate of decrease in J from the EP equation is now less than that from the KP equation. In summary,

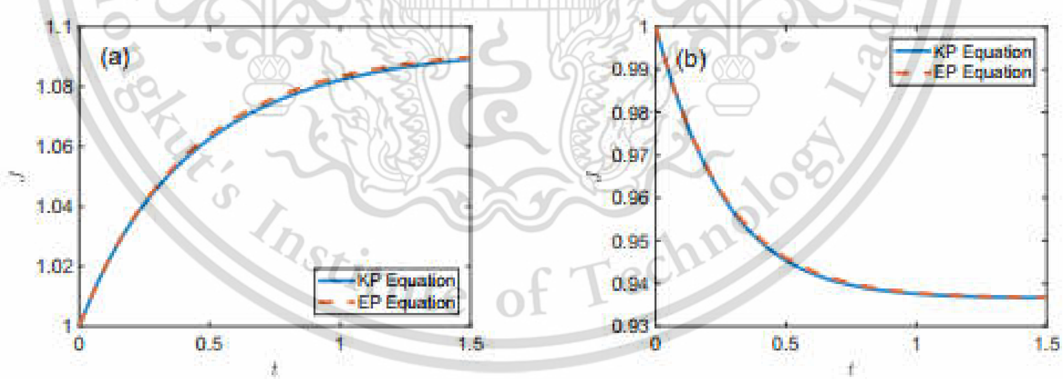

Figure A.1: Comparison of time-dependent deformation behavior from KP equation and EP equation. The system is subjected to constant external pressure that results in (a) tensile deformation ($\bar{P}_{ext} = 0.7\bar{P}_{int}|_{J=1}$) and (b) compressive deformation ($\bar{P}_{ext} = 1.3\bar{P}_{int}|_{J=1}$). Note: All physical variables are in non-dimensionalized quantities.

not only the simulation results obtained from both models are in good agreement but they also seem very slightly different in predicting time-dependent deformation, in particular, at the transient region. Whereas, the steady-state deformation value predicted by both models are identical. Therefore, both models can be interpreted as the compatible technique for investigating time-dependent deformation behavior in solid material.

A.2 Viscoelastic-Creep and Parametric Study One-Dimensional Solid

In figure A.2(a), the viscoelastic-creep behavior from the PFC model is shown from the plot of the strain $e(t)$ with $\Delta\bar{P} = \pm 0.05\bar{P}_0$. Initially, the system is at $e = 0$. After the pressure changes, e increases or decreases exponentially until the convergence value is reached. The positive e indicates tensile deformation which results from the positive $\Delta\bar{P}$; on the other hand, the negative e implies compressive deformation which corresponds to the negative $\Delta\bar{P}$. This time-dependent strain response from a step change in pressure is indicative of the viscoelastic-creep behavior.

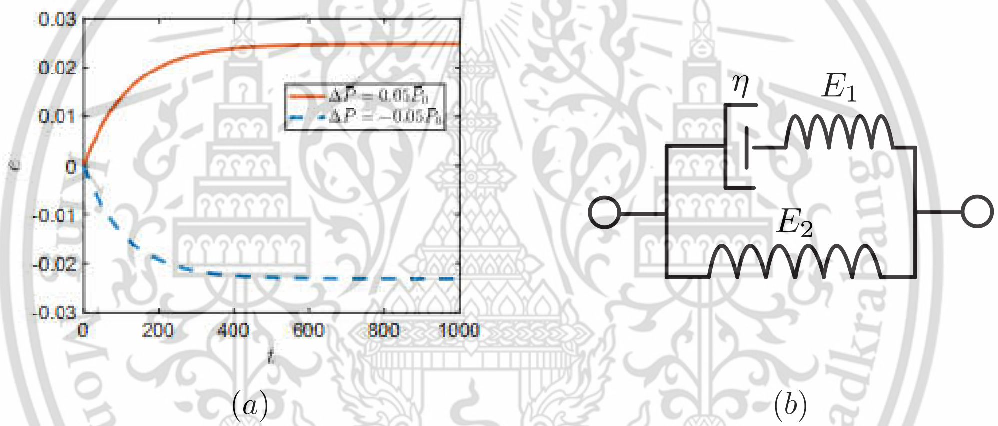

Figure A.2: (a) Plot of strain responses from the step changes in the pressure $\Delta\bar{P} = \pm 0.05\bar{P}_0$. In both simulations, $\epsilon = 0.3$ and $|\bar{\rho}_0| = 0.15$. (b) Schematic illustration of a spring-damper system. Note: All physical variables are in non-dimensionalized quantities.

In figure A.3, the dependence of e_∞ and τ on $|\bar{\rho}_0|$ is shown for the tensile deformation. First, figure A.3(a) shows that e_∞ decreases as $|\bar{\rho}_0|$ increases. To interpret the result, we consider the definition of e_∞ from equation (A.3) which indicates that $e_\infty \propto 1/E_2$.

$$e(t) = e_\infty \left[1 - exp(-\frac{t}{\tau})\right], \qquad e_\infty = \frac{\sigma}{E_2}, \qquad \tau = \eta\left(\frac{E_1 + E_2}{E_1 E_2}\right), \tag{A.3}$$

Therefore, the increase in the density, which leads to decreased e_∞, implies an increase in E_2 or the overall stiffness of the system. Second, figure A.3(b) shows that τ decreases with increased $|\bar{\rho}_0|$. From the definition of τ in equation (A.3), the term $(E_1+E_2)/E_1E_2$ is not expected to change significantly and, therefore, $\tau \propto \eta$. This proportionality indicates that the increase in the density, which leads to decreased τ, results in lower η or lower damping capacity of the system. Combining the results from figures A. 3(a) and A.3(b), we can see that the PFC model predicts high-density materials to exhibit high stiffness and low damping capacity. This prediction agrees in general with materials such as metals and ceramics [145].

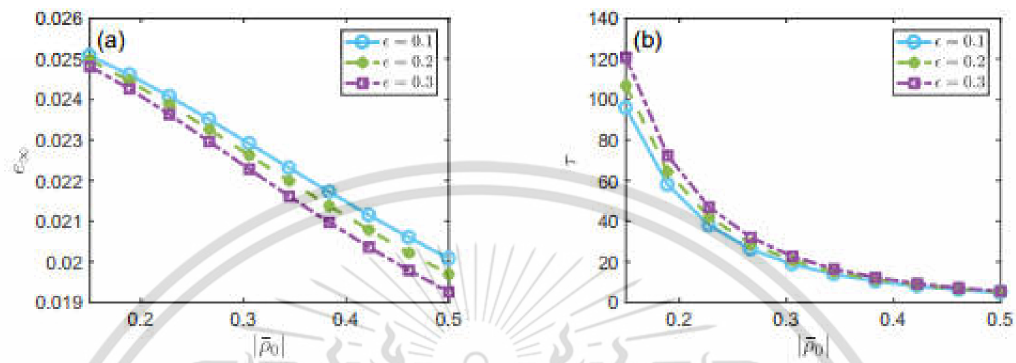

Figure A.3: Plots of e_∞ and τ as the functions of $|\bar{\rho}_0|$ for the tensile deformation ($\Delta\bar{P} = 0.05\bar{P}_0$). Note: All physical variables are in non-dimensionalized quantities.

In figure A.4, the dependence of e_∞ and τ on ϵ is shown for the tensile deformation. First, figure A.4(a) shows that as ϵ decreases, e_∞ increases. We note that ϵ is related to the degree of undercooling from the solidification temperature; therefore, a higher (lower) ϵ value corresponds to lower (higher) temperature. Then, the result from figure A.4(a) indicates that increasing temperature (lowering ϵ) leads to higher e_∞ or lower stiffness of the system. Second, figure A.4(b) shows that τ decreases with decreasing ϵ; however τ is less affected by ϵ for higher values of $|\bar{\rho}_0|$. This result indicates that, at lower density, increasing temperature (lowering ϵ) leads to lower damping capacity while at higher density, the damping capacity is less affected by temperature. Combining the results from figures A.4(a) and A.4(b), we find that the PFC model predicts, for lower-density materials, that higher temperature leads to lower stiffness and lower damping capacity. The decrease in materials stiffness with increased temperature is typically observed experimentally. Also, the decrease in damping capacity (faster strain response) at higher temperature agrees with what is generally observed in creep phenomena; in other words, the relaxation time in the creep phenomena generally increases with temperature.

Despite the agreement between the predictions from the PFC model and experimental observations, further developments need to be implemented in order to better understand the viscoelastic behavior from the PFC model; these improvements include extension to three-dimensional structures, more extensive parametric study, and investigation into other viscoelastic phenomena such as mechanical-hysteresis behavior.

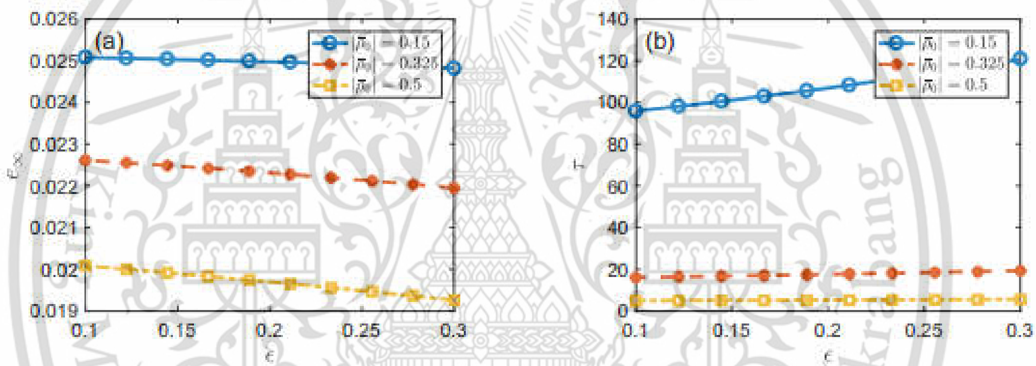

Figure A.4: Plots of e_∞ and τ as the functions of ϵ for the tensile deformation ($\Delta\bar{P} = 0.05\bar{P}_0$). Note: All physical variables are in non-dimensionalized quantities.

APPENDIX B

Publication List

In this research, we published our research papers in the following international conference proceedings and journals.

1. Em-Udom, J., and N. Pisutha-Arnond. ”Pressure-Controlled Dynamic Equation for the Phase-Field Crystal Method.” IOP Conference Series: Materials Science and Engineering. Vol. 361. No. 1. IOP Publishing, 2018.
2. Em-Udom, J., and N. Pisutha-Arnond. ”Investigation on Viscoelastic-Creep Behavior of the Phase-Field Crystal Method.” IOP Conference Series: Materials Science and Engineering. Vol. 361. No. 1. IOP Publishing, 2018.
3. Em-Udom, Jatupon, and Nirand Pisutha-Arnond. ”Investigation of Viscoelastic-Creep and Mechanical-Hysteresis Behaviors of Hydrostatically-Stressed Crystal using the Phase Field Crystal Method .” Advances in Mathematical Physics (In press), Hindawi.
4. Em-Udom, Jatupon, and Nirand Pisutha-Arnond. ”Prediction of mechanical-hysteresis behavior and complex moduli using the phase field crystal method with modified pressure controlled dynamic equation.” Materials Research Express (2019) (In press), IOP Publishing.

IOP Conference Series: Materials Science and Engineering

PAPER • OPEN ACCESS

Pressure-Controlled Dynamic Equation for the Phase-Field Crystal Method

To cite this article: J Em-Udom and N Pisutha-Arnond 2018 *IOP Conf. Ser.: Mater. Sci. Eng.* **361** 012006

9th International Conference on Mechatronics and Manufacturing (ICMM 2018) IOP Publishing
IOP Conf. Series: Materials Science and Engineering **361** (2018) 012006 doi:10.1088/1757-899X/361/1/012006

Pressure-Controlled Dynamic Equation for the Phase-Field Crystal Method

J Em-Udom and N Pisutha-Arnond[1,2]

Department of Industrial Engineering, Faculty of Engineering, King Mongkut's Institute of Technology Ladkrabang, Bangkok 10520, Thailand

E-mail: [1]nirand.pi@kmitl.ac.th

Abstract. The phase-field crystal (PFC) method is a density-functional-type materials model with atomic resolution on diffusive timescale, and has been shown to be a robust tool for modeling materials phenomena. In this study, a pressure-controlled dynamic equation for the PFC model was developed to describe a system under externally applied hydrostatic pressure. The formulation is based on the established frameworks including the thermodynamics of solids, kinematics of deformation, and non-equilibrium thermodynamics. The proposed equation exhibits the tensile and compressive deformation rates that are different from those from the recently-proposed pressure-controlled dynamic equation. The derivation in this work also provides a framework that can be readily extended to describe a more complex system such as multi-component solid under non-hydrostatic stress.

1. Introduction

With increasing computing performance and availability, computational materials study has become a promising alternative to experimental study in terms of expanding our understanding of materials behavior and providing insight into new phenomena. Among wide ranges of available computational materials techniques, the phase-field crystal (PFC) method [1], has shown to be a robust materials modeling tool. The appeal of the PFC method is that the model exhibits atomic-scale resolution while operating in diffusive timescale, which has advantages over the conventional phase field model in terms of accuracy and self-consistency, and over other atomistic models in terms of computational expense. Such advantages result in numerous applications of the PFC method in describing materials phenomena such as liquid-solid transition, elasticity, plasticity, dislocation dynamics, and crack propagation (see Ref. [2] for comprehensive review in this topic).

The original formulation of the PFC method describes non-equilibrium behavior of a system through the minimization of the free energy under controlled temperature, mass, and volume. Due to the controlled-volume condition, the pressure is naturally not independent and cannot be directly controlled. Although this controlled-volume condition is applicable to many situations, it is often more experimentally relevant to simulate materials behavior under a pressure-controlled condition. Recently, Kocher and Provatas [3] proposed the scheme where the pressure-controlled dynamic equation is added to the PFC formulation to control the (internal) pressure through the specified external pressure. Although this equation can be successfully used to obtain equilibrium

[2] Corresponding author

9th International Conference on Mechatronics and Manufacturing (ICMM 2018) IOP Publishing
IOP Conf. Series: Materials Science and Engineering **361** (2018) 012006 doi:10.1088/1757-899X/361/1/012006

states of a system, the validity of the non-equilibrium behavior from this equation needs to be investigated due to certain postulations that might not be fully consistent with the established non-equilibrium thermodynamic framework.

Therefore, in this work, we proposed an alternative pressure-controlled dynamic equation that is consistent with the non-equilibrium thermodynamic framework. The equation is based on the thermodynamic description of solids by Larché and Cahn [4], the balance laws and kinematics of deformation from the work by Mishin et al. [5], the balance law from the Reynolds transport theorem [6, 7], and the linear relations between driving forces and fluxes from the classical irreversible thermodynamics [7, 8]. The result shows that the equation proposed in this work exhibits higher (lower) deformation rate under tensile (compressive) deformation than that exhibited by the equation by Kocher and Provatas [3]. Moreover, the derivation presented in this work provides a framework that can be readily extended to describe a more complex situation such as a multi-component system under non-hydrostatic stress.

The paper is organized as follows. In section 2, we provide background information on the PFC method and the pressure-controlled dynamic equation recently proposed by Kocher and Provatas [3]. In section 3, we present the derivation of the alternative pressure-controlled dynamic equation and show the comparison between the proposed and the original equations in Section 4. In Section 5, we provide a summary of our work.

2. PFC Method

The central part of the PFC method is the expression of the Helmholtz free energy which is written in terms of dimensionless quantities [9]:

$$F = \int_V f d\vec{r}\,,\; f = \frac{\rho}{2}\left(-\epsilon + \left(1+\nabla^2\right)^2\right)\rho + \frac{\rho^4}{4}, \tag{1}$$

where f is the free energy density, ρ is the atomic number density field, ϵ is the model parameter related to temperature. The evolution of ρ is driven by dissipative dynamics through the conserved Cahn-Hilliard equation:

$$\frac{\partial \rho}{\partial t} = \nabla^2 \mu \equiv \nabla^2 \left(\frac{\delta F}{\delta \rho}\right), \tag{2}$$

where $\mu = \delta F/\delta\rho$ is the chemical potential and can be obtained from the variational derivative of F with respect to ρ. The evolution equation (2) evolves the system along the free-energy-minimizing path under fixed temperature, mass and volume (or computational domain). This indicates that the (internal) pressure, the conjugate variable to the volume, is not independent. To provide a more direct control over the internal pressure, Kocher and Provatas [3] proposed an evolution equation for the volume or the pressure-controlled dynamic equation:

$$\frac{dV}{dt} = M\left(\bar{P}_{\text{int}} - \bar{P}_{\text{ext}}\right), \tag{3}$$

where $\bar{P}_{\text{int}} = (1/V)\int_V (-f + \mu\rho)\, d\vec{r}$ is the averaged internal pressure, $\bar{P}_{\text{ext}}$ is the externally applied pressure, and M is the mobility. The above equation provides a driving force for the system to deform (change in V) to minimize $\bar{P}_{\text{int}} - \bar{P}_{\text{ext}} \equiv \Delta\bar{P}$. If $\Delta\bar{P} > 0$, the system undergoes tensile deformation while $\Delta\bar{P} < 0$ results in compressive deformation.

3. Derivation of the Alternative Pressure-Controlled Dynamic Equation

3.1. Thermodynamics of Solids

We first introduce the thermodynamic description of solids proposed by Larché and Cahn [4] which considers the solids as networks of lattices occupied by atomic species and vacancies.

9th International Conference on Mechatronics and Manufacturing (ICMM 2018) IOP Publishing
IOP Conf. Series: Materials Science and Engineering **361** (2018) 012006 doi:10.1088/1757-899X/361/1/012006

For a hydrostatically-stressed, single-component solid, the number of lattices sites (N_L) can be written as

$$N_L = N_A + N_v, \tag{4}$$

where N_A and N_v are the numbers of lattices occupied by the atomic species and vacancies, respectively. The internal energy, E, is then postulated to have the following functional dependence: $E(S, V, N_A, N_v)$, where S is the entropy and V is the volume. We can then write the differential of E as [10]

$$dE = TdS - PdV + \mu_A dN_A + \mu_v dN_v, \tag{5}$$

where T is temperature, μ_A and μ_v are the chemical potentials. Next, we consider the energy density $e_{V'} = E/V'$, where V' is the volume at the undeformed state. It can be shown using the standard thermodynamic relationships such as the Euler relation and Gibbs-Duhem equation that [10]

$$de_{V'} = Tds_{V'} - PdJ + \mu_{Av} d\rho_{A'}, \tag{6}$$

where $s_{V'} = S/V'$, $\rho_{A'} = N_A/V'$, $J = V/V'$, and $\mu_{Av} = \mu_A - \mu_v$. In arriving at the expression for $de_{V'}$, we use the assumption that the network is conserved or $\rho_{A'} + \rho_{v'} = \rho_{L'} \equiv$ Constant, where $\rho_{v'} = N_v/V'$ and $\rho_{L'} = N_L/V'$. Alternative to $e_{V'}$ which is defined by the undeformed volume (Lagrangian frame), we can define $e_V = E/V = e_{V'}/J$ which is the energy density defined by the deformed volume (Eulerian frame). By using the transformations, $e_{V'} = Je_V$, $\rho_{A'} = J\rho_A$, and $s_{V'} = Js_V$, we obtain the differential of e_V:

$$de_V = Tds_V - \frac{(P + f_v - \mu_{Av}\rho_A)}{J} dJ + \mu_{Av} d\rho_A, \tag{7}$$

where $f_V = e_V - Ts_V$ is the Helmhotlz free energy density (Eulerian frame). Finally, we rearrange the expression of de_V to arrive at the differential of s_V:

$$Tds_V = de_V + \frac{(P + f_V - \mu_{Av}\rho_A)}{J} dJ - \mu_{Av} d\rho_A. \tag{8}$$

3.2. Balance Equations

Here, we introduce the balance equations for mass, internal energy and entropy. We centralize the description of deformation by using a lattice velocity field, $\vec{v}_L$, which is the velocity of the imaginary network of indestructible sites called "markers" [5]. Consequently, the relationship between the lattice material time derivative and the partial derivative can be written as

$$\frac{d^L}{dt} = \frac{\partial}{\partial t} + \vec{v}_L \cdot \nabla. \tag{9}$$

Let us first consider the mass balance equation. In the absence of site creation and annihilation, the density of the material species i, where i can be A or v, changes through the equation:

$$\frac{\partial \rho_i}{\partial t} + \nabla \cdot \left(\rho_i \vec{v}_L + \vec{J}_i^L\right) = 0, \tag{10}$$

where $\vec{J}_i^L$ is the flux of the species i relative to the lattice. Using equation (9), we arrive at [5]

$$\frac{d^L \rho_i}{dt} + \rho_i \nabla \cdot \vec{v}_L + \nabla \cdot \vec{J}_i^L = 0. \tag{11}$$

9th International Conference on Mechatronics and Manufacturing (ICMM 2018) IOP Publishing
IOP Conf. Series: Materials Science and Engineering **361** (2018) 012006 doi:10.1088/1757-899X/361/1/012006

For the energy balance equation, we first consider the fact that the total energy of the system comprises of the internal, kinetic, and potential energies; however, the latter two can be neglected if the system is stationary and is not influenced by an external field such as gravity. Therefore, the balance equation for the energy is [5]

$$\frac{\partial e_V}{\partial t} + \nabla \cdot \left(e_V \vec{v}_L + \vec{J}_E^L \right) = \dot{w}, \tag{12}$$

where $\dot{w}$ is the rate of mechanical work per unit volume and $\vec{J}_E^L$ is the flux of the internal energy relative to the lattice. In the absence of an applied field and the assumption of the mechanical equilibrium, we have $\dot{w} = \boldsymbol{\sigma} : \nabla \vec{v}_L$, where $\boldsymbol{\sigma}$ is the Cauchy stress tensor. Furthermore, for a system under hydrostatic pressure, $\bar{P}_{\text{ext}}$, the stress tensor becomes $\boldsymbol{\sigma} = -\bar{P}_{\text{ext}} I$, where I is the identity tensor. The mechanical work then reduces to $\dot{w} = -\bar{P}_{\text{ext}} \nabla \cdot \vec{v}_L$. Using the expression for $\dot{w}$ and equation (9), the energy balance equation becomes [5]

$$\frac{d^L e_V}{dt} + e_V \nabla \cdot \vec{v}_L + \nabla \cdot \vec{J}_E^L = -\bar{P}_{\text{ext}} \nabla \cdot \vec{v}_L. \tag{13}$$

Lastly, the entropy balance is postulated to be [5]

$$\frac{\partial s_V}{\partial t} + \nabla \cdot \left(s_V \vec{v}_L + \vec{J}_S^L \right) = \dot{s}, \tag{14}$$

where the entropy change is affected by the entropy flux relative to the lattice, $\vec{J}_S^L$, and entropy generation, $\dot{s}$, due to irreversibility. Using equation (9), we arrive at [5]

$$\frac{d^L s_V}{dt} + s_V \nabla \cdot \vec{v}_L + \nabla \cdot \vec{J}_S^L = \dot{s}. \tag{15}$$

3.3. Entropy Production

In this section, we derive the expression for the entropy production, $\dot{s}$, which will be used to identify the corresponding flux and force for the phenomenological relation in the next subsection. We consider the fundamental equation (8) derived earlier and replace the differential with the lattice material time derivative to obtain

$$T \frac{d^L s_V}{dt} = \frac{d^L e_V}{dt} + \frac{(P + f_V - \mu_{Av} \rho_A)}{J} \frac{d^L J}{dt} - \mu_{Av} \frac{d^L \rho_A}{dt}. \tag{16}$$

Using the balance equations (11) and (13), and the identity $d^L J/dt = J \nabla \cdot \vec{v}_L$, we arrive through lengthy but straightforward derivation

$$\frac{d^L s_V}{dt} + s_V \nabla \cdot \vec{v}_L + \nabla \cdot \vec{J}_S^L = -\vec{J}_Q^L \cdot \frac{\nabla T}{T^2} - \vec{J}_A^L \cdot \frac{\nabla \mu_{Av}}{T} + (P - \bar{P}_{\text{ext}}) \frac{\nabla \cdot \vec{v}_L}{T}, \tag{17}$$

where $\vec{J}_Q^L = T \vec{J}_S^L = \vec{J}_E^L - \mu_{Av} \vec{J}_A^L$ is the heat flux relative to the lattice. Compared the above equation with equation (15), we can identify the entropy production to be

$$T \dot{s} = -\vec{J}_Q^L \cdot \frac{\nabla T}{T} - \vec{J}_A^L \cdot \nabla \mu_{Av} + \nabla \cdot \vec{v}_L (P - \bar{P}_{\text{ext}}). \tag{18}$$

Following Ref. [11], the form of the above equation allows us to identify that one of the fluxes is $\nabla \cdot \vec{v}_L$ and the corresponding force is $P - \bar{P}_{\text{ext}}$.

9th International Conference on Mechatronics and Manufacturing (ICMM 2018) IOP Publishing
IOP Conf. Series: Materials Science and Engineering **361** (2018) 012006 doi:10.1088/1757-899X/361/1/012006

3.4. Phenomenological Relations and Pressure-Controlled Dynamic Equation

Based on the classical irreversible thermodynamics framework, it is postulated that the forces and fluxes are related by the phenomenological (linear) law [12]:

$$J_\alpha = \sum_\beta L_{\alpha\beta} X_\beta, \tag{19}$$

where J_α represents thermodynamic fluxes, X_β represents thermodynamic forces and $L_{\alpha\beta}$ represents phenomenological coefficients. Using the assumption of symmetry properties of materials [5], the linear law reduces to

$$J_\alpha = L_{\alpha\alpha} X_\alpha. \tag{20}$$

Considering the flux and force identified in the previous subsection, we can write the phenomenological relation as

$$\nabla \cdot \vec{v}_L = L_P \cdot (P - \bar{P}_{\text{ext}}), \tag{21}$$

where L_P is the phenomenological coefficient. From the Reynolds transport theorem [6, 7], we can write the balance law as

$$\frac{dV}{dt} = \int_V (\nabla \cdot \vec{v}_L) d\vec{r}. \tag{22}$$

Substituting equation (21) into equation (22), we finally arrive at the pressure-controlled dynamic equation:

$$\frac{dV}{dt} = L_P \int_V (P - \bar{P}_{\text{ext}}) d\vec{r}. \tag{23}$$

4. Numerical Results

To highlight the difference between equation (3) (referred to as the KP equation) and equation (23) (referred to as the EP equation), we set $M = L_p V'$ (time scaling) and rearrange the KP equation to obtain $dJ/dt = L_P \left(\bar{P}_{\text{int}} - \bar{P}_{\text{ext}}\right) = L_P \Delta\bar{P}$, where $J = V/V'$ and V' is the volume at the initial state. For the EP equation, we assume that[4] $P = -f + \mu\rho$ and thus the EP equation becomes $dJ/dt = JL_P \left(\bar{P}_{\text{int}} - \bar{P}_{\text{ext}}\right) = JL_P \Delta\bar{P}$. From these alternative expressions of the KP and EP equations, one can see the extra J factor in the right-hand side of the EP equation. This extra factor causes the rate of deformation (dJ/dt) from the EP equation to be different from that of the KP equation. For tensile deformation from the initial state ($J(0) = 1$), one can see that $J(t) > 1$ and the deformation rate from the EP equation will be higher than that from the KP equation. On the other hand, for compressive deformation, $J(t) < 1$ and the deformation rate from the EP equation will be lower than that from the KP equation. This behavior can also be shown from numerical calculations in figure 1. In figure 1(a), the system undergoes tensile deformation ($\Delta\bar{P} > 0$) and the rate of increase in J from the EP equation is greater than that from the KP equation. In figure 1(b), the system is subjected to compressive deformation ($\Delta\bar{P} < 0$) and the rate of decrease in J from the EP equation is now less than that from the KP equation.

[4] See Ref. [13] for a more rigorous definition of the pressure of the solid phase.

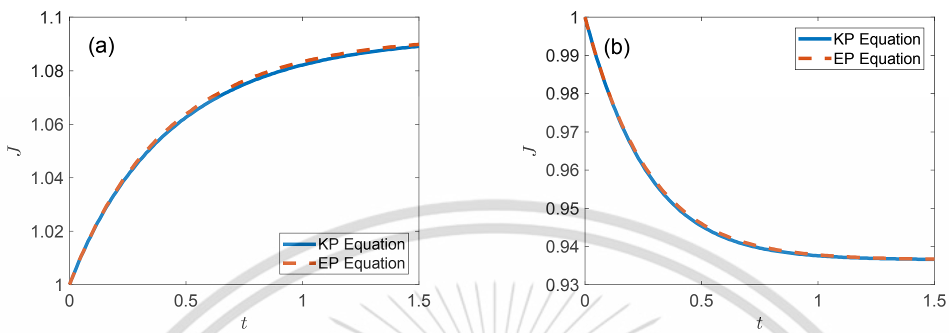

Figure 1. Comparison of time-dependent deformation behavior from equation (3) (KP equation) and equation (23) (EP equation). The system is subjected to constant external pressure that results in (a) tensile deformation ($\bar{P}_{\text{ext}} = 0.7\bar{P}_{\text{int}}|_{J=1}$) and (b) compressive deformation ($\bar{P}_{\text{ext}} = 1.3\bar{P}_{\text{int}}|_{J=1}$).

5. Summary

In this work, we developed the pressure-controlled dynamic equation for a single-component solid under applied hydrostatic pressure. The derivation is based on the established theories such as the thermodynamics of solids, kinematics of deformation, and non-equilibrium thermodynamics. The resulting equation (EP equation) exhibits non-equilibrium behavior that is different from that from the previously proposed pressure-controlled dynamics equation (KP equation). The deformation rate from the EP equation is higher (lower) than that from the KP equation for the tensile (compressive) deformation. The derivation presented in this work also provides a platform for further extension to describe a more complex system such as multi-component solid under non-hydrostatic stress.

Acknowledgments

This research was supported by the NSTDA-University-Industry Research Collaboration (NUI-RC) program under grant No. NUI-RC-M33-22-59-001D, King Mongkut's Institute of Technology Ladkrabang (KMITL) Research Fund under Grant No. KREF 015803, Thailand Research Fund (TRF) under Grant No. TRG5880008, and High Performance Computing Services from NECTEC (Thailand). The authors are indebted to Assoc.Prof.Wicharn Techidheera and Dr.Sasawat Mahabunphachai for their helpful discussion and support.

References

[1] Elder K R, Katakowski M, Haataja M and Grant M 2002 *Physical Review Letters* **88** 245701
[2] Emmerich H, Löwen H, Wittkowski R, Gruhn T, Tóth G I, Tegze G and Gránásy L 2012 *Advances in Physics* **61** 665–743
[3] Kocher G and Provatas N 2015 *Physical Review Letters* **114** 155501
[4] Larché F and Cahn J W 1973 *Acta Metallurgica* **21** 1051–1063
[5] Mishin Y, Warren J, Sekerka R and Boettinger W 2013 *Physical Review B* **88** 184303
[6] Malvern L E 1977 *Introduction to the Mechanics of a Continuous Medium* (Pearson)
[7] Rudnicki J W 2014 *Fundamentals of Continuum Mechanics* (John Wiley & Sons)
[8] De Groot S R and Mazur P 2013 *Non-Equilibrium Thermodynamics* (Courier Corporation)
[9] Wu K A and Karma A 2007 *Physical Review B* **76** 184107
[10] Voorhees P, Johnson W, Henry E and Frans S 2004 *Solid State Physics* **59**
[11] Balluffi R W, Allen S and Carter W C 2005 *Kinetics of Materials* (John Wiley & Sons)
[12] Lebon G, Jou D and Casas-Vázquez J 2008 *Understanding Non-Equilibrium Thermodynamics* (Springer)
[13] Chan V W L, Pisutha-Arnond N and Thornton K 2017 *Computational Materials Science* **135** 205–213

IOP Conference Series: Materials Science and Engineering

PAPER • OPEN ACCESS

Investigation on Viscoelastic-Creep Behavior of the Phase-Field Crystal Method

To cite this article: J Em-Udom and N Pisutha-Arnond 2018 *IOP Conf. Ser.: Mater. Sci. Eng.* **361** 012009

9th International Conference on Mechatronics and Manufacturing (ICMM 2018) IOP Publishing
IOP Conf. Series: Materials Science and Engineering **361** (2018) 012009 doi:10.1088/1757-899X/361/1/012009

Investigation on Viscoelastic-Creep Behavior of the Phase-Field Crystal Method

J Em-Udom and N Pisutha-Arnond[1,2]

Department of Industrial Engineering, Faculty of Engineering, King Mongkut's Institute of Technology Ladkrabang, Bangkok 10520, Thailand

E-mail: [1]`nirand.pi@kmitl.ac.th`

Abstract. The phase-field crystal (PFC) method is a promising computational model with atomistic resolution and diffusive time-scale. In this study, we investigated the viscoelastic-creep behavior exhibited by the PFC model. We considered a one-dimensional crystal subjected to step changes in pressure and studied the time-dependent strain response from the system. The parametric study shows that the PFC model predicts the materials with higher density to exhibit higher stiffness and lower damping capacity while an increase in temperature results in lower stiffness and damping capacity. These predictions agree with experimental observations and show promising capability of the PFC method to model viscoelastic phenomena.

1. Introduction

Due to rapid increase in computing performance and theoretical development, computational methods are becoming powerful tools in facilitating materials advancement. However, many problems in computational materials science involve length and time scales of many orders of magnitude. This large span of length and time scales is a challenge for atomistic models, such as molecular dynamics (MD) and density functional theory (DFT), in that these models are typically applicable in prohibitively-small length and time regimes. On the other hand, continuum models, such as the phase field (PF) models, naturally reside in phenomenologically-relevant length and time scales, but often suffer from lack of atomistic resolution and self-consistency. In the past decade, the phase-field crystal (PFC) method [1] emerged as a robust tool to address these issues. The appeal of the PFC method lies in its atomistic resolution and diffusive time scale, which give the model advantages over the PF method in terms of accuracy and self-consistency and over the MD and DFT in terms of computational expenses. Due to these advantages, the PFC method has been used to predict various materials properties and model several materials phenomena (see Ref. [2] for comprehensive review in this topic).

Despite various applications of the PFC method, especially in deformation-related phenomena, the viscoelastic behavior exhibited by the model has not been extensively studied. Viscoelasticity is a combination of elasticity and viscosity, and is an important characteristic in vibration-damping materials, noise-controlled applications, and microelectromechanical system (MEMS). Therefore, in this work, we investigated the viscoelastic behavior exhibited by the PFC model. In particular, we considered the viscoelastic-creep behavior of a one-dimensional crystalline solid subjected to step changes in pressure, and analyzed the time-dependent strain

[2] Corresponding author

9th International Conference on Mechatronics and Manufacturing (ICMM 2018) IOP Publishing
IOP Conf. Series: Materials Science and Engineering **361** (2018) 012009 doi:10.1088/1757-899X/361/1/012009

response of the system. From the parametric study, we found that the PFC method predicts higher-density materials to have higher stiffness and damping capacity. Also, an increase in temperature results in lower stiffness and lower damping capacity. These predictions agree with experimental observations and show promising capability of the PFC method to model viscoelastic phenomena. Nevertheless, further investigation is needed in order to better understand the viscoelstic behavior from the PFC model; future improvements include extension to three-dimensional structures, more extensive parametric study, and investigation into other viscoelastic phenomena.

The paper is organized as follows. In section 2, we review the PFC method and the pressure-controlled dynamic equation recently proposed by Em-Udom and Pisutha-Arnond [3]. In section 3, we describe the simulation and analysis procedures. The simulation results and discussion are presented in section 4. Lastly, we provide a summary of our work in section 5.

2. Phase-Field Crystal Method

In the PFC method, the two central ingredients are the energy expression and evolution equations. For the energy expression, we consider the Helmholtz free energy, F, which can be written in terms of dimensionless quantities as [4]

$$F = \int_V f_v d\vec{r} \equiv \int_V \left(\frac{\rho^4}{4} + \frac{\rho}{2} \left[-\epsilon + \left(1 + \nabla^2\right)^2 \right] \rho \right) d\vec{r}, \tag{1}$$

where f_v is the free energy density, $\rho \equiv \rho(\vec{r})$ is the atomic number density field, ϵ is the model parameter related to temperature, and V is the volume. This free energy is minimized by a constant density profile (representing a liquid phase) and a periodic density profile (representing a crystalline phase). The latter profile can be written in terms of a Fourier expansion of the form

$$\rho(\vec{r}, t) = \bar{\rho}(t) + \sum_j A_j(t) e^{i\vec{G}_j \cdot \vec{r}} + \text{c.c.}, \tag{2}$$

where $\vec{G}_j$ is the reciprocal lattice vector, A_j is the amplitude of the density wave corresponding to $\vec{G}_j$, $\bar{\rho}$ is the average number density, and c.c. denotes the complex conjugate. The second ingredient of the PFC method, which is the evolution equations, governs the time evolution of the state of the system. In this work, we employ two evolution equations. The first is the Cahn-Hilliard type equation that evolves $\rho(\vec{r}, t)$ through dissipative dynamics and with mass conservation [5]:

$$\frac{\partial \rho}{\partial t} = L_\mu \nabla^2 \mu \equiv L_\mu \nabla^2 \left(\frac{\delta F}{\delta \rho} \right), \tag{3}$$

where $\mu = \delta F / \delta \rho$ is the chemical potential, L_μ is the mass-diffusion coefficient. The second equation is the pressure-controlled dynamic equation recently proposed in Ref. [3] to simulate the deformation of a system under externally-applied pressure $\bar{P}_{\text{ext}}$:

$$\frac{dV}{dt} = L_P \int_V (P - \bar{P}_{\text{ext}}) d\vec{r}, \tag{4}$$

where $P = -f_v + \mu\rho$ is the internal pressure and L_P is the deformation coefficient.

3. Method

In this section, we describe the method to simulate, analyze and study the viscoelastic-creep behavior in the PFC model. To simulate the viscoelastic-creep behavior, we consider a one-dimensional crystalline phase with the density field $\rho(x, t) = \bar{\rho}(t) + \sum_j A_j(t) \cos(G_j x)$, where x

9th International Conference on Mechatronics and Manufacturing (ICMM 2018) IOP Publishing
IOP Conf. Series: Materials Science and Engineering **361** (2018) 012009 doi:10.1088/1757-899X/361/1/012009

is the spatial coordinate. The system is initially at equilibrium and this state of the system is characterized by three state variables. First is the mass per unit-cell $N_0 = \bar{\rho}_0 L_0$, where L_0 is the initial unit-cell length and $\bar{\rho}_0 \equiv \bar{\rho}(0)$ is the initial average density. The second state variable is the average pressure $\bar{P}_0 = 1/L_0 \int_{L_0} P dx$, and the third is the temperature which is related to the model parameter ϵ. Then, the system is subjected to step changes in the average pressure quantified by $\Delta\bar{P} = \bar{P}_0 - \bar{P}_{\text{ext}}$. From equation (4), the nonzero $\Delta\bar{P}$ will lead to deformation characterized by the change in the unit-cell length $L(t)$ and the strain $e(t) = (L(t) - L_0)/L_0$. During the deformation, we enforce mass conservation by changing the average density according to $\bar{\rho}(t) = N_0/L(t) = \bar{\rho}_0 L_0/L(t)$, and we also allow the system to attain the equilibrium condition in all deformation states by evolving the density profile using equation (3) until a steady state is reached for each value of $L(t)$.

To analyze the viscoelastic-creep behavior, we fit $e(t)$ from the simulations to the solution of a standard linear solid model [6] which is typically used to describe viscoelastic behavior. In particular, we consider a spring-damper system subjected to uniform stress σ as shown in figure 1. The strain response from this system is governed by $de/dt + \frac{E_1 E_2}{\eta(E_1+E_2)} e = \frac{E_1}{\eta(E_1+E_2)} \sigma$, where E_1 and E_2 are the spring constants and η is the damping coefficient [6]. The solution to this ordinary differential equation is

$$e(t) = e_\infty \left[1 - \exp\left(-\frac{t}{\tau} \right) \right], \quad e_\infty = \frac{\sigma}{E_2}, \quad \tau = \eta \left(\frac{E_1 + E_2}{E_1 E_2} \right), \tag{5}$$

where e_∞ and τ are the strain value at $t = \infty$ and the relaxation time, respectively. When equation (5) is fitted to $e(t)$ from the PFC simulations, the values of e_∞ and τ, which characterize the viscoelastic-creep behavior, can be extracted for further study.

To study the viscoelastic-creep behavior exhibited by the PFC model, we investigate the dependence of e_∞ and τ on the PFC model parameters. In this parametric study, we use $\Delta\bar{P} = \pm 0.05\bar{P}_0$, $\epsilon = [0.1, 0.3]$, and $|\bar{\rho}_0| = [0.15, 0.5]$. The values of $\Delta\bar{P}$ are selected to yield tensile ($\Delta\bar{P} > 0$) and compressive ($\Delta\bar{P} < 0$) deformation. The ranges of ϵ and $|\bar{\rho}_0|$ are selected from the crystalline region in the phase diagram shown in Ref. [5]. Other fixed simulation and model parameters are $L_\mu = 1$, $L_P = 0.5$, $L_0 = 2\pi\sqrt{2}$, Δx (grid spacing) $= L_0/16$. The time steps for equations (3) and (4) are 0.01 and 0.5, respectively.

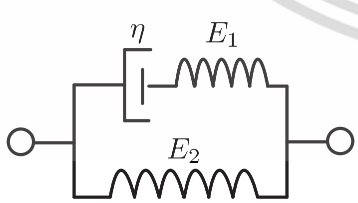

Figure 1. Schematic illustration of a spring-damper system.

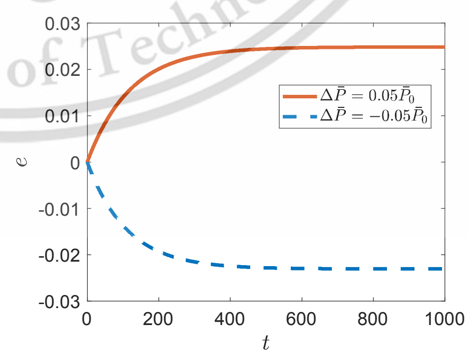

Figure 2. Plot of strain responses from the step changes in the pressure $\Delta\bar{P} = \pm 0.05\bar{P}_0$. In both simulations, $\epsilon = 0.3$ and $|\bar{\rho}_0| = 0.15$.

9th International Conference on Mechatronics and Manufacturing (ICMM 2018) IOP Publishing
IOP Conf. Series: Materials Science and Engineering **361** (2018) 012009 doi:10.1088/1757-899X/361/1/012009

4. Results and Discussion

In figure 2, the viscoelastic-creep behavior from the PFC model is shown from the plot of the strain $e(t)$ with $\Delta\bar{P} = \pm 0.05\bar{P}_0$. Initially, the system is at $e = 0$. After the pressure changes, e increases or decreases exponentially until the convergence value is reached. The positive e indicates tensile deformation which results from the positive $\Delta\bar{P}$; on the other hand, the negative e implies compressive deformation which corresponds to the negative $\Delta\bar{P}$. This time-dependent strain response from a step change in pressure is indicative of the viscoelastic-creep behavior.

In figure 3, the dependence of e_∞ and τ on $|\bar{\rho}_0|$ is shown for the tensile deformation. First, figure 3(a) shows that e_∞ decreases as $|\bar{\rho}_0|$ increases. To interpret the result, we consider the definition of e_∞ from equation (5) which indicates that $e_\infty \propto 1/E_2$. Therefore, the increase in the density, which leads to decreased e_∞, implies an increase in E_2 or the overall stiffness of the system. Second, figure 3(b) shows that τ decreases with increased $|\bar{\rho}_0|$. From the definition of τ in equation (5), the term $(E_1 + E_2)/E_1E_2$ is not expected to change significantly and, therefore, $\tau \propto \eta$. This proportionality indicates that the increase in the density, which leads to decreased τ, results in lower η or lower damping capacity of the system. Combining the results from figures 3(a) and 3(b), we can see that the PFC model predicts high-density materials to exhibit high stiffness and low damping capacity. This prediction agrees in general with materials such as metals and ceramics [7].

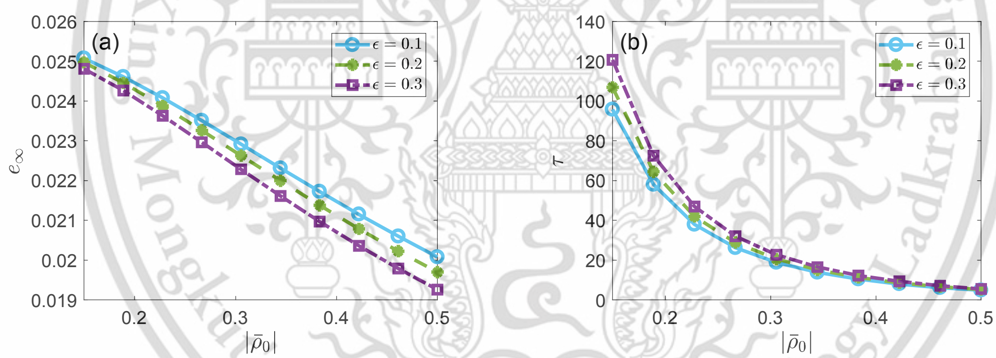

Figure 3. Plots of e_∞ and τ as the functions of $|\bar{\rho}_0|$ for the tensile deformation ($\Delta\bar{P} = 0.05\bar{P}_0$).

In figure 4, the dependence of e_∞ and τ on ϵ is shown for the tensile deformation. First, figure 4(a) shows that as ϵ decreases, e_∞ increases. We note that ϵ is related to the degree of undercooling from the solidification temperature [1]; therefore, a higher (lower) ϵ value corresponds to lower (higher) temperature. Then, the result from figure 4(a) indicates that increasing temperature (lowering ϵ) leads to higher e_∞ or lower stiffness of the system. Second, figure 4(b) shows that τ decreases with decreasing ϵ; however τ is less affected by ϵ for higher values of $|\bar{\rho}_0|$. This result indicates that, at lower density, increasing temperature (lowering ϵ) leads to lower damping capacity while at higher density, the damping capacity is less affected by temperature. Combining the results from figures 4(a) and 4(b), we find that the PFC model predicts, for lower-density materials, that higher temperature leads to lower stiffness and lower damping capacity. The decrease in materials stiffness with increased temperature is typically observed experimentally. Also, the decrease in damping capacity (faster strain response) at higher temperature agrees with what is generally observed in creep phenomena; in other words, the relaxation time in the creep phenomena generally increases with temperature [6]. Despite the agreement between the predictions from the PFC model and experimental observations, further developments need to be implemented in order to better understand the viscoelastic behavior

9th International Conference on Mechatronics and Manufacturing (ICMM 2018) IOP Publishing
IOP Conf. Series: Materials Science and Engineering **361** (2018) 012009 doi:10.1088/1757-899X/361/1/012009

from the PFC model; these improvements include extension to three-dimensional structures, more extensive parametric study, and investigation into other viscoelastic phenomena.

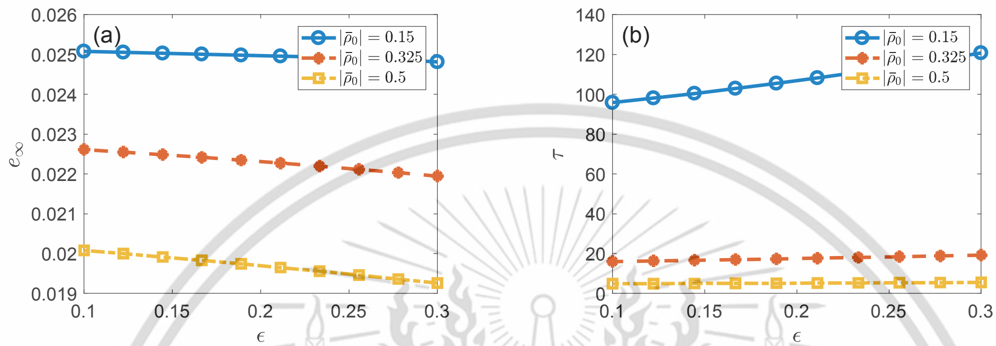

Figure 4. Plots of e_∞ and τ as the functions of ϵ for the tensile deformation ($\Delta\bar{P} = 0.05\bar{P}_0$).

5. Summary

In this work, we explored the viscoelastic creep behavior exhibited by the PFC model. We considered a one-dimensional crystalline solid subjected to step changes in pressure and the resulting time-dependent strain response was analyzed. From the parametric study, we found that the PFC model predicts higher-density materials to exhibit higher stiffness but lower damping capacity; this prediction agrees in general with materials such as metals and ceramics. Also, increasing temperature leads to lower material stiffness and damping capacity. This prediction agrees with experimental observations where materials typically become less stiff at high temperature and the relaxation time (proportional to the damping capacity) in creep phenomena generally decreases with temperature. The agreement between the PFC predictions and experimental observations shows promising capability of the PFC method to model viscoelastic phenomena. Nevertheless, further investigation is needed in order to better understand the viscoelstic behavior from the PFC model; future improvements include extension to three-dimensional structures, more extensive parametric study, and investigation into other viscoelastic phenomena.

Acknowledgments

This research was supported by the NSTDA-University-Industry Research Collaboration (NUI-RC) program under grant No. NUI-RC-M33-22-59-001D, Thailand Research Fund (TRF) under Grant No. TRG5880008, and High Performance Computing Services from (Thailand) National Electronics and Computer Technology Center (NECTEC). The authors are indebted to Dr.Sasawat Mahabunphachai for helpful discussion and support on the research.

References

[1] Elder K, Katakowski M, Haataja M and Grant M 2002 *Physical Review Letters* **88** 245701
[2] Emmerich H, Löwen H, Wittkowski R, Gruhn T, Tóth G I, Tegze G and Gránásy L 2012 *Advances in Physics* **61** 665–743
[3] Em-Udom J and Pisutha-Arnond N *(accepted) IOP Conference Series: Materials Science and Engineering*
[4] Wu K A and Karma A 2007 *Physical Review B* **76** 184107
[5] Elder K and Grant M 2004 *Physical Review E* **70** 051605
[6] Lakes R S 2009 *Viscoelastic Materials* (Cambridge University Press)
[7] Zhang J, Perez R and Lavernia E 1993 *Journal of Materials Science* **28** 2395–2404

Investigation of Viscoelastic-Creep and Mechanical-Hysteresis Behaviors of Hydrostatically-Stressed Crystal using the Phase Field Crystal Method

J Em-Udom* and N Pisutha-Arnond†

Department of Industrial Engineering, Faculty of Engineering,

King Mongkut's Institute of Technology Ladkrabang, Ladkrabang, Bangkok, Thailand

(Dated: October 30, 2019)

Abstract

The phase field crystal (PFC) method is a density-functional-type model with atomistic resolution and operating on diffusive time scales which has been proved to be an efficient tool for predicting numerous materials phenomena. In this work, we first propose a method to predict viscoelastic-creep and mechanical-hysteresis behaviors in body-centered-cubic (BCC) solid using PFC method that is incorporated with pressure-controlled dynamics equation which enables convenient control of deformation by specifying external pressure. To achieve our objective, we use constant pressure for the viscoelastic-creep study, and sinusoidal pressure oscillation for the mechanical-hysteresis study. The parametric studies show that the relaxation time in the viscoelastic-creep phenomena is proportional to temperature. Also, mechanical-hysteresis behavior and the complex moduli predicted by the model is consistent with that of the standard linear solid model in a low-frequency pressure oscillation. Moreover, the impact of temperature on complex moduli is also investigated within the solid-stabilizing range. These results qualitatively agree with experimental and theoretical observations reported in the previous literature. We believe that our work should contribute to extending the capability of PFC method to investigate the deformation problem when the externally applied pressure is required.

* ejatupon1@gmail.com

† nirand.pi@kmitl.ac.th

I. INTRODUCTION

The phase field crystal (PFC) method has emerged as a computational model with atomistic resolution and diffusive time scale. The method has an advantage over the molecular dynamics (MD) in terms of the time scale that is not restricted by lattice vibration time; this is due to the specification of the order parameter as the local-time-average atomic number density and the evolution of the order parameter through dissipative dynamics. The method also has advantage over the phase field (PF) method in terms of atomic resolution and self consistency; these benefit stems from the free energy functional that can be minimized by the periodic order-parameter field whereas the free energy functional of PF method is formulated by spatially uniform field which diminishes numerous physical features that occurs due to the periodicity of crystalline phases e.g. spatial symmetry, elastic and plastic interaction, the nucleation, multiple crystal orientations and the motion of dislocations [1–3]. The PFC method was first introduced by Elder et al. [1, 2] and has been extensively used to study materials phenomena and behavior ranging from phase transformation [4, 5], topological defect dynamics (vacancy [6], grain-boundary [7–9], dislocation [3, 10, 11], crack [12]) to elasticity and elastic constants [13–15] and plasticity [11, 16]. Moreover, the PFC method was also interpreted and derived according to the classical density functional theory (CDFT) of freezing point of view [4]. This derivation provided an additional field variable which extended the capability of PFC method to investigate the material phenomena in a more complex situation such as phase transformation [4, 17] and segregation induced grain-boundary premelting [18] in binary alloys.

Although there were numerous successful PFC studies on the mechanical behavior of materials, such as elasticity, plasticity, and phase transformation in pure materials and binary alloys. The investigation of viscoelastic behavior and the related properties predicted by the PFC model is still limited and not thoroughly explored. Thus, it is of interest to study the capability of the PFC model to predict this phenomena. Viscoelasticity is the behavior with both viscous and elastic characteristics; thus materials with viscoelastic behavior can return to its original configuration when unloaded but does so in a time dependent manner. The viscous property also leads to the fact that materials response depends on the rate at which it is deformed [19, 20]. Viscoelastic effect has played significant roles in many materials ranging from amorphous polymers [21], semi-crystalline polymers [22], biopolymers [23], bitumen materials [24] to metals at very high temperature [25]. Furthermore, viscoelasticity governs many engineering applications in various fields including damping material design for noise reduction [26, 27] and vibration control in engineering structure [28], shape-memory ceramics and polymers [29], piezoelectric material [30], self-healing materials [31], viscoelastic gel in surgery application [32], low-loss materials [33] and nanoscale resonators [34, 35].

In quantifying the viscoelastic effect, there are three types of studies: viscoelastic-creep, stress relaxation and mechanical-hysteresis. In this work, we not only focus on the viscoelastic-creep but also extend our study to mechanical-hysteresis behavior and its related parameters in body-centered-cubic (BCC) solid (3D case) predicted by the PFC method, unlike our previous works [36, 37] which were solely limited to viscoelastic-creep in one-dimensional (1D case) crystal study, moreover, the mechanical hysteresis behavior and its related parameters were not addressed in those works. Since the studies of viscoelastic-creep and mechanical-hysteresis involve measuring the strain response from an applied stress, we also need a method to control the applied stress and thus we employ the PFC model that is incorporated with our previously-proposed pressure-controlled dynamics (PCD) equation [37]. The use of the PCD equation enables convenient control of deformation using external pressure which allows studies of experimentally-observed phenomena involving a system under different types of applied pressure; we will refer to this particular PFC method as PFC-PCD model. The PCD equation is similar to the the dynamic equation introduced by Kocher and Provatas [38]. They used their PCD equation to control internal pressure by specifying external pressure to investigate the full spectrum of solid-liquid-vapor transitions, unfortunately, the viscoelastic-creep and mechanical-hysteresis behaviors which can be produced from that equation were not focused area and, of course, not addressed in their study [38]. The difference between two PCD versions is due to the different derivation process which our version is established regarding thermodynamic of hydrostatically-stressed crystal solid proposed by Larche' and Cahn [39] and classical irreversible thermodynamic frameworks [40–42]. Moreover, the deviation of viscoelastic-creep behavior in 1D crystal between two PCD versions was also investigated in our previous study [37]. The advantage of the PCD equation is that it enables the external pressure to be specified as an input to the simulation, which allows the system volume, or the strain response, to be measured; this is in contrast to the conventional PFC simulations where volume, or grid spacing, is an independent variables [43].

For the investigation of viscoelastic behavior, we simulate a hydrostatic stress, BCC solid subjected to two types of applied pressure: constant pressure for the viscoelastic-creep study and sinusoidal pressure oscillation for mechanical-hysteresis study. We find that, in both cases, the solid exhibits delayed strain responses from the applied pressure which is indicative of viscoelasticity; and the degree of viscoelasticity can be controlled by the parameter in the PCD equation. Furthermore, the strain responses from the simulations can be compared with functional forms of the solutions to the standard linear solid model to extract viscoelastic quantities and properties. These properties includes relaxation time of viscoelastic creep, and the complex moduli from the hysteresis. The parametric studies show that the relaxation time is proportional to temperature while the magnitude of deformation at steady-state condition is proportional to both temperature and atomic density. Also, the dynamic behavior, mechanical hysteresis and complex moduli predicted by PFC-PCD equation under sinusoidal pressure oscillation is consistent to that of standard linear solid model at certain frequency range. However, at very frequency, the behavior exhibited by the PFC-PCD model differs from that of standard linear solid model. The reason behind this difference is thoroughly analyzed by conducting Taylor's expansion on PCD equation in appendix C. Moreover, the impact of temperature on complex moduli is also investigated and the results well agree with experimental and theoretical observation. We are positive that our work should provide the extension of capability for PFC method to investigate the deformation problem in a real crystalline solid when externally applied pressure is necessary.

This paper is organized as follows. In Section II, we provide the background information on the PFC method, the pressure-control dynamics equation, and the standard linear solid model. In Section III, the method of simulation is presented. The results and discussions are provided in Section IV and we conclude the work with the summary in Section V.

II. BACKGROUND

A. PFC Method

The PFC method is characterized by its free energy functional and the dynamic equation. The simplest free energy functional was introduced by Elder and coworkers [1, 2]:

$$\mathcal{F} = \int w(\rho)\ d\mathbf{r}, \qquad w(\rho) \equiv \frac{\rho}{2}\left[a_t + \lambda(q_0^2 + \nabla^2)^2\right]\rho + g_t\frac{\rho^4}{4}, \tag{1}$$

where $w(\rho)$ is the free energy density, a_t, g_t, λ and q_0 are fitting parameters, ρ is the atomic number-density field. This PFC free energy functional can be minimized by a constant ρ profile, representing a liquid phase, and a periodic ρ profile, representing a crystalline solid phase. The density periodic field ϕ can be expressed in terms of Fourier expansion of the form

$$\phi(\mathbf{r}, \bar{\rho}) = \bar{\rho} + \sum_j A_j e^{i\mathbf{G}_j \cdot \mathbf{r}} + \text{c.c.}, \tag{2}$$

where $\mathbf{G}_j$ is a reciprocal lattice vector (RLV), A_j is an amplitude of the density wave corresponding to $\mathbf{G}_j$, $\bar{\rho}$ is an average atomic-number density, and c.c. denotes a complex conjugate. The minimization of $\mathcal{F}$ essentially results in the truncation of the summation in Eq. (2) to terms with small values of $|\mathbf{G}_j|$ as the terms of with higher values of $|\mathbf{G}_j|$ have vanishingly small A_j. Consequently, this particular PFC model (Eq. (1)) favors crystal structures that can be constructed from single set of RLVs such as stripe, hexagonal, and BCC structures in one, two and three dimensions, respectively. To this end, one can construct the so-called "one-mode" approximation of the BCC crystal by limiting the terms in Eq. (2) to those corresponding to $\langle 110 \rangle$ RLVs or $|\mathbf{G}_j| = 2\pi\sqrt{2}/L_a$, where L_a is the lattice parameter. By assuming that A_j of the terms with the same $|\mathbf{G}_j|$ are equivalent, one obtain

$$\rho_{\text{one}} = \bar{\rho} + 4A_s \left[\cos(q_a r_1)\cos(q_a r_2) + \cos(q_a r_1)\cos(q_a r_3) + \cos(q_a r_2)\cos(q_a r_3)\right], \tag{3}$$

where $q_a = 2\pi/L_a$ and A_s is the density-wave amplitude.

To simplify the expressions in Eq. (1), one can non-dimensionalize the variables by using the following substitutions [2]:

$$\tilde{\mathbf{r}} \equiv q_0\mathbf{r}, \qquad \tilde{\epsilon} \equiv -\frac{a_t}{\lambda q_0^4}, \qquad \tilde{\rho} \equiv \sqrt{\frac{g_t}{\lambda q_0^4}}\rho, \qquad \tilde{\mathcal{F}} \equiv \frac{g_t}{\lambda^2 q_0^{8-d}}\mathcal{F}, \qquad \tilde{w} \equiv \frac{g_t}{\lambda^2 q_0^8}w, \tag{4}$$

where the quantities with tildes are non-dimensional and $d = 3$ is the dimensionality of the problem. The expressions in Eq. (1) simplifies to

$$\tilde{\mathcal{F}} = \int \tilde{w}(\tilde{\rho})\; d\tilde{\mathbf{r}}, \qquad \tilde{w}(\tilde{\rho}) = \frac{\tilde{\rho}}{2}\left[-\tilde{\epsilon} + \left(1 + \tilde{\nabla}^2\right)^2\right]\tilde{\rho} + \frac{\tilde{\rho}^4}{4}. \tag{5}$$

where ϵ can be interpreted as the degree of undercooling which is inversely proportional to temperature. The one-mode approximation of the BCC crystal becomes

$$\tilde{\rho}_{\text{one}} = \tilde{\bar{\rho}} + 4\tilde{A}_s \left[\cos(\tilde{q}_a \tilde{r}_1)\cos(\tilde{q}_a \tilde{r}_2) + \cos(\tilde{q}_a \tilde{r}_1)\cos(\tilde{q}_a \tilde{r}_3) + \cos(\tilde{q}_a \tilde{r}_2)\cos(\tilde{q}_a \tilde{r}_3)\right], \tag{6}$$

where $\tilde{q}_a = q_a/q_0 = 2\pi/(L_a q_0) = 2\pi/\tilde{L}_a$. The value of $\tilde{q}_a$ can be determined from minimization of the free energy density [44] leading to $\tilde{q}_a = 1/\sqrt{2}$ and, consequently, $\tilde{L}_a = 2\pi\sqrt{2}$.

One can also approximate the ranges of $\tilde{\epsilon}$ and $\bar{\tilde{\rho}}$ where the BCC solid is stable. This is achieved by calculating the free energy density of the solids using the one-mode approximations for stripes, hexagonal, and BCC structures and the free energy of the liquid using a uniform density. Then the phase diagram can be determined from the common tangent construction and the ranges of $\tilde{\epsilon}$ and $\bar{\tilde{\rho}}$ where the BCC solid is stable can be obtained [45].

The evolution equation for $\tilde{\rho}$ is the Cahn-Hilliard type which involves dissipative dynamics and mass conservation [2]

$$\frac{\partial\tilde{\rho}}{\partial\tilde{t}} = \tilde{L}_\mu \tilde{\nabla}^2 \tilde{\mu}, \quad \tilde{\mu} = (1-\tilde{\epsilon})\tilde{\rho} + \tilde{\rho}^3 + 2\tilde{\nabla}^2\tilde{\rho} + \tilde{\nabla}^4\tilde{\rho} \tag{7}$$

where $\tilde{L}_\mu$ is the mobility coefficient and $\tilde{\mu} = \delta\tilde{\mathcal{F}}/\delta\tilde{\rho}$ is the diffusion potential. This equation can be used to simulate evolution of $\tilde{\rho}$ under specified (or fixed) temperature (from the value of $\tilde{\epsilon}$), mass (from the value of $\bar{\tilde{\rho}}$), and volume (from value of grid spacing); typical simulations under this condition are solidification and microstructural evolution. One can also vary the grid spacing to simulate the evolution of the density profile under specified time-dependent deformation [43]. In the context of the viscoelastic behavior, this technique would be appropriate for the stress-relaxation calculation; however for the viscoelastic-creep and mechanical-hysteresis studies, where the system is subjected to specified external stress, additional dynamic equation is needed.

B. Pressure-Controlled Dynamic Equation

The study of viscoelastic creep and mechanical hysteresis involve specifying the external stress, or, in this study, external pressure, and investigate how the (average) internal pressure

$$\bar{\tilde{P}}_{\text{int}} = \frac{1}{\tilde{V}} \int \left(-\tilde{f} + \tilde{\mu}\tilde{\rho}\right) d\tilde{\mathbf{r}} \tag{8}$$

changes temporally; this requires the dynamic equation that contains external pressure as an independent variable. Such equation, referred to as the pressure-controlled dynamic (PCD) equation, was first introduced by Kocher and Provatas [38] expressed as

$$\frac{d\tilde{V}}{d\tilde{t}} = \tilde{L}'_{\text{def}} \left(\bar{\tilde{P}}_{\text{int}} - \bar{\tilde{P}}_{\text{ext}}\right), \tag{9}$$

where $\tilde{\bar{P}}_{\rm ext}$ is the externally applied pressure, and $\tilde{L}'_{\rm def}$ is the mobility coefficient. This equation can be used in conjunction with Eq. (7) to simulate the system under specified $\tilde{\bar{P}}_{\rm ext}$. If the external pressure is higher (lower) than the internal pressure, or $\tilde{\bar{P}}_{\rm ext} > \tilde{\bar{P}}_{\rm int}$ ($\tilde{\bar{P}}_{\rm ext} < \tilde{\bar{P}}_{\rm int}$), the value of $d\tilde{V}/d\tilde{t}$ will be negative (positive) which indicates that the system will undergo compressive (tensile) deformation.

A slightly modified version of the PCD was recently proposed by Em-Udom and Pisutha-Arnond [37]. The equation is expressed as

$$\frac{d\tilde{V}}{d\tilde{t}} = \tilde{L}_{\rm def}\tilde{V}(\tilde{\bar{P}}_{\rm int} - \tilde{\bar{P}}_{\rm ext}), \tag{10}$$

where $\tilde{L}_{\rm def}$ is the mobility coefficient. This equation was developed using the principle of thermodynamics of hydrostatically-stressed solid [39, 46] and classical irreversible thermodynamic framework [40–42]. The comparison between results between equation (9) and (10) shows that the steady-state behavior obtained from both equations are identical; however, the non-equilibrium behaviors are different. This difference is due to the extra volume term ($\tilde{V}$) on the right-hand side of Eq. (10). This extra volume terms results in higher deformation rate in tension (due to increasing $\tilde{V}$) than the deformation rate in compression (due to decreasing $\tilde{V}$). Nevertheless, for small deformation, the numerical difference from the Eqs. (9) and (10) is unlikely to change the qualitative interpretation of the results. Despite the fact that we employ Eq. (9) in this work, the choice of the PCD equation is immaterial for this study. Hereafter, we will refer to the PFC method that incorporates the PCD equation as PFC-PCD model. Lastly, the tilde notation will also be omitted for simplicity. The more detail on PFC-PCD model are provided in Appendix A.

C. Standard Linear Solid Model

We review the standard linear solid model (SLS) which is a method of modeling viscoelasticity using linear combinations of springs and dampers as shown in Fig. 1. The strain response from this model will be compared with that from the PFC-PCD simulation in order to extract viscoelastic quantities and properties. The governing differential equation for the SLS model is [20, 47]

$$(E_1 + E_2)\frac{de}{dt} + \frac{E_1 E_2}{\eta}e = \frac{E_1}{\eta}\sigma + \frac{d\sigma}{dt} \tag{11}$$

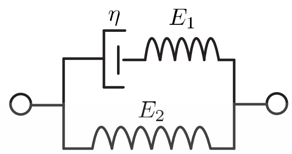

FIG. 1. Schematic illustration of standard Linear Solid Model (SLS) Model.

where e is the strain response from the applied stress σ. Equation (11) can be written in simple form as follows

$$\frac{de}{dt} + Ke = \sigma' + \tau \frac{d\sigma'}{dt} \tag{12}$$

where $K = E_1 E_2/(\eta(E_1 + E_2))$ and $\tau = \eta/E_1$. The variable σ' is the scaled quantity defined as $\sigma' = \sigma/\left(\tau(E_1 + E_2)\right)$.

For the creep behavior, we consider the case where the system (initially at zero stress and strain) is subject to constant stress.

$$\sigma'(t) = \bar{\sigma}'. \tag{13}$$

The corresponding strain is then

$$e(t) = e_\infty \left[1 - \exp\left(-\frac{t}{\tau_c}\right)\right] \tag{14}$$

where $e_\infty = \bar{\sigma}'/K$ is the deformation at $t = \infty$ and $\tau_c = 1/K$ is the relaxation time; the subscript "c" indicate the creep phenomena. The quantities e_∞ is the deformation at steady-state while τ_c relates to the rate at which the system reaches the steady-state deformation. The plot of the strain response is shown as an example in Fig. 2. For the hysteresis behavior, we consider the system induced by harmonic excitation given by

$$\sigma'(t) = \sigma'_A \sin(\omega t) \tag{15}$$

where σ'_A is the stress amplitude, $\omega = 2\pi f$ is the angular frequency, and f is the frequency. At steady state, the strain response yield the solution (see Appendix B):

$$e(t) = e_A \sin(\omega t - \delta) \tag{16}$$

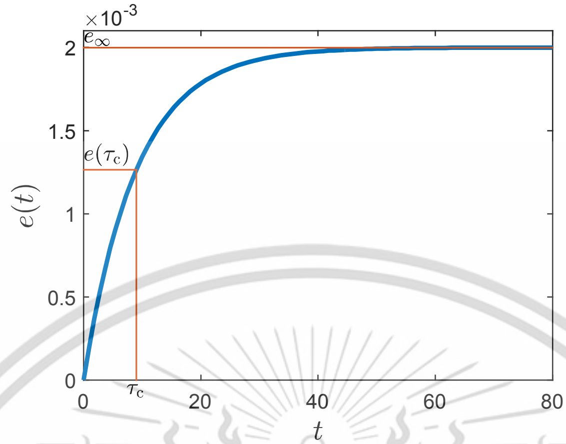

FIG. 2. Viscoelastic creep under step load at the same $e_\infty = 2 \cdot 10^{-3}$ condition and $\tau_c = 9.0$ where t (x-axis) is time variable and $e(t)$ (y-axis) is strain response at time t.

where

$$e_A = \sigma'_A \sqrt{\frac{1 + (\tau\omega)^2}{K^2 + \omega^2}} \tag{17}$$

is the strain amplitude. As a result, the amplitude ratio, A_r, is

$$A_\mathrm{r} = \frac{\sigma'_A}{\sigma_A} \sqrt{\frac{1 + (\tau\omega)^2}{K^2 + \omega^2}} \tag{18}$$

Also, the loss tangent factor,

$$\delta = \arctan\left[\left(\frac{1 - \tau K}{K + \tau\omega^2}\right)\omega\right], \tag{19}$$

defines the phase angle due to time-delayed response. From the solution the complex moduli (or dynamic modulus) can be defined from (all derivation detail is given in Appendix B)

$$G'_\mathrm{complex} \equiv \frac{\sigma'}{e_A} = \frac{K + j\omega}{1 + j\tau\omega} = G'_\mathrm{storage} + jG'_\mathrm{loss}. \tag{20}$$

The quantity G'_complex is a property of viscoelastic materials and can be written further as $G'_\mathrm{complex} = G'_\mathrm{storage} + jG'_\mathrm{loss}$, where G'_storage is the storage modulus and G'_loss is the loss modulus. The quantity G'_storage measures the stored energy and is an elastic response of material while G'_loss measures energy dissipation and is a viscous response of a material. The expressions for G'_storage and G'_loss can be obtained from rearranging the last equality in

Eq. (20), yielding

$$G'_{\text{storage}} = \frac{K + \tau\omega^2}{1 + (\tau\omega)^2}, \quad G'_{\text{loss}} = \frac{(1 - \tau K)\omega}{1 + (\tau\omega)^2}. \tag{21}$$

The loss tangent, $\tan(\delta)$, is the ratio of storage and loss modulus or $\tan(\delta) = G'_{\text{loss}}/G'_{\text{storage}}$; this quantity is a measure of damping in the material.

The behavior of the SLS model a function of excitation frequency is shown in Fig. 3(a). At low frequencies, $\tan(\delta)$ or δ is low, which indicates that the system behaves in an elastic manner. This is due to fact that the dashpot in Fig. 1 has sufficient time to displace, resulting in the stress and strain profiles that are almost in phase. The value of G'_{storage} is relatively small compared with that at higher frequencies due to large strain amplitude (Fig. 3(b)). At high frequencies, the system also behaves elastically as seen from small $\tan(\delta)$; at this condition, the change in stress is too rapid for the dashpot to operate and thus the strain response is in phase with the stress profile. Due to small strain amplitude, the value of G'_{storage} is relatively large.

At intermediate frequencies, a considerable amount of phase lag occurs, as shown schematically in Fig. 3(c), showing a more viscous behavior, and the stress-strain profiles can be plotted to exhibit hysteresis loop as shown in Fig. 3(d) where the area inside the loop represent the energy loss. At the frequency where $\tan(\delta)$ is maximum, the system exhibit the highest damping capacity and, in real materials, this condition is important for damping applications.

III. METHOD OF SIMULATION

In this section, we describe the setup and method of simulations. In all simulations, we construct a BCC unit-cell under hydrostatic pressure (Fig. 4) with a periodic $N \times N \times N$ grid where $N = 16$ and the lattice parameter $L_a = 2\pi\sqrt{2}$; this results in the reference grid spacing, $\Delta r_0 = \sqrt{2}\pi/8$ in all dimensions, and the reference volume $V_0 = (2\pi\sqrt{2})^3$. The initial density profile is constructed with the one-mode approximation in Eq. (6), where the reference density, $\bar{\rho}_0$, is specified. The profile is then relaxed using the evolution equation (Eq. (7)), while fixing $\Delta r = \Delta r_0$ and $\bar{\rho} = \bar{\rho}_0$, until the equilibrium density profile is reached. At this state, the reference internal pressure, $\bar{P}_0$, can be calculated using Eq. (8). Also, the numerical method employed to solve the evolution equation, and also the PCD equation (Eq.

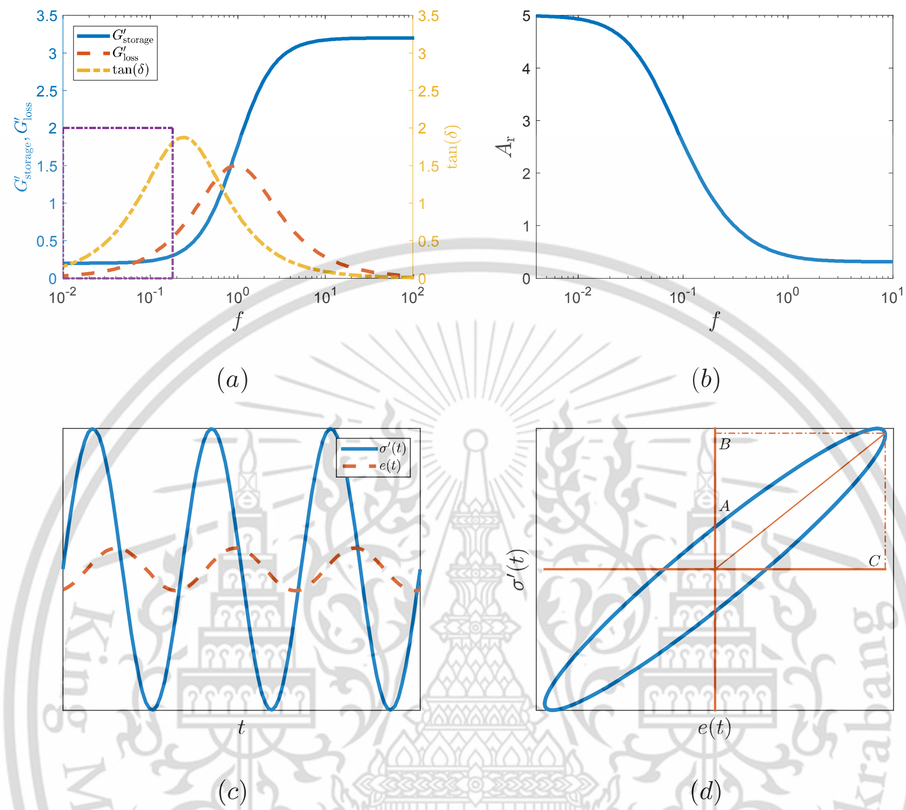

FIG. 3. Hysteresis behavior regarding SLS model. (a) Complex Moduli; Storage modulus G'_{storage} (solid-line on y-axis), loss modulus G'_{loss} (dash-line on y-axis) and loss tangent factor $\tan(\delta)$ (densed dash-line on y-axis) established by SLS model at condition $\sigma'_A = 0.00075$, $K = 0.3750$ and $\tau = 0.1667$ and frequency, f (x-axis), ranges between (0.01,100): Box area depicts FIG. 12(b); (b) Amplitude ratio, A_{r} (y-axis), at frequency, f (x-axis), ranges between (0.004,10) (c) System response schematic demonstrates phase lag between stress or pressure input at time t, $\sigma'(t)$ (solid-line), and strain response at time t, $e(t)$ (dash-line) (d) Mechanical-Hysteresis schematic plot; strain response at time t, $e(t)$ (x-axis), vs stress or pressure input at time t, $\sigma'(t)$ (y-axis).

(10)), is the Fourier pseudo-spectral method where Fourier transform is used to calculate spatial derivatives and the forward finite difference scheme is used to discretize the time derivative (see Appendix A). For the viscoelastic simulations, the PCD equation is employed where different profiles of $\bar{P}_{\text{ext}}(t)$ are specified and the change in the volume is used to update

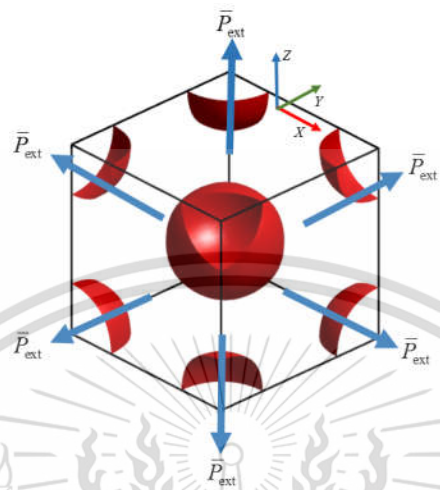

FIG. 4. BCC unit-cell under hydrostatic pressure schematic using isosurface construction; $\sigma_{\mathrm{ii}} = \bar{P}_{\mathrm{ext}}$ depicts stress in $\{\mathrm{ii}\}$ direction where all σ_{ij} components, shear stress components $\{\mathrm{i} \neq \mathrm{j}\}$, are equal to zero.

the grid spacing through the relation

$$\Delta r(t) = \left(\frac{V(t)}{N^3}\right)^{\frac{1}{3}}. \tag{22}$$

We note that the grid spacing $\Delta r(t)$ is identical in all directions due to the assumption of crystal under hydrostatic stress. During the simulation, the mass conservation is imposed by changing the average density through

$$\bar{\rho}(t) = \bar{\rho}_0 \frac{V_0}{V(t)}. \tag{23}$$

Also, the mechanical equilibrium is maintained throughout the deformation process; this is accomplished by relaxing the system using the evolution equation at every time step of the time evolution from the PCD equation. The system response is characterized by the strain defined by

$$e(t) = \frac{\Delta r(t) - \Delta r_0}{\Delta r_0}, \tag{24}$$

which is identical in all directions. The profiles of $e(t)$ and $\bar{P}_{\mathrm{ext}}(t)$ is then used to quantify the viscoelastic behavior predicted form the PFC-PCD method.

Two types of $\bar{P}_{\mathrm{ext}}(t)$ are used in this study. For the viscoelastic creep simulation, the applied pressure is set to

$$\bar{P}_{\text{ext}}(t) = \bar{\mathcal{P}}_{\text{ext}}, \tag{25}$$

where $\bar{\mathcal{P}}_{\text{ext}}$ is a constant. The values of $\bar{\mathcal{P}}_{\text{ext}}$ are chosen such that the pressure deviation from the reference pressure

$$\Delta \bar{P}_0 \equiv \frac{\bar{P}_0 - \bar{\mathcal{P}}_{\text{ext}}}{\bar{P}_0} \tag{26}$$

is positive or negative; the former leads to tensile deformation while the latter results in compressive deformation. The quantities e_∞ and τ_c are numerically extracted from the strain response, $e(t)$, where e_∞ is the values of $e(t)$ at large t, and τ_c is the value of t at $e(\tau_c) = e_\infty(1 - \exp(-1)) \approx 0.6321 e_\infty$ (see Eq. (14) and Fig. 2).

For the hysteresis simulation, the applied pressure is set to

$$\bar{P}_{\text{ext}}(t) = \bar{P}_0 - \bar{P}_A \sin(\omega t), \tag{27}$$

where $\bar{P}_A$ is the pressure amplitude. The pressure deviation from the reference pressure will then be

$$\Delta \bar{P}_0(t) \equiv \frac{\bar{P}_0 - \bar{P}_{\text{ext}}(t)}{\bar{P}_0} = \frac{\bar{P}_A}{\bar{P}_0} \sin(\omega t). \tag{28}$$

With this type of pressure function, the system is then allowed to evolve temporally until the steady-stead strain-response is reached. The strain response profile at steady state will exhibit the sinusoidal behavior similar to Fig. 3(a) and we can numerically measure the strain amplitude e_A in order to calculate the amplitude ratio $A_r = e_A/\bar{P}_A$. When plotting the hysteresis loop as in Fig. 3(d), the complex moduli and loss tangent can be calculated by numerically identify the values of A (pressure value at zero strain), B (pressure value at maximum strain), and C (maximum strain value). Then we evaluate the expressions: $G'_{\text{storage}} = B/C$, $G'_{\text{loss}} = A/C$, and $\tan(\delta) = G'_{\text{loss}}/G'_{\text{storage}}$. We note that in all hysteresis simulations, $\bar{P}_A$ is set to $0.02\bar{P}_0$.

Finally, the values of $\bar{P}_0$ and ϵ in all simulations are restricted to the range of $(-0.248, -0.260)$ and $(0.175, 0.200)$, respectively. This values of $\bar{P}_0$ and ϵ ensures the stability of the bcc crystal as shown in the phase diagram in Ref. [45].

IV. RESULTS AND DISCUSSIONS

A. Viscoelastic-Creep Behavior

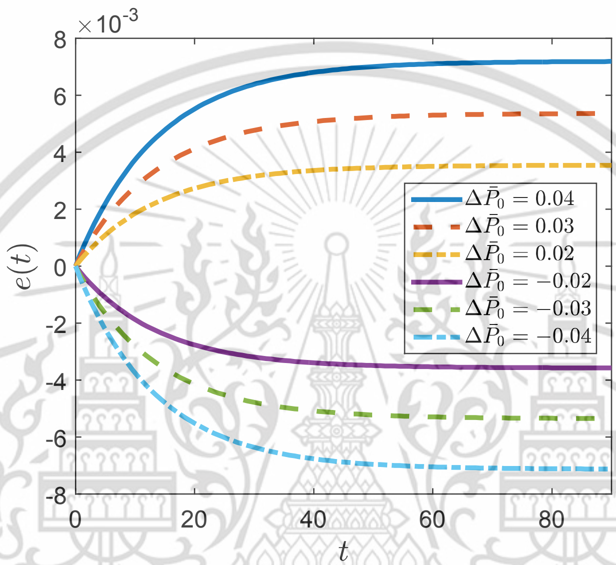

FIG. 5. Viscoelastic-creep behaviors, $e(t)$, under different values of constant pressure, $\Delta\bar{P}_0$, at condition $|\bar{\rho}_0| = 0.2600$, $\epsilon = 0.2000$ and $L_{\text{def}} = 1$ where t (x-axis) is time variable and $e(t)$ (y-axis) is strain response at time t. The results show the capability of PCD equation to control e_∞ through $\Delta\bar{P}_0$.

In this part, we show the viscoelastic-creep behavior exhibited by the PFC-PCD model and demonstrate the dependence of this behavior on $\Delta\bar{P}_0$ and L_{def}. In Fig. 5, we aim to show the strain response from different values of $\Delta\bar{P}_0$. The graphs show the strain, initially at zero, increase or decrease gradually until the steady-state values (denoted as e_∞) are reached. This delayed responses obtained from the simulations are indicative of the viscoelastic-creep behavior; this means that the PFC model combined with the PCD equation is capable of modeling viscoelastic behavior. Also, depending on the values of $\Delta\bar{P}_0$ either tensile or compressive deformations are realized. When $\Delta\bar{P}_0 > 0$, or $\bar{\mathcal{P}}_{\text{ext}} < \bar{P}_0$, tensile deformation is obtained while $\Delta\bar{P}_0 < 0$, or $\bar{\mathcal{P}}_{\text{ext}} > \bar{P}_0$, results in compressive deformation. The magnitudes of e_∞ (steady-state deformation) also scale with the magnitudes of $\Delta\bar{P}_0$, as expected from the elastic effect in the PFC model (Eq. (1)).

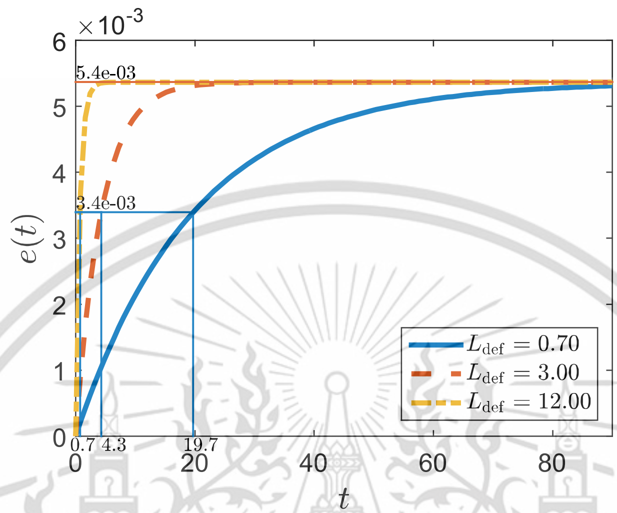

FIG. 6. Viscoelastic-creep behaviors, $e(t)$, under different values of L_{def} at condition $|\bar{\rho}_0| = 0.2600$, $\epsilon = 0.2000$ and $\Delta\bar{P}_0 = 0.03$ where t (x-axis) is time variable and $e(t)$ (y-axis) is strain response at time t. The results demonstrate the capability of PCD equation to control relaxation time, τ_c, through L_{def}.

Next, Fig. 6 shows how viscoelastic behavior is affected by L_{def}. From the figure, the increase in L_{def} results in $e(t)$ approaching e_∞ in a faster rate, or smaller τ_c; this means that the increase in L_{def} leads to the faster strain response or higher degree of elasticity. This results demonstrates that L_{def} can be used to adjusted the degree of viscoelasticity ranging from highly viscous to highly elastic. The capability to control the degree of viscoelastic creep can be used to tune the PFC-PCD model to different types of materials.

The degree of viscoelasticity is also affected by ϵ (inverse of temperature), as shown in Fig. 7. From the figure, the values of τ_c decreases as the values of ϵ increases for the range of $\bar{\rho}_0$ where solid is stable. Since ϵ is inversely proportional to temperature, this indicates that the system response faster, or becomes more elastic, as temperature decreases; this prediction agrees with the experimental observation where relaxation time in creep phenomena decreases with temperature.

We note that the results from Fig. 6 and Fig. 7 assume that L_{def} and ϵ are independent from one another. Nevertheless, since both L_{def} and ϵ both affects the viscoelasticity behavior, it is likely that L_{def} and ϵ (or temperature) are related. From the derivation in [37], L_{def} originates from linear phenomenological law in the classical irreversible thermodynamic framework. Therefore, the dependence of L_{def} on temperature could be introduced by considering a more rigorous treatment of this phenomenological law.

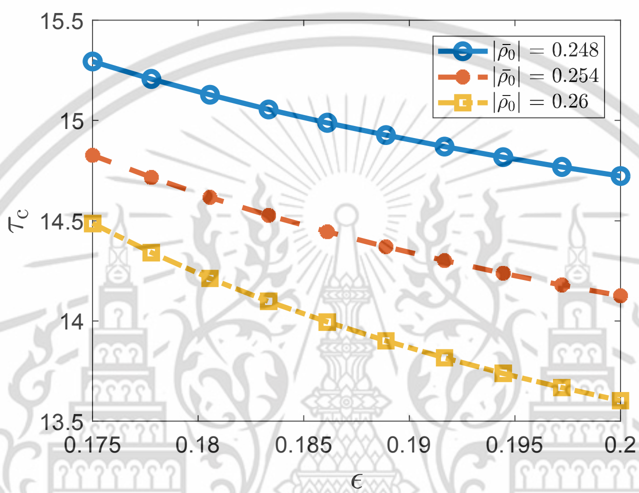

FIG. 7. Viscoelastic-creep parametric study under step pressure; Influence of temperature, ϵ (x-axis), parameter on relaxation time, τ_c (y-axis), parameter at ϵ parameter ranges between $(0.175, 0.200)$ with three different atomic density, $|\bar{\rho}_0|$, values. All numerical experiments are based on step pressure input ($\Delta \bar{P}_0 = 0.02$). It should be noted that the ϵ parameter is inversely related to temperature.

Lastly, we report how the stiffness changes with ϵ and $\bar{\rho}_0$. This is shown in Fig. 8(a) and 8(b), where the values of e_∞ are plot as functions of ϵ and $\bar{\rho}_0$, respectively. Since $\Delta \bar{P}_0$ is the same in all simulations, lower e_∞ values indicates higher stiffness and vice versa. From Fig. 8(a), e_∞ decreases as ϵ increases while, from Fig. 8(b) e_∞ increases as $|\bar{\rho}_0|$ increases. This indicates that the stiffness is higher at lower temperature and lower atomic densities. These results are qualitatively consistent with theoretical framework [13, 48] and experimental observation [49–51]. We note that stiffness is not a viscoelastic property and the consistency of the stiffness-variation with ϵ and $\bar{\rho}_0$ originates from the PFC free energy (Eq. (1)), not the PCD equation. Nevertheless, these stiffness results demonstrate the application of the PCD equation since it allows convenient calculation of e_∞ from specified values of $\Delta \bar{P}_0$.

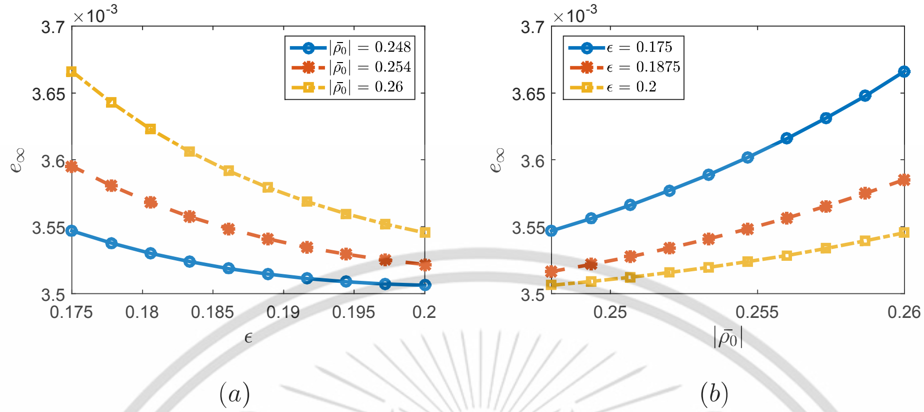

FIG. 8. Viscoelastic-creep parametric study under step pressure; (a) Influence of temperature, ϵ (x-axis), parameter on e_∞ (y-axis) at ϵ parameter ranges between $(0.175, 0.200)$ with three different $|\bar{\rho}_0|$ values (b) Influence of atomic density, $\bar{\rho}_0$ (x-axis), parameter on e_∞ (y-axis) at $|\bar{\rho}_0|$ parameter ranges between $(0.248, 0.260)$ with three different ϵ values. All numerical experiments are based on step pressure input ($\Delta\bar{P}_0 = 0.02$). It should be noted that the ϵ parameter is inversely related to temperature.

B. Hysteresis Behavior

In this part, we report the hysteresis behavior exhibited by the PFC-PCD model and demonstrate the dependency of this behavior on f (pressure oscillation frequency), L_{def} (PCD parameter), and ϵ (inverse of temperature). The steady-state strain response from the PFC-PCD model is shown Fig. 9(a)-(c) while the strain response from the SLS model is shown in Fig. 9(d)-(f) for comparison. For the $f = 0.004$ and $f = 0.0232$, the PFC-PCD model shows the phase lag between the strain and pressure profiles and also the increase in the phase lag with increasing frequencies; these results which qualitatively agree with the result from the SLS model. However, the phase lag from the PFC-PCD model does not decreases at high frequency as in the SLS model as shown for $f = 100$; the strain response from the PFC-PCD model still shows significant phase lag while for the SLS model, both stress and strain profiles are in phase. The results indicates that the PFC-PCD model does not exhibit elastic behavior at very frequency. This suggests that even though the PFC-PCD model is capable of exhibiting viscoelastic response (or phase lag) from the oscillating pressure, the applicability of this phenomena is still limited to the low frequency excitation.

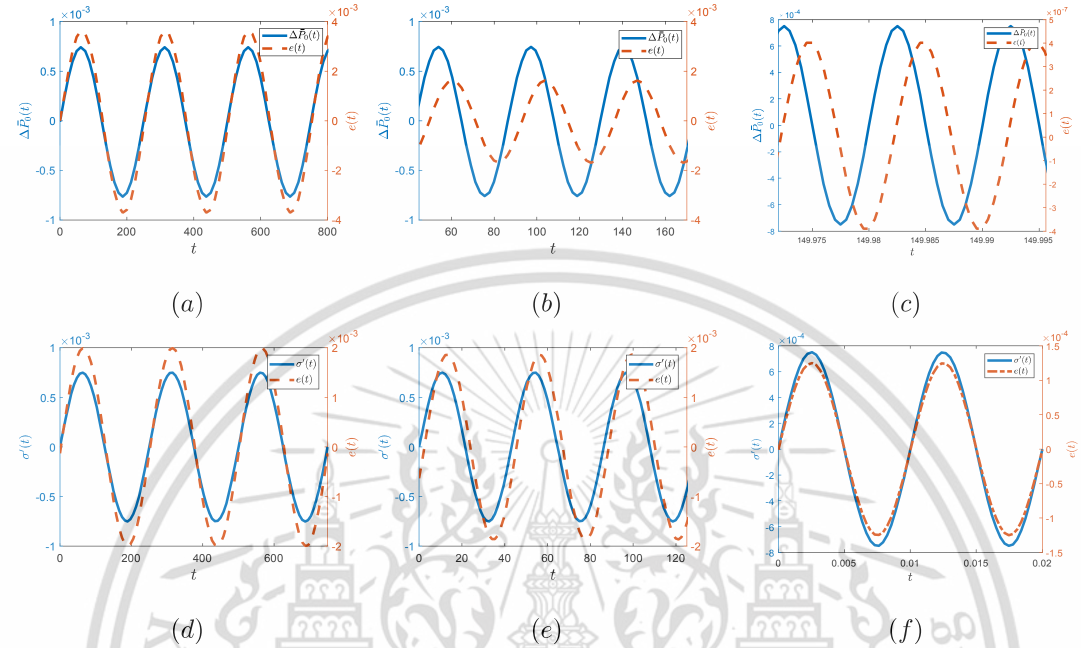

FIG. 9. Influence of frequency, f, on system response; sinusoidal pressure input $\Delta\bar{P}_0(t)$ (solid-line on y-axis) and strain response $e(t)$ (dash-line on y-axis) established by PCD equation (a) $f = 0.004$ (b) $f = 0.0232$ (c) $f = 100$; at condition $|\bar{\rho}_0| = 0.2600$, $\epsilon = 0.1750$ and $L_{\text{def}} = 1$; sinusoidal input $\sigma'(t)$ (solid-line on y-axis) and strain response $e(t)$ (dash-line on y-axis) established by SLS model regarding equation (16) (d) $f = 0.004$ and (e) $f = 0.0232$ (f) $f = 100$ at condition $\sigma'_A = 0.00075$, $K = 0.3750$ and $\tau = 1.6670$.

Another comparison between the PFC-PCD and the SLS model can be shown in Fig. 10 where the amplitude ratios are shown. Both the PFC-PCD and the SLS model shows reducing amplitudes with increasing frequencies and both amplitude ratios exhibit qualitatively similar functional forms. However, the amplitude ratio from the PFC-PCD model is vanishingly small at high frequencies while the amplitude ratio form the SLS model remains at finite values. The values of the amplitude ratio can also be seen from the hysteresis loop in Fig. 11 where the results in Fig. 9 are plotted on a stress/pressure-strain axes. As the frequency increase, the hysteresis loop rotates counter-clockwise, indicating smaller strain amplitude (or amplitude ratio). At $f = 100$, the hysteresis loop from the PFC-PCD model almost form a vertical line due to essentially zero amplitude ratio while the hysteresis loop from the SLS model remains tilted away from the y-axis. This extremely small amplitude

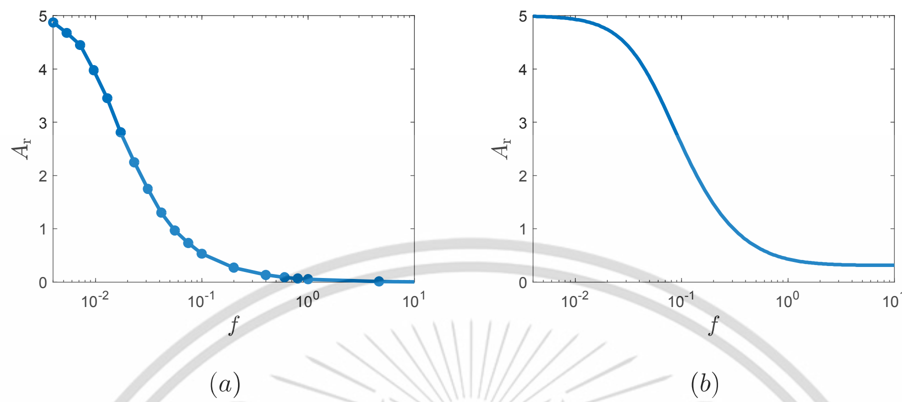

FIG. 10. Influence of frequency, f (x-axis), on amplitude ratio, A_r (y-axis), parameter under sinusoidal input (a) PCD equation; at condition $|\bar{\rho}_0| = 0.2600$ and $\epsilon = 0.1750$ (b) SLS model.

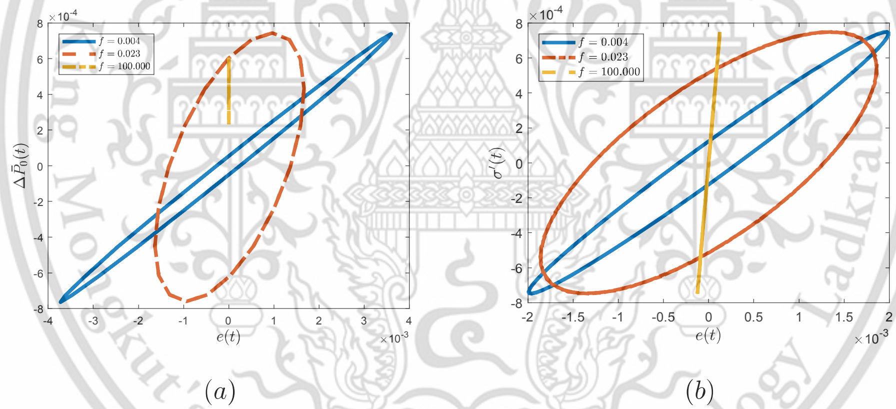

FIG. 11. Influence of frequency, f on Mechanical-Hysteresis behavior (a) Mechanical-Hysteresis established by PCD equation at condition $|\bar{\rho}_0| = 0.2600$, $\epsilon = 0.1750$ (b) Mechanical-Hysteresis established by SLS model at condition $\sigma'_A = 0.00075$, $K = 0.3750$ and $\tau = 1.6670$ where $e(t)$ (x-axis) is strain response at time t whereas $\Delta\bar{P}_0(t)$ (y-axis) and $\sigma'(t)$ (y-axis) are pressure input at time t established by PCD equation and SLS model, respectively.

ratio indicates that the system produce almost zero strain from the input pressure, which leads to unnaturally large values of the moduli (G'_{storage} and G'_{loss}). Therefore, the application of the PFC-PCD method to model dynamic viscoelastic behavior should be limited to low frequency excitation. Nevertheless, at the low frequency, the prediction of G'_{storage}, G'_{loss} and $\tan(\delta)$ are in good agreement with the results from the SLS model as shown in Fig. 12.

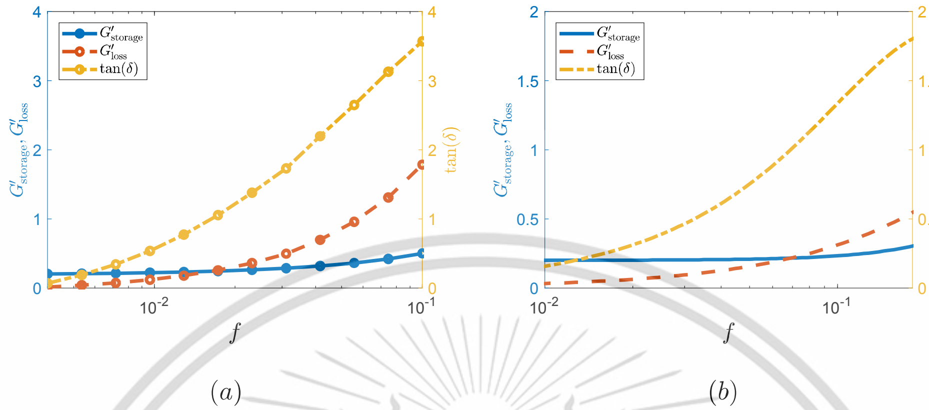

FIG. 12. Influence of frequency, f (x-axis), on Complex Moduli (y-axis); G'_{storage} (storage modulus), G'_{loss} (loss modulus) and $\tan(\delta)$ (loss tangent factor); (a) Complex Moduli (y-axis) established by PCD equation at condition $|\bar{\rho}_0| = 0.2600$ and $\epsilon = 0.1750$ (b) Complex Moduli (y-axis) established by SLS model at condition $\sigma'_A = 0.00075$, $K = 0.3750$ and $\tau = 0.1667$ and f ranges between (0.01,0.18).

To further investigate into the difference between the results from the PFC-PCD and those from the SLS model, we expand the PCD equation in terms of strain and perform the Taylor's expansion to the first order with respect to strain; the details of the derivation are shown in Appendix C. Compared with the SLS equation, the transformed PCD equation lacks the term with the time derivative of stress. This analysis indicates that the PCD equation is more similar to the Kelvin-Voigt model than the SLS model. The Kelvin-Voigt model consists of a spring and a dashpot in parallel and is capable of reproducing the creep phenomena, but not the stress relaxation. This similarity between the PCD and the Kelvin-Voigt models explains why the PFC-PCD model can reproduce creep phenomena, but not the dynamic behavior similar to the SLS model. We note that the lack of similarity to the SLS model not only applies to our recently proposed PCD equation [36] but also applies to the PCD equation propose by Kocher and Provatas [38] since the functional forms of both equations are the same. Nevertheless, this analysis suggests the possibility of improving the PFC-PCD model by modifying the PCD equation in such a way that the effect of the term with the time derivative of stress is present.

Similar to the result from the viscoelastic-creep study, the PCD parameter L_{def} can be

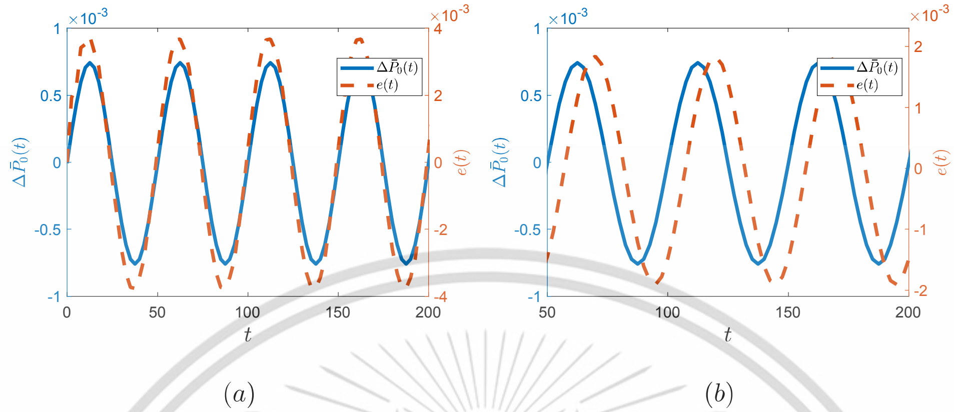

FIG. 13. Influence of L_{def} parameter on system response; sinusoidal pressure input $\Delta \bar{P}_0(t)$ (solid-line on y-axis) and strain response $e(t)$ (dash-line on y-axis) at time t (x-axis); (a) $L_{\text{def}} = 10$ (b) $L_{\text{def}} = 1$; at $|\bar{\rho}_0| = 0.2600$, $\epsilon = 0.1750$ and $f = 0.02$.

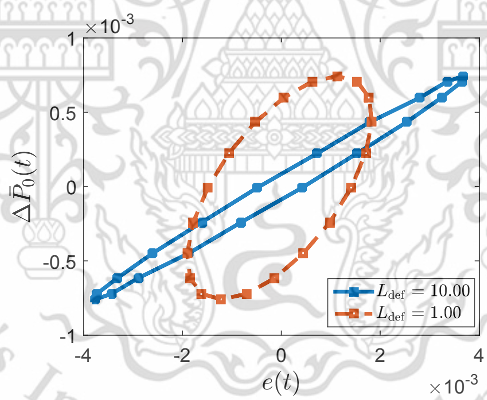

FIG. 14. Influence of L_{def} on Mechanical-Hysteresis behavior at condition $|\bar{\rho}_0| = 0.2600$, $\epsilon = 0.1750$ and $f = 0.02$ where $e(t)$ (x-axis) is strain response at time t and $\Delta \bar{P}_0(t)$ (y-axis) is pressure input at time t established by PCD equation.

used to control the degree of viscoelasticity. Figures 13(a) and (b) show the strain response with different values of L_{def} at fixed pressure-oscillation frequency. The hysteresis loops from these results are also shown in Fig. 14. The results show that decreasing the value of L_{def} lead to higher phase lag (Fig. 13) and higher damping capacity (Fig. 14). This indicates that lowering L_{def} value leads to the system having in a more viscous manner. The opposite is also true where increasing L_{def} leads to a more elastic response from the system.

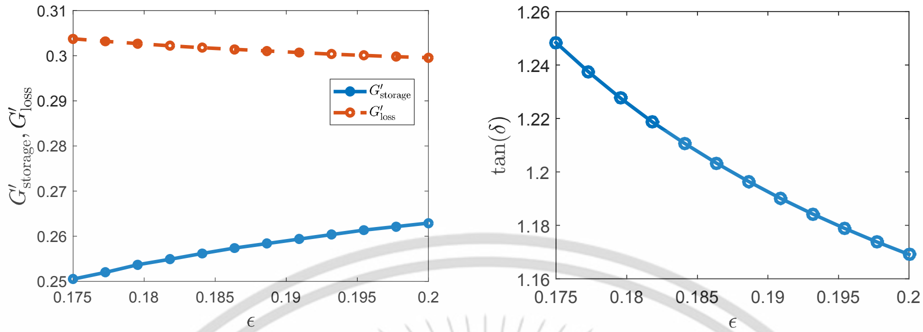

(a) (b)

FIG. 15. Influence of temperature, ϵ (x-axis), parameter on (a) Storage modulus, G'_{storage} (solid-line on y-axis), and loss modulus, G'_{loss} (dash-line on y-axis), and (b) Loss tangent factor, $\tan(\delta)$ (y-axis), at $|\bar{\rho}_0| = 0.2600$ and $f = 0.02$. It should be noted that the ϵ parameter is inversely related to temperature.

The influence of ϵ on G'_{storage}, G'_{loss}, and $\tan(\delta)$ is shown in Fig. 15. Figure 15(a) shows that an increase in ϵ (decrease in temperature) leads to an increase in G'_{storage} and a decrease in G'_{loss}. As $\tan(\delta) = G'_{\text{loss}}/G'_{\text{storage}}$, the values of $\tan(\delta)$ decreases with increasing ϵ, as shown in Fig. 15(b). The results show that as temperature decreases, the system behaves in a less viscous manner and with reducing damping capacity. These trends qualitatively agree with polymeric materials below glass transition [52] and metals such as aluminum alloy [53].

It should be noted that particular form of the PFC free energy (Eq. (1)) is applicable to crystalline materials such as metals [45]; therefore, it might seem that the results from this work only pertains to these types of materials. Nevertheless, since the viscoelastic behavior originates from the PCD equation, not the PFC free energy, alternative form PFC free energy (Eq. (1)) can be used and the modified PFC-PCD model should still exhibit similar viscoelastic behavior as well as similar dependence of viscoelastic properties on the PFC-PCD model parameters. The capability to generalize the PFC free energy allows modeling of viscoelastic behavior in different types of materials such as polymeric materials where viscoelasticity is much more pronounced than that in metals.

V. CONCLUSION

In this study, we aim to show the capability and the limitation of PFC-PCD model which was first employed to investigate the viscoelastic-creep and mechanical-hysteresis behaviors in BCC (3D case) unit cell under hydrostatic pressure. To achieve our goal, we implement two types of pressure profiles in our analysis: constant pressure input for viscoelastic-creep study and sinusoidal pressure oscillation for mechanical hysteresis study where all PFC parameters: temperature and atomic density parameters are established in a solid stable region. The conclusions for each analysis are summarized as below

1. In viscoelastic-creep study, we first investigate the influence of two PCD parameters: magnitude of pressure input, and mobility coefficient on viscoelastic-creep behavior. Regarding the results, we find the magnitude of pressure input scales with that of deformation at steady-state time both tensile and compressive loads. Whereas, the mobility coefficient can be used to control the degree of viscosity of deformation in that higher mobility results in higher elasticity as well as lower mobility leads to higher viscosity. This evidence suggests that we can control both the magnitude of deformation and the degree of viscoelasticity through PCD parameters. Second, we study the impact of PFC parameters: temperature on relaxation time and the magnitude of deformation at steady-state condition as well as atomic density parameter on the magnitude of deformation at steady-state condition. Regarding the results, we find that the system response faster, less relaxation time, and less deformation, more stiffness, at lower temperature which is generally consistent with theoretical framework and experimental observation. Also, the system exhibits larger deformation, less stiffness, at higher atomic density that shows an agreement with previous work.

2. In dynamic behavior study, we first focus on studying the impact of excitation frequency on strain response, amplitude ratio, mechanical-hysteresis and complex moduli. The results predicted by PFC-PCD model indicate that the system displays more phase lag between sinusoidal pressure oscillation and strain response with reducing amplitude ratio at increased frequency which qualitatively agrees with that of SLS model. However, at very frequency range, the results exhibited by both models are inconsistent. This finding can also be observed in mechanical-hysteresis loop. The hysteresis

loop exhibited by PFC-PCD becomes vertical line which indicates the system produce almost zero strain. This finding produces unusually large values of complex moduli unlike SLS model prediction. Furthermore, we show that mobility coefficient can also be used to control the degree of viscoelasticity in dynamic behavior under sinusoidal pressure oscillation. The impact of temperature on complex moduli predicted by the PFC-PCD model is also in good agreement with experimental observation.

Finally, we show that PCD model is more similar to Kelvin-Voigt model than SLS model regarding Taylor's expansion in appendix C. This deviation seems not to cause any difference in viscoelastic-creep behavior but mechanical-hysteresis behavior tends to differ from the SLS model at very frequency. However, the prediction of the model is well agreed with the SLS model at the low-frequency range. Therefore, the application of PFC-PCD method to predict dynamic viscoelastic behavior should be limited in some certain frequency region. This analysis provides the possibility of enhancing the PFC-PCD model by modifying the PCD equation in a more proper way which might be addressed in future improvement.

VI. DATA AVAILABILITY

The data used to support the findings of this study are available from the corresponding author upon request.

VII. CONFLICTS OF INTEREST

The authors declare that they have no conflicts of interest.

VIII. ACKNOWLEDGMENT

This research was supported by the NSTDA-University-Industry Research Collaboration (NUI-RC) program under grant No. NUI-RC-M33-22-59-001D, Thailand Research Fund (TRF) under Grant No. TRG5880008, the New Researcher Scholarship of Coordinating Center for Thai Government Science and Technology Scholarship Students, Ministry of Science and Technology (FDA-CO-2561-840g-TH), King Mongkut's Institute of Technology

Ladkrabang Research Fund under Grant No. KREF046103, and High Performance Computing Services from (Thailand) National Electronics and Computer Technology Center (NECTEC). The authors are also indebted to Dr.Sasawat Mahabunphachai for his helpful discussion and encouragement on the research.

Appendix A: PFC-PCD equations and their numerical scheme

The PFC-PCD equation consists of two governing equations; Cahn-Hilliard (CH) type equation and pressure-controlled dynamics (PCD) equation. The first equation is involved dissipative dynamics and mass conservation equation Ref. [2] formulated in partial differential equation (PDE) with four independent variables $(\tilde{t}, \tilde{r}_1, \tilde{r}_2, \tilde{r}_3)$; time variable with three spatial coordinate variables

$$\frac{\partial \tilde{\rho}}{\partial \tilde{t}} = \tilde{L}_\mu \tilde{\nabla}^2 \frac{\delta \tilde{\mathcal{F}}}{\delta \tilde{\rho}} \tag{A1}$$

where $\tilde{\rho} \equiv \tilde{\rho}(\tilde{t}, \tilde{r}_1, \tilde{r}_2, \tilde{r}_3)$ is density field variable in three dimensional space. $\tilde{L}_\mu$ is the mobility coefficient. $\tilde{\nabla}^2(\cdot) = \partial^2(\cdot)/\partial\tilde{r}_1^2 + \partial^2(\cdot)/\partial\tilde{r}_2^2 + \partial^2(\cdot)/\partial\tilde{r}_3^2$ is three dimensional Laplacian operator. $\delta\tilde{\mathcal{F}}/\delta\tilde{\rho} \equiv \tilde{\mu}$ is the variational derivative of $\tilde{\mathcal{F}}$ by $\tilde{\rho}$ which defines a chemical potential $\tilde{\mu}$. The free energy functional $\tilde{\mathcal{F}}$ can be expressed

$$\tilde{\mathcal{F}} = \int \frac{\tilde{\rho}}{2}\left[-\tilde{\epsilon} + \left(1 + \tilde{\nabla}^2\right)^2\right]\tilde{\rho} + \frac{\tilde{\rho}^4}{4}\, d\tilde{\mathbf{r}} \tag{A2}$$

or in alternative form

$$\tilde{\mathcal{F}} = \int \tilde{w}\left(\tilde{\rho}\right)\, d\tilde{\mathbf{r}}, \quad \tilde{\mathcal{F}} = \int \left[\left(1 - \tilde{\epsilon}\right)\frac{\tilde{\rho}^2}{2} + \frac{\tilde{\rho}^4}{4} + \tilde{\rho}\tilde{\nabla}^2\tilde{\rho} + \frac{\tilde{\rho}}{2}\tilde{\nabla}^4\tilde{\rho}\right] d\tilde{\mathbf{r}} \tag{A3}$$

where $\tilde{\nabla}^4(\cdot) = \partial^4(\cdot)/\partial\tilde{r}_1^4 + \partial^4(\cdot)/\partial\tilde{r}_2^4 + \partial^4(\cdot)/\partial\tilde{r}_3^4 + 2\partial^4(\cdot)/\partial\tilde{r}_1^2\partial\tilde{r}_2^2 + 2\partial^4(\cdot)/\partial\tilde{r}_1^2\partial\tilde{r}_3^2 + 2\partial^4(\cdot)/\partial\tilde{r}_2^2\partial\tilde{r}_3^2$. The free energy density variable, $\tilde{w}\left(\tilde{\rho}\right)$, can be expressed in expansion form as

$$\begin{aligned}\tilde{w}\left(\tilde{\rho}\right) = {} & \left(1 - \tilde{\epsilon}\right)\frac{\tilde{\rho}^2}{2} + \frac{\tilde{\rho}^4}{4} + \tilde{\rho}\frac{\partial^2\tilde{\rho}}{\partial\tilde{r}_1^2} + \tilde{\rho}\frac{\partial^2\tilde{\rho}}{\partial\tilde{r}_2^2} + \tilde{\rho}\frac{\partial^2\tilde{\rho}}{\partial\tilde{r}_3^2} + \frac{\tilde{\rho}}{2}\frac{\partial^4\tilde{\rho}}{\partial\tilde{r}_1^4} + \frac{\tilde{\rho}}{2}\frac{\partial^4\tilde{\rho}}{\partial\tilde{r}_2^4} + \frac{\tilde{\rho}}{2}\frac{\partial^4\tilde{\rho}}{\partial\tilde{r}_3^4} \\ & + \tilde{\rho}\frac{\partial^4\tilde{\rho}}{\partial\tilde{r}_1^2\partial\tilde{r}_2^2} + \tilde{\rho}\frac{\partial^4\tilde{\rho}}{\partial\tilde{r}_1^2\partial\tilde{r}_3^2} + \tilde{\rho}\frac{\partial^4\tilde{\rho}}{\partial\tilde{r}_2^2\partial\tilde{r}_3^2}\end{aligned} \tag{A4}$$

Denote that $\tilde{w}\left(\tilde{\rho}\right) \equiv \tilde{f}(\tilde{\rho}, \tilde{\rho}_{\tilde{r}_1\tilde{r}_1}, \tilde{\rho}_{\tilde{r}_2\tilde{r}_2}, \tilde{\rho}_{\tilde{r}_3\tilde{r}_3}, \tilde{\rho}_{\tilde{r}_1\tilde{r}_1\tilde{r}_1\tilde{r}_1}, \tilde{\rho}_{\tilde{r}_2\tilde{r}_2\tilde{r}_2\tilde{r}_2}, \tilde{\rho}_{\tilde{r}_3\tilde{r}_3\tilde{r}_3\tilde{r}_3}, \tilde{\rho}_{\tilde{r}_1\tilde{r}_1\tilde{r}_2\tilde{r}_2}, \tilde{\rho}_{\tilde{r}_1\tilde{r}_1\tilde{r}_3\tilde{r}_3}, \tilde{\rho}_{\tilde{r}_2\tilde{r}_2\tilde{r}_3\tilde{r}_3})$ where each independent variable of $\tilde{f}$ is defined by

$$\begin{gathered}\tilde{\rho}_{\tilde{r}_1\tilde{r}_1} = \frac{\partial^2\tilde{\rho}}{\partial\tilde{r}_1^2}, \quad \tilde{\rho}_{\tilde{r}_2\tilde{r}_2} = \frac{\partial^2\tilde{\rho}}{\partial\tilde{r}_2^2}, \quad \tilde{\rho}_{\tilde{r}_3\tilde{r}_3} = \frac{\partial^2\tilde{\rho}}{\partial\tilde{r}_3^2} \\ \tilde{\rho}_{\tilde{r}_1\tilde{r}_1\tilde{r}_1\tilde{r}_1} = \frac{\partial^4\tilde{\rho}}{\partial\tilde{r}_1^4}, \quad \tilde{\rho}_{\tilde{r}_2\tilde{r}_2\tilde{r}_2\tilde{r}_2} = \frac{\partial^4\tilde{\rho}}{\partial\tilde{r}_2^4}, \quad \tilde{\rho}_{\tilde{r}_3\tilde{r}_3\tilde{r}_3\tilde{r}_3} = \frac{\partial^4\tilde{\rho}}{\partial\tilde{r}_3^4} \\ \tilde{\rho}_{\tilde{r}_1\tilde{r}_1\tilde{r}_2\tilde{r}_2} = \frac{\partial^4\tilde{\rho}}{\partial\tilde{r}_1^2\partial\tilde{r}_2^2}, \quad \tilde{\rho}_{\tilde{r}_1\tilde{r}_1\tilde{r}_3\tilde{r}_3} = \frac{\partial^4\tilde{\rho}}{\partial\tilde{r}_1^2\partial\tilde{r}_3^2}, \quad \tilde{\rho}_{\tilde{r}_2\tilde{r}_2\tilde{r}_3\tilde{r}_3} = \frac{\partial^4\tilde{\rho}}{\partial\tilde{r}_2^2\partial\tilde{r}_3^2}\end{gathered} \tag{A5}$$

To solve equation (A1), $\tilde{\mu}$ variable must be reformulated as a function of $\tilde{\rho}$ and its derivative. Therefore, we need to find $\delta\tilde{\mathcal{F}}/\delta\tilde{\rho}$ by using functional derivative definition

$$\begin{aligned}\frac{\delta\tilde{\mathcal{F}}}{\delta\tilde{\rho}} = \frac{\partial\tilde{f}}{\partial\tilde{\rho}} + \frac{\partial^2}{\partial\tilde{r}_1^2}\left(\frac{\partial\tilde{f}}{\partial\tilde{\rho}_{\tilde{r}_1\tilde{r}_1}}\right) + \frac{\partial^2}{\partial\tilde{r}_2^2}\left(\frac{\partial\tilde{f}}{\partial\tilde{\rho}_{\tilde{r}_2\tilde{r}_2}}\right) + \frac{\partial^2}{\partial\tilde{r}_3^2}\left(\frac{\partial\tilde{f}}{\partial\tilde{\rho}_{\tilde{r}_3\tilde{r}_3}}\right) + \frac{\partial^4}{\partial\tilde{r}_1^4}\left(\frac{\partial\tilde{f}}{\partial\tilde{\rho}_{\tilde{r}_1\tilde{r}_1\tilde{r}_1\tilde{r}_1}}\right) \\ + \frac{\partial^4}{\partial\tilde{r}_2^4}\left(\frac{\partial\tilde{f}}{\partial\tilde{\rho}_{\tilde{r}_2\tilde{r}_2\tilde{r}_2\tilde{r}_2}}\right) + \frac{\partial^4}{\partial\tilde{r}_3^4}\left(\frac{\partial\tilde{f}}{\partial\tilde{\rho}_{\tilde{r}_3\tilde{r}_3\tilde{r}_3\tilde{r}_3}}\right) + \frac{\partial^4}{\partial\tilde{r}_1^2\tilde{r}_2^2}\left(\frac{\partial\tilde{f}}{\partial\tilde{\rho}_{\tilde{r}_1\tilde{r}_1\tilde{r}_2\tilde{r}_2}}\right) \\ + \frac{\partial^4}{\partial\tilde{r}_1^2\tilde{r}_3^2}\left(\frac{\partial\tilde{f}}{\partial\tilde{\rho}_{\tilde{r}_1\tilde{r}_1\tilde{r}_3\tilde{r}_3}}\right) + \frac{\partial^4}{\partial\tilde{r}_2^2\tilde{r}_3^2}\left(\frac{\partial\tilde{f}}{\partial\tilde{\rho}_{\tilde{r}_2\tilde{r}_2\tilde{r}_3\tilde{r}_3}}\right)\end{aligned} \tag{A6}$$

Evaluate each derivative term on the right hand side of equation (A6)

$$\begin{gathered}\frac{\partial\tilde{f}}{\partial\tilde{\rho}} = (1-\tilde{\epsilon})\,\tilde{\rho} + \tilde{\rho}^3 + \frac{\partial^2\tilde{\rho}}{\partial\tilde{r}_1^2} + \frac{\partial^2\tilde{\rho}}{\partial\tilde{r}_2^2} + \frac{\partial^2\tilde{\rho}}{\partial\tilde{r}_3^2} + \frac{1}{2}\left(\frac{\partial^4\tilde{\rho}}{\partial\tilde{r}_1^4} + \frac{\partial^4\tilde{\rho}}{\partial\tilde{r}_2^4} + \frac{\partial^4\tilde{\rho}}{\partial\tilde{r}_3^4} + 2\frac{\partial^4\tilde{\rho}}{\partial\tilde{r}_1^2\partial\tilde{r}_2^2} + 2\frac{\partial^4\tilde{\rho}}{\partial\tilde{r}_1^2\partial\tilde{r}_3^2} + 2\frac{\partial^4\tilde{\rho}}{\partial\tilde{r}_2^2\partial\tilde{r}_3^2}\right) \\ \frac{\partial^2}{\partial\tilde{r}_1^2}\left(\frac{\partial\tilde{f}}{\partial\tilde{\rho}_{\tilde{r}_1\tilde{r}_1}}\right) = \frac{\partial^2\tilde{\rho}}{\partial\tilde{r}_1^2},\quad \frac{\partial^2}{\partial\tilde{r}_2^2}\left(\frac{\partial\tilde{f}}{\partial\tilde{\rho}_{\tilde{r}_2\tilde{r}_2}}\right) = \frac{\partial^2\tilde{\rho}}{\partial\tilde{r}_2^2},\quad \frac{\partial^2}{\partial\tilde{r}_3^2}\left(\frac{\partial\tilde{f}}{\partial\tilde{\rho}_{\tilde{r}_3\tilde{r}_3}}\right) = \frac{\partial^2\tilde{\rho}}{\partial\tilde{r}_3^2} \\ \frac{\partial^4}{\partial\tilde{r}_1^4}\left(\frac{\partial\tilde{f}}{\partial\tilde{\rho}_{\tilde{r}_1\tilde{r}_1\tilde{r}_1\tilde{r}_1}}\right) = \frac{1}{2}\frac{\partial^4\tilde{\rho}}{\partial\tilde{r}_1^4},\quad \frac{\partial^4}{\partial\tilde{r}_2^4}\left(\frac{\partial\tilde{f}}{\partial\tilde{\rho}_{\tilde{r}_2\tilde{r}_2\tilde{r}_2\tilde{r}_2}}\right) = \frac{1}{2}\frac{\partial^4\tilde{\rho}}{\partial\tilde{r}_2^4},\quad \frac{\partial^4}{\partial\tilde{r}_3^4}\left(\frac{\partial\tilde{f}}{\partial\tilde{\rho}_{\tilde{r}_3\tilde{r}_3\tilde{r}_3\tilde{r}_3}}\right) = \frac{1}{2}\frac{\partial^4\tilde{\rho}}{\partial\tilde{r}_3^4} \\ \frac{\partial^4}{\partial\tilde{r}_1^2\tilde{r}_2^2}\left(\frac{\partial\tilde{f}}{\partial\tilde{\rho}_{\tilde{r}_1\tilde{r}_1\tilde{r}_2\tilde{r}_2}}\right) = \frac{\partial^4\tilde{\rho}}{\partial\tilde{r}_1^2\partial\tilde{r}_2^2},\quad \frac{\partial^4}{\partial\tilde{r}_1^2\tilde{r}_3^2}\left(\frac{\partial\tilde{f}}{\partial\tilde{\rho}_{\tilde{r}_1\tilde{r}_1\tilde{r}_3\tilde{r}_3}}\right) = \frac{\partial^4\tilde{\rho}}{\partial\tilde{r}_1^2\partial\tilde{r}_3^2},\quad \frac{\partial^4}{\partial\tilde{r}_2^2\tilde{r}_3^2}\left(\frac{\partial\tilde{f}}{\partial\tilde{\rho}_{\tilde{r}_2\tilde{r}_2\tilde{r}_3\tilde{r}_3}}\right) = \frac{\partial^4\tilde{\rho}}{\partial\tilde{r}_2^2\partial\tilde{r}_3^2}\end{gathered} \tag{A7}$$

Substitute each term of equation (A7) into equation (A6). Then, the chemical potential $\tilde{\mu}$ is literally obtained

$$\tilde{\mu} = (1-\tilde{\epsilon})\,\tilde{\rho} + \tilde{\rho}^3 + 2\tilde{\nabla}^2\tilde{\rho} + \tilde{\nabla}^4\tilde{\rho} \tag{A8}$$

Finally, the equation (A1) becomes

$$\frac{\partial\tilde{\rho}}{\partial\tilde{t}} = \tilde{L}_\mu\left[(1-\tilde{\epsilon})\,\tilde{\nabla}^2\tilde{\rho} + \tilde{\nabla}^2\tilde{\rho}^3 + 2\tilde{\nabla}^4\tilde{\rho} + \tilde{\nabla}^6\tilde{\rho}\right] \tag{A9}$$

where $\tilde{\nabla}^6(\cdot) = \partial^6(\cdot)/\partial\tilde{r}_1^6 + \partial^6(\cdot)/\partial\tilde{r}_2^6 + \partial^6(\cdot)/\partial\tilde{r}_3^6 + 3\partial^6(\cdot)/\partial\tilde{r}_1^2\partial\tilde{r}_2^4 + 3\partial^6(\cdot)/\partial\tilde{r}_1^2\partial\tilde{r}_3^4 + 3\partial^6(\cdot)/\partial\tilde{r}_2^2\partial\tilde{r}_3^4 + 3\partial^6(\cdot)/\partial\tilde{r}_1^4\partial\tilde{r}_2^2 + 3\partial^6(\cdot)/\partial\tilde{r}_1^4\partial\tilde{r}_3^2 + 3\partial^6(\cdot)/\partial\tilde{r}_2^4\partial\tilde{r}_3^2 + 6\partial^6(\cdot)/\partial\tilde{r}_1^2\partial\tilde{r}_2^2\partial\tilde{r}_3^2$. It is obvious that equation (A9) is the sixth-order nonlinear partial differential equation (6OD-NPDE) which can be expressed in a full description as

$$\frac{\partial\tilde{\rho}}{\partial\tilde{t}} = \tilde{L}_{\mu}\left[(1-\tilde{\epsilon})\left(\frac{\partial^2\tilde{\rho}}{\partial\tilde{r}_1^2}+\frac{\partial^2\tilde{\rho}}{\partial\tilde{r}_2^2}+\frac{\partial^2\tilde{\rho}}{\partial\tilde{r}_3^2}\right)+\left(\frac{\partial^2\tilde{\rho}^3}{\partial\tilde{r}_1^2}+\frac{\partial^2\tilde{\rho}^3}{\partial\tilde{r}_2^2}+\frac{\partial^2\tilde{\rho}^3}{\partial\tilde{r}_3^2}\right)+2\left(\frac{\partial^4\tilde{\rho}}{\partial\tilde{r}_1^4}+\frac{\partial^4\tilde{\rho}}{\partial\tilde{r}_2^4}+\frac{\partial^4\tilde{\rho}}{\partial\tilde{r}_3^4}\right)\right]$$
$$+\tilde{L}_{\mu}\left[2\left(2\frac{\partial^4\tilde{\rho}}{\partial\tilde{r}_1^2\partial\tilde{r}_2^2}+2\frac{\partial^4\tilde{\rho}}{\partial\tilde{r}_1^2\partial\tilde{r}_3^2}+2\frac{\partial^4\tilde{\rho}}{\partial\tilde{r}_2^2\partial\tilde{r}_3^2}\right)+\left(\frac{\partial^6\tilde{\rho}}{\partial\tilde{r}_1^6}+\frac{\partial^6\tilde{\rho}}{\partial\tilde{r}_2^6}+\frac{\partial^6\tilde{\rho}}{\partial\tilde{r}_3^6}\right)\right]$$
$$+\tilde{L}_{\mu}\left[\left(3\frac{\partial^6\tilde{\rho}}{\partial\tilde{r}_1^2\partial\tilde{r}_2^4}+3\frac{\partial^6\tilde{\rho}}{\partial\tilde{r}_1^2\partial\tilde{r}_3^4}+3\frac{\partial^6\tilde{\rho}}{\partial\tilde{r}_2^2\partial\tilde{r}_3^4}+3\frac{\partial^6\tilde{\rho}}{\partial\tilde{r}_1^4\partial\tilde{r}_2^2}+3\frac{\partial^6\tilde{\rho}}{\partial\tilde{r}_1^4\partial\tilde{r}_3^2}+3\frac{\partial^6\tilde{\rho}}{\partial\tilde{r}_2^4\partial\tilde{r}_3^2}+6\frac{\partial^6\tilde{\rho}}{\partial\tilde{r}_1^2\partial\tilde{r}_2^2\partial\tilde{r}_3^2}\right)\right] \tag{A10}$$

In order to solve equation (A10) numerically, there are two options which can be employed; finite difference method (FD) and fourier spectral method (FSM). In this study, not only the periodic boundary condition is governed but also the equation itself has a very high derivative order in spatial coordinate which demands a lot of numerical expense if FD scheme is used. Therefore, FSM method is more appropriate than FD in terms of numerical accuracy and numerical expense to solve equation (A10). To employ FSM scheme, we begin with equation (A9). If we apply fourier transform both sides, we obtain

$$\frac{d\hat{\tilde{\rho}}}{d\tilde{t}} = \tilde{L}_{\mu}\left[-(1-\tilde{\epsilon})\,|\mathbf{K}|^2\hat{\tilde{\rho}} - |\mathbf{K}|^2\hat{\tilde{\rho}}^3 + 2|\mathbf{K}|^4\hat{\tilde{\rho}} - |\mathbf{K}|^6\hat{\tilde{\rho}}\right] \tag{A11}$$

Then, the 6OD-NPDE is literally reduced to empirical ordinary differential equation which depends on time constraint only; where $\hat{\tilde{\rho}} \equiv \hat{\tilde{\rho}}(\mathbf{K},\tilde{t})$ is fourier transform of $\tilde{\rho}$. $\hat{\tilde{\rho}}^3 \equiv \hat{\tilde{\rho}}^3(\mathbf{K},\tilde{t})$ is fourier transform of $\tilde{\rho}^3$ which can be described as below

$$\hat{\tilde{\rho}}(\mathbf{K},\tilde{t}) = \int_{-\infty}^{+\infty}\tilde{\rho}(\tilde{\mathbf{r}},\tilde{t})e^{-j\mathbf{K}\cdot\tilde{\mathbf{r}}}d\tilde{\mathbf{r}}$$
$$\hat{\tilde{\rho}}^3(\mathbf{K},\tilde{t}) = \int_{-\infty}^{+\infty}\tilde{\rho}^3(\tilde{\mathbf{r}},\tilde{t})e^{-j\mathbf{K}\cdot\tilde{\mathbf{r}}}d\tilde{\mathbf{r}} \tag{A12}$$

$\mathbf{K} \equiv \mathbf{K}(\mathbf{k}_{\tilde{r}_1},\mathbf{k}_{\tilde{r}_2},\mathbf{k}_{\tilde{r}_3})$ is a vector in fourier space and each fourier wave vector component $\mathbf{k}_{\tilde{r}_i}$ is defined by

$$\mathbf{k}_{\tilde{r}_i} = \frac{2\pi}{L_{\tilde{r}_i}}\left[0,1,2,...,\frac{N_{\tilde{r}_i}}{2}-1,-\frac{N_{\tilde{r}_i}}{2},-\frac{N_{\tilde{r}_i}}{2}+1,-\frac{N_{\tilde{r}_i}}{2}+2,..,-1\right],\quad \forall i\in\{1,2,3\} \tag{A13}$$

where $L_{\tilde{r}_i}$ is lattice parameter along $\tilde{r}_i$ direction and our study uses $L_{\tilde{r}_i} = 2\pi\sqrt{2}$ for $\forall i \in \{1,2,3\}$. $N_{\tilde{r}_i}$ is number of grid points along $\tilde{r}_i$ direction which we employ $\tilde{r}_i = 16$ for

$\forall i \in \{1,2,3\}$. It should be note that

$$
\begin{aligned}
|\mathbf{K}|^2 &= \mathbf{k}_{\tilde{r}_1}^2 + \mathbf{k}_{\tilde{r}_2}^2 + \mathbf{k}_{\tilde{r}_3}^2 \\
|\mathbf{K}|^4 &= \mathbf{k}_{\tilde{r}_1}^4 + \mathbf{k}_{\tilde{r}_2}^4 + \mathbf{k}_{\tilde{r}_3}^4 + 2\mathbf{k}_{\tilde{r}_1}^2\mathbf{k}_{\tilde{r}_2}^2 + 2\mathbf{k}_{\tilde{r}_1}^2\mathbf{k}_{\tilde{r}_3}^2 + +2\mathbf{k}_{\tilde{r}_2}^2\mathbf{k}_{\tilde{r}_3}^2 \\
|\mathbf{K}|^6 &= \mathbf{k}_{\tilde{r}_1}^6 + \mathbf{k}_{\tilde{r}_2}^6 + \mathbf{k}_{\tilde{r}_3}^6 + 3\mathbf{k}_{\tilde{r}_1}^2\mathbf{k}_{\tilde{r}_2}^4 + 3\mathbf{k}_{\tilde{r}_1}^2\mathbf{k}_{\tilde{r}_3}^4 + 3\mathbf{k}_{\tilde{r}_2}^2\mathbf{k}_{\tilde{r}_3}^4 + 3\mathbf{k}_{\tilde{r}_1}^4\mathbf{k}_{\tilde{r}_2}^2 + 3\mathbf{k}_{\tilde{r}_1}^4\mathbf{k}_{\tilde{r}_3}^2 + 3\mathbf{k}_{\tilde{r}_2}^4\mathbf{k}_{\tilde{r}_3}^2 + 6\mathbf{k}_{\tilde{r}_1}^2\mathbf{k}_{\tilde{r}_2}^2\mathbf{k}_{\tilde{r}_3}^2
\end{aligned}
\tag{A14}
$$

We employ semi-implicit scheme [54] to solve equation (A11). The forward difference approximation for time derivative term is given as

$$
\frac{d\hat{\tilde{\rho}}}{d\tilde{t}} = \frac{\hat{\tilde{\rho}}^{n+1} - \hat{\tilde{\rho}}^{n}}{\Delta\tilde{t}} \tag{A15}
$$

where $\hat{\tilde{\rho}}^{n+1}$ and $\hat{\tilde{\rho}}^{n}$ denote $\hat{\tilde{\rho}}$ at time $\tilde{t}+\Delta\tilde{t}$ and $\tilde{t}$, respectively. Substitute equation (A15) in equation (A11)

$$
\frac{\hat{\tilde{\rho}}^{n+1} - \hat{\tilde{\rho}}^{n}}{\Delta\tilde{t}} = \tilde{L}_{\mu}\left[-(1-\tilde{\epsilon})\,|\mathbf{K}|^2\hat{\tilde{\rho}}^{n+1} - |\mathbf{K}|^2\hat{\tilde{\rho}}^{3n} + 2|\mathbf{K}|^4\hat{\tilde{\rho}}^{n+1} - |\mathbf{K}|^6\hat{\tilde{\rho}}^{n+1}\right] \tag{A16}
$$

where $\hat{\tilde{\rho}}^{n+1}$ and $\hat{\tilde{\rho}}^{3n}$ are $\hat{\tilde{\rho}}$ at time $\tilde{t}+\Delta\tilde{t}$ and $\hat{\tilde{\rho}}^{3}$ at time $\tilde{t}$, respectively. Rearrange above equation, we obtain

$$
\left[1 + \Delta\tilde{t}\tilde{L}_{\mu}\left[(1-\tilde{\epsilon})\,|\mathbf{K}|^2 - 2|\mathbf{K}|^4 + |\mathbf{K}|^6\right]\right]\hat{\tilde{\rho}}^{n+1} = \hat{\tilde{\rho}}^{n} - \Delta\tilde{t}\tilde{L}_{\mu}|\mathbf{K}|^2\hat{\tilde{\rho}}^{3n} \tag{A17}
$$

and it yields

$$
\hat{\tilde{\rho}}^{n+1} = \frac{\hat{\tilde{\rho}}^{n} - \Delta\tilde{t}\tilde{L}_{\mu}|\mathbf{K}|^2\hat{\tilde{\rho}}^{3n}}{\left[1 + \Delta\tilde{t}\tilde{L}_{\mu}\left[(1-\tilde{\epsilon})\,|\mathbf{K}|^2 - 2|\mathbf{K}|^4 + |\mathbf{K}|^6\right]\right]} \tag{A18}
$$

Finally, $\hat{\tilde{\rho}}^{n+1}$ variable which is in reciprocal space can be converted into the real space variable by using inverse fourier transform

$$
\tilde{\rho}^{n+1}(\tilde{\mathbf{r}}) = \frac{1}{(2\pi)^d}\int_{-\infty}^{+\infty}\hat{\tilde{\rho}}^{n+1}(\mathbf{K})e^{j\mathbf{K}\cdot\tilde{\mathbf{r}}}d\mathbf{K} \tag{A19}
$$

where d is dimensionality of the problem. This variable will be used to calculate $\tilde{\bar{P}}_{\text{int}}$ in pressure-controlled dynamics equation further. Next, the second important equation is the PCD equation which was developed regarding thermodynamic of hydrostatically-stressed crystal solid [39] and classical irreversible thermodynamic frameworks [40–42]. The advantage of this equation is that it allows to create the deformation in PFC model by specifying external pressure as an input variable unlike the conventional PFC simulations where volume, or grid spacing, is an input variable [43]. This equation is given as below

$$\frac{d\tilde{V}}{d\tilde{t}} = \tilde{L}_{\mathrm{def}}\tilde{V}(\tilde{\bar{P}}_{\mathrm{int}} - \tilde{\bar{P}}_{\mathrm{ext}}) \tag{A20}$$

To solve PCD equation, we use forward difference scheme for time derivative term.

$$\frac{d\tilde{V}}{d\tilde{t}} = \frac{\tilde{V}^{n+1} - \tilde{V}^{n}}{\Delta\tilde{t}} \tag{A21}$$

Then, equation (A20) becomes

$$\frac{\tilde{V}^{n+1} - \tilde{V}^{n}}{\Delta\tilde{t}} = \tilde{L}_{\mathrm{def}}\tilde{V}^{n}\left(\tilde{\bar{P}}^{n}_{\mathrm{int}} - \tilde{\bar{P}}^{n}_{\mathrm{ext}}\right) \tag{A22}$$

where $\tilde{V}^{n+1}$ and $\tilde{V}^{n}$ is volume at time $\tilde{t} + \Delta\tilde{t}$ and $\tilde{t}$, respectively. Also, $\tilde{\bar{P}}^{n}_{\mathrm{int}}$ and $\tilde{\bar{P}}^{n}_{\mathrm{ext}}$ is $\tilde{\bar{P}}_{\mathrm{int}}$ and $\tilde{\bar{P}}_{\mathrm{ext}}$ at time $\tilde{t}$. Then, the equation (A22) yields

$$\tilde{V}^{n+1} = \tilde{V}^{n} + \Delta\tilde{t}\tilde{L}_{\mathrm{def}}\tilde{V}^{n}\left(\tilde{\bar{P}}^{n}_{\mathrm{int}} - \tilde{\bar{P}}^{n}_{\mathrm{ext}}\right) \tag{A23}$$

Finally, we literally obtain a new volume value at next time step as we required. It should be noted that $\tilde{\bar{P}}^{n}_{\mathrm{int}}$ is

$$\tilde{\bar{P}}^{n}_{\mathrm{int}} = \frac{1}{\tilde{V}^{n}}\int\left(-\tilde{f}^{n} + \tilde{\mu}^{n}\tilde{\rho}^{n}\right)d\tilde{\mathbf{r}} \tag{A24}$$

where

$$\begin{aligned} \tilde{f}^{n} &= (1-\tilde{\epsilon})\frac{\tilde{\rho}^{2n}}{2} + \frac{\tilde{\rho}^{4n}}{4} + \tilde{\rho}^{n}\left[\tilde{\nabla}^{2}\tilde{\rho}\right]^{n} + \frac{\tilde{\rho}^{n}}{2}\left[\tilde{\nabla}^{4}\tilde{\rho}\right]^{n} \\ \tilde{\mu}^{n} &= (1-\tilde{\epsilon})\tilde{\rho}^{n} + \tilde{\rho}^{3n} + 2\left[\tilde{\nabla}^{2}\tilde{\rho}\right]^{n} + \left[\tilde{\nabla}^{4}\tilde{\rho}\right]^{n} \end{aligned} \tag{A25}$$

All superscripts, n, regarding equation (A25) which appear in all $(\cdot)^{n}$ represent those physical quantities, $(\cdot)$, at time $\tilde{t}$.

Appendix B: Standard Linear Solid Model

In this appendix, we aim to derive the expressions for the complex modulus and strain response from the SLS model under harmonic excitation. First, we derive complex modulus under dynamic excitation. Consider a more general form of the stress (scaled quantity):

$$\sigma'^{*}(t) = \sigma'_A \exp\left[j\left(\omega t + \delta\right)\right], \quad \sigma'^{*}(t) = \sigma'^{*}_A \exp\left(j\omega t\right) \tag{B1}$$

where σ'_A is the amplitude, ω is angular frequency and σ'^{*}_A is complex amplitude defined by $\sigma'^{*}_A \equiv \sigma'_A \exp\left(j\delta\right) = \sigma'^{*}_A \cos(\delta) + j\sigma'^{*}_A \sin(\delta)$. At steady state the strain response will also exhibit a harmonic function with the same frequency; therefore, one can postulate the functional form of the strain as an input function [20]:

$$e^{*}(t) = e_A \exp(j\omega t) \tag{B2}$$

where e_A is strain amplitude. Substituting Eqs. (B1) and (B2) into equation (12), we obtain

$$\frac{\sigma'^{*}_A}{e_A} \equiv \frac{\sigma'_A}{e_A}\cos(\delta) + j\frac{\sigma'_A}{e_A}\sin(\delta) = \frac{K + j\omega}{1 + j\tau\omega} \tag{B3}$$

This equation defines $G'_{\text{complex}} = G'_{\text{storage}} + jG'_{\text{loss}}$ where each of $\sigma'_A \cos(\delta)/e_A$ and $\sigma'_A \sin(\delta)/e_A$ is G'_{storage} and G'_{loss}, respectively. Therefore, we literally obtain

$$G'_{\text{storage}} = \frac{K + \tau\omega^2}{1 + (\tau\omega)^2}, \quad G'_{\text{loss}} = \frac{(1 - \tau K)}{1 + (\tau\omega)^2}\omega \tag{B4}$$

To derive solution expression, we consider stress as an input function

$$\sigma'^{*}(t) = \sigma'_A \exp\left(j\omega t\right) \tag{B5}$$

and propose strain function written as

$$e^{*}(t) = e^{*}_A \exp\left(j\omega t\right) \tag{B6}$$

Substituting Eqs. (B5) and (B6) into equation (12) to obtain

$$e^{*}(t) = \left[\frac{1 + j\tau\omega}{K + j\omega}\right]\sigma'_A \exp(j\omega t), \quad e^{*}_A = \left[\frac{1 + j\tau\omega}{K + j\omega}\right]\sigma'_A \tag{B7}$$

For a particular case where $\sigma'(t) = \sigma'_A \sin(\omega t) = \text{Im}[\sigma'^{*}(t)]$, therefore, the strain response corresponding to this case can be obtained by

$$e(t) = \text{Im}\left[e^{*}(t)\right] \tag{B8}$$

that yields

$$e(t) = \frac{\sigma'_A}{\sqrt{K^2 + \omega^2}} \sin(\omega t - \phi) + \frac{\tau \sigma'_A \omega}{\sqrt{K^2 + \omega^2}} \cos(\omega t - \phi) \tag{B9}$$

where $\phi = \arctan(\omega/K)$, which can be reduced to

$$e(t) = e_A \sin(\omega t - \delta) \tag{B10}$$

where

$$e_A = \sigma'_A \sqrt{\frac{1 + (\tau\omega)^2}{K^2 + \omega^2}}, \quad \delta = \arctan\left[\left(\frac{1 - \tau K}{K + \tau\omega^2}\right)\omega\right] \tag{B11}$$

It should be noted that $e_A = |e^*_A|$.

Appendix C: Dynamic similarity between PCD equation and SLS model

In this appendix, we demonstrate how dynamic similarity between PCD equation (10) and SLS model equation (12) can be established using Taylor's expansion [55] at infinitesimal deformation around the reference state. First, we begin with PCD equation

$$\frac{dV}{dt} = L_P V(\bar{P}_{\text{int}} - \bar{P}_{\text{ext}}), \tag{C1}$$

where $\bar{P}_{\text{int}} = \int_V P_{\text{int}} dV/V$ and $Pext$ represents the average internal pressure and external applied pressure with $V(t) = L(t)^3$ where L is crystal length parameter. If we denote that

$$\varphi(V) = \int_V P_{\text{int}} dV \tag{C2}$$

and V represents a current volume. It should be noted that $dV = dx_1 dx_2 dx_3$ where all dx_{i} are spatial coordinate in Eulerian description. The integration boundary for each coordinate is $x_{\text{i}} = 0$ to $x_{\text{i}} = L(t)$ where $L(t) = L_0\,[1 + e(t)]$ and $e(t) = (L(t) - L_0)\,/L_0$. Equation (C2) becomes

$$\varphi(e) = \int_0^{L_0[1+e(t)]} \int_0^{L_0[1+e(t)]} \int_0^{L_0[1+e(t)]} P_{\text{int}}\ dx_1 dx_2 dx_3 \tag{C3}$$

If we assume infinitesimal deformation, small strain can be written as $e(t) = e_0 + \Delta e$ where $e_0 = 0$ and $\Delta e = e(t) - e_0$. Therefore, equation (C3) can be written in expansion form [55]

$$\varphi(e_0 + \Delta e) = \varphi(e_0) + \left.\frac{d\varphi}{de}\right|_{e=e_0} \Delta e + \frac{1}{2!}\left.\frac{d^2\varphi}{de^2}\right|_{e=e_0} \Delta e^2 + R_3(\Delta e^3) \tag{C4}$$

where $\varphi(e_0)$ represents $\int_V PdV$ at $e = e_0$ and $R_3(\Delta e^3)$ represents higher order derivative term as a function of Δe^3. In case of infinitesimal deformation, the higher order term, Δe^n where $n \geq 2$, can be truncated then equation (C4) is reduced to

$$\varphi(e) \approx \varphi(e_0) + \psi_{e=e_0} \Delta e \tag{C5}$$

where $\psi_{e=e_0} = d\varphi/de|_{e=e_0}$. Also, $\bar{P}_{\text{ext}}$ can be written

$$\bar{P}_{\text{ext}} = \bar{P}_0 - \Delta \bar{P}_{\text{ext}} \tag{C6}$$

where $\bar{P}_0$ represents average reference pressure calculated under undeformed state

$$\bar{P}_0 = \frac{\varphi(e_0)}{L_0^3}, \quad V_0 = L_0^3 \tag{C7}$$

and $\Delta\bar{P}_{\text{ext}}$ represents the deviation part of $\bar{P}_{\text{ext}}$ from $\bar{P}_0$. Since $V \equiv V(L(e))$ is a composite function, therefore, the time derivative regarding equation (C1) can be expressed by chain's rule

$$\frac{dV}{dt} = \frac{dV}{dL}\cdot\frac{dL}{de}\cdot\frac{de}{dt} \tag{C8}$$

where $dV/dL = 3L^2$ and $dL/de = L_0$. Substitute equation (C5)-(C8) into equation (C1), we obtain

$$3L_0L^2\frac{de}{dt} = L_PL^3\left[\frac{\varphi(e_0+\Delta e)}{L^3} - \bar{P}_0 + \Delta\bar{P}_{\text{ext}}\right], \tag{C9}$$

that yields

$$\frac{de}{dt} = \frac{L_P}{3}(1+e)\left[\frac{\varphi(e_0)+\psi_{e=e_0}\Delta e}{L_0^3(1+e)^3} - \bar{P}_0 + \Delta\bar{P}_{\text{ext}}\right], \tag{C10}$$

Note that $\Delta e = e$. This equation can be reduced to

$$\frac{de}{dt} = \frac{L_P}{3}\left[\frac{\varphi(e_0)}{L_0^3}(1+e)^{-2} + \frac{\psi_{e=e_0}e}{L_0^3}(1+e)^{-2} - \bar{P}_0(1+e) + \Delta\bar{P}_{\text{ext}}(1+e)\right], \tag{C11}$$

Regarding binomial expansion, we know that $(1+e)^{-2} \approx 1-2e$ for the first term approximation if $0 \leq e << 1$. Equation (C11) becomes

$$\frac{de}{dt} = \frac{L_P}{3}\left[\frac{\varphi(e_0)}{L_0^3} - \frac{2\varphi(e_0)}{L_0^3}e + \frac{\psi_{e=e_0}}{L_0^3}e - \frac{2\psi_{e=e_0}}{L_0^3}e^2 - \bar{P}_0 - \bar{P}_0e + \Delta\bar{P}_{\text{ext}} + \Delta\bar{P}_{\text{ext}}e\right] \tag{C12}$$

If we neglect e^2 and $\Delta\bar{P}_{\text{ext}}e$ and use the fact that $\varphi(e_0)/L_0^3 = \bar{P}_0$, equation (C12) turns into

$$\frac{de}{dt} = \frac{L_P}{3}\left[-3\bar{P}_0e + \frac{\psi_{e=e_0}}{L_0^3}e + \Delta\bar{P}_{\text{ext}}\right] \tag{C13}$$

Then, equation (C13) finally yields the simplified model of PCD equation as

$$\frac{de}{dt} + \frac{L_P}{3}\left[3\bar{P}_0 - \frac{\psi_{e=e_0}}{L_0^3}\right]e = \frac{L_P}{3}\Delta\bar{P}_{\text{ext}} \tag{C14}$$

which obviously has structure like a Kelvin-Voigt model

$$\frac{de}{dt} + Ke = \sigma' \tag{C15}$$

where $K \equiv L_P\left(3\bar{P}_0 - \psi_{e=e_0}/L_0^3\right)/3$ and $\sigma' \equiv L_P\Delta\bar{P}_{\text{ext}}/3$. Equation (C15) is slightly different from SLS model equation (12) in that $\tau d\sigma'/dt$ term is introduced on the right hand side in SLS model. This deviation does not cause the difference in viscoelastic-creep behavior produced by both PCD model and SLS model solution under constant pressure. However, in case of the mechanical-hystersis, although this behavior produced by PCD equation is deviated with that of SLS model and behaves like Kelvin-Voigt model at elevated frequency range, it consistently predicts the similar results with SLS model at low frequency. This can be described by the solution obtained from both models under sinusoidal load, $\sigma'(t) = \sigma'_A \sin(\omega t)$. According to equation (B9), the strain solution produced by SLS model is $e(t) = \sigma'_A \sin(\omega t - \phi)/\sqrt{K^2+\omega^2} + \tau\sigma'_A\omega\cos(\omega t - \phi)/\sqrt{K^2+\omega^2}$. However, if $0 \leq \omega << 1$, the solution will converge to $e(t) = \sigma'_A \sin(\omega t - \phi)/\sqrt{K^2+\omega^2}$ which is almost identical to that of a simplified model of PCD equation.

---

[1] K. R. Elder, M. Katakowski, M. Haataja, and M. Grant, Physical Review Letters **88**, 245701 (2002).

[2] K. R. Elder and M. Grant, Physical Review E **70**, 051605 (2004).

[3] J. Berry, M. Grant, and K. Elder, Physical Review E **73**, 031609 (2006).

[4] K. Elder, N. Provatas, J. Berry, P. Stefanovic, and M. Grant, Physical Review B **75**, 064107 (2007).

[5] T. Pusztai, G. Tegze, G. I. Tóth, L. Környei, G. Bansel, Z. Fan, and L. Gránásy, Journal of Physics: Condensed Matter **20**, 404205 (2008).

[6] P. Y. Chan, N. Goldenfeld, and J. Dantzig, Physical Review E **79**, 035701 (2009).

[7] T. Hirouchi, T. Takaki, and Y. Tomita, International Journal of Mechanical Sciences **52**, 309 (2010).

[8] J. Berry, K. Elder, and M. Grant, Physical Review B **77**, 224114 (2008).

[9] J. Mellenthin, A. Karma, and M. Plapp, Physical Review B **78**, 184110 (2008).

[10] P. Stefanovic, M. Haataja, and N. Provatas, Physical review letters **96**, 225504 (2006).

[11] P. Y. Chan, G. Tsekenis, J. Dantzig, K. A. Dahmen, and N. Goldenfeld, Physical review letters **105**, 015502 (2010).

[12] S. Hu and S. Wang, Physica B: Condensed Matter **552**, 104 (2019).

[13] N. Pisutha-Arnond, V. Chan, K. Elder, and K. Thornton, Physical Review B **87**, 014103 (2013).

[14] Z.-L. Wang, Z.-F. Huang, and Z. Liu, Physical Review B **97**, 144112 (2018).

[15] W. Zhou, J. Wang, Z. Wang, Y. Huang, C. Guo, J. Li, and Y. Guo, Chinese Physics B **26**, 090702 (2017).

[16] P. Stefanovic, M. Haataja, and N. Provatas, Physical Review E **80**, 046107 (2009).

[17] M. Greenwood, N. Ofori-Opoku, J. Rottler, and N. Provatas, Physical Review B **84**, 064104 (2011).

[18] Y.-L. Lu, T.-T. Hu, G.-M. Lu, and Z. Chen, Physica B: Condensed Matter **451**, 128 (2014).

[19] L. Roderic S, Viscoelastic solids, CRC press, (1998).

[20] W. N. Findley and F. A. Davis, Creep and relaxation of nonlinear viscoelastic materials, Courier Corporation, (2013).

[21] J. D. Ferry, Viscoelastic properties of polymers, John Wiley & Sons, (1980).

[22] Drozdov, Computational materials science **39**, 729 (2007).

[23] E. Frey, K. Kroy, and J. Wilhelm, Viscoelasticity of biopolymer networks and statistical mechanics of semiflexible polymers, Elsevier, (1999).

[24] H. Di Benedetto, F. Olard, C. Sauzéat, and B. Delaporte, Road Materials and Pavement Design **5**, 163 (2004).

[25] I. Ritchie, K. Sprungmann, and M. Sahoo, Le Journal de Physique Colloques **46**, C10 (1985).

[26] J. Kim and J.-Y. Choi, Smart materials and structures **14**, 587 (2005).

[27] R. Fan, G. Meng, J. Yang, and C. He, Journal of Sound and Vibration **319**, 58 (2009).

[28] S. Elias and V. Matsagar, Annual Reviews in Control **44**, 129 (2017).

[29] K. Otsuka and C. M. Wayman, Shape memory materials, Cambridge university press, (1999).

[30] C. Rosen, B. V. Hiremath, and R. Newnham, Piezoelectricity, Springer Science & Business Media, (1992).

[31] S. R. White, N. Sottos, P. Geubelle, J. Moore, M. Kessler, S. Sriram, E. Brown, and S. Viswanathan, Nature **409**, 794 (2001).

[32] R. O. St, C. Weiss, J. L. Denlinger, and E. A. Balazs, Clinical orthopaedics and related research , 269 (1980).

[33] V. B. Braginsky, V. Mitrofanov, and V. I. Panov, Systems with small dissipation, University of Chicago Press, (1985).

[34] H. G. Craighead, Science **290**, 1532 (2000).

[35] R. Lifshitz and M. L. Roukes, Physical review B **61**, 5600 (2000).

[36] E. Jatupon and P. Nirand, IOP Conference Series: Materials Science and Engineering, IOP Publishing, Vol. 361 pp. 012009 (2018).

[37] J. Em-Udom and N. Pisutha-Arnond, IOP Conference Series: Materials Science and Engineering, IOP Publishing, Vol. 361 pp. 012006 (2018).

[38] G. Kocher and N. Provatas, Physical Review Letters **114**, 155501 (2015).

[39] F. Larché and J. W. Cahn, Acta metallurgica **21**, 1051 (1973).

[40] S. R. De Groot and P. Mazur, Non-Equilibrium Thermodynamics, Courier Corporation, (2013).

[41] Y. Mishin, J. Warren, R. Sekerka, and W. Boettinger, Physical Review B **88**, 184303 (2013).

[42] G. Lebon, D. Jou, and J. Casas-Vázquez, Understanding Non-Equilibrium Thermodynamics, Springer, (2008).

[43] T. Hirouchi, T. Takaki, and Y. Tomita, Computational Materials Science **44**, 1192 (2009).

[44] N. Provatas and K. Elder, Phase-field methods in materials science and engineering, John Wiley & Sons, (2011).

[45] K.-A. Wu and A. Karma, Physical Review B **76**, 184107 (2007).

[46] P. Voorhees and W. C. Johnson, Solid State Physics-Advances in Research and Applications **59**, 1 (2004).

[47] R. S. Lakes, Viscoelastic Materials, Cambridge University Press, (2009).

[48] J. Wachtman Jr, W. Tefft, D. Lam Jr, and C. Apstein, Physical review **122**, 1754 (1961).

[49] P. M. Sutton, Physical Review **91**, 816 (1953).

[50] W. Chancellor, A. Wolfenden, and G. Ludtka, Journal of Nuclear Materials **171**, 389 (1990).

[51] R. Bruls, H. Hintzen, G. De With, and R. Metselaar, Journal of the European Ceramic Society **21**, 263 (2001).

[52] D. I. Jones, Handbook of viscoelastic vibration damping, John Wiley & Sons, (2001).

[53] L. Licitra, D. D. Luong, O. M. Strbik III, and N. Gupta, Materials & Design **66**, 504 (2015).

[54] L. Q. Chen and J. Shen, Computer Physics Communications **108**, 147 (1998).

[55] G. B. Arfken and H. J. Weber, Mathematical methods for physicists, AAPT, (1999).

Prediction of Mechanical-Hysteresis Behavior and Complex Moduli Using the Phase Field Crystal Method with Modified Pressure Controlled Dynamic Equation

J Em-Udom* and N Pisutha-Arnond†

Department of Industrial Engineering, Faculty of Engineering,

King Mongkut's Institute of Technology Ladkrabang, Ladkrabang, Bangkok, Thailand

(Dated: November 26, 2019)

Abstract

Damping materials have been used in numerous engineering applications. The important property that plays a key role in this type of material is a damping capacity which is related to mechanical-hysteresis behavior of viscoelasticity. During the last decade, the phase-field-crystal (PFC) model has emerged as a robust tool to predict various material phenomena. This density-functional-type model has the advantage over a conventional phase-field model in terms of atomistic resolution and molecular dynamics in terms of computational expense. In this work, we propose a method to predict mechanical-hysteresis behavior and its related complex moduli parameters using a modified-pressure-controlled dynamics (MPCD) equation incorporating with the PFC model, denoted as PFC-MPCD method, in a three-dimensional solid structure. We modify the previously proposed pressure-controlled dynamics (PCD) equation by introducing the pressure-time derivative term which allows us to produce the results consistent with the standard linear solid model (SLS) at the broader frequency range. We apply sinusoidal pressure oscillation and compare the results predicted by both models. The results demonstrate that mechanical-hysteresis behavior and complex moduli parameters predicted by PFC-MPCD method are in good agreement with those of SLS model and consistent with numerous experimental observations whereas the results produced by original PCD equation tends to exhibit inaccurate results at the very frequency. We expect that this new PFC-MPCD method can be extended to a more complex system and still be capable to exhibit the accurate mechanical-hysteresis behavior and complex moduli parameters which results in predicting more reliable damping capacity parameter in damping material design.

* ejatupon1@gmail.com

† nirand.pi@kmitl.ac.th

I. INTRODUCTION

Damping materials have been used in many engineering applications and, in particular, in energy absorption such as vibration isolation and impact absorber. One of the most important properties that plays a key role in energy absorption is the damping capacity of material. This parameter indicates the ability of material in dissipating energy during the deformation which can be measured through mechanical-hysteresis curve of viscoelasticity. Viscoelasticity is the mechanical behavior which is characterized by three phenomena; viscoelastic-creep, stress relaxation and mechanical-hysteresis behavior. To select the appropriate materials in specific tasks, therefore, we need to predict these properties accurately and know the suitable working condition of these damping materials.

In the past few decades, computational materials science has emerged as an alternative choice to predict various material properties and phenomena. This new technique can help speeding up the design process and reducing the cost of the real experimental study. To predict this damping capacity accurately, we need a computational technique that incorporates microstructures which influences the material properties and can reproduce a correct mechanical-hysteresis behavior.

During the last decade, the phase-field-crystal (PFC) method has appeared as a promising tool to investigate numerous material phenomena. In the PFC model, its free energy functional is minimized by periodic density field which provides elastic effects and microstructural features e.g. multiple crystal orientations, grain boundary and dislocations which is more appealing than conventional phase field (PF) model in terms of self-consistency. Moreover, this method is restricted to operate on diffusive time-scales which give an advantage over molecular dynamics (MD) in terms of computational expense. The PFC model was first introduced by Elder et al. [1] which its free energy functional was minimized by periodic function that found in many physical systems even in crystalline structure. This model that incorporated elastic and plastic properties [2] was used to study various range of material phenomena such as phase transformation [3, 4], topological defect dynamics such as crack [2, 5], elasticity [6–8] to plasticity [9, 10]. This method could also be used to model microstructural defects such as vacancy [11], grain-boundary [12–14] and dislocation [10, 15]. The PFC method has the potential to predict damping capacity and how damping capacity is affected by different types of material, environment condition and microstructures.

Recently, we investigated the predicting capability of the PFC model incorporating with previously proposed pressure-controlled dynamics (PCD) equation to reproduce viscoelastic behavior of the materials, referred to as PFC-PCD method. This PCD equation enables us to exhibit the deformation by specifying the externally applied pressure as an input which allows us to study viscoelastic-creep and mechanical-hysteresis behaviors where the externally applied pressure is required as an input. This is in contrast to a previously proposed scheme by Hirouchi et al. [16] where the deformation was controlled by specifying the grid spacing as an input variable which is suitable for studying stress relaxation problem. Nonetheless, the damping capacity of the material is closely related to mechanical-hystersis behavior and its related parameters, therefore, the stress relaxation which can be produced by this scheme is not focused in our study.

The existing PFC model that we used here is the original formulation proposed by Elder [2] which incorporates the pressured-controlled-dynamics (PCD) equation proposed by Kocher and Provatas [17]. We used this PFC-PCD method to investigate viscoelastic-creep behavior for one-dimensional crystal in our previous works [18, 19] and extended those works to three dimensional solid [20]. According to the results, we observed that the PFC-PCD method could only exhibit viscoelastic-creep phenomena correctly, however, it could not predict the accurate mechanical-hysteresis behavior, in particular, at high-pressure oscillation frequency [20]. All complex moduli parameters obtained from mechanical-hysteresis curve produced by the model monotonically increased with pressure oscillation frequency instead of exhibiting the limited value in storage modulus and predicting at least one peak location in loss modulus and loss tangent factor which generally agree with the real solid material regardless of the actual damping mechanism [21]. This means that the existing PFC-PCD method is incorrect to predict mechanical-hysteresis behavior with the real solid material, in particular, at very frequency. This inaccuracy will cause the problem in predicting the suitable working condition for damping material when the peak frequency location, the location that energy is mostly dissipated, is needed to be specified. Thus, the modification to the existing PFC-PCD method is required to produce more accurate mechanical-hysteresis behavior.

Therefore, in this work, we propose the modified PFC-PCD method to address this limitation. We modify the pressure-control by adding pressure time derivative term to the existing PCD equation, referred to as MPCD equation. This additional term comes from comparing the Taylor expansion of the existing PCD equation with the standard linear solid (SLS) model which is typically used to investigate viscoelasticity in solid materials [22–24]. According to the numerical study, the results demonstrate that the PFC model which incorporates MPCD equation, referred to as PFC-MPCD method, can predict mechanical-hysteresis behavior and complex moduli parameters consistent with SLS model at the broaden pressure-oscillation frequency range. In particular, the complex moduli predicted by our method are in good agreement with the experimental observations which can be found in numerous sources i.e. [25–27] for alloy, [28–30] for rubber and [31] for elastomer. This is in contrast to PFC-PCD method which produces the results inconsistent with SLS model and experimental observations, especially, at the high-frequency range. We expect that this new PFC-MPCD method can be extended to more complex system with microstructural features such as grain boundary, dislocation or surface and still be capable to exhibit the accurate mechanical-hysteresis behavior and complex moduli parameters which results in predicting more reliable damping capacity parameter in damping material design.

This paper is organized as follows. In Section II, we provide the background information on the PFC method, the pressure-control dynamics equation, and the standard linear solid model. In section III, we introduce a new PFC-MPCD method and provide an insight into this model structure using its approximated Taylor expansion formulation. In Section IV, the method of simulation is presented. The results and discussions are provided in Section V and we conclude the work with the summary in Section VI.

II. BACKGROUND

A. PFC-PCD Method

The non-dimensional PFC free energy functional form employed in our study is given as Ref. [1, 2] below

$$\mathcal{F} = \int f(\rho)\ d\mathbf{r}, \qquad f(\rho) = \frac{\rho}{2}\left[-\epsilon + \left(1+\nabla^2\right)^2\right]\rho + \frac{\rho^4}{4}. \tag{1}$$

where ϵ can be interpreted as the degree of undercooling which is inversely proportional to temperature and ρ is the density field variable. The evolution equation for ρ is the

Cahn-Hilliard type which involves dissipative dynamics and mass conservation [2]

$$\frac{\partial \rho}{\partial t} = L_\mu \nabla^2 \mu, \quad \mu = (1-\epsilon)\rho + \rho^3 + 2\nabla^2\rho + \nabla^4\rho \tag{2}$$

where L_μ is the mobility coefficient and $\mu = \delta\mathcal{F}/\delta\rho$ is the diffusion potential. This equation can be used to simulate evolution of ρ under specified (or fixed) temperature (from the value of ϵ), mass (from the value of $\bar{\rho}$), and volume (from value of grid spacing); typical simulations under this condition are solidification and microstructural evolution. One can also vary the grid spacing to simulate the evolution of the density profile under specified time-dependent deformation [16]. In the context of the viscoelastic behavior, this technique would be appropriate for the stress-relaxation calculation; however for the viscoelastic-creep and mechanical-hysteresis studies, where the system is subjected to specified external stress, additional dynamic equation is needed.

The PCD equation was first introduced by Kocher and Provatas [17]. The advantage of this equation is that it enables us to control internal pressure $\bar{\mathcal{P}}_{\text{int}}$ by specifying the external pressure. In their work, this equation was employed to investigate the full spectrum of solid-liquid-vapor transition problem. This PCD equation which refers to the original PCD method can be written as below

$$\frac{dV}{dt} = L'_{\text{def}}\left(\bar{\mathcal{P}}_{\text{int}} - \bar{\mathcal{P}}_{\text{ext}}\right), \tag{3}$$

where V is system volume which changes with time, $\bar{\mathcal{P}}_{\text{ext}}$ is the externally applied pressure, L'_{def} is the mobility coefficient and the internal pressure $\bar{\mathcal{P}}_{\text{int}}$ can be defined by

$$\bar{\mathcal{P}}_{\text{int}} = \frac{1}{V}\int(-f + \mu\rho)\, d\mathbf{r} \tag{4}$$

This PCD equation when incorporates CH model Eq. (2) which adopts PFC free energy functional Eq. (1) will refer to as PFC-PCD method . We employed this method to investigate viscoelastic-creep behavior for one-dimensional crystal in our previous studies [18, 19] and extended to three dimensional solid structure [20]. According to the results, although the PFC-PCD method predicted a reliable viscoelastic-creep behavior [18–20], however, it could not produce a mechanical-hysteresis behavior correctly, in particular, at high pressure oscillation frequency range [20] which might cause a problem in predicting a suitable working condition for damping materials.

B. Standard Linear Solid Model

The standard linear solid (SLS) is a model of modeling viscoelastic behavior of viscoelastic material known as Zener model [22–24]. It exhibits more realistic behavior involving single exponent in both viscoelastic-creep and stress-relaxation. Furthermore, this model predicts the finite storage moduli at high frequency range and providing peak locations for both loss factor parameters. The simplified governing equation of the SLS model is given as below

$$\frac{de}{dt} + K'e = \mathcal{P}' + \tau'\frac{d\mathcal{P}'}{dt} \tag{5}$$

where e is strain response predicted by the model. $\mathcal{P}'$ is external applied pressure. K' is the elastic coefficient which represents the elastic part of the model. τ' is the shape factor coefficient which enables us to adjust the peak magnitude of all loss factors. To exhibit mechanical-hysteresis behavior, the sinusoidal pressure oscillation is required. So, the $\mathcal{P}'$ can be specify as

$$\mathcal{P}'(t) = \mathcal{P}'_A \sin(\omega t) \tag{6}$$

where $\mathcal{P}'_A$ is the amplitude of sinusoidal pressure oscillation. The $\omega = 2\pi f$ is angular frequency and f is the frequency of sinusoidal pressure oscillation input. The t variable is time domain. Substitute Eq. (6) in Eq. (5), it becomes

$$\frac{de}{dt} + K'e = \mathcal{P}'_A \sin(\omega t) + \tau'\mathcal{P}'_A\omega\cos(\omega t). \tag{7}$$

Then, Eq. (7) yields the solution below

$$e(t) = E_A \sin(\omega t - \delta), \tag{8}$$

where E_A is the strain oscillation amplitude. The δ parameter is phase angle which defines time-delayed response due to viscoelastic effect. Both parameters are functions of frequency as shown below

$$E_A = \mathcal{P}'_A\sqrt{\frac{1+(\tau'\omega)^2}{K'^2+\omega^2}}, \quad \delta = \arctan\left[\frac{1-\tau'K'}{K'+\tau'\omega^2}\right]\omega \tag{9}$$

The strain responses $e(t)$ corresponding to pressure input $\mathcal{P}'(t)$ at various sinusoidal pressure oscillation frequencies are illustrated in Fig. 1(a)-(c). The figures demonstrates that the amplitude and phase angle are affected by pressure-oscillation frequency. The governing

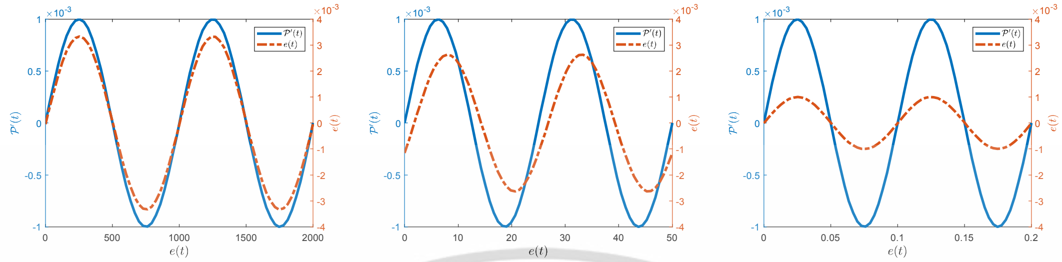

(a) (b) (c)

FIG. 1. Influence of frequency, f, on system response; sinusoidal pressure oscillation $\mathcal{P}'(t)$ (solid-line) and strain response $e(t)$ (dash-line) established by SLS Model (a) $f = 0.001$ (b) $f = 0.04$ (c) $f = 10$; at parameter condition $\mathcal{P}'_{\text{A}} = 0.001$, $K' = 0.3$ and $\tau' = 1$.

equations which describe these changes are given by Eq. (9) and illustrated in Fig. 2(a) and Fig. 2(b). Another important aspect is mechanical-hysteresis behavior curve showed in Fig. 2(c). It is established according to $e(t)$ vs. $\mathcal{P}'(t)$ based on Eq. (6) and Eq. (8). This curve provides us with the information about the energy dissipation during each oscillation cycle at specific frequency. Furthermore, this curve also contributes us the viscoelastic-measure-parameter called complex moduli parameters. These parameters consist of storage moduli (E'), loss moduli (E'') and loss tangent factor ($\tan(\delta)$). Each parameter is frequency dependent function governed by Eq. (10) (Derivation of complex moduli parameters is provided in Appendix A).

$$E' = \frac{K' + \tau'\omega^2}{1 + (\tau'\omega)^2}, \quad E'' = \left[\frac{1 - \tau'K'}{1 + (\tau'\omega)^2}\right]\omega$$
$$\tan(\delta) = \left[\frac{1 - \tau'K'}{K' + \tau'\omega^2}\right]\omega \tag{10}$$

The illustration of these parameters are given in Fig. 2(d). The E' parameter provides the measure of stored energy which represents the elastic part of the material. Whereas, the E'' parameter provides the energy dissipation or heat loss during the deformation. This parameter depicts the viscous portion of the material and $\tan(\delta)$ parameter is defined by the ratio between loss modulus and storage modulus; $\tan(\delta) = E''/E'$, which provides a measure of damping in the material. If this parameter is greater than unity, the system behaves liquid-like material while the opposite case the system exhibits solid-like material.

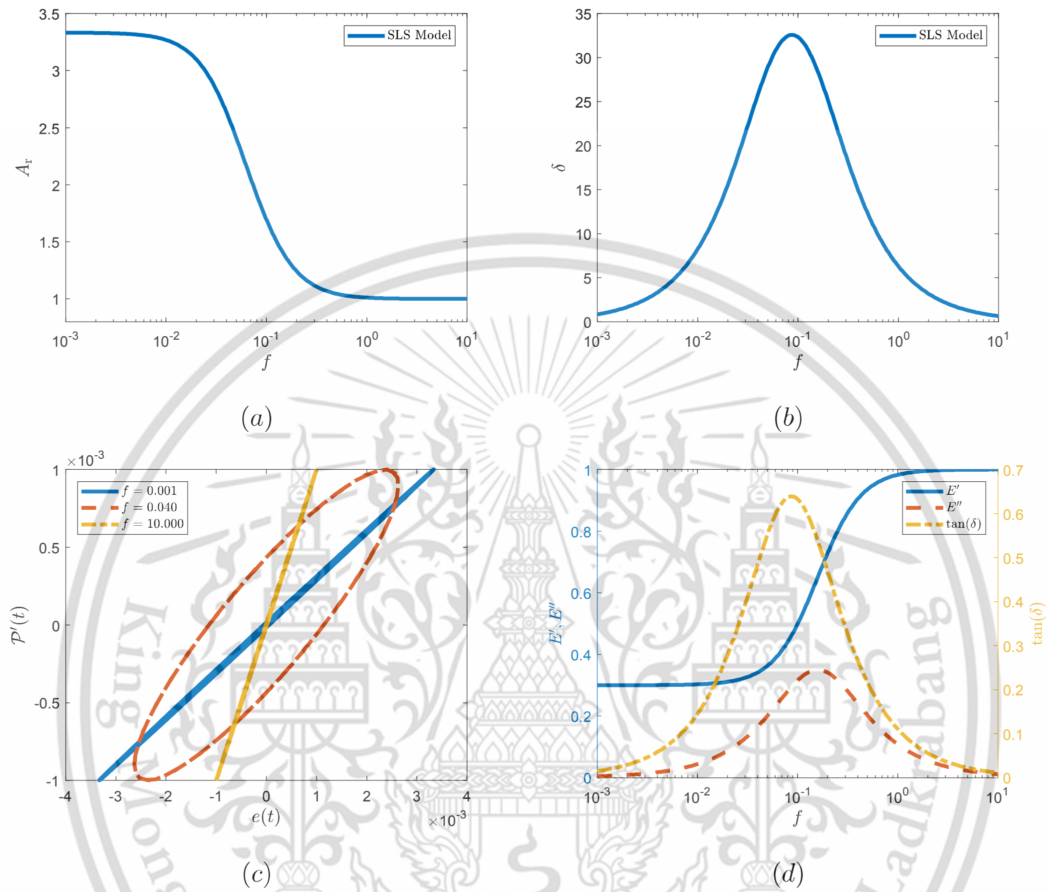

FIG. 2. Influence of frequency, f, on (a) System amplitude ratio A_r defined by $E_A/\mathcal{P}'_A$ (b) Phase angle δ under pressure sinusoidal oscillation at parameter condition $\mathcal{P}'_A = 0.001$, $K' = 0.3$ and $\tau' = 1$; (c) Mechanical-Hysteresis curve established by $e(t)$ vs. $\mathcal{P}'(t)$ corresponding to the response provided in Fig. 1 (d) Complex moduli parameters at parameter condition $\mathcal{P}'_A = 0.001$, $K' = 0.3$ and $\tau' = 1$.

III. MODIFIED PRESSURE-CONTROLLED DYNAMICS EQUATION

A. MPCD Equation

Mechanical-hysteresis is one of the behaviors which characterizes viscoelasticity. This behavior requires sinusoidal pressure oscillation as an input to establish mechanical-hysteresis curve. According to our previous study [20], we found the existing PFC-PCD method predicted mechanical-hysteresis curve inaccurately, in particular, at high pressure oscillation frequency when compared to the SLS model. With regard to the Taylor expansion [20], we observed that the PCD equation closely resembled Kelvin-Voigt model which can only exhibit viscoelastic-creep but not mechanical-hysteresis in solid material, in particular, at high frequency range. This inaccuracy arose from the missing pressure time derivative term in the existing PCD equation. Therefore, we have introduced this pressure time derivative term to the existing equation. We refer to this new modified PCD version as MPCD equation as shown below

$$\frac{dV}{dt} = L'_{\text{def}} \left(\bar{\mathcal{P}}_{\text{int}} - \bar{\mathcal{P}}_{\text{ext}} - \tau \frac{d\bar{\mathcal{P}}_{\text{ext}}}{dt} \right), \tag{11}$$

where $d\bar{\mathcal{P}}_{\text{ext}}/dt$ is the time pressure derivative term which is introduced to the existing PCD equation. τ is the shape factor coefficient that enables us to adjust the magnitude of peak in the loss factor parameters. This additional term helps MPCD equation in producing mechanical-hysteresis behavior consistent with SLS model, in particular, at high pressure oscillation frequency where the existing version is failed. It should be noted that the MPCD equation is established according to the SLS model (Zener model) which restricts the model to describing viscoelastic-creep and relaxation in exponential manner [22]. Therefore, this limitation also applies to the MPCD equation.

B. Approximated Dynamics Behavior of MPCD Equation

In this section, we aim to demonstrate that the approximation behavior of MPCD equation is consistent with SLS model. We begin with the definition of V

$$V(t) = L(t)^3, \quad L(t) = L_a\,(1 + e(t)) \tag{12}$$

where $V(t)$ is current volume at time t. L_a is the length of unit cell in the reference state. $L(t)$ is the length of unit cell at time t. $e(t)$ is strain at time t. It is obvious that we can alter volume time derivative term to strain time derivative term by chain's rule.

$$\frac{dV}{dt} = \frac{dV}{dL} \cdot \frac{dL}{de} \cdot \frac{de}{dt} \tag{13}$$

where $dV/dt = 3L^2$, $dL/de = L_a$. Substitute Eq. (13) into Eq. (11), we obtain

$$3L^2 L_a \frac{de}{d\tilde{t}} = L'_{\text{def}} \left(\bar{\mathcal{P}}_{\text{int}} - \bar{\mathcal{P}}_{\text{ext}} - \tau \frac{d\bar{\mathcal{P}}_{\text{ext}}}{dt} \right), \tag{14}$$

Note that $\mathcal{P}_{\text{int}} = -f + \mu\rho$, The equation (4) becomes

$$\bar{\mathcal{P}}_{\text{int}} = \frac{1}{V}\int_{\tilde{V}} \mathcal{P}_{\text{int}}\; d\mathbf{r} \tag{15}$$

Since $\bar{\mathcal{P}}_{\text{int}}$ changes its value with $e(t)$, therefore, $\bar{\mathcal{P}}_{\text{int}}$ can be written as a function of $e(t)$. However, if the small deformation is postulated around the undeformed state, $e_0 = 0$, $\bar{\mathcal{P}}_{\text{int}}$ can be written in Taylor expansion form [32] as

$$\bar{\mathcal{P}}_{\text{int}}(e_0 + \Delta e) = \bar{\mathcal{P}}_{\text{int}}(e_0) + \left.\frac{d\bar{\mathcal{P}}_{\text{int}}}{de}\right|_{e=e_0} \Delta e + \frac{1}{2!}\left.\frac{d^2\bar{\mathcal{P}}_{\text{int}}}{de^2}\right|_{e=e_0} \Delta e^2 + ... \tag{16}$$

where $e = e_0 + \Delta e$ and $\bar{\mathcal{P}}_{\text{int}}(e_0)$ is average internal pressure at undeformed state. If we approximate $\bar{\mathcal{P}}_{\text{int}}(e_0 + \Delta e)$ only at first derivative expansion, equation (16) yields

$$\bar{\mathcal{P}}_{\text{int}}(e_0 + \Delta e) \approx \bar{\mathcal{P}}_0 + \left.\frac{d\bar{\mathcal{P}}_{\text{int}}}{de}\right|_{e=e_0} \Delta e, \quad \bar{\mathcal{P}}_0 = \bar{\mathcal{P}}_{\text{int}}(e_0) \tag{17}$$

Substitute Eq. (17) into Eq. (14), we obtain

$$\frac{de}{dt} = \frac{1}{3}\frac{L'_{\text{def}}}{L_a^3}(1 + \Delta e)^{-2}\left(\Delta\bar{\mathcal{P}}_{\text{ext}} + \tilde{\tau}\frac{d\Delta\bar{\mathcal{P}}_{\text{ext}}}{d\tilde{t}} + \left.\frac{d\bar{\mathcal{P}}_{\text{int}}}{de}\right|_{e=e_0} \Delta e\right) \tag{18}$$

Note that $\Delta\bar{\mathcal{P}}_{\text{ext}} = \bar{\mathcal{P}}_0 - \bar{\mathcal{P}}_{\text{ext}}$ and $\Delta e \equiv e$ since $e_0 = 0$. Regarding the binomial series of $(1 + \Delta e)^{-2} = 1 - 2\Delta e + 3\Delta e^2 - ...$ Ref. [32]. Consider only the first term of the expansion; $(1 + \Delta e)^{-2} \approx 1 - 2\Delta e$. Substitute this relation into Eq. (18). We obtain

$$\frac{de}{dt} - \frac{1}{3}\frac{L'_{\text{def}}}{L_a^3}\left.\frac{d\bar{\mathcal{P}}_{\text{int}}}{de}\right|_{e=e_0} e = \frac{1}{3}\frac{L'_{\text{def}}}{L_a^3}\Delta\bar{\mathcal{P}}_{\text{ext}} + \frac{\tau}{3}\frac{L'_{\text{def}}}{L_a^3}\frac{d\Delta\bar{\mathcal{P}}_{\text{ext}}}{dt} \tag{19}$$

It should be noted that $d\bar{\mathcal{P}}_{\text{int}}/de|_{e=e_0} < 0$. If we denote $d\bar{\mathcal{P}}_{\text{int}}/de|_{e=e_0} = -K_{\mathcal{P}}$, where, $K_{\mathcal{P}} > 0$. Finally, Eq. (19) becomes

$$\frac{de}{dt} + \frac{K_{\mathcal{P}}}{3}\frac{L'_{\text{def}}}{L_a^3}\, e = \frac{1}{3}\frac{L'_{\text{def}}}{L_a^3}\Delta\bar{\mathcal{P}}_{\text{ext}} + \frac{\tau}{3}\frac{L'_{\text{def}}}{L_a^3}\frac{d\Delta\bar{\mathcal{P}}_{\text{ext}}}{dt} \tag{20}$$

Equation (20) has the structure like SLS model Eq. (5) where the pressure time derivative term is included on the right hand side of the equation. Nonetheless, the viscoelastic behavior stems from the MPCD equation not from PFC free energy. According to Eq. (20), it is obvious that the PFC free energy only influences the $K_{\mathcal{P}}$ variable, the second term on the left-hand side of Eq. (20), but not the structure of the equation. Therefore, the alternative choices of PFC free energy Eq. (1) can be applied and the PFC-MPCD method should still produce similar viscoelastic behavior correspond to those PFC free energy choices.

IV. METHOD OF SIMULATION

For simplicity in all numerical experiments, the PFC free energy functional used in this study is given by Eq. (1); it should be noted that MPCD equation can be used with any free energy functional forms which is not limited to Eq. (1). This free energy functional formulation is minimized by periodic density field of a body-centered-cubic (BCC) crystal structure. The one-mode approximation of the BCC crystal can be written as

$$\rho_{\mathrm{one}} = \bar{\rho} + 4A_s \left[\cos(q_a r_1)\cos(q_a r_2) + \cos(q_a r_1)\cos(q_a r_3) + \cos(q_a r_2)\cos(q_a r_3)\right], \tag{21}$$

where $q_a = 2\pi/L_a$. The value of q_a can be determined from minimization of the free energy density [33] leading to $q_a = 1/\sqrt{2}$ and, consequently, $L_a = 2\pi\sqrt{2}$.

One can also approximate the ranges of ϵ and $\bar{\rho}$ where the BCC solid is stable. This is achieved by calculating the free energy density of the solids using the one-mode approximations for stripes, hexagonal, and BCC structures and the free energy of the liquid using a uniform density. Then the phase diagram can be determined from the common tangent construction and the ranges of ϵ and $\bar{\rho}$ where the BCC solid is stable can be obtained [34].

In all simulations, we construct a BCC unit-cell with a periodic $N \times N \times N$ grid where $N = 16$ and the lattice parameter $L_a = 2\pi\sqrt{2}$. This results in the reference grid spacing, $\Delta r_0 = \sqrt{2}\pi/8$ in all dimensions, and the reference volume $V_0 = (2\pi\sqrt{2})^3$. The initial density profile is constructed with the one-mode approximation in Eq. (21), where the reference density, $\bar{\rho}_0$, is specified. The profile is then relaxed using the evolution equation (Eq. (2)), while fixing $\Delta r = \Delta r_0$ and $\bar{\rho} = \bar{\rho}_0$, until the equilibrium density profile is reached. At this state, the reference internal pressure, $\bar{\mathcal{P}}_0$, can be calculated using Eq. (4). Also, the numerical method employed to solve the evolution equation (Eq. (2)), PCD equation (Eq. (3)), and the MPCD equation (Eq. (11)) is the Fourier pseudo-spectral method where Fourier transform is used to calculate spatial derivatives and the forward finite difference scheme is used to discretize the time derivative. For the viscoelastic simulations, both PCD and MPCD equations are employed where pressure sinusoidal oscillation profile of $\bar{\mathcal{P}}_{\mathrm{ext}}(t)$ is specified and the change in the volume is used to update the grid spacing through the relation

$$\Delta r(t) = \left(\frac{V(t)}{N^3}\right)^{\frac{1}{3}}. \tag{22}$$

We note that the grid spacing $\Delta r(t)$ is identical in all directions due to the assumption of crystal under hydrostatic stress. During the simulation, the mass conservation is imposed by changing the average density through

$$\bar{\rho}(t) = \bar{\rho}_0 \frac{V_0}{V(t)}. \tag{23}$$

Also, the mechanical equilibrium is maintained throughout the deformation process; this is accomplished by relaxing the system using the evolution equation at every time step of the time evolution from the PCD and MPCD equations. The system response is characterized by the strain defined by

$$e(t) = \frac{\Delta r(t) - \Delta r_0}{\Delta r_0}, \tag{24}$$

which is identical in all directions. The profiles of $e(t)$ and $\bar{\mathcal{P}}_{\text{ext}}(t)$ is then used to quantify the viscoelastic behavior predicted form the PFC-PCD and PFC-MPCD methods. In hysteresis simulation, the applied pressure is set to

$$\bar{\mathcal{P}}_{\text{ext}}(t) = \bar{\mathcal{P}}_0 - \bar{\mathcal{P}}_A \sin(\omega t), \tag{25}$$

where $\bar{\mathcal{P}}_A$ is the pressure amplitude. The pressure deviation from the reference pressure will then be

$$\Delta\bar{\mathcal{P}}_0(t) \equiv \frac{\bar{\mathcal{P}}_0 - \bar{\mathcal{P}}_{\text{ext}}(t)}{\bar{\mathcal{P}}_0} = \frac{\bar{\mathcal{P}}_A}{\bar{\mathcal{P}}_0} \sin(\omega t). \tag{26}$$

With this type of pressure function, the system is then allowed to evolve temporally until the steady-stead strain-response is reached. The strain response profile at steady state will exhibit the sinusoidal behavior similar to Fig. 1 and we can numerically measure the strain amplitude e_A in order to calculate the amplitude ratio $A_r = e_A/\bar{\mathcal{P}}_A$ and phase angle δ. When plotting the hysteresis loop as indicated in Fig. 2(c), the complex moduli and loss tangent can be calculated by numerically identify the values of A (pressure value at zero strain), B (pressure value at maximum strain), and C (maximum strain value) as shown in Fig. 3. Then we evaluate the expressions: $E' = B/C$, $E'' = A/C$, and $\tan(\delta) = E''/E'$. We note that in all hysteresis simulations, $\bar{\mathcal{P}}_A$ is set to $0.02\bar{\mathcal{P}}_0$. Finally, all parameters obtained from numerical study according to PFC-PCD and PFC-MPCD methods have been thoroughly compared and discussed. It should be noted that the values of $\bar{\rho}_0$ and ϵ in all simulations are restricted at -0.260 and 0.175, respectively. These values of $\bar{\rho}_0$ and ϵ ensure the stability of the BCC crystal as shown in the phase diagram provided by Wu et al. Ref. [34].

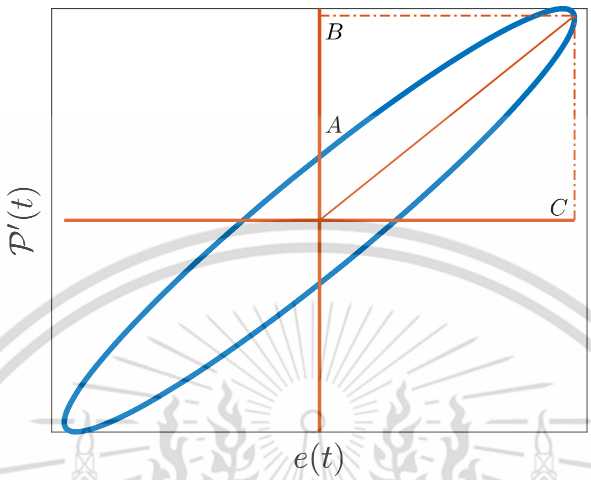

FIG. 3. Hysteresis scheme provides all complex moduli parameter information; Storage modulus $E' = B/C$, Loss modulus $E'' = A/C$ and Loss tangent factor $\tan(\delta) = E''/E'$; A is pressure at zero strain, B is pressure at maximum strain and C is maximum strain value.

V. RESULTS AND DISCUSSION

A. Strain Response and Mechanical Hysteresis Behavior

In this part, we demonstrate the strain response under sinusoidal pressure oscillation and its mechanical-hysteresis behavior exhibited by PFC-MPCD and PFC-PCD methods. The steady-state strain responses regarding the PFC-MPCD method are given Fig. 4(a)-(c) whereas the strain responses regarding the PFC-PCD method are shown in Fig. 4(d)-(f) for comparison. According the numerical results at oscillation frequency $f = 0.004$ and $f = 0.1$, the steady-state strain response predicted by both methods are in good agreement to each other. Both methods demonstrate the strain amplitude reduction and increased phase lag (phase angle) at elevated oscillation frequency. These results are qualitatively consistent with those of SLS model prediction in Fig. 1 (a)-(b). However, at oscillation frequency $f = 1$, both methods seem to behave differently. The amplitude of strain response exhibited by PFC-MPCD method tends to decline to the finite value while phase lag between strain response and pressure oscillation predicted by this method seems to be in-phase at this frequency. On the contrary, the amplitude of strain response exhibited by PFC-PCD method tends

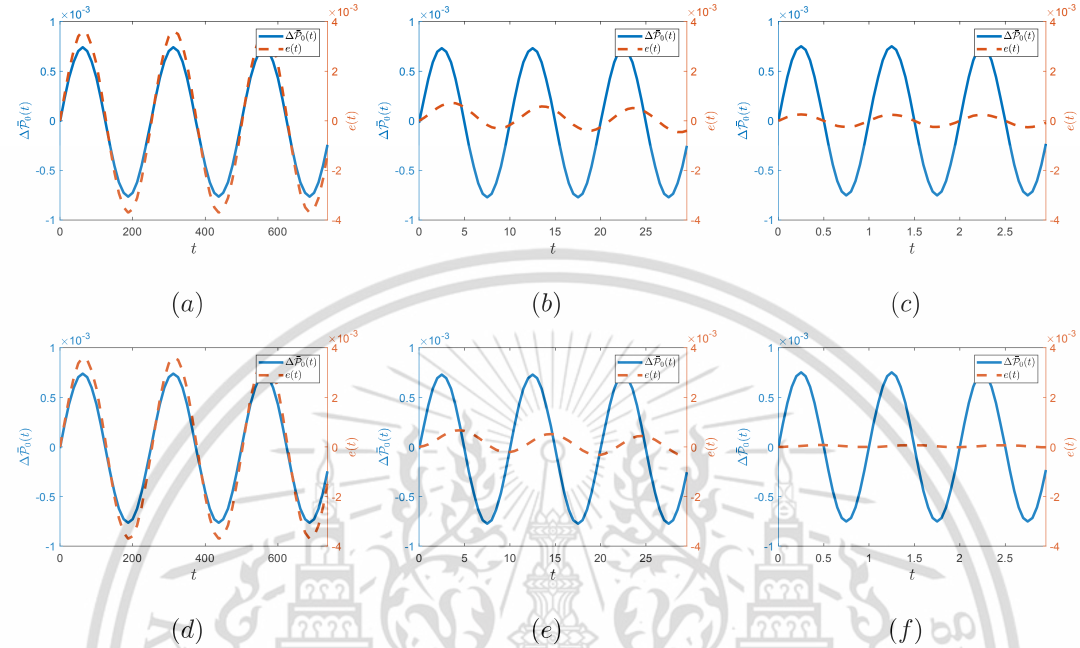

FIG. 4. Influence of frequency, f, on system response; Sinusoidal pressure input $\Delta\bar{\mathcal{P}}_0(t)$ (solid-line) and strain response $e(t)$ (dash-line) established by PFC-MPCD method (a) $f = 0.004$ (b) $f = 0.1$ (c) $f = 1$ at $\tau = 0.9814$; Sinusoidal pressure input $\Delta\bar{\mathcal{P}}_0(t)$ (solid-line) and strain response $e(t)$ (dash-line) established by PFC-PCD method (d) $f = 0.004$ and (e) $f = 0.1$ (f) $f = 1$. Note that all simulation parameters are set at $|\bar{\rho}_0| = 0.2600$, $\epsilon = 0.1750$ and $L_{\mathrm{def}} = (2\pi\sqrt{2})^3$.

to vanish. Moreover, the phase lag between the strain response and pressure oscillation predicted by the PFC-PCD method becomes larger at this frequency which is contrast to SLS model prediction as shown Fig. 1(c). To obtain more insight into these phenomena, we study the impact of frequency f on amplitude ratio A_{r} and phase lag (δ) exhibited by PFC-MPCD and PFC-PCD methods as indicated in Fig. 5(a)-(b). It is obvious that both methods exhibit amplitude ratio reduction with increasing frequency. However, this prediction according to the PFC-PCD method tends to vanishingly small at high-frequency range whereas the prediction regarding PFC-MPCD method remains at finite value. Besides, the phase lag predicted by both methods tends to increase at elevated frequency but until the certain value is reached. In particular, the result exhibited by PFC-MPCD method tends to reduce its magnitude with increasing frequency after its peak location, unlike PFC-PCD method prediction which tends to exhibit higher phase lag without the peak location.

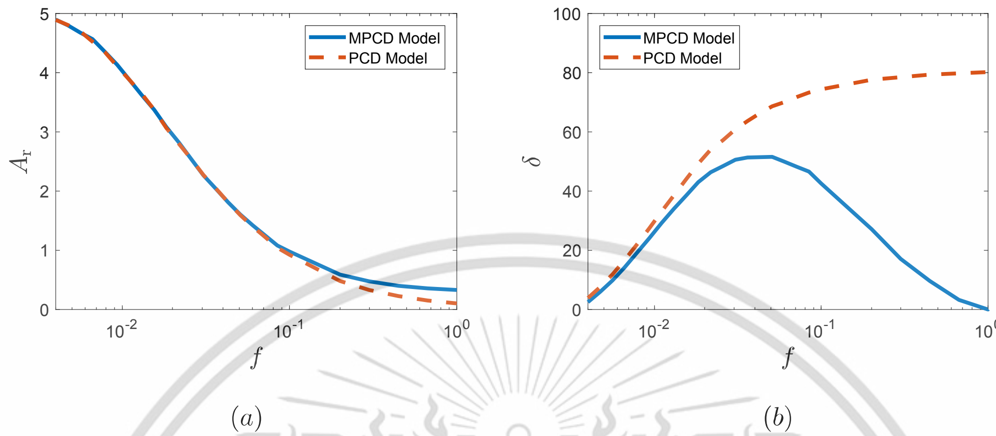

FIG. 5. Influence of frequency, f, on (a) Amplitude ratio (A_r) predicted by PFC-MPCD method (solid-line) and PFC-PFC method (dash-line) and on (b) Phase angle (δ) or Phase lag predicted by PFC-MPCD method (solid-line) and PFC-PFC method (dash-line). Note that all simulation parameters are set at $|\bar{\rho}_0| = 0.2600$, $\epsilon = 0.1750$, $L_{\text{def}} = (2\pi\sqrt{2})^3$ and $\tau = 0.9814$ for PFC-MPCD method.

These results obtained from the numerical study indicate that the prediction demonstrated by both methods are consistent at low-frequency range but tends to differ at high frequency.

The magnitude of the amplitude ratio can also be illustrated in the mechanical-hysteresis loop according to Fig. 6(a)-(b) where the results in Fig. 4(a)-(f) are plotted on a pressure-strain axis. As the frequency increases, the hysteresis loops predicted by both methods rotate counter-clockwise, indicating smaller strain amplitude (or amplitude ratio). At frequency $f = 1$, the hysteresis loop predicted by the PFC-PCD method almost forms a vertical line with the y-axis in Fig. 6(b) because the amplitude ratio is driven to an extremely small value or almost zero amplitude. This is in contrast to the hysteresis loop predicted by PFC-MPCD method which remains tilted away from the y-axis as indicated by Fig. 6(a); this figure shows that strain amplitude has not been driven to zero amplitude at the high-frequency range.

In summary, the results demonstrated by PFC-MPCD method as shown in Fig. 5(a)-(b) and Fig. 6(a) qualitatively agree with the SLS model as indicated in Fig. 2(a)-(c). While, all those results exhibited by PFC-PCD method as illustrated in Fig. 5(a)-(b) and Fig. 6(b) tend to differ from the SLS model, in particular, at the high-frequency range as indicated in Fig. 2(a)-(c).

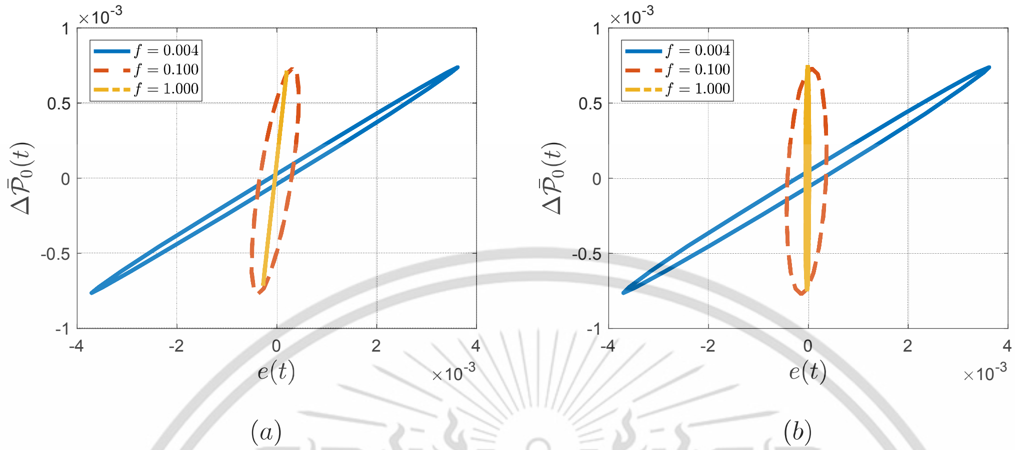

FIG. 6. Influence of frequency, f, on mechanical-hysteresis behavior (a) Mechanical-hysteresis behavior predicted by PFC-MPCD method corresponding to Fig. 4 (a)-(c) at $\tau = 0.9814$; (b) Mechanical-hysteresis behavior predicted by PFC-PCD method corresponding to Fig. 4 (d)-(f). Note that all simulation parameters are set at $|\bar{\rho}_0| = 0.2600$, $\epsilon = 0.1750$ and $L_{\mathrm{def}} = (2\pi\sqrt{2})^3$.

B. Prediction of Complex Moduli Parameters

In this part, we aim to demonstrate the difference in complex moduli parameters prediction between PFC-MPCD method and PFC-PCD method. All complex moduli parameters exhibited by the PFC-MPC method are illustrated in Fig. 7(a). while the results obtained from the PFC-PCD method are showed in Fig. 7(b) for comparison. According to the numerical study, the storage modulus (E') predicted by PFC-MPCD tends to monotonically increased with increasing frequency and becomes constant at the certain frequency while loss modulus (E'') and loss tangent factor ($\tan(\delta)$) tends to increase in magnitude until their peak locations are reached. This is in good agreement with the SLS model prediction in Fig. 2(d) and consistent with real solid behavior [21]. In particular, all results predicted by PFC-MPCD method are agreeing with numerous experimental observations which can be found in [25, 26] for shear and young modulus, which are proportional to storage modulus, in In-Sn and Pb-Sn as well as for loss angle in some alloys [27] which is related to loss tangent factor. Besides, this consistency is even more pronounced in rubber [28–30] and in elastomer [31]. This is in contrast to the results obtained from PFC-PCD prediction in Fig. 7(b) where all complex moduli parameters monotonically increased with increasing frequency without

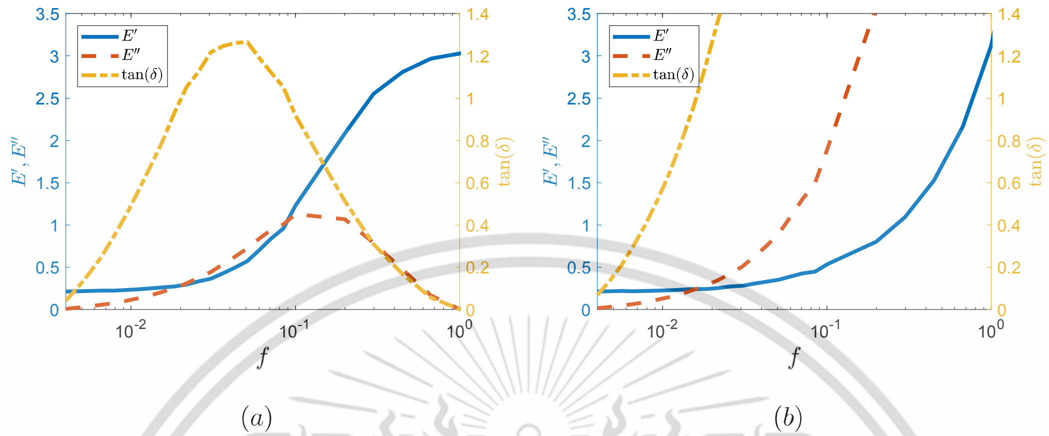

FIG. 7. Influence of frequency, f, on complex moduli parameters (a) Predicted by PFC-MPCD method; Storage modulus (E') (solid-line), Loss modulus (E'') (dash-line) and Loss tangent factor ($\tan(\delta)$) (dense-dash-line) at $\tau = 0.9814$ (b) Predicted by PFC-PCD method; Storage modulus (E') (solid-line), Loss modulus (E'') (dash-line) and Loss tangent factor ($\tan(\delta)$) (dense-dash-line). Note that all simulation parameters are set at $|\bar{\rho}_0| = 0.2600$, $\epsilon = 0.1750$ and $L_{\mathrm{def}} = (2\pi\sqrt{2})^3$.

peaks location for loss modulus (E'') and loss tangent factor ($\tan(\delta)$) as well as without the certain frequency value which allows storage modulus E' to become constant.

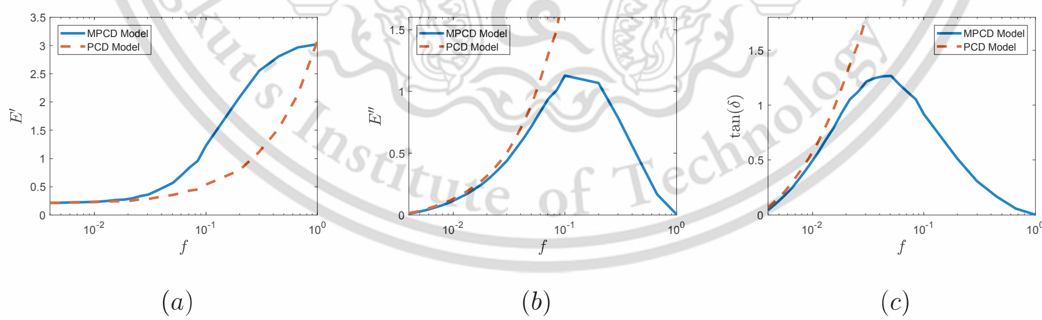

FIG. 8. Influence of frequency, f, on complex moduli parameters (a) Storage modulus (E'); predicted by PFC-MPCD method (solid-line) and PFC-PCD method (dash-line) (b) Loss modulus (E''); predicted by PFC-MPCD method (solid-line) and PFC-PCD method (dash-line) (c) Loss tangent factor ($\tan(\delta)$) predicted by PFC-MPCD method (solid-line) and PFC-PCD method (dash-line). Note that all simulation parameters are set at $|\bar{\rho}_0| = 0.2600$, $\epsilon = 0.1750$, $L_{\mathrm{def}} = (2\pi\sqrt{2})^3$ and $\tau = 0.9814$ for PFC-MPCD method.

To further investigate into the difference between the results predicted by PFC-MPCD and PFC-PCD methods, we compare each parameter exhibited by both methods in Fig. 8(a)-(c). It is obvious that the results obtained from both methods are in good agreement in a low-frequency range but tend to differ at very frequency. All complex moduli parameters obtained from PFC-PCD method prediction have increased as increasing frequency without the limit. This is unlike the results obtained from PFC-MPCD method prediction. Although all complex moduli predicted by the method increases as increasing frequency, they tend to become limited at a certain frequency value. In particular, all loss parameters, loss modulus (E'') and loss tangent factor ($\tan(\delta)$), predicted by the PFC-MPCD method can demonstrate at least one peak location. These observations are in good agreement with the real solid behavior suggested by Ref. [21] and experimental evidence that can be found in [25–31]. The peak location in loss modulus (E'') parameter also indicates the information on the suitable working frequency where the energy is most dissipated in damping material design. On the contrary, the PFC-PCD method cannot provide this information as indicated in Fig. 8(b). It should be noted that the particular form of the PFC free energy Eq. (1) is applicable to crystalline materials such as metals [34]; therefore, it might seem that the results from this work only restricts to these types of materials. However, since the viscoelastic behavior originates from the MPCD equation, not the PFC free energy, the alternative choices of PFC free energy Eq. (1) can be used and the PFC-MPCD method should still exhibit similar viscoelastic behavior correspond to those PFC free energy choices. The capability to generalize the PFC free energy enables us to model viscoelastic behavior in different types of materials such as polymeric materials and elastomer where viscoelasticity behavior is much more pronounced than that in metals.

VI. CONCLUSION

In this work, we propose a new modified pressure-controlled dynamics (MPCD) equation incorporating with the phase-field-crystal (PFC) method which refers to as PFC-MPCD method. This PFC-MPCD method differs from the original PFC-PCD method in that the pressure time derivative term has been introduced to the new version which enables the method to predict mechanical-hysteresis behavior and complex moduli parameters correctly, in particular, at very frequency range where the original PFC-PCD method is incapable.

This modification is inspired by the standard linear solid (SLS) model; generally used to predict various viscoelastic phenomena in a solid structure such as viscoelastic-creep, stress-relaxation and mechanical-hysteresis behavior; where the pressure time derivative term is available in its formulation. This time derivative term has played a key role in producing mechanical-hysteresis behavior correctly. The numerical study regarding PFC-MPCD method demonstrates a good agreement between the results predicted by PFC-MPCD method and SLS model in many aspects. In the system response aspect, the PFC-MPCD method shows that the magnitude of strain amplitude reduces with increased sinusoidal pressure oscillation frequency but then becomes finite value at very frequency. This is in contrast to the PFC-PCD method where the magnitude of strain amplitude vanishes at very frequency range. Furthermore, the magnitude of phase angel predicted by PFC-MPCD method is consistent with SLS model unlike PFC-PCD method exhibits extremely large magnitude of phase angle at the high-frequency range without the peak location like SLS and PFC-MPCD method prediction. In mechanical-hysteresis behavior aspect, the prediction of mechanical-hysteresis behavior obtained from both methods is in good agreement at early frequency. However, the mechanical-hysteresis curve predicted by PFC-PCD method tends to be vertical with y-axis which indicates that the system produces zero strain at a very frequency which is inconsistent with SLS and PFC-MPCD method which produce a limited strain value at a very frequency while all loss parameters predicted by the method pass through at least one peak location. These results generally agree with the real solid material behavior and experimental observations which is in contrast to PFC-PCD method prediction at the high-frequency range. In summary, the PFC-PCD method can generally be employed to predict mechanical-hysteresis behavior and complex moduli parameters, however, the application should be limited at the low-frequency range where the viscous effect is not dominated. Whereas, the PFC-MPCD method is more suitable to use in predicting mechanical-hysteresis behavior and complex moduli parameters at the broader pressure oscillation frequency. This is consistent with a real solid material behavior which allows us to predict a suitable working condition for damping materials. We expect that our method can be extended to a more complex system with microstructural features such as grain boundary, dislocation, surface or even with other free energy functional form where viscoelasticity behavior is much more pronounced and still be capable to exhibit the accurate mechanical-hysteresis behavior and complex moduli parameters.

VII. ACKNOWLEDGMENT

This research was supported by the NSTDA-University-Industry Research Collaboration (NUI-RC) program under grant No. NUI-RC-M33-22-59-001D, Thailand Research Fund (TRF) under Grant No. TRG5880008, the New Researcher Scholarship of Coordinating Center for Thai Government Science and Technology Scholarship Students, Ministry of Science and Technology (FDA-CO-2561-840g-TH), King Mongkut's Institute of Technology Ladkrabang Research Fund under Grant No. KREF046103, and High Performance Computing Services from (Thailand) National Electronics and Computer Technology Center (NECTEC). The authors are also indebted to Dr.Sasawat Mahabunphachai for his helpful discussion and encouragement on the research.

Appendix A: Derivation of Complex Moduli

In this appendix, we aim to derive all complex moduli parameters regarding SLS model using Laplace transform technique [24]. To achieve our objective, we begin with Eq. (5) as below

$$\frac{de}{dt} + K'e = \mathcal{P}' + \tau'\frac{d\mathcal{P}'}{dt} \tag{A1}$$

We apply Laplace transform both sides to obtain

$$s\hat{e} + K'\hat{e} = \hat{\mathcal{P}}' + \tau' s\hat{\mathcal{P}}' \tag{A2}$$

where $\hat{e}$ is Laplace transform of e. $\hat{\mathcal{P}}'$ is the Laplace transform of $\mathcal{P}'$. Rearrange Eq. (A2), it yields

$$\hat{\mathcal{P}}' = \hat{e}\,\frac{K'+s}{1+\tau' s} \tag{A3}$$

Denote that $e(t) = e_A \sin(\omega t)$, then, $\hat{e} = e_A\omega/\left(\omega^2 + s^2\right)$. Substitute this relation in Eq. (A3), it yields

$$\hat{\mathcal{P}}' = \frac{e_A\omega}{\omega^2+s^2}\cdot\frac{K'+s}{1+\tau' s} \tag{A4}$$

Using partial fraction technique

$$\hat{\mathcal{P}}' = \frac{B+As}{\omega^2+s^2} + \frac{C}{1+\tau' s} \tag{A5}$$

Rearrange Eq. (A5), we obtain

$$\hat{\mathcal{P}}' = \frac{B + C\omega^2 + (A+B\tau')s + (C+A\tau')s^2}{(\omega^2+s^2)(1+\tau' s)} \tag{A6}$$

To find each coefficient (A, B, C) value, we denote that

$$\begin{aligned} A\tau' + C &= 0 \\ A + B\tau' &= e_A\omega \\ B + C\omega^2 &= e_A\omega K' \end{aligned} \tag{A7}$$

Then, each coefficient value is

$$\begin{aligned} A &= \frac{1-\tau' K'}{1+(\tau'\omega)^2}\omega e_A \\ B &= \frac{K'+\tau'\omega^2}{1+(\tau'\omega)^2}\omega e_A \\ C &= \frac{\tau' K'-1}{1+(\tau'\omega)^2}\omega\tau' e_A \end{aligned} \tag{A8}$$

Substitute Eq. (A8) in Eq. (A5), we obtain

$$\hat{\mathcal{P}}' = \frac{K' + \tau'\omega^2}{1 + (\tau'\omega)^2} \cdot \frac{e_A\omega}{\omega^2 + s^2} + \frac{(1 - \tau'K')\,\omega}{1 + (\tau'\omega)^2} \cdot \frac{e_A s}{\omega^2 + s^2} + \frac{(\tau'K' - 1)\,\tau'\omega}{1 + (\tau'\omega)^2} \cdot \frac{e_A}{(1 + \tau's)} \tag{A9}$$

Using inverse Laplace transform on both sides, Eq. (A9) finally becomes

$$\mathcal{P}'(t) = e_A\left[\frac{K' + \tau'\omega^2}{1 + (\tau'\omega)^2}\right]\sin(\omega t) + e_A\omega\left[\frac{1 - \tau'K'}{1 + (\tau'\omega)^2}\right]\cos(\omega t) - e_A\omega\left[\frac{1 - \tau'K'}{1 + (\tau'\omega)^2}\right]e^{-t/\tau'} \tag{A10}$$

Denote that

$$\mathcal{P}'_0\cos(\delta) = e_A\left[\frac{K' + \tau'\omega^2}{1 + (\tau'\omega)^2}\right], \quad \mathcal{P}'_0\sin(\delta) = e_A\omega\left[\frac{1 - \tau'K'}{1 + (\tau'\omega)^2}\right] \tag{A11}$$

It should be noted that $(\mathcal{P}'_0/e_A)\cos(\delta) = E'$ and $(\mathcal{P}'_0/e_A)\sin(\delta) = E''$ where E' is storage modulus and E'' is loss modulus which can be expressed as below

$$\begin{gathered} E' = \frac{K' + \tau'\omega^2}{1 + (\tau'\omega)^2}, \quad E'' = \left[\frac{1 - \tau'K'}{1 + (\tau'\omega)^2}\right]\omega \\ \tan(\delta) = \left[\frac{1 - \tau'K'}{K' + \tau'\omega^2}\right]\omega \end{gathered} \tag{A12}$$

in which $\tan(\delta)$ represents loss tangent factor defined by E''/E'.

---

[1] K. R. Elder, M. Katakowski, M. Haataja, and M. Grant, Physical Review Letters **88**, 245701 (2002).

[2] K. R. Elder and M. Grant, Physical Review E **70**, 051605 (2004).

[3] K. Elder, N. Provatas, J. Berry, P. Stefanovic, and M. Grant, Physical Review B **75**, 064107 (2007).

[4] T. Pusztai, G. Tegze, G. I. Tóth, L. Környei, G. Bansel, Z. Fan, and L. Gránásy, Journal of Physics: Condensed Matter **20**, 404205 (2008).

[5] S. Hu and S. Wang, Physica B: Condensed Matter **552**, 104 (2019).

[6] N. Pisutha-Arnond, V. Chan, K. Elder, and K. Thornton, Physical Review B **87**, 014103 (2013).

[7] Z.-L. Wang, Z.-F. Huang, and Z. Liu, Physical Review B **97**, 144112 (2018).

[8] W. Zhou, J. Wang, Z. Wang, Y. Huang, C. Guo, J. Li, and Y. Guo, Chinese Physics B **26**, 090702 (2017).

[9] P. Stefanovic, M. Haataja, and N. Provatas, Physical Review E **80**, 046107 (2009).

[10] P. Y. Chan, G. Tsekenis, J. Dantzig, K. A. Dahmen, and N. Goldenfeld, Physical review letters **105**, 015502 (2010).

[11] P. Y. Chan, N. Goldenfeld, and J. Dantzig, Physical Review E **79**, 035701 (2009).

[12] T. Hirouchi, T. Takaki, and Y. Tomita, International Journal of Mechanical Sciences **52**, 309 (2010).

[13] J. Berry, K. Elder, and M. Grant, Physical Review B **77**, 224114 (2008).

[14] J. Mellenthin, A. Karma, and M. Plapp, Physical Review B **78**, 184110 (2008).

[15] P. Stefanovic, M. Haataja, and N. Provatas, Physical review letters **96**, 225504 (2006).

[16] T. Hirouchi, T. Takaki, and Y. Tomita, Computational Materials Science **44**, 1192 (2009).

[17] G. Kocher and N. Provatas, Physical Review Letters **114**, 155501 (2015).

[18] J. Em-Udom and N. Pisutha-Arnond, in IOP Conference Series: Materials Science and Engineering, Vol. 361 (IOP Publishing, 2018) p. 012006.

[19] J. Em-Udom and N. Pisutha-Arnond, in IOP Conference Series: Materials Science and Engineering, Vol. 361 (IOP Publishing, 2018) p. 012009.

[20] J. Em-Udom and N. Pisutha-Arnond, Advances in Mathematical Physics, Hindawi **(Submitted)** (2019).

[21] T. Pritz, Journal of Sound and Vibration **214**, 83 (1998).

[22] R. S. Lakes, Viscoelastic Materials (Cambridge University Press, 2009).

[23] W. N. Findley and F. A. Davis, Creep and relaxation of nonlinear viscoelastic materials (Courier Corporation, 2013).

[24] L. Dai and R. N. Jazar, Nonlinear Approaches in Engineering Applications (Springer, 2012).

[25] R. Lakes and J. Quackenbush, Philosophical Magazine Letters **74**, 227 (1996).

[26] P. Buechner, D. Stone, and R. Lakes, Scripta materialia **41**, 561 (1999).

[27] G. Cagnoli, L. Gammaitoni, J. Kovalik, F. Marchesoni, and M. Punturo, Physics Letters A **255**, 230 (1999).

[28] A. R. Payne and J. R. Scott, Engineering design with rubber (Maclaren, 1960).

[29] Y. Wada, R. Ito, and H. Ochiai, Journal of the Physical Society of Japan **17**, 213 (1962).

[30] L. Rouleau, R. Pirk, B. Pluymers, and W. Desmet, Journal of Aerospace Technology and Management **7**, 200 (2015).

[31] V. Sessner, A. Jackstadt, W. Liebig, L. Kärger, and K. Weidenmann, Journal of Composites Science **3**, 3 (2019).

[32] G. B. Arfken and H. J. Weber, Mathematical methods for physicists (AAPT, 1999).

[33] N. Provatas and K. Elder, Phase-field methods in materials science and engineering (John Wiley & Sons, 2011).

[34] K.-A. Wu and A. Karma, Physical Review B **76**, 184107 (2007).

ประวัติผู้เขียน

ชื่อ-นามสกุล นาย จตุพล เอมอุดม
วัน เดือน ปีเกิด 9 พฤษภาคม 2525 อำเภอ เมือง จังหวัด อุดรธานี
ที่อยู่ 75/29 ม.สินทวีการ์เด้น 2 ถ.สุขุมวิท ต.บ้านฉาง อ.บ้านฉาง จ.ระยอง 21130
ประวัติการศึกษา 2542-2546 วิศวกรรมศาสตรบัณฑิต สาขา วิศวกรรมเครื่องกล จุฬาลงกรณ์มหาวิทยาลัย
2546-2550 วิศวกรรมศาสตรมหาบัณฑิต สาขา วิศวกรรมเครื่องกล จุฬาลงกรณ์มหาวิทยาลัย
ความชำนาญเฉพาะด้าน 1.) การออกแบบและตรวจสอบอุปกรณ์รับแรงดันที่ใช้ในอุตสาหกรรมปิโตรเลียม และ ปิโตรเคมิคอล
2.) การประเมินสภาพความพร้อมการใช้งานของอุปกรณ์รับแรงดันที่ใช้ในอุตสาหกรรมปิโตรเลียม และ ปิโตรเคมิคอล ตามมาตรฐาน ASME/API
3.) การออกแบบพัฒนาโปรแกรมคอมพิวเตอร์เพื่อช่วยในการตัดสินใจในการแก้ปัญหาด้านวิศวกรรมวัสดุ และ ประเมินอายุการใช้งานของอุปกรณ์ที่ใช้ในกระบวนการผลิตในกลุ่มอุตสากรรมปิโตรเลียม และ ปิโตรเคมิคอล
ประสบการณ์การทำงานและผลงานวิจัย
พ.ศ.2550-2554 วิศวกรตรวจสอบอุปกรณ์การกลั่นโรงกลั่นน้ำมัน บริษัท บางจากปิโตรเลียม จำกัด มหาชน
พ.ศ.2554-2558 วิศวกรแมคคานิคอลอินทีกริตี้ บริษัท ร่วมทุนระหว่าง เครือซีเมนต์ไทย กับ ดาวเคมิคอล สหรัฐอเมริกา
พ.ศ.2558-ปัจจุบัน นักศึกษาปริญญาเอกเต็มเวลาที่ ภาควิชา วิศวกรรมอุตสาหการ คณะ วิศวกรรมศาสตร์ สถาบันเทคโนโลยีพระจอมเกล้าเจ้าคุณทหารลาดกระบัง ภายใต้การสนับสนุนเงินทุนจากโครงการพัฒนาศักยภาพบุคลากรเพื่อการวิจัยและพัฒนาสำหรับภาคอุตสาหกรรม (NSTDA-University-Industry Research Collaboration, NUI-RC) ภายใต้หมายเลขสัญญา NUI-RC-M33-22-59-001D สวทช.